HOKKAIDO UNIVERSITY

Title	Geostatistical Reservoir Modeling of Trending Heterogeneity Specified in Focused Recharge Zone : A Case Study of Toyohira River Alluvial Fan, Sapporo, Japan
Author(s)	Sakata, Yoshitaka
Citation	. ( ) 10909
Issue Date	2013-03-25
DOI	10.14943/doctoral.k10909
Doc URL	http://hdl.handle.net/2115/52995
Type	theses (doctoral)
File Information	Doctoral Thesis_ Y.SAKATA_Feb_2013.pdf

Instructions for use

Doctoral Thesis

Geostatistical Reservoir Modeling of Trending Heterogeneity Specified in Focused Recharge Zone:

A Case Study of Toyohira River Alluvial Fan, Sapporo, Japan

By

Yoshitaka SAKATA

Submitted for the Degree of Doctor of Philosophy

Department of Natural History of Sciences
Graduate School of Science
Hokkaido University, Sapporo, Japan

February, 2013

Table of Contents

Abstract

Coarse alluvial deposits are increasingly important as water reservoirs, especially in arid and semi-arid regions. Coarse alluvial deposits consist mainly of poorly sorted sand and gravel, and the geologic heterogeneity is generally large and trending as a result of depositional and post-depositional processes. Geostatistical approaches in groundwater reservoir modeling are various, but are often based on the assumption of stationarity. This assumption is not necessarily valid in coarse alluvial deposits, and a standard approach in trending heterogeneity is to separate the target variable (e.g., hydraulic conductivity) into a global trend component and a residual component. However, the trend component has rarely been determined because of scarcity and uncertainty in measurements, especially in deep parts of deposits.

This dissertation primarily covers a focused recharge zone around and beneath a losing river flowing on coarse alluvial deposits. The zone is just one part of a basin, and is thus limited in area. However, the complex system of groundwater flow and solute transport is directly reflected in the large and trending heterogeneity. First, surface water infiltration from the riverbed induces downward groundwater flows. Next, lateral flow components are gradually added, and the magnitudes are changed depending on geologic heterogeneity. In particular, connected voids in gravel deposits give rise to preferential groundwater flows. If the depth dependence of permeability exhibits, for example, a coarsening-upward trend, the groundwater flows accumulate in the shallower parts. As a result of the complex flow system, solute concentration and water temperature are characterized specifically in space and time. Thus, detailed research in a limited zone will reveal the trending heterogeneity in coarse alluvial deposits, and will allow assessment of its importance in groundwater modeling.

Targeting the Toyohira River alluvial fan (Sapporo, Hokkaido, Japan), this dissertation presents well data analysis, flow measurements, permeability modeling, and stochastic simulation. First, vertical hydraulic gradient in the fan is mapped to elucidate the three-dimensional groundwater flow system in the fan, and to determine the focused recharge zone along the Toyohira River. The wide range of uncertainty in available well data is addressed by combining a filtering process, kriging interpolation, and cross-validation. Consequently, the reasonably accurate maps show that there are downward groundwater flows in the fan and a negative peak in

vertical hydraulic gradient along the losing river.

A synoptic survey of discharge is performed to determine losing section in the Toyohira River, and to estimate the rate of seepage loss. The synoptic survey of the Toyohira River proves especially difficulty due to the unsteady turbulent flow and roughness of the gravel bed. This research develops survey methodology employing a high-accuracy current meter and a detailed arrangement of verticals. As a result, the relative uncertainty in discharge measurements is only 2-4%, and the distinct losing section is found in the mid-fan. The seepage rate is estimated to be about 1 m^3/s.

Depth dependence of permeability in the fan deposits is also examined to detect the global trend in the vertical direction. For this purpose, this study uses the index "matrix packing level" for relatively undisturbed cores of gravel deposits, and finds good correlation between slug test results and core properties. The vertical profiles of estimated hydraulic conductivity are analyzed by using moving average and linear regression methods. Hence, in the apex and mid-fan, an exponential function of permeability is formulated, of which the exponent decay is two- to three orders of magnitude larger than that in consolidated rock. No vertical trend in permeability is found in the fan-toe, indicating that the vertical trend in the upper fan is formed by depositional processes with high-energy flows.

Stochastic simulation of trending heterogeneity is also performed by using the exponent model derived from the field observations. Sequential Gaussian simulation is applied to produce 100 realizations of hydraulic conductivity in each study case. The variations in hydraulic heads, river leakage, and groundwater temperature are calculated in each realization by using a high-resolution two-dimensional cross-sectional model. The calculated results are compared with measurements in observation wells, and optimal realizations that satisfy error estimators are extracted in each study case. Consequently, modeling of trending heterogeneity is indispensable for describing groundwater flow and heat transport in the focused recharge zone, because several optimal realizations are obtained in the case of trending heterogeneity and none in the case of stationary heterogeneity. Compared with whether there is trending or stationary heterogeneity, other uncertain factors (river conditions, thermal diffusivity, the range of variograms of residuals, and temperature-dependent effects) less significantly affect the optimal solutions. On the other

hand, a block-averaged model of trending heterogeneity also yields optimal realizations that are slightly inferior to those of a high-resolution model in terms of agreement between calculations and observations. However, the number of optimal realizations is larger than that of a high-resolution model, indicating the applicability of block averaging to a larger basin model.

A current avenue of the research is to expand the two-dimensional high-resolution model to a three-dimensional basin model, not only for the Toyohira River alluvial fan but also for other coarse alluvial aquifers. Lastly, this dissertation discusses several problems to be addressed with the advanced model in order to determine hydrogeologic sequences, diffuse recharge, urbanization effects, and upscaling procedure.

Acknowledgements

Figures

Tables

Abbreviations

a: practical range of variogram

ADCP: Acoustic Doppler current profiler

ADV: Acoustic Doppler velocimeter

B: Nugget of variogram

C: Sill of variogram

$C(x_i, x_j)$: Covariance between x_i and x_j

CV: Cross validation

d: Diameter of grain size

d_e: effective grain diameter (d_{20} in this study)

D: Day

DEM: Digital elevation model

$E[x]$: Statistical expectation of x

GLS: generalized least squares

GTE: Groundwater table elevation in meter above sea level

GTD: Groundwater table depth from ground surface

h: Hydraulic head

$\boldsymbol{h}$: the vector between measurement points

HRDB: Hokkaido Regional Development Bureau

ISO: International Organization for Standardization

K: Hydraulic conductivity

K': Hydraulic conductivity estimated by permeability model

$\overline{K}$: Hydraulic conductivity averaged by estimated K'

KED: Kriging with external drift

KP: Distance from the confluence of the Toyohira and the Ishikari Rivers

L_i: length fraction of each matrix packing level i, the index i ranges between 1 and 4

m: Meter

m asl: Meter above mean sea level in the Tokyo bay

ME: Mean error

OFG: Open framework gravel

OLS: ordinary least squares

pdf: probability density function

Pe: Peclet number

phi: Negative value of base-2 logarithm of d

Q: River Discharge

$Re(\boldsymbol{x})$: Residual component of common logarithm of K

RK: Regression kriging

$RMSE$: Root mean squared error

$RMSN$: Normalized root mean squared error

SDE: Screen depth elevation

SEAWAT: A Computer Program for Simulation of Three-Dimensional Variable-Density

Groundwater Flow developed by USGS

SGS: Sequential Gaussian Simulation

u: Uncertainty of attribute, indicating relative percent of attribute, standard deviation

UK: Universal kriging

USGS: U.S. Geological Survey

Var[$\boldsymbol{x}$]: Variance in statistics of $\boldsymbol{x}$

VHG: Vertical hydraulic gradient

Y: Common logarithm of K

$\bar{Y}$: Common logarithm of averaged K

$\gamma(\boldsymbol{h})$: Variogram of lag $\boldsymbol{h}$

1 Introduction

1.1 Research motivation

The world faces unprecedented challenges concerning water resources, particularly in arid and semi-arid regions, which occupy 47.2% of Earth's land surface (UNEP 1991). Recent Intergovernmental Panel on Climate Change estimates (Kundzewicz et al. 2007) indicate that between 1.4 and 2.1 billion people live in areas experiencing water stress and these numbers are growing under pressures from population growth and climate change. In such regions, groundwater resources have immense value in terms of natural storage of water and potential storage that can be managed.

Coarse alluvial deposits are not major components in stratigraphic records of the land surface (Rust 1979). However, gravel deposits have generally served as vast reservoirs and significantly contributed to industry, agriculture, and urbanization in Japan and around the world. In particular, thick and monotonic gravel sequences are often seen adjacent to high relief terrain in arid and semi-arid environments, where sparse vegetation and occasional intense rainfall promote aggradation of coarse deposits. However, the extent of coarse deposits is often limited, particularly around the foot of mountains, and so the groundwater capacity is not inexhaustible. Sustainable use of water, especially in urbanized and developing areas, is threatened by excessive withdrawal, contaminant infiltration, watershed development, climate change, and other factors. In addition, the interaction between surface water and groundwater reduces the flow rates to the minimal values required for riparian environments. The permeability of coarse alluvial deposits is generally high, and zones of dewatering and pollution are rapidly and widely expanding. Hydrogeologic heterogeneity unpredictably complicates the spatial and temporal range of an aquifer's influence.

Numerous models have been used in practice to interpret actual flows and transports in groundwater systems. Recently, various models have been developed of parameters such as flow, solute transport, reactive transport, multiphase flow, and energy flow. A complete groundwater model that gives predictions in exact agreement with measurements is ideal but never obtainable. The practical reason is a lack of hydrologic and hydrogeologic information, especially in deep parts of deposits. For example, hydraulic conductivity K ranges over several orders of magnitude,

even in the same geologic sequence. This is because K depends on various properties of geologic materials, such as grain size, porosity, sorting, and packing. Geostatistical approaches are commonly used in many groundwater models to realize spatial variability of K in a target aquifer. However, the approach is commonly based on an assumption of stationarity, that is, constant mean and variance in the domain. Moreover, in alluvial deposits, geologic heterogeneity generally shows horizontal and vertical trends as a result of depositional and post-depositional processes. A standard geostatistical approach in nonstationary fields is to separate the target variable (e.g., K) into a global trend component and a residual component; however, the global trend has rarely been determined because of scarcity and uncertainty in measurements, especially in deep parts of deposits. The necessity of performing many measurements conflicts with the advantage of geostatistics.

This dissertation presents research on trending heterogeneity in coarse alluvial deposits and the development of an approach to modeling their large and trending heterogeneity. For the purpose, attention is paid to the area of a focused recharge zone. Focused recharge zones are typically found beneath and around losing rivers as a result of interaction between surface water and groundwater. The focused recharge zone corresponds to just a part of the regional three-dimensional groundwater system, but spatial and temporal distributions of hydraulic head and groundwater temperature are typically characterized by trending heterogeneity. Regarding the Toyohira River alluvial fan (Sapporo, Hokkaido, Japan), this dissertation covers well data analysis, flow measurements, permeability modeling, and stochastic simulations. This fan is taken up as a representative case for this research object because of its large and trending heterogeneity in gravel deposits.

1.2 Thesis outline

Chapter 1—Introduction

This chapter first describes the motivation for this research, followed by the standard approaches and their problems in groundwater modeling, typically in coarse alluvial deposits. Next, the aim and scope for addressing the typical problems are pointed out. This chapter further describes the study site, including its topography, hydrogeology, and previous investigations.

Chapter 2—Regional mapping of vertical hydraulic gradient by well data analysis and kriging interpolation

This chapter describes a mapping method of hydraulic head for delineating the three-dimensional groundwater flow system in the fan, and for determining the focused recharge zone. For this purpose, mapping groundwater table elevation and vertical hydraulic gradient is performed. The mapping process comprises long-term water-level analysis and kriging interpolation to address the wide range of uncertainty in conventional well data. This content is included in a published paper entitled "Regional mapping of vertical hydraulic gradient using uncertain well data: a case study of the Toyohira River alluvial fan, Japan" (Sakata and Ikeda 2013) in the Journal of Water Resource and Protection, 5(8) in press.

Chapter 3—Synoptic survey for quantifying discharge and leakage in gravel-bed river

Chapter 3 presents an improvement in synoptic survey methodology for specifying the focused recharge zone and for estimating the rate of seepage loss in the zone. This chapter firstly points out how to reduce the discharge uncertainty in gravel-bed rivers. A high-accuracy current meter is applied and verticals are arranged in detail. In addition, the efficiency of the proposed method is indicated as a result of comparisons with other methods.

This content is included in a published paper entitled "Quantification of longitudinal river discharge and leakage in an alluvial Fan by synoptic survey using handheld ADV" (Sakata and Ikeda 2013) in the *Journal of Japan Society of Hydrology and Water Resources*, 25(2), 89-102.

Chapter 4—Realization of heterogeneity in permeability of gravel deposits

In chapter 4, a permeability model of gravel deposits is constructed by using a relatively undisturbed core. A degree of packing of fine sediments between gravel grains is visually classified by four packing levels, and a good relation between slug test results and core properties

is established. A depth dependence of permeability is formulated as an exponential function from estimated profiles of *K* by combining moving averaging and straight regression methods.

This content is included in two published papers: "A distribution model of permeability derived from undisturbed gravelly samples in alluvial fan" (Sakata et al., 2011) in *Japanese Geotechnical Journal* 6, 109−119 [in Japanese] and "Depth dependence and exponential models of permeability in alluvial fan gravel deposits" (Sakata and Ikeda 2013) in *Hydrogeology Journal*, 21, 73-89, doi: 10.1007/s10040-013-0961-8

Chapter 5―Numerical modeling and simulation of flow and heat transport coupling

Chapter 5 first includes observation results on groundwater levels and temperatures in observation wells located along an off-stream transect in the focused recharge zone. Trend and variogram analyses and conditional simulation of permeability are further described. Multiple distributions of hydraulic conductivity *K* are realized by sequential Gaussian simulation. Then, groundwater flow and heat transport are calculated by using a high-resolution two-dimensional model. Finally, the optimal realizations are extracted through a comparison with calculation and measurements results.

This content is included in a published paper entitled "Effectiveness of a high resolution model on groundwater simulation in an alluvial fan" (Sakata and Ikeda 2012) in *Geophysical Bulletin of Hokkaido University*, 75, 73-89.

Chapter 6―Conclusions and future directions

The final chapter summarizes key research topics and results. The chapter also includes recommendations for constructing a three-dimensional regional model in future work.

Figure 1.1 shows a flow chart of this study.
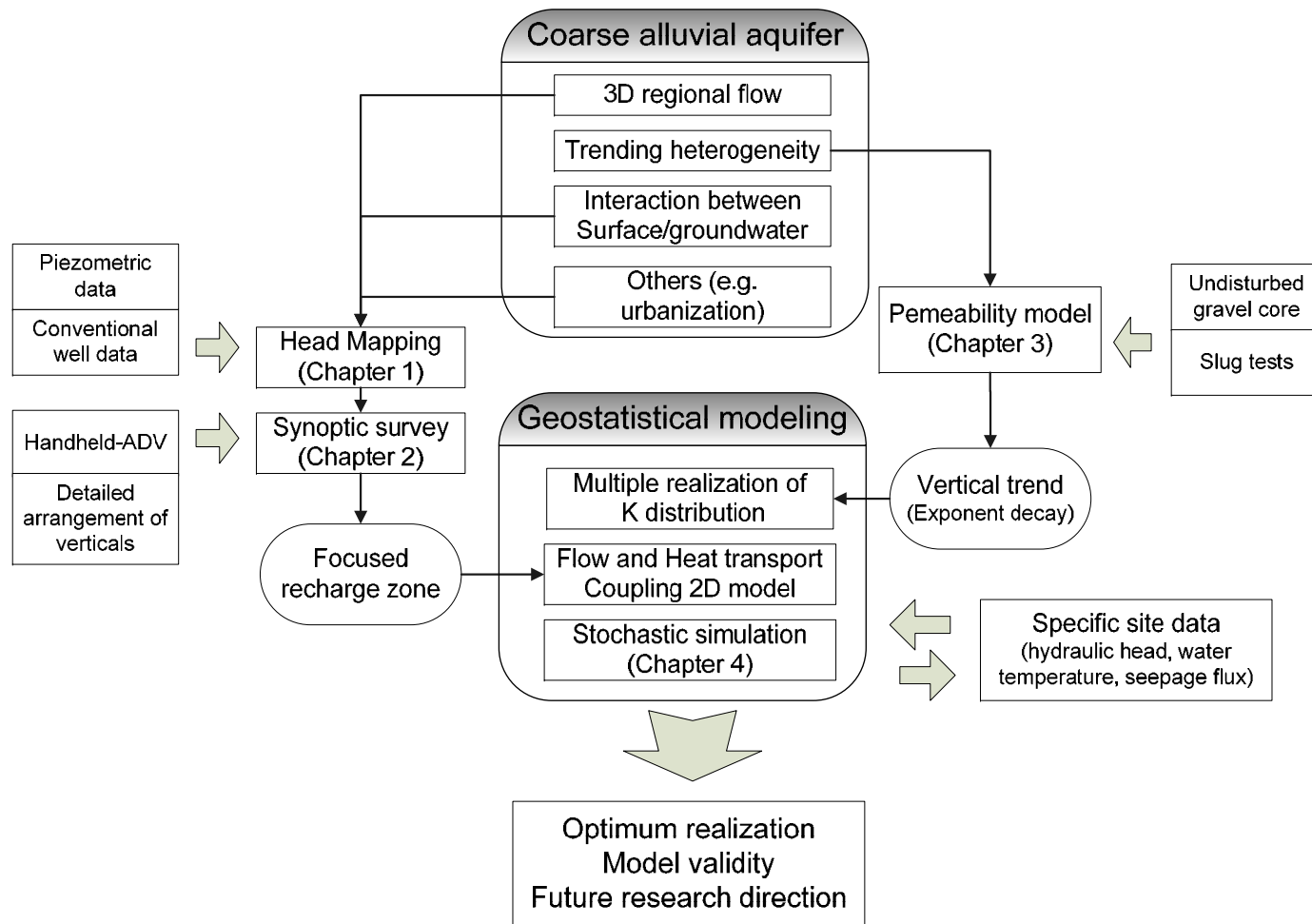
Figure 1.1 Study context

1.3 Standard approach and problems in groundwater studies

The governing equation of groundwater flow is derived by combining the mass conservation equation and Darcy's law (Appendix I-1). The equation is mathematically represented as a partial differential equation of hydraulic head. Hydraulic head is the potential of groundwater flow. The equation contains several parameters, including hydraulic conductivity, specific storage, and sink/source terms. Solving the equation requires appropriate boundary conditions, such as the no-flow condition, Dirichlet condition, Neumann condition, and Cauchy condition. In the transient simulation, initial conditions are also important for obtaining reasonable solutions.

No information about these parameters and conditions is obtainable throughout the entire model domain, so groundwater models inherently have discrepancies derived from uncertainty. In most case, it is difficult to construct sufficient models that give calculation results in exact agreement with measurements in terms with hydraulic head or solute concentration. A fundamental problem in groundwater modeling is how various parameters are determined in space and time. This section discusses standard approaches to groundwater modeling in more detail, and points out their inevitable problems, especially in coarse alluvial deposits. Here, the term "coarse alluvial deposits" is used for poorly sorted sand and gravel, typically containing 50% or more gravel (particles greater than 2 mm in diameter). In fact, the physical characteristics of the deposits (e.g., grain size distribution and porosity) are dependent on mainly the depositional system by fluvial or debris flows.
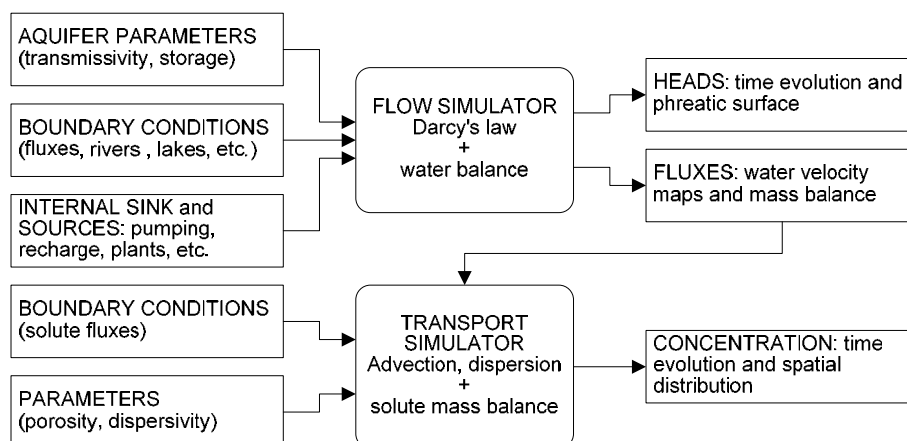
Figure 1.2 Connection of groundwater flow and solute transport models (Carrera and Mathias 2010)

Mapping of groundwater head

A standard way to delineate groundwater flow systems in typical sites is mapping of hydraulic head. Maps of hydraulic head are often translated into maps of hydraulic gradient, which indicate the magnitude and direction of groundwater flows at given points. These maps also play a fundamental role in numerical modeling of groundwater by providing initial conditions and calibration data. Hydraulic heads for mapping should be measured with piezometers having a short, single screen. However, piezometer installation is typically time-consuming and uneconomical, and the number of piezometers is therefore usually limited at each site. As a result, only two-dimensional horizontal cross-sectional maps are produced in most cases, under the assumption that the variance in hydraulic head is very small from the groundwater table to the bottom of the aquifer. The conventional two-dimensional map is useful for an interpretation of groundwater flow systems, where vertical flows of groundwater are negligible at any point. This assumption is satisfied in several topographic regions with gently sloping terrain, such as an anastomosing fluvial plain. However, vertical flows of groundwater generally occur in coarse alluvial deposits because the deposits are bounded in the upper basin by steep land slopes. A description for three-dimensional flow system requires many more measurements of hydraulic head. Water levels measured in individual wells and boreholes are also available and expected to be useful to compensate for the scarcity of piezometric data. In fact, these data have been considered to be unusable for scientific studies because these data include wide-ranging but inseparable uncertainty.

Groundwater recharge estimation

Groundwater recharge is entry via infiltration from the ground surface into the saturated zone, and is important as internal sink/source terms in groundwater models. In general, groundwater recharge is divided into two types: diffuse recharge from precipitation and snowmelt, and focused recharge from typical water bodies. Quantitative modeling of diffuse recharge has generally proved difficult because it has spatial variability and temporal variability both subject to systematic and random error. On the other hand, focused recharge is relatively conveniently modeled around surface water bodies. In particular, intermittent focused recharge from ephemeral streams is often the dominant recharge mechanism in arid and semi-arid regions, and water

budget methods are often applied for estimating stream loss (Healy 2010). This research employs a conventional treatment of focused recharge zone, such that uncertainty in groundwater recharge is assumed to be negligible and trending heterogeneity (another uncertain parameter) can be discussed in more detail. Among water budget methods, a synoptic survey of discharge is a widely used and effective method to determine focused recharge (Woessner 2000; Weight 2008). However, such surveys have been carried out in only small and gentle rivers due to uncertainty in discharge measurement. In typical gravel-bed rivers, unsteady turbulent flow and roughness of the bed boundary significantly affect the application of synoptic surveying in focused recharge estimation.

Realization of *K* with large and trending heterogeneity

Hydraulic conductivity K, a proportionality coefficient in Darcy's law, generally spans several orders of magnitude, even in the same geologic setting. The spatial variability of K is related to various geologic material properties such as grain size, porosity, sorting, and packing. An application of geostatistical and stochastic methods for groundwater reservoir modeling has become common practice to address large heterogeneity (Koltermann and Gorelick 1994; Dagan 1997; Jang and Liu 2005; Eaton 2006; Lee et al. 2007). Another zonal and deterministic approaches have been more popular in practice, and various optimization methods are developed (e.g., Horino 1992). However, the deterministic approaches are less flexible because only one optimal realization of K in the target domain is obtained under insufficient measurements of K. The geostatistical approach is considered to be more effective in groundwater modeling of coarse alluvial deposits, because coarse alluvial deposits often consist of monotonic gravelly sequences and have few obvious boundaries, necessitating the zonal approach.

Figure 1.3 shows an illustration of heterogeneity in coarse alluvial deposits, in this case, alluvial fan gravel deposits. On a basin scale, various sequences are seen that consist of clast-supported gravel (well sorted), matrix-supported gravel (less sorted), sand, silt and others. The sequences result from the complex and changing depositional processes. In general, however, a downward fining trend is generally caused by decreasing flow energy. This trend is called "trending heterogeneity" by Freeze and Cherry (1979). Humped heterogeneity is also seen on the basin scale and indicates that transmissivity peaks in the mid-fan area as a result of sorting

trends; in other words, sheetflood and channel bar deposits in the mid-fan to lower fan are much better sorted in comparison with the debris and mud flows in the upper fan. In alluvial fan aquifers, a humped trend is probably more common than a simple downward trend (Cehrs 1979; Neton et al. 1994).

In the vertical direction, the stratigraphic sequences have large heterogeneity because they are composed of various hydrofacies due to depositional and post-depositional processes. For example, coarsening/thickening or fining/thinning sequences are often formed by progradation, retrogradation, and basin subsidence (Neton 1994). However, these trends are not necessarily reflected in vertical profiles of hydraulic conductivity K because it is a complex function of various factors of geologic materials (porosity, packing, sorting, etc.). In addition, no obvious trend has been found in the profiles of K, owing to a combination of large heterogeneity and scarce measurements. The post-depositional processes that influence K (e.g., compaction) have rarely been considered in coarse alluvial deposits. For example, typical disturbed cores of gravel deposits provide less information about porosity structure related to permeability, and the physical properties from logging and surveying indicate weaker correlation with K. Consequently, the vertical profiles have proved especially difficult in alluvial shallow deposits.

Being fundamentally based on an assumption of stationarity, geostatistics lacks versatility in groundwater reservoir modeling. This assumption is invalidated by trending heterogeneity of geologic deposits, for example, where K decreases overall as the grain size gradually decreases with increasing depth. The problem is called a "non-stationary problem" in geostatistics, and has been discussed in the literature (e.g., de Marsily 1986; Wackernagel 2003). One simple way to address non-stationary problem is to separate target attribute (e.g., K in this case) into a global trend component and a random residual component. The standard method for handling non-stationarity requires many measurements to reveal the global trend in large variations of K, which conflicts with the advantage of geostatistics.

Horizontal direction

lower fan | mid fan | upper fan

A
down-fan fining trend
(Blissenbach 1954;
Hooke 1967;Bull 1972)

Grain Size(AMGS)

B
trending heterogeneity
(after Freeze and Cherry 1979)

K, T, S, SC, n

C
"humped" heterogeneity
(after Wilson 1973;Cehrs 1979)

K, T, S, SC, n

Distance
(from border fault)

downfan

Distal ← Proximal

	Lower fan	Mid fan	Fan head
Dominant	Streamflow/Stream channel	Sieve deposition Sheet flood	Debris flow
Common	Sheet flood	Streamflow/Stream channel	Sieve deposition
Rare	Sieve deposition Debris flow	Debris flow	Sheet flood Streamflow/Stream channel

Fan head

Mid fan

Lower fan

Sourceland

Fm+C

St and Sh

Gm

Gms

Facies description

Major facies	Gm:	Horizontally bedded clast-supported gravel, commonly imbricate.
	Gms:	Muddy matrix-supported gravel; lacks imbrication and internal stratification
	Gt:	Trough cross-bedded clast-supported gravel
Minor facies	Gp:	Planar cross-bedded gravel, transitional from clast-supported through sand matrix-supported to sand (facies Sp)
	Sh:	Horizontally stratified sand
	St:	Trough cross-stratified sand
	Sp:	Planar cross-stratified sand
	Fm:	Massive fine sandy mud or mud
	Fl:	Laminated or cross-laminated very fine sand, silt or mud.
	P:	Concretionary carbonate (pedogenic)

Vertical direction

INCREASING FAULTING AND UPLIFT

RETREAT OF SCARP FRONT AND LOWERING

a PROGRADING

DECREASING OR CEASING FAULTING

b BACKSTEPPING

thickness (10's to 1000's m)

thickness (10's to 1000's m)

Average Maximum Grain Size(AMGS); K, T, S, SC, n

D
coarsening-upward sequence

E
fining-upward sequence

Figure 1.3 Illustrative trending heterogeneity in an alluvial fan, modified from Neton (1994) and Einsele (2000)

Numerical modeling of groundwater flow and solute transport

Compared with analytic modeling, numerical modeling of groundwater is much more applicable to the complexity and uncertainty of aquifer parameters and boundary conditions. In particular, simulations coupling ground water flow and solute transport are often conducted to delineate a heterogonous aquifer because solute concentration is more sensitive to heterogeneity than hydraulic head is. However, the coupled model involves more difficulties than the uncoupled flow model: 1) scarce measurements of solute concentrations, 2) higher uncertainty in parameters of fluid and aquifer (e.g., diffusivity), and 3) numerical errors associated with spatial and temporal discretization. For example, a high-resolution model (e.g., grid spacing of 1 m) is needed to obtain detailed, accurate results to solve for the solute concentration, but excessive resolution is inappropriate for larger-scale models (e.g., a three-dimensional basin model) due to computational limitations.

1.4 Aims and scope

The previous section points out several problems in groundwater reservoir modeling of coarse alluvial deposits. This section describes the aim and scope for addressing the inherent problems.

Scope 1: Research on focused recharge zones

In this dissertation, special attention is paid to the focused recharge zone around the losing river. A schematic vertical system of groundwater flow and solute transport is shown in Figure 1.4. The water table is smoothly connected between surface water and groundwater, and the water table forms a mound around the river, indicating seepage loss through the riverbed. The infiltrated water first moves primarily in the vertical direction, and then its direction varies widely in the horizontal and vertical directions, depending on hydraulic gradient. In addition, the magnitudes of individual flow vectors are spatially variable according to K at a given point. Solute components and surface water heat are also transported from the river to the deeper zone. As a result of the preferential flows, sharp solute concentration fronts surround the losing river. Assuming a decreasing trend of K in the aquifer, the flow vectors of groundwater would largely accumulate in the shallower zone, and the contours of solute concentration are characterized by this accumulation. Therefore, the focused recharge zone is just a part of the regional three-dimensional system of groundwater, but the complex flow field is directly reflected in the geologic heterogeneity. In other words, this research on a focused recharge zone offers an effective method for revealing the trending heterogeneity in the groundwater flow and solute transport system.

Scope 2: Field and analysis methods for reduction of data uncertainty

This research also has a typical scope regarding how to reduce uncertainty in field measurements. Available water levels for head mapping are filtered, interpolated by kriging, and cross-validated (Chapter 2). A synoptic survey method is developed that employs a high-accuracy current meter and a detailed arrangement of verticals (Chapter 3). An exponential model in vertical K profiles of formulated through a moving average method (Chapter 4).

Scope 3: Permeability model of alluvial fan gravel deposits

A number of K values in a vertical profile are needed to reveal a global trend (i.e., depth dependence) of K in coarse alluvial deposits. A permeability model of gravel deposits is newly

established by using relatively undisturbed cores, which provide typical information on porosity structure in the deep zone. For this purpose, an additional "matrix packing level" index is proposed, and length fractions of each packing level are measured in each core. The permeability model of gravel deposits consists of effective grain size and length fractions, and the constants are optimally set. The profiles of core properties in the fan-apex, mid-fan, and fan-toe are transformed to profiles of estimated K. The depth dependence of K is then represented as an exponential model through regression analysis using the profiles of estimated K.

Scope 4: Stochastic simulation of trending heterogeneity

Residuals of K from the global trend are expected to be stationary. If this assumption is valid and the variogram of Re is known, multiple realizations of K in the analysis domain can be produced by geostatistical methods. This study applies sequential Gaussian simulation, which is among the most practical and widely used geostatistical methods, yielding 100 realizations of K in each study case. Groundwater flow and heat transport simulation is then performed under each condition of K, and optimal realizations to satisfy the criterion are extracted from among the realizations. Two study cases, namely, trending heterogeneity and stationary heterogeneity, are prepared to assess an importance of modeling trending heterogeneity in the focused recharge zone. Moreover, other study cases are examined to discuss other uncertain parameters such as anisotropy of the unit cell, River conditions (vertical hydraulic conductivity in river-bed material and river width), range of the variogram, thermal dispersivity, and temperature dependence of fluid properties.

Scope 5: Application of heat tracer and high-resolution model

The previous section describes three obstacles to obtaining robust solutions in solute transport simulations. The first and second problems are addressed by using heat as a groundwater tracer by exploiting the similarity between temperature transport and solute transport: compared with other solute components, heat can be measured with greater ease and accuracy, and the representative values of thermal parameters are obtained from the literature. The third problem is also addressed by using a high-resolution grid model. The Péclet number Pe is commonly used as a criterion for setting grid size:

$$Pe = \frac{\rho_w c_w qL}{k_e} \quad (1.1)$$

where ρ_w is the density of fluid, c_w is the specific heat per unit volume of water, q is Darcy's specific discharge, L is a characteristic length, and k_e is the effective (bulk) thermal conductivity. Darcy's specific discharge is calculated by multiplying K by hydraulic gradient. Equation (1.1) indicates that stable solutions require finer grid-spacing as K increases. Coarse alluvial deposits in particular have extremely high K values, and so a high-resolution grid model of 1 m grid-spacing is necessary to satisfy the criterion.

The program "SEAWAT" is utilized for variable density and transient groundwater flow in porous media. K in a geologic material consists of fluid density and viscosity in addition to intrinsic permeability, such that K is inherently dependent on groundwater temperature. In most conventional models, the effect of temperature is ignored. Recent studies, however, suggest the importance of temperature dependence with respect to solution robustness in groundwater modeling (Ma and Zheng 2010; Engeler et al. 2011). SEAWAT also calculates groundwater flow and temperature transport with greater accuracy by using iterative processes.

A block-averaging model consisting of 5 m square cells is also prepared for comparison with the high-resolution model. Upscaling of a high-resolution model to a basin-scale model is a long-standing problem in groundwater modeling (Deutsch 2002; Zhang et al. 2006; Zhang et al. 2010). This is because K depends on scale, that is, microscale (e.g., drilling cores; several meters or less), mesoscale (e.g., facies; 10 to 100 m), and macroscale (basin scale, 100 m or more). The discrepancy between the different discretized models shows a direction of upscaling in groundwater modeling of coarse alluvial deposits.
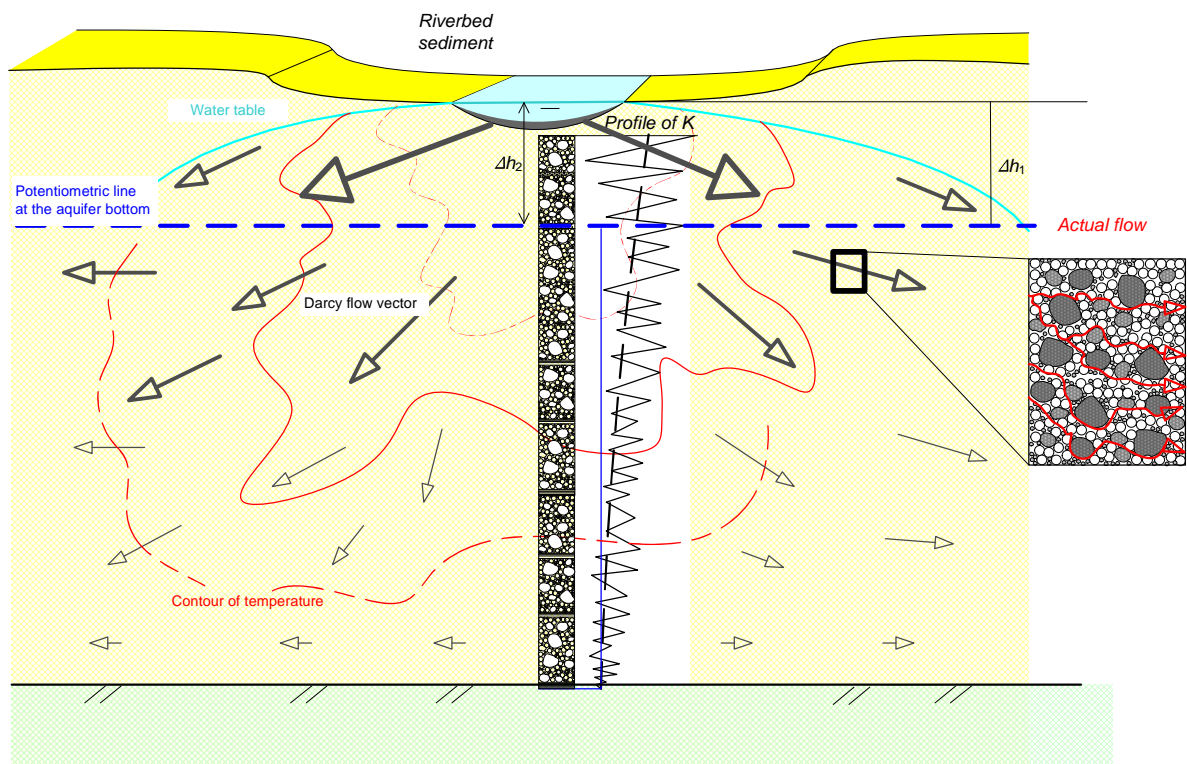
Figure 1.4 Schematic system of groundwater flow and solute transport in a

focused recharge zone

1.5 Description of study site

An alluvial fan (*Senjyouchi* in Japanese) is a body of alluvial material deposited at the foot of a range of hills or mountains by a stream that debouches from the area undergoing erosion above the apex. Alluvial fans are commonly found in arid and semi-arid regions with tectonically active mountains where there is an abundant supply of sediment. Alluvial fans also occur in subtropical, arctic, alpine, and humid temperate environments around the world (Lecce 1990). For example, Japan, despite having a humid climate, also has over 200 alluvial fans (Saito 1980). The following reasons explain fan development in Japan: steep land slopes, mountainous terrain, tectonic activity, and base rocks of relatively a recent epoch with low resistivity to erosion. Ono (1990) also documented that alluvial fans in Japan (and in Korea) occurred mainly because of climate change, particularly during the early half of the glacial age (90,000-40,000 yr B.P.) and the short time of the Holocene epoch.

The study site is the Toyohira River alluvial fan in Sapporo, Japan (Figure 1.5). Sapporo City is the largest in the northern part of Japan and has a population exceeding 1.9 million. The Toyohira River alluvial fan is located at latitude 43°N and longitude 141°E, where the Toyohira River flows northward out of Tertiary mountains and debouches on a plain. The fan has a radius of about 7 km and an area of about 31 km^2. The Toyohira River is also about 72.5 km long and has a watershed area of about 900 km^2. In the watershed, the annual mean precipitation between 1981 and 2010 is 1,107 mm. Snow falls on the fan to a total depth of more than 5 m in the winter. The flow gaging stations are located at the distal part (KP 11.1; Kariki station; Figure 1.6a) and the apex (KP 18.0; Moiwa station), respectively, where KP denotes the distance in kilometers from the confluence with the Ishikari River, one of the main rivers of Japan. The median value of daily mean river flow through the fan are 12.6 m^3/s for the period of record 1975–2010; maximum instantaneous peak discharge reached 700 m^3/s in August 1981. The discharge in the river is continuously controlled by two dams: the Jyouzankei Dam and the Hoheikyo Dam, which were constructed in 1972 and 1988, respectively. At the upper point 10 km from the fan, water intake is conducted for electricity generation. The water after the generation flows into the Yamahana River, which meets the Toyohira River at KP 18.8, where the Toyohira River usually reaches its peak flow rate

throughout the fan. Two other tributaries of the Toyohira River flow through the fan: the Makomanai River and the Shojin River. The flows of both tributaries are too small to affect the flow of the Toyohira River. In addition, water is continuously pumped from the Toyohira River at KP 17.4 (no more than about 0.3 m^3/s) to maintain the Sousei River, flowing northward through the city.

Management of the river, especially during low discharge, has recently become problematic due to increases in water intake and the active interaction between the surface water and groundwater. In addition, contaminants in some wells such as natural arsenic and artificial volatile organic compounds have reached concentrations that are higher than stipulated levels (Sapporo city 2008; 2011). Various groundwater analyses have been conducted to examine the river management issues, and the results of several of these analyses have obtained fairly good agreement with at least part of the measured factors (i.e., groundwater heads, the recharge and water budget or contaminant transport).
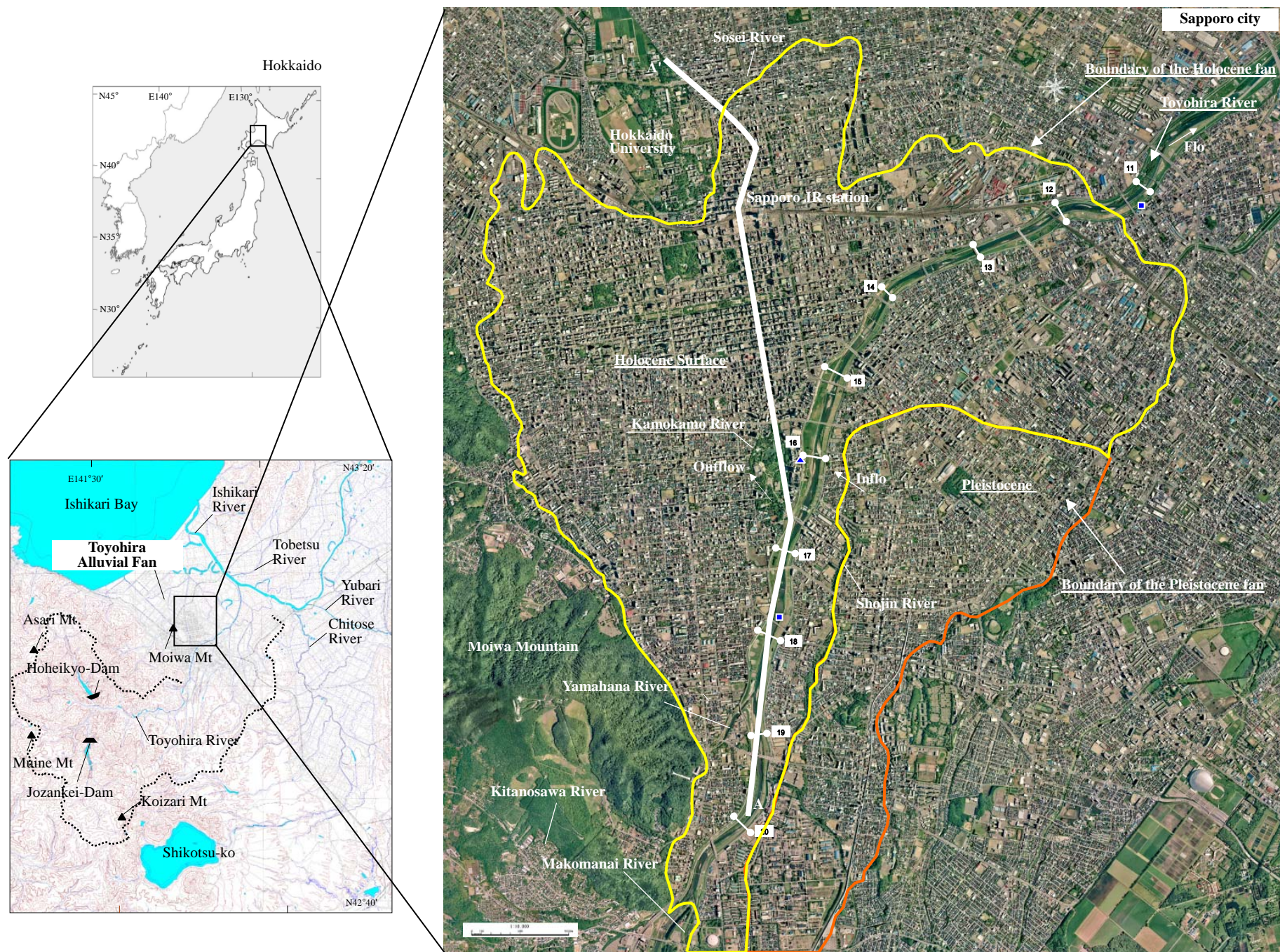
Figure 1.5 Study site: the Toyohira River alluvial fan. The aerial photograph was taken on 3-4 June 2004 by Sin Engineering Consultant, Co., Ltd. The topographic boundaries of the Holocene and Pleistocene fans are taken from an existing geologic map (Osanai et al. 1974; Ishida et al. 1980)

a

b
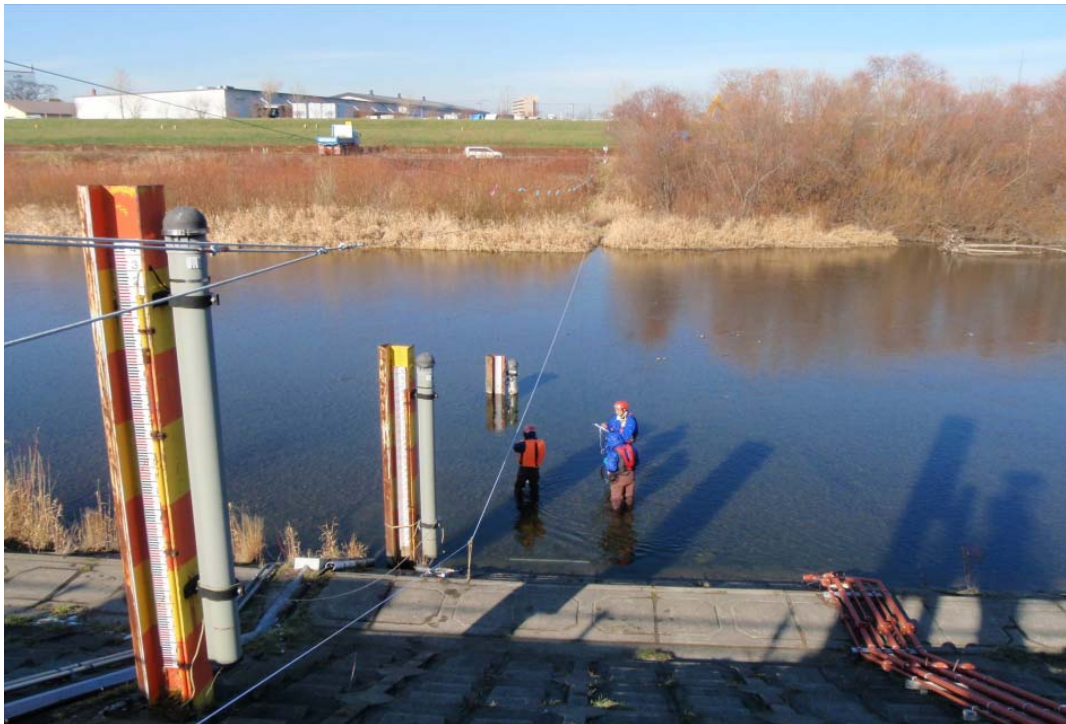
Figure 1.6 Photographic scenes of the Toyohira River: a) at the apex (KP 20.4)

and b) at the Kariki gaging station (KP 11.1)

1.5.1 Geomorphology and development history

The fan is surrounded by Tertiary volcanic mountains (the Sapporo southwest mountains) to the west, the Tukisamu hills to the east, and the lowland to the north (Figure 1.7). The fan is a compound fan comprising a western Holocene fan at 70–10 m asl (above mean sea level) and an eastern Pleistocene fan at 90–20 m asl. The Holocene and Pleistocene fans are respectively called *Sapporo-men* and *Hiragichi-men* in Japanese. The fans are topographically different in mean inclination of the fan surface; 9/1,000 in the Pleistocene fan and 7.5/1,000 in the Holocene fan. The topographic boundary between the surfaces is recognized as an abrupt cliff of several meters in height along the east bank of the river upstream from KP 15. Daimaru (1989; 2003) suggested that the Toyohira River alluvial fan developed as follows: (1) the Pleistocene fan was formed when the sea level was lower in the last glacial period; (2) as the sea level rose in the early Holocene, the Toyohira River shifted toward the west, crossing through the Pleistocene fan, and gradually formed the Holocene fan; (3) in the late Holocene, the river shifted its channel eastward as sediments were deposited. Lobes A, B, and C in the fan-toe of the Holocene fan indicate the eastward transition of the river channel, and lobe D corresponds to the present course of the river. Recently, Nagaoka et al. (2008) suggested that the Hiragishi surface formed by deposition from the earlier age, namely, the last glacial age, because the upper fluvial terraces including the Shikotsu volcanic deposits at 41,000 yr B.P. (Hu et al. 2001) were eroded by the river.
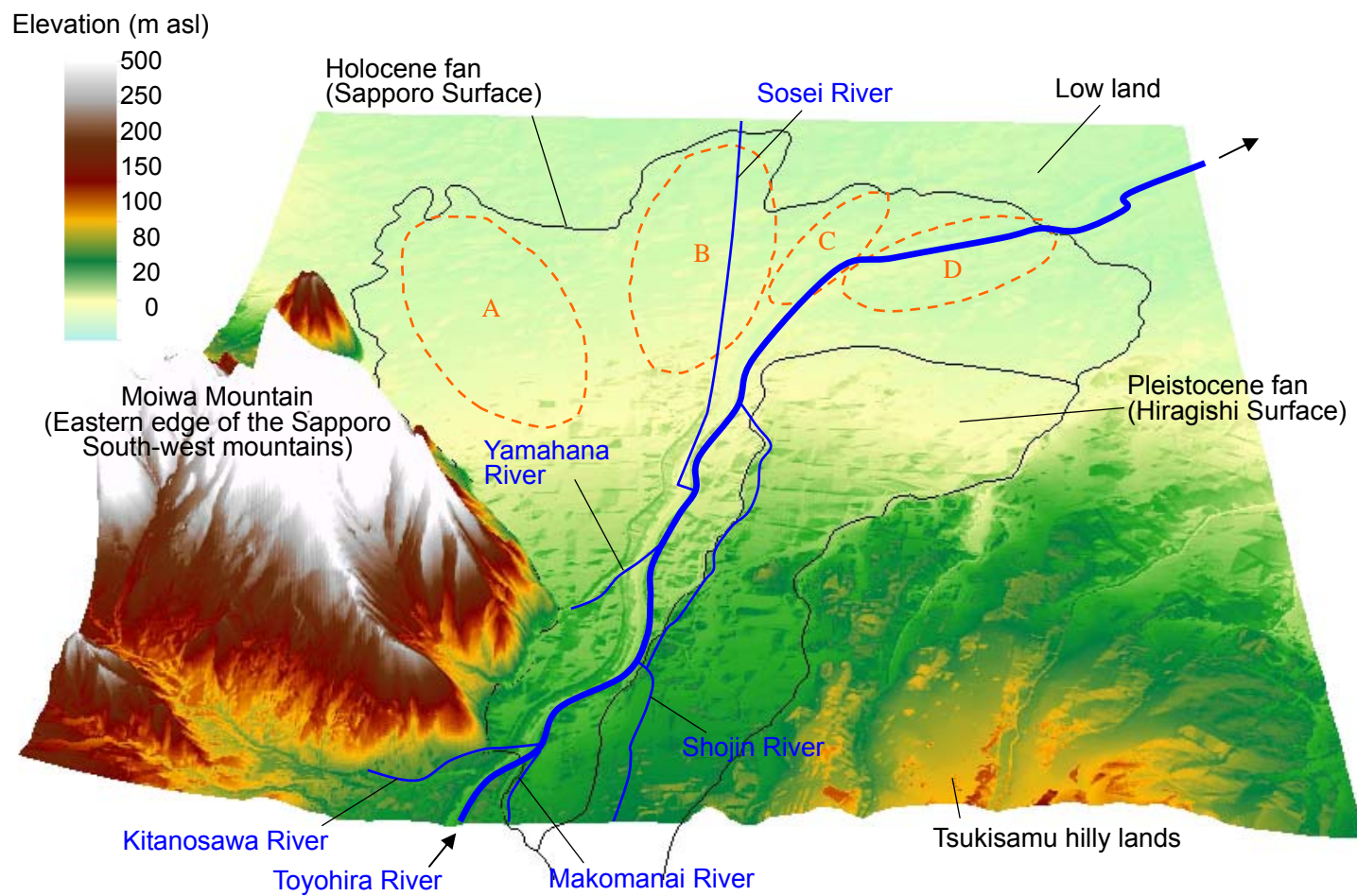
Figure 1.7 A bird's eye view of the Toyohira Alluvial fan, indicating its topographic features

1.5.2   Subsurface hydrogeology

Thousands of drillings for civil development have been performed in the Toyohira River alluvial fan, and the fan's subsurface hydrogeology are described in the literature by using these geologic data (e.g., Kato et al. 1995; Oka 2005; Sagayama et al. 2007; Hu et al. 2010). Figure 1.8 shows two vertical cross sections along the longitudinal direction (see

Figure 1.5); the upper panel is the large-scale cross section made by Oka (2005), and the lower panel is the small-scale cross section prepared for this dissertation. The bedrock distributed around the alluvial fan is Neogene sedimentary rocks and volcanic rocks (andesitic lava, pyroclastic rocks, etc.) from the Neogene and Quaternary. The Neogene sedimentary rocks are classified into the Otarunai-gawa formation and the Nishino formation. The basement strata appear just beneath the riverbed at the uppermost of the fan (KP 18–20; Figure 1.9a). The fan basement suddenly inclines northward to a depth of several hundreds of meters. The inclination is caused by a tectonic process (the Ishikari Depression) and is a main factor in the fan development incorporating a large amount of debris from the upper mountains. As a result of this depression, in the mid to the distal parts, the bedrock is covered by Pliocene to early Pleistocene deposits called as Zaimoku-zawa formation. Over almost the entire fan, except for the fan-apex, the thickness of the Zaimoku-zawa formation is of the order of 10^2 m, and the maximum thickness is over 800 m around the fan-toe (see "Naebo" in Figure 1.8a). The Pleistocene deposits consist of alternating gravels, sand, silts, clays, and humus. Instead of base rock, Pleistocene marine sediments (−50 to −30 m asl) serve as a hydrogeologic basement for the subsurface.

Recently, Hu et al. (2010) divided the upper formations into four aquifers: Pleistocene nos. III and IV, and Holocene nos. I and II. The Pleistocene no. IV aquifer consists of alternating gravel, sand, and silt layers tens of meters thick, indicating that the bottom aquifer formed before the fan developed, that is, in the fluvial or shallow-sea environment. On the other hand, both the Pleistocene no. III and Holocene no. II aquifers consist mainly of alluvial fan deposits, that is, poorly sorted sandy gravel with andesitic cobbles (Figure 1.9b). The grain size of the riverbed has a mean diameter of 50–100 mm, a maximum diameter of 100–500 mm, and a sand fraction less than 10% (Hokkaido Regional Development Bureau 2006a). There is an obvious distinction in the thickness of fan deposits between the Holocene and the Pleistocene fans: the total thickness is

over 100 m at the upper middle of Holocene fan, and less than 50 m at the distal part, while the thickness ranged between only 5 m to 30 m in the Pleistocene fan. However, conventional drilling cores (largely disturbed) show only the thicknesses of gravel deposits, and due to their large disturbance, the hydrogeologic details in the gravel sequences are not clear, except for accompanying thin silt beds. Permeability in the fan deposits is high but greatly variable due to geologic heterogeneity. Yamaguchi (1965) suggested that a zone of extremely high permeability was probably located at a depth of ~30 m because the wells screens accumulated in the shallow depths.

The Holocene no. I aquifer is distributed in only the northern part of the fan (i.e., the fan-toe), and is geologically and topographically continuous in the lowland. The less permeable aquifer consists of sandy beds, clayey beds, and peaty beds, which were transported in the late Holocene.

Figure 1.8 indicates potentiometric contours of groundwater head manually plotted by using head measurements in several piezometric nests. Alluvial fans have steep ground surfaces from the apex to the distal part, resulting in downslope and downward directional flows (Tolman 1937). In theory, the topographic-driven flow system is induced as a type of regional three-dimensional groundwater flow system (Tóth 2009). The potentiometric contours in Figure 1.8 show groundwater flows in the fan are three-dimensional; horizontally from the apex to the distal part and vertically from the ground surface to the deeper aquifer. The three-dimensional flows of groundwater occur because of not only the steep land surfaces, but also the seepage loss around the focused recharge zone.

Figure 1.8 Geologic profiles along a longitudinal direction (NW direction) in

Sapporo City: a) The upper profile of the basin scale is modified from Oka

(2003), and b) the lower of subsurface scale is made by several stratigraphic

columns based on an aquifer classification in Hu et al. (2010b)

a

b

Figure 1.9 Photographic outcrops in the Toyohira River: a) tuff breccia of the

Nishino formation (KP21.0); b) gravelly bed indicating imbrication (KP16.5)

1.5.3　Previous groundwater studies

Alluvial fans are hydrologically and hydrogeologically well-studied in Japan (Kayane and Yamamoto 1971; Kayane 1991; Huh et al. 2010a). The first study of groundwater in the Toyohira alluvial fan was probably conducted by Fukutomi (1928). This pioneer produced a groundwater-table map before World War II by using 3,400 pieces of well-head data collected in the Holocene fan, and documented the following: 1) the groundwater table was shallower than the depth of only about 5 m; 2) the table became gradually shallower northward; and 3) the table crossed the ground surface at an elevation of about 15 m asl, such that several springs called "memu" formed along this level.

In the 1960s, groundwater resources in the fan attracted increasing interest with the economic growth in Japan, and many studies and investigations are performed to reveal the hydrogeologic structures in the fan, and to assess the capacity of groundwater (Kawata and Obara 1958; Sasson Keizai Kyougikai 1963; Ozaki et al. 1965; Yamaguchi et al. 1965; Obara 1969). Numerous water wells were installed at various depths throughout the aquifers, especially no. II and no. III. A total pumping rate exceeded 100,000 m^3/day in 1963, and the pumping rate continued for at least half a century according to the annual reports compiled by Sapporo City. From 1969 to 1994, the Nanboku, Tozai, and Toho subway lines were constructed in turn, and heavy pumping for construction caused significant drawdowns of water levels around the lines. As a result, many shallow wells stopped pumping and the springs at the distal part dried up (Nakao 1983). After the construction, the subway lines resulted in drainage, and the groundwater water levels remained low. Hence, the vulnerability and sustainability of groundwater resources in the fan have been threatened due to withdrawal and drainage as a result of the city's development. In addition, the annual average temperature at the Sapporo District Meteorological Observatory suddenly increased, probably due to the heat island effect, as well as global warming. The rate of increase is reported to be 2.3 °C per 100 yr from 1901 to 2000; for the winter low temperature in particular, the rate reaches 5.2 °C per 100 yr. Climate change might also have significant effects on the surface water/groundwater budget in the fan (Hu et al. 2010).

The estimation of seepage loss has been a longstanding issue for the management of the river, especially during the low-flow periods (Hokkaido Regional Development Bureau 2006a), and

repeated synoptic surveys of discharge have been carried out (Ozaki et al. 1965; Yanagiya 1995; Tanaka et al. 2010). However, the estimated values were significantly different due to large uncertainty of measurement in the turbulent flows.

A variety of groundwater modeling studies has been conducted to address the issues described above. First, two-dimensional planar models were applied in the 1990s (Furukawa 1997). The simulation models showed that the groundwater heads were in approximate agreement with the measurements, and that the seepage loss was estimated at 20 million m^3/yr (0.6 m^3/s), indicating the river leakage was the main source of groundwater in the fan. Next in the 2000s, three-dimensional models were constructed to capture the complexity of the groundwater flow system (Koizumi et al. 2008; Sakata and Ito 2009). Koizumi's model aimed to evaluate the influence of climate change on the water budget in the fan, while Sakata and Ito's previous model is aimed to reveal the mechanism of seepage loss around the river. In both models, K was assumed to be homogeneous in each aquifer (i.e., nos. I to IV), and the values were optimally determined to obtain agreement in hydraulic head between measurements and calculations. The zonal approach, however, continued to give the discrepancies in seepage loss between calculated and measured values. Large heterogeneity of K probably influenced the simulation results more significantly than other uncertain parameters (i.e., diffuse recharge or urbanization effects). The practical problem is a starting point for this study.

1.6   Summary

Coarse alluvial deposits are valuable water reservoirs, especially in arid and semi-arid regions, but their large and trending heterogeneity is problematic in groundwater modeling. The aim of this thesis is to reveal the importance of modeling trending heterogeneity in coarse alluvial deposits. For this purpose, the target area for this research is specified as a focused recharge zone around a losing river, such that various other uncertain factors (e.g., diffuse recharge) can be neglected. In the focused recharge zone, this research involves head mapping, synoptic surveying, permeability modeling, and stochastic simulation. The first aim is reducing the uncertainty in head mapping, synoptic surveying, and exponential modeling of permeability. The second aim is to establish a permeability model for gravel deposits by using the *matrix packing level* index of relatively undisturbed cores. The third aim is to utilize heat transport simulation to obtain numerical solutions to solute transport problems. In addition, a high-resolution model is used to obtain a steady solution to conduction-convection equation. Flow and heat transport coupling code is utilized, which includes an algorithm for the temperature dependence of fluid to obtain more rigorous solutions. Sensitivity analysis is conducted to evaluate the importance of trending heterogeneity in the groundwater flow system, and to assess other uncertain parameters. The program "SEAWAT" is utilized for variable density and transient groundwater flow in porous media. In particular, a block-averaging model is also designed construct an advanced basin model for future work. A high-resolution grid model is required for the low value of the Péclet number.

The Toyohira River alluvial fan, Sapporo, Japan, was selected as a representative field in this investigation. The fan has a typical three-dimensional groundwater flow system due to steep terrain and fan deposits with high permeability. Urbanization complicates the three-dimensional flow system. The complexity of the groundwater flow system has been indicated in the previous investigations, and trending heterogeneity in the gravel sequences are required for describing the flow system in a more quantitative manner.

2 Regional mapping of vertical hydraulic gradient by well data analysis and kriging interpolation

2.1 Introduction

Maps of hydraulic head in observation wells are basic elements for planning water resource development, monitoring and protecting water quality, and conceptualizing groundwater flow and solute transport. These maps also play a fundamental role in numerical modeling of groundwater by providing initial conditions and calibration data. In practice, hydraulic head maps closely correspond to 2D horizontal cross sections: one or several potentiometric contour maps in confined aquifer(s), and the groundwater table map in an unconfined aquifer. Such conventional 2D maps are effective for visualizing groundwater flow systems in flat plains or in localized areas where vertical components are relatively small. On a wider regional scale, topographic and geologic variations result in a 3D groundwater flow system characterized by vertical flows (Tóth 2009). Measuring the upward and downward flows of groundwater allows for identification of discharge and recharge areas. In addition, vertical flows beneath bodies of water are interesting for evaluating the exchange between surface water and groundwater. Also, excessive withdrawal and numerous understructures in urbanized and developing regions can capture natural discharges for artificial use elsewhere. Areal information on vertical groundwater flows is no less critical than horizontal flows for interpreting actual 3D groundwater flow systems.

Vertical hydraulic gradient (VHG) is generally used for delineating the direction and magnitude of vertical groundwater flows (e.g., Fritz and Mackley 2010). Theoretically, hydraulic gradient can be calculated by derivation of hydraulic head (Abriola and Pinder 1982; Philip and Kitanidis 1989; Pardo-Igúzquiza and Chica-Olmo 2004). In situ measurement of VHG is performed using piezometer nests, which contain multiple piezometers in close proximity at different depths. However, installing piezometers is expensive and time-consuming, and so the number of piezometers at a particular site is usually limited, and piezometer nests are less frequently made. For these reasons, VHG maps are often produced, but are typically limited to a relatively local area, such as fluvial channels (for quantifying surface/groundwater interaction) and polluted sites (for monitoring contaminant plume). On a wider regional scale, VHG mapping is rarely performed, and delineation of regional groundwater flow systems is often just a 2D horizontal map with schematic

vertical cross sections.

Comparable information can often be gleaned from the available water level data in individual water wells and boreholes. In many urbanized and developing regions, numerous records of wells and boreholes are maintained. However, water wells do not have a short single screen, but rather multiple long screens installed for water intake. The water level actually does not integrate the heads on a vertical section, depending on heterogeneity around the well (McIlvride and Rector 1988; Rushton 2003). Uncertainty also arises from differing measurement times, even in the same well, as a result of precipitation, artificial intake, climate change, and other events. Such uncertainty in each well is often calibrated based on other water variations at neighboring location and depth (Taylor and Alley 2001), but it is difficult to classify and quantify uncertainty in all of the available data. Therefore, a statistical approach is required for dealing such uncertainty. One traditional approach is to plot well depth versus depth to static water level from the groundwater table (Freeze and Cherry 1979). Under the assumption of a single topographic region, the plot determines whether the region is a recharge or discharge area. However, recharge and discharge areas in a basin are typically complex, and so it is not known a priori whether the site can be treated as a single topographic region. In the plot method, the groundwater table is a common datum surface, but the depth to the groundwater table is not uniform on such a regional scale, and varies depending on topography, geology, and other factors.

The object of this study is to expand the concept of the plot method to be more generalized on a regional scale. This study proposes regional mapping of VHG using kriging interpolation of conventional well data. The datum surface of VHG is, as in the plot method, the groundwater table (here, groundwater table elevation (GTE) in particular). A VHG map provides information not only on whether recharge or discharge occurs, but also on magnitude of vertical groundwater flows. Kriging is a popular interpolation tool for mapping of hydraulic head and gradient (Wackernagel 2003). Variogram analysis is conducted to reveal spatial variability of the variables, and best linear unbiased estimators (BLUEs) are obtained for any node with its variance. Kriging also reproduces measurements of head exactly, regardless of whether its uncertainty (e.g., measurement error) is included. This is undesirable in this mapping because the available data have a wide range of uncertainties. Numerical tests show that uncertainty in kriging estimates increases with relative

measurement errors (e.g., Lamotte and Delay 1997). It is important for kriging to take into account measurement errors such as uncertainty in spatial variability (Saito and Goovaerts 2002). This poses a conflict in the analysis of conventional well data. Available data, as much as possible, are collected to compensate for reliable measurements of limited number, while such a dataset includes larger variance due to wide-ranging measurement errors. For these reasons, an appropriate filtering process is required to strike a balance between the volume and uncertainty of the dataset.

Here, the Toyohira River alluvial fan, Sapporo, Japan, is used as a case study on VHG mapping. Over 1,000 water levels are compiled, and then a portion of the data is extracted by using long-term water level analysis in observation wells. Water levels in individual wells are also grouped by well depth into shallow wells and deep wells. A GTE map is first produced using the shallow well data. Individual VHG values in the deep wells are calculated from their water levels, prior estimated GTE, and representative values of screen depth elevation. There are two problems in this process. (1) VHG is, in typical practice, calculated to determine the screen elevation between the top and bottom elevations, which are often separated by several tens of meters or more. In this study, three cases, namely, the top, middle, and bottom elevations are used, and then the resulting maps are compared. (2) Regional mapping of GTE and VHG includes a non-stationary problem. In this study, the deterministic drift in GTE is formulated as a linear relation with the ground surface elevation. Moving neighborhood kriging is also used in VHG mapping. Cross-validation is conducted to evaluate the validity in the GTE and VHG maps. The actual groundwater flow system in the fan is examined from the resulting GTE and VHG maps.

2.2   Material and methods

2.2.1   Data preparation

Numerous water wells and boreholes have been constructed in and around the Toyohira River alluvial fan. The target region including the fan is defined in the range of the *X* coordinate (north-south) as $-101,000$ to $-111,000$ m and the *Y* coordinate (east-west) as $-77,000$ to $-68,000$ m on the Japanese coordinate system (the Japanese Geodetic Datum 2000: JGD2000). The extent loosely corresponded to latitude from 43°05′13″ to 42°59′52′N and longitude from 141°18′15″ to 141°24′58″E. In this study, a total of 1,392 water level data are firstly compiled (Figure 2.1). A

portion of these data are publicly available in publications of the Geological Survey of Hokkaido (Yamaguchi et al. 1965; Obara 1969) and a digital shape file of the Hokkaido region (National and Regional Policy Bureau 2007). Other data are from private or unpublished reports. Since the 1970s, groundwater level and quality in the fan have been monitored by the Hokkaido Regional Development Bureau and the Geological Survey of Hokkaido. The observation wells are shown as solid squares in (Figure 2.1, and details about the wells are listed in Table 2.1.
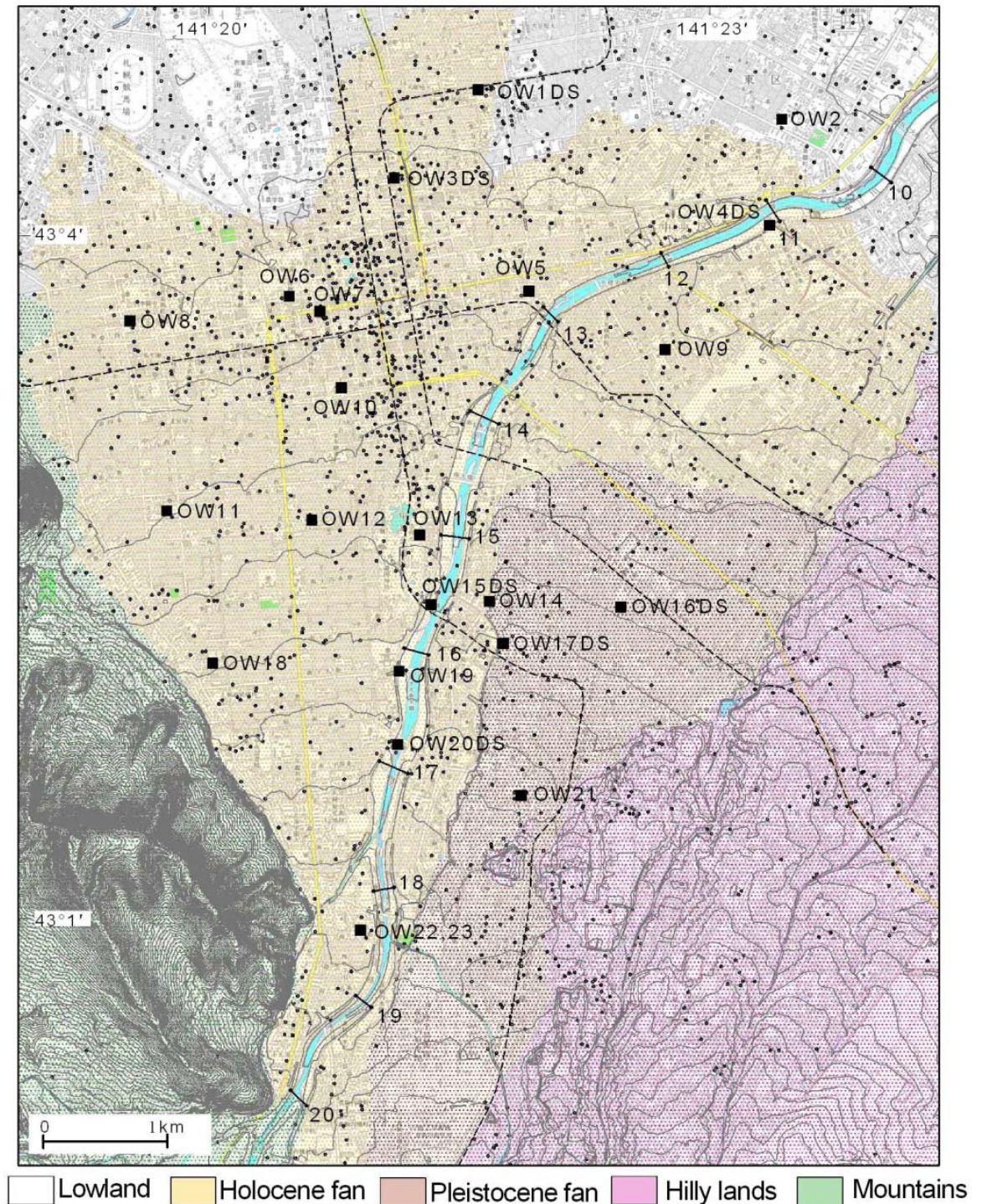
Figure 2.1 Location maps and topographic features of the study area: the Toyohira River alluvial fan. Small points are the wells and boreholes that provided water level data before filtering (n = 1,392). Solid squares are long-term observation wells, details of which are listed in Table 1. Bold black line shows the position of the cross section in Figure 2. Gray dashed lines are subway lines constructed in the city. Figure 1c also shows ground surface contours with 1 m interval from 5 to 80 m asl, and short lines along the river indicate KP which denote the distance (in kilometers) along the river channel upstream from the confluence with the Ishikari River.

Table 2.1 Long term observation wells in the Toyohira River alluvial fan

Well[a]	Location[b]			Measurement period		Screen depth (m)		Class[c]
	Londitude	Latitude	GH	Start date	End date			
OW1D	04' 39"	21' 41"	13.54	1-Jan-79	31-Dec-08	31.5	37.0	D
OW1S	04' 39"	21' 41"	13.78	20-Jun-73	31-Dec-09	10.0	18.0	S
OW2	04' 32"	23' 30"	11.11	20-Jun-73	9-Mar-11	11.0	16.5	S
OW3D	04' 15"	21' 11"	15.70	19-Mar-11	17-Aug-12	43.0	44.0	D
OW3S	04' 15"	21' 11"	15.70	19-Mar-11	17-Aug-12	10.0	15.0	S
OW4D	04' 04"	23' 26"	14.01	10-Mar-06	31-Dec-08	44.0	48.0	D
OW4S	04' 04"	23' 26"	13.97	10-Mar-06	31-Dec-08	10.0	14.0	S
OW5	03' 46"	22' 00"	18.05	9-Jun-73	31-Dec-09	11.5	17.0	S
OW6	03' 44"	20' 34"	18.12	3-Dec-93	31-Dec-09	27.0	32.5	D
OW7	03' 40"	20' 45"	18.96	9-Dec-80	23-Mar-93	27.0	32.5	D
OW8	03' 37"	19' 37"	17.33	3-Jan-77	31-Dec-08	54.5	60.0	D
OW9	03' 31"	22' 49"	15.87	20-Jun-73	31-Dec-09	4.5	13.5	S
OW10	03' 20"	20' 53"	23.47	23-Oct-73	11-May-02	14.0	19.5	S
OW11	02' 47"	19' 51"	25.04	11-Sep-80	31-Dec-09	9.5	15.0	S
OW12	02' 45"	20' 43"	28.14	25-Oct-79	10-Mar-11	8.0	19.0	S
OW13	02' 41"	21' 22"	29.74	1-Jan-91	31-Mar-12	17.2	30.2	D
OW14	02' 24"	21' 47"	34.22	17-Dec-80	31-Dec-09	16.5	22.0	D
OW15D	02' 23"	22' 34"	35.11	1-Jan-79	31-Dec-08	28.5	34.0	D
OW15S	02' 23"	22' 34"	35.13	1-Nov-73	10-Mar-11	14.5	20.0	S
OW16D	02' 23"	21' 26"	31.30	9-Jun-10	17-Aug-12	62.0	64.0	D
OW16S	02' 23"	21' 26"	31.30	9-Jun-10	17-Aug-12	2.5	7.5	S
OW17D	02' 13"	21' 52"	39.36	10-Mar-06	31-Dec-08	22.0	30.0	D
OW17S	02' 13"	21' 52"	39.37	1-Jan-07	31-Dec-09	15.0	19.0	S
OW18	02' 07"	20' 08"	34.61	11-Sep-80	31-Dec-09	9.5	15.0	S
OW19	02' 05"	21' 15"	35.20	25-Sep-10	17-Aug-12	4.0	5.0	S
OW20D	01' 46"	21' 15"	39.00	10-Aug-10	17-Aug-12	99.0	100.0	D
OW20S	01' 46"	21' 15"	39.00	9-Jun-10	17-Aug-12	2.5	7.5	S
OW21	01' 33"	21' 59"	53.41	20-Jun-73	10-Mar-11	8.0	19.0	S
OW22	00' 57"	21' 02"	54.01	6-Jun-73	10-Mar-11	7.7	13.2	S
OW23	00' 55"	21' 04"	53.38	10-Mar-06	31-Dec-09	25.0	26.5	D

[a]Original names of wells in Japanese are omitted, and numberings are given from the north to the south. D and S, respectively, denote deep and shallow wells in close proximity (i.e., piezometer nests). [b]Location is common at 43°N or 141°E, and GH denotes ground height (m asl). [c]D and S denote deep and shallow wells, respectively.

Furthermore, in 2010 the authors observed water levels at some of the individual wells and in a longitudinal distribution of river stages to obtain more valid data.

Figure 2.2 Photos of water level measurement in observation wells; a) OW20S, b) OW6

The records for each well or borehole contained all or some of the following items: location, total depth, installed screen length(s) and position(s), geology, pumping and non-pumping (static) water levels, and pumping or logging test results. Figure 2.3 shows that well depths and screen lengths are variously distributed: most well depths range from 30 to 50 m, and the screen lengths are almost evenly distributed until 50 m.

a

Depth (m)

Frequency

b

Screen length (m)

Frequency
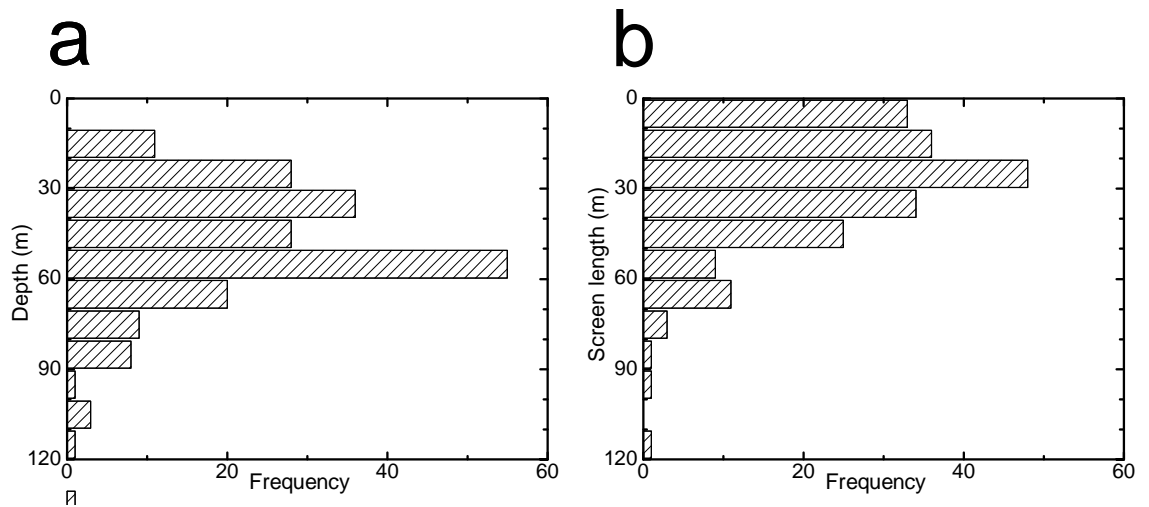
Figure 2.3 Histograms of well depths (a) and screen lengths (b). Screen length is the distance from the top to bottom of screens. The wells ($n = 203$) are those used for analysis; the depths are over 20 m, and the water levels are measured since 1988

Over the past 50 years, static water levels have been measured at various times, but often only during initial construction. In most records, dates of observations are given in year only, not month or date. The hydraulic head mapping firstly required the extraction of data representative of the target period, which, in this study, is the present. The filtering process is based on the long-term water level variations at the 30 observation wells listed in Table 2.1. From 1969 to 1994, three subway lines were in turn constructed in Sapporo, and during this period heavy pumping was repeatedly conducted for dry work. The annual mean variations in the observation wells are evaluated to detect the dewatering period. The differences between daily means in each observation wells and total mean after the period are also statistically represented as box plots to assess daily fluctuations. The annual trends in observation wells are evaluated by using nonparametric techniques: the Mann-Kendall test (Mann 1945; Kendall 1975) and Sen's slope estimation (Sen 1968). The traditional techniques have been widely used to test for randomness against trends (e.g., Wen and Chen 2006; Soderberg and Hennet 2007). In this study, the trend analysis is archived using a free Excel macro (Salmi et al. 2002).

The extracted water levels are divided into two categories: shallow wells of up to 20 m deep and deep wells of greater than 20 m deep. Groundwater levels in the shallow wells are considered to be nearly equal to the groundwater table at the time and location, because the water tables are

observed initially at ≤20 m depth during the drilling of wells and boreholes in the fan. On the other hand, groundwater levels in the deep wells might be affected by VHG at the location.

The data set is input into a geographical information system (GIS). GIS makes it feasible to interpolate environmental variables through built-in applications based on deterministic or geostatistical techniques (Burrough and McDonnell 1998; Johnson 2009). In this study, ArcGIS v.10 (ESRI, Inc.) is used for analysis and mapping.

2.2.2   Kriging interpolation

Kriging gives the BLUE and its variance at any given point by using neighbor measurements and a variogram model. Maps of target variables, GTE and VHG in this study, are generated by kriging interpolation on a regular grid cell. The accuracy of the maps depends on the number and distances of reliable measurements, and on the variogram model. The experimental variogram, which characterizes the spatial variability of the data, is defined as half the average squared difference between two attributed values (Deutsch and Journel 1998). In this study, variogram modeling (i.e., production of the experimental variogram and parameterization of the theoretical variogram) is performed by using the software Surfer 10 (Golden Software).

Ordinary kriging and simple kriging are fundamental techniques in geostatistics. The difference between them is small, but ordinary kriging is more useful in practice because ordinary kriging filters the unknown mean required for simple kriging by adding the constraint that the kriging weights sum to one. Ordinary kriging assumes stationary conditions where the mean of the unknown is constant. If the unknown is not stationary but locally stationary in a certain neighborhood, ordinary kriging is also applied within the local area (de Marsily 1986; Goovaerts 1997; Deutsch and Journel 1998; Wackernagel 2003). Moving neighborhood kriging is conducted by setting a search radius less than the distance in which the stationary assumption is satisfied. The groundwater table forms a subdued replica of the topography, and GTE may not even be local stationary on a wider regional scale. For example, cokriging has been applied for estimating GTE (Hoeksema et al. 1989; Chung and Rogers 2012). In other approaches, a trend component (drift) is formulated as a function of an auxiliary variable. By definition, regionalized variable $Z(\boldsymbol{x})$ is conceptualized as a sum of a grobal trend component (drift) $m(\boldsymbol{x})$, a spatial auto-correlation

component $e'(\boldsymbol{x})$ and a purely random component $e''(\boldsymbol{x})$ as:

$$Z(\boldsymbol{x}) = m(\boldsymbol{x}) + e'(\boldsymbol{x}) + e''(\boldsymbol{x}) \qquad (2.1)$$

Universal kriging and kriging with external drift have been performed (Aboufirassi and Mariño 1983; Desbarats et al. 2002), in which kriging weights and drift parameters are simultaneously solved in the kriging system. Alternatively, the drift and residuals are fitted separately and then summed; this approach is applied in various techniques such as residual kriging, kriging combined with regression, and regression kriging. The applicability also has been indicated through comparison studies (e.g., Knotters et al. 1995; Hengl 2007; Nikroo et al. 2010). The formulas and parameters of drift are firstly determined by ordinary least squares (OLS). Statistically, unbiased parameters of drift are also determined by the iterative process of generalized least squares (GLS) (Cressie 1993; Hengl 2007). GLS is a sophisticated but laborious process. The first OLS drift should be satisfactory but slightly inferior (Kitanidis 1993; Minasny and McBratney 2007). In this study, a simple linear relation is established between the GTE at each shallow well and its ground surface elevation. The relation is defined as the drift of GTE. The GTE value is thus represented as

$$GTE_i = m_i + \varepsilon_i = aGSE_i + b + \varepsilon_i, \qquad (2.2)$$

where GTE_i is the groundwater table elevation estimated at a shallow well, i is the index of the shallow well, m_i is the deterministic drift derived from the topography, ε_i is random spatially correlated residual, and GSE_i is the ground surface elevation at the shallow well. Elevation in this paper is given in meters above mean sea level. If GSE_i in many wells is not available, GSE_i is estimated from a high-resolution digital elevation map (DEM) by using the GIS application. The spatial variability of residuals, ε_i is estimated as a variogram model, and residual map is produced by ordinary kriging assuming a stationary condition. In this study, the grid size used is 100 m by 100 m. The size is set based on the accuracy of well location data. The drift map is prepared by combining DEM and Equation (1). The GTE map is finally obtained by adding the residual map to the drift map. The raster calculation in GIS is used for this process. The groundwater table depth (GTD) is also mapped by subtracting the GTE map from the DEM.

Following GTE mapping, the VHG value at each deep well is calculated as

$$VHG_j = (WLE_j - GTE_j) / (GTE_j - SDE_j), \qquad (2.3)$$

where VHG_j is the individual VHG value in a deep well and j is the index of the deep well. A

positive (negative) value indicates upward (downward) groundwater flow. WLE_j is the water level elevation, GTE_j is the GTE extracted from the prior GTE map through the GIS application. SDE_j is the representative value of screen depth elevation between the top and bottom screen depths. SDE_j is considered to differ among the deep wells, and its determination is problematic. In this study, three cases, namely, the top, middle, and bottom elevations of screens, are used for individual VHG calculation (Figure 2.4). The VHG values in the different cases are respectively mapped by ordinary kriging interpolation. The experimental variograms show some probability of nonstationary in VHG, so moving neighborhood kriging is applied.
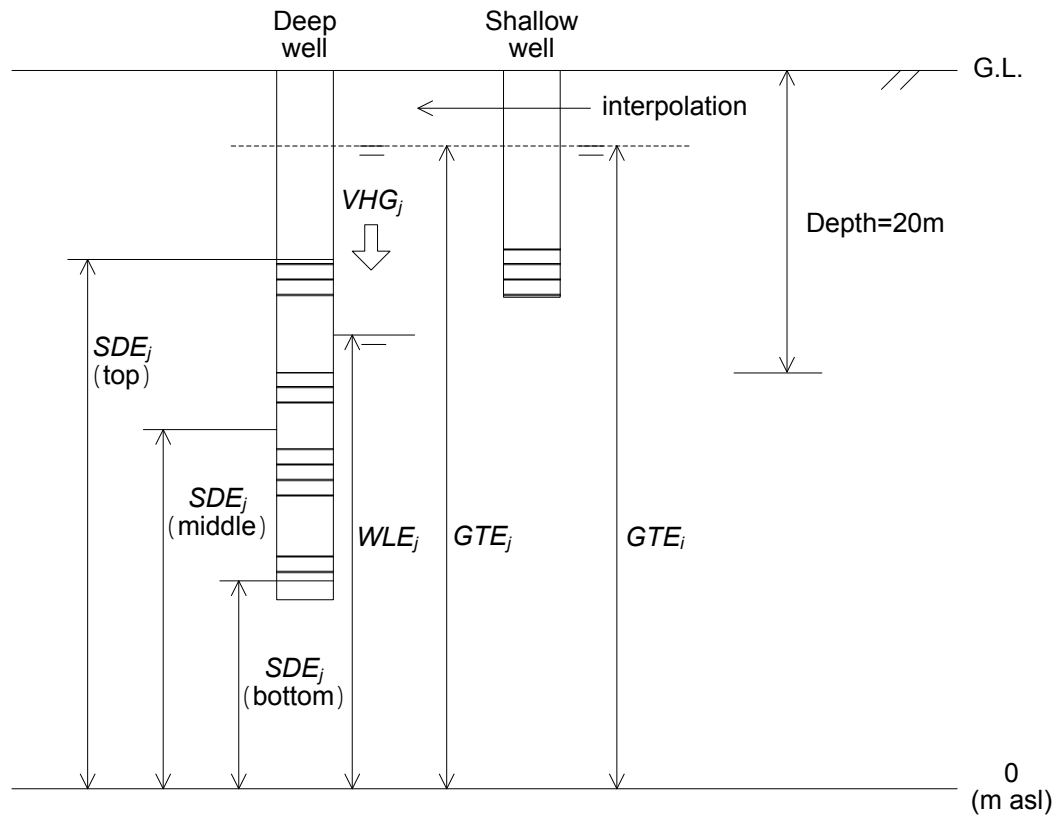
Figure 2.4 Definition of inputs for each well (piezometer)

2.2.3   Cross-validation

Cross-validation is used to verify the resulting GTE and VHG maps. For the GTE map, cross-validation is performed for residuals at all of the shallow wells, and then the residuals are translated to GTE estimates by summing the topographic drift. The resulting GTE estimates are compared with the measurements, GTE_i. For the VHG maps, cross-validation is conducted at all of

the deep wells in each case of different SDE_j values. The mean error (ME), root mean square error ($RMSE$), and mean square standard error (MSSE) are used for error estimation:

$$ME \quad \frac{1}{n}\sum_1^n \left(z(\pmb{x}_i) - z^*(\pmb{x}_i) \right) \qquad (2.4)$$

$$RMSE \quad \sqrt{\frac{1}{n}\sum_1^n \left(z(\pmb{x}_i) - z^*(\pmb{x}_i) \right)^2} \quad (2.5)$$

$$MSSE \quad \frac{1}{n}\sum_1^n \frac{\left(z(\pmb{x}_i) - z^*(\pmb{x}_i) \right)^2}{\sigma_i^2} \qquad (2.6)$$

where n is the number of wells (shallow wells for GTE mapping, or deep wells for VHG mapping), $z(\pmb{x}_i)$ is the measured GTE or VHG value, $z^*(\pmb{x}_i)$ is the estimated GTE or VHG using the $n-1$ other data, and σ_i^2 is the kriging standard deviation, which is the prediction error at location $\pmb{x}_i$. The selected variogram model and its optimized parameters are adequate when the ME and $RMSE$ values are close to zero, and the $MSSE$ value is close to one with a tolerance range $[1-3\sqrt{2/n}, 1+3\sqrt{2/n}]$ (Chilès and Delfiner 1999).

2.3   Results and discussion

2.3.1   Data filtering

The annual mean water variations at the observation wells are shown in Figure 2.5a. The groundwater level variations show drawdowns in two typical seasons, i.e. winter and summer, the former related to low recharge due to snow covering, and the latter due to (Fukami 2010).

Significant drops in water level are seen in most observation wells during 1985−1987, which are years when subway construction occurred. The dewatering is not obvious in the apex at OW18 and OW22U, which are located far from the subway lines. Water levels almost completely recover in a few wells starting from 1988, but in most wells the levels remain low.

Figure 2.5b shows box plots of the differences of daily means from the total mean in each observation well since 1988. The box plots statistically show daily fluctuations after the subway construction, and water levels from that year are within a range of a few meters except in special cases, such as heavy precipitation.
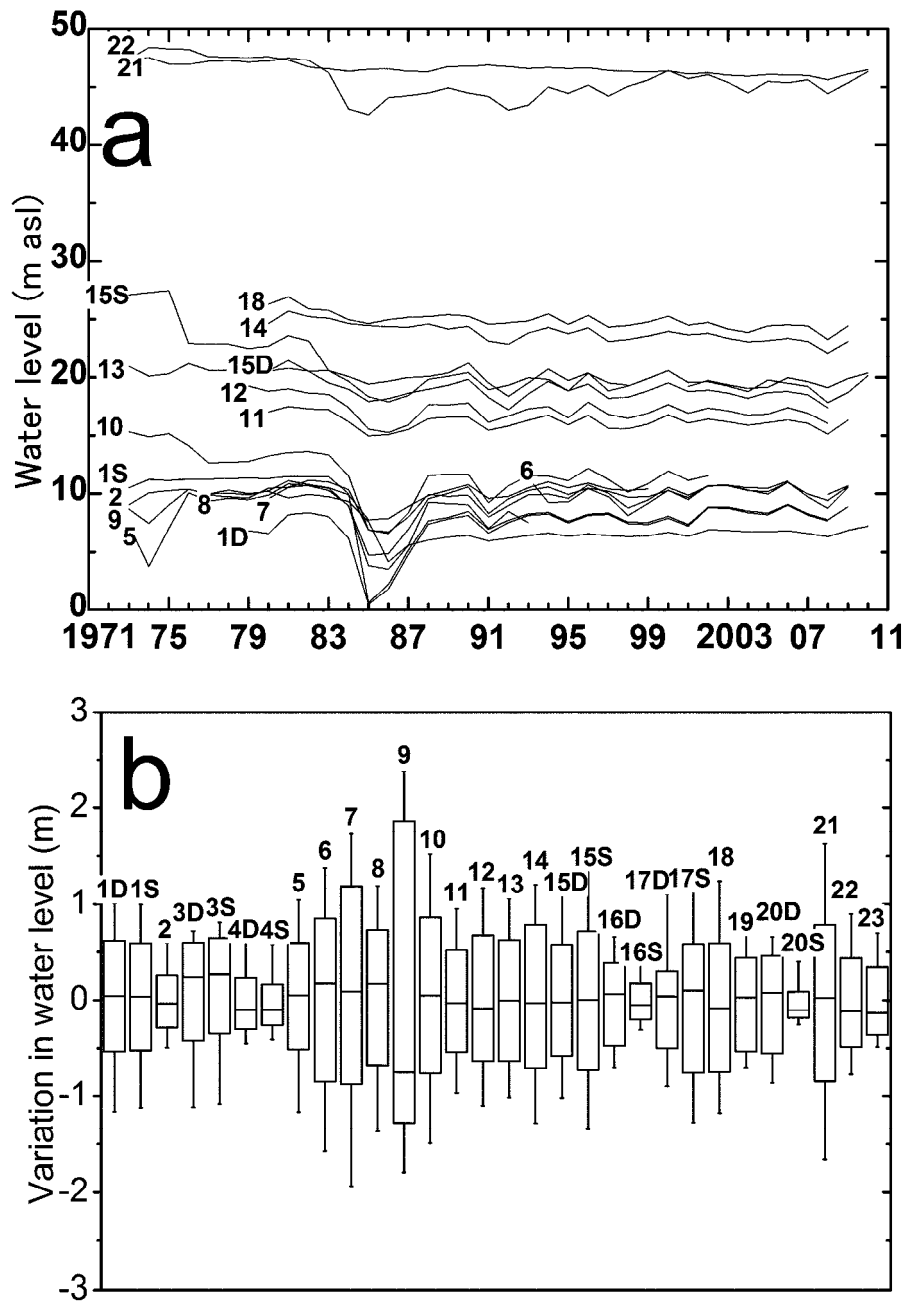
Figure 2.5 (a) Long-term variations in annual mean water levels and (b) box plots of groundwater levels in the observation wells. Variations are produced in the observation wells from hourly data covering at least 3 years. Box plots indicate differences of daily mean levels from the total mean level in each observation well since 1988. Boxes from the left to the right correspond to the numbering of the observation wells (Table 2.1). The bars represent, from above, values of upper 90%, upper quartile, mean, lower quartile, and lower 90%

The results of the Mann-Kendall test and the Sen's slope estimates since 1988 are summarized in Table 2.2. Positive trends are seen in an area of the distal part, and negative trends in an area of the apex.

Positive trends likely indicate a change of water intake (e.g., a decrease in pumping rate) around the distal part. Conversely, negative trends indicate decreasing total water storage in the fan. In future work, we will discuss the fan's groundwater vulnerability and its changes in more detail. The magnitudes of Sen's slopes are mostly less than 0.05, and the largest is no more than 0.07. For such trends, total variations in water levels from 1988 to the present remained less than a few meters. This indicates that the long-term trends since 1988 approximately contain the seasonal and annual fluctuations shown in the box plots.

The above results suggest that the water levels before 1988 were probably affected by subway construction, and that the water levels after 1988 were affected by daily fluctuation and long-term trends but appear nearly random within the range of a few meters. Consequently, in this study only post-1988 data is used for our analysis. If multiple measurements are available at the same well, the data with the latest date are used. Automatic records, often updated hourly, are averaged over the full post-1988 measurement period. The extracted water levels obtained since 1988 are divided into two categories: shallow wells of up to 20 m deep ($n = 216$), and deep wells of greater than 20 m deep ($n = 203$).

Table 2.2 Results of Mann-Kendall test and Sen's slope estimation on annual mean water levels (1988–2010)

Well[a]	Slope[b]	Significance[c]
OW1D	0.039	*
OW1S	0.036	*
OW2	0.034	***
OW5	0.022	NS
OW6	0.032	NS
OW8	0.053	*
OW9	0.010	NS
OW10	−0.001	NS
OW11	−0.014	NS
OW12	−0.014	NS
OW13	−0.011	NS
OW14	−0.060	**
OW15D	−0.032	NS
OW15S	−0.050	*
OW18	−0.049	**
OW21	0.066	**
OW22	−0.044	***

[a]Only wells observed for a period of 10 years or longer since 1988 are used. [b]Sen's slopes are estimated in m/yr. [c]***, $p < 0.001$; **, $p < 0.01$; *, $p < 0.05$; NS, $p \geq 0.1$.

2.3.2　GTE and GTD maps

Linear fitting is performed between the water levels in shallow wells and ground surface elevations, and the OLS drift parameters resulted in slope of 0.970, an intercept of −3.33. The correlation coefficient R^2 of 0.96 is sufficiently high.

Figure 2.6 shows the experimental variogram of the residuals, ε_i. A spherical model is used as the theoretical variogram model after a comparison among authorized models:

Figure 2.6 Omnidirectional variogram and fitted spherical model for residuals of GTE_i,

$$\gamma(h) \quad B \quad (C \quad B)\left[\frac{3}{2}\frac{h}{a} - \frac{1}{2}\left(\frac{h}{a}\right)^3\right] \tag{2.7}$$

Here, B is the nugget effect, C is the partial sill, a is the range, and h is the separation distance. Anisotropy of the spatial variability is a main consideration in hydraulic head mapping (Kitanidis 1993). In this study, isotropy in residuals is assumed because the topographic drift includes anisotropy, and cross-validation results are satisfactory. The fitted model and optimal parameters are shown in Figure 2.6.

Figure 2.7shows the cross-validation results. The ME and MSSE values are, in large part, close to zero and one, respectively, indicating the suitability of the mapping. The RMSE value means that the prediction errors are within several meters. Such estimation errors of this level are regrettably inevitable under the uncertainty of conventional well data, owing to daily fluctuation and long-term trends. However, the errors are insignificant for discussing the GTE map on a 101 m order scale.

Figure 2.7 Cross-validation results of GTE above sea level

Figure 2.8 shows the estimated maps of GTE and GTD. Variance maps are omitted here, but the above cross-validation shows that uncertainty is within acceptable limits. The steep land-surface slope of the fan contributes to the substantial driving force from the apex to the distal part. The GTE inclines northward between about 5–60 m asl. within a distance of only about 5 km. A GTE mound and shallow GTD zone also appear along the river at KP 14–19, indicating the interaction between surface water and groundwater through the riverbed. The radius of the GTE mound and shallow GTD zone is no more than 1 km from the river channel. The groundwater table is deep (GTD ≥ 6 m) except around the river. Over 80 years ago, the groundwater table was shallower in the Holocene fan, and the GTD was less than 0–5 m (Fukutomi 1928). In contrast to previously published water table contours before subway construction (Yamaguchi 1983), the dewatering of the fan exceeds 5 m from the middle to distal parts. In the southeast part of the Pleistocene fan, the groundwater table is especially deep (GTD > 10 m), indicating an incorporation of groundwater recharge by highland and dewatering by subway lines, as also indicated in the VHG map discussed below.
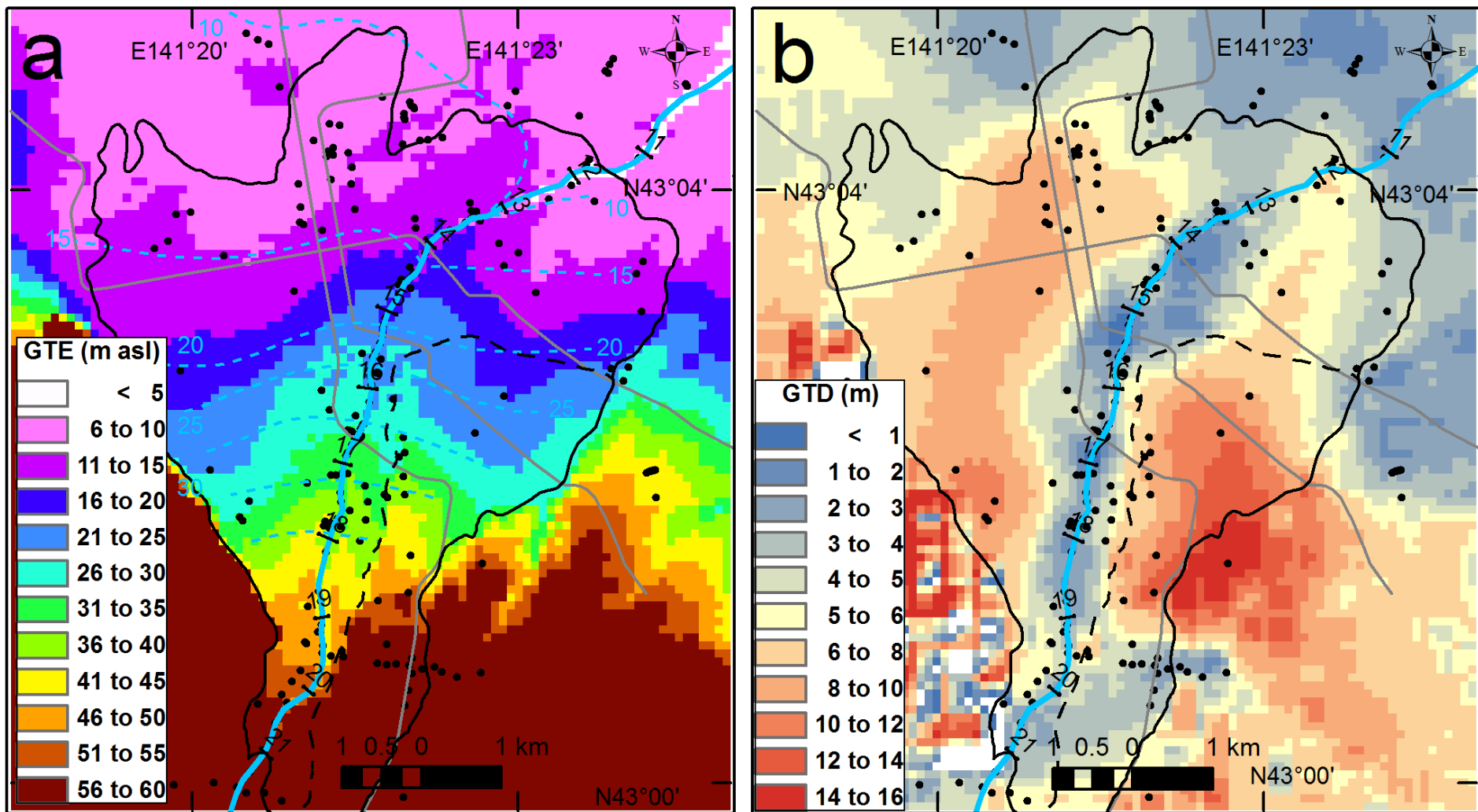
Figure 2.8 Maps of (a) GTE and (b) GTD in the Toyohira River alluvial fan. Scattered black circles map shallow wells, boreholes, and observation points for river stages. The black solid line denotes the topographic area of the alluvial fan, including the broken boundary line between the Holocene fan and the Pleistocene fan. Short bars along the river denote transects with KP values. The gray lines indicate subway lines through the fan. The broken sky blue lines are water table contours with 5 m intervals (m asl) in April 1960 before subway lines were constructed (Yamaguchi 1983)

2.3.3 VHG map

(1) Comparison among results of three cases

Figure 8 shows variograms of individual VHG values for three cases: the top, middle, and bottom screen depth elevations. The spherical models are used for fitting as GTE. The nugget and partial sill values are largest in the case of the top elevations, and smallest in the case of the bottom elevations. This is a natural result because the denominator on the right side in Equation (2) becomes larger as the screen depth, SDE_j, increases. In other words, kriging variances also become smaller as greater screen depths are selected for VHG calculation. The variogram models in these cases do not converge over a distance of 2,000 m, indicating the possibility of a spatial trend in VHG. For the potential trend, the VHG mapping is conducted by moving neighborhood kriging with a search radius of 1,000 m.
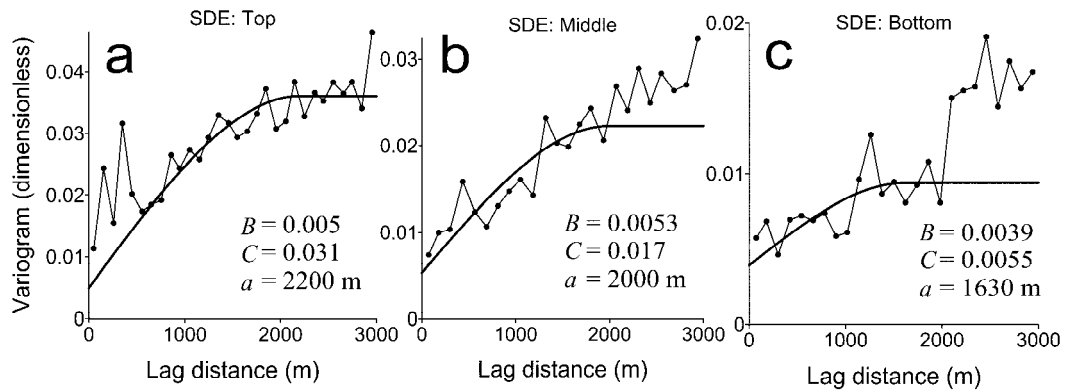
Figure 2.9 Omnidirectional variogram and fitted spherical model for VHG_j in three cases: (a) top, (b) middle, and (c) bottom screen depth elevations used for VHG calculation

Table 2.3 summarizes the results of cross-validating the deep wells in the three cases. The *ME* values indicate an absence of bias in all the cases (Table 3a). The *RMSE* values are slightly different among the cases, decreasing with greater screen depth. On the other hand, the variation in *MSSE* values differs among the cases, and the value in the case of the bottom screen depths is only within the tolerance interval [0.70, 1.30] ($n = 203$). The cross-validation results are also compared in terms of error with respect to reliable VHG data (Table 2.3 b). In the distal part with small VHG values (OW1 to 4), kriging estimates and variances insignificantly differ among the cases. In the middle to the apex with negative VHG values (OW15 to 20), differences in the estimates are relatively clear. Particularly at OW15 and OW16, the prediction errors are unacceptable in the case of the top screen depths, but are relative small in the case of the bottom screen depths.

The comparison of cross-validations among the cases indicates that VHG is not constant and hydraulic heads change inconsistently in the vertical direction, especially in the middle to apex of the fan. As a result, the GTE map of only the bottom screen depths holds an acceptable accuracy for such a 3D system. The approach for VHG mapping is strongly affected by which screen depth is used as a representative position of water level, and the deepest value (i.e., the bottom of screen) can be expected to reduce uncertainty because of the large denominator for individual VHG calculations.

Table 2.3 Cross validation results for VHG mapping: (a) error estimators and (b) Comparison with reliable VHG measurements at piezometer nests

a

Case[a]	Error estimators[b]		
	ME	*RMSE*	*MSSE*
Top	0.00	0.19	2.67
Middle	0.00	0.13	1.55
Bottom	−0.01	0.09	1.18

[a]Cross-validation is conducted in three cases, the top, middle, and bottom screen depths for VHG calculation. [b]*ME*, *RMSE*, and *MSSE* are, respectively, mean error, root mean square error, and mean square standard error (dimensionless).

b

Well[a]	Measurements[b]			Cross-validation results[c]					
				Top		Middle		Bottom	
	WLE	GTE	VHG	Est	Var	Est	Var	Est	Var
OW1D&S	7.95	8.13	-0.01	−0.04	0.02	−0.02	0.01	−0.01	0.01
OW3D&S	9.19	9.37	0.00	−0.06	0.02	−0.03	0.01	−0.02	0.01
OW4D&S	6.14	5.81	0.01	−0.07	0.02	−0.06	0.02	−0.04	0.01
OW15D&S	18.69	19.56	−0.06	−0.38	0.02	−0.23	0.01	−0.20	0.01
OW16D&S	20.51	28.17	−0.13	−0.32	0.01	−0.21	0.01	−0.17	0.01
OW17D&S	24.05	27.73	−0.26	−0.28	0.01	−0.28	0.01	−0.22	0.01
OW20D&S	17.32	36.78	−0.20	−0.26	0.02	−0.19	0.01	−0.14	0.01

[a]Deep (D) and shallow (S) wells are installed in close proximity as piezometer nests. [b]*WLE* is water level (m asl) in the deep well, and *GTE* is groundwater table elevation (m asl) in the shallow well. *GTE* and *WLE* are mean values of all hourly data from 1988. Individual VHG values (dimensionless) are calculated by Equation (2) using the middle screen depths in the deep wells. (2). [c]Est and Var indicate kriging estimates and variance (dimensionless), respectively.

(2) VHG distribution in the fan

Figure 2.12 show the obtained VHG and its variance maps in the case of the bottom screen depths. The VHG map visually and directly shows the magnitude and extent of positive or negative peaks of VHG. The variance of VHG is no more than 0.01 throughout the fan because deep wells for analysis are distributed with a sufficiently high density. The positive and negative peaks correspond to recharge and discharge zones of the fan. The mapped VHG values are negative in most of the fan, indicating that vertical flows of groundwater are mainly downward. In most alluvial fans, the distal part is believed to be the discharge area because of the regional flow system. In the Toyohira River alluvial fan, however, weakly positive VHG values no more than 0.05 are found in only a part of the northwest area of the distal part. The disappearance of the discharge area in the fan is likely due to dewatering of the aquifer in the Holocene fan via heavy pumping and drainage to the subway lines. The most negative peak of VHG (VHG < −0.3) appears in the Pleistocene fan. The high, steep land surface in the area can be identified as a recharge area. In addition, the water variations (Figure 2.5a) show dewatering by the subway construction in the center of the negative peak (observation well at OW15D and S). Incorporating the recharge and the dewatering occurs the negative peak in the Pleistocene fan.

The areal relation between river stage and groundwater table indicated that the shallow groundwater system is areally divided into three sections: (1) KP> 19; the groundwater table is higher than the river stage (gaining); (2) KP 15.5-19; the river stage is higher than the groundwater table, and both are continuous with natural slope (losing), (3) KP< 15.5; the groundwater table is nearly equal or higher than the river stage (constant or gaining). The negative (orange) zone at KP 15.5−19 nearly corresponds to the GTE mound and shallow GTD zone, indicating infiltration from the river. The northern (lower) part (KP 15.5−17.0) is in especially good agreement with the distinct losing section found by a synoptic discharge survey (Sakata and Ikeda 2012a). However, the northern peak crosses two subway lines, and heads northwestward along the lines. The dewatering around the subway lines also induces a negative peak of VHG, and increases seepage loss from the riverbed. On the other hand, in the southern (upper) part (KP 17.0−19.0), the rate of seepage loss is not clearly detected by the synoptic discharge survey. The section corresponds to the sudden depression of the consolidated rock shown in Figure 1.9. The steep inclination of the

basement, in other words the sudden increase in the thickness of aquifer, probably induces an accumulation of downward groundwater flow at the head. This highlights the potential applicability of the VHG map in obtaining information about hydrogeologic structure at considerable depth, which is usually accomplished by other geophysical methods such as seismic investigations.

Figure 2.10 Maps of (a) VHG and (b) VHG variance in the Toyohira River alluvial fan. The elevations of top screens in the deep wells (circles) are used for individual VHG values. The cross-validation (Table 2.3) showed the maps are statistically inferior than Figure 2.12.

Figure 2.11 Maps of (a) VHG and (b) VHG variance in the Toyohira River alluvial fan. The elevations of middle screens in the deep wells (circles) are used for individual VHG values. The cross-validation (Table 2.3) showed the maps are statistically inferior than Figure 2.12
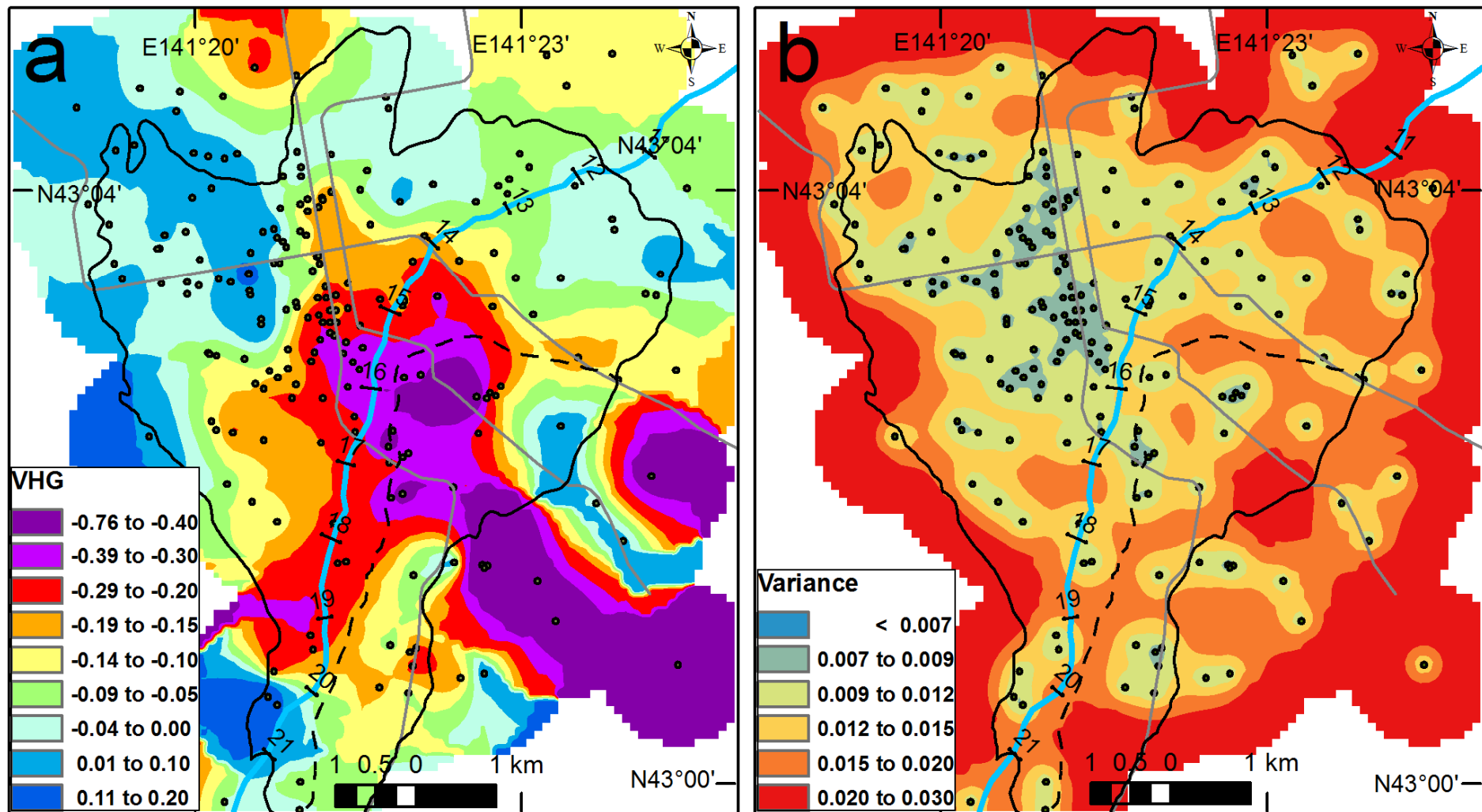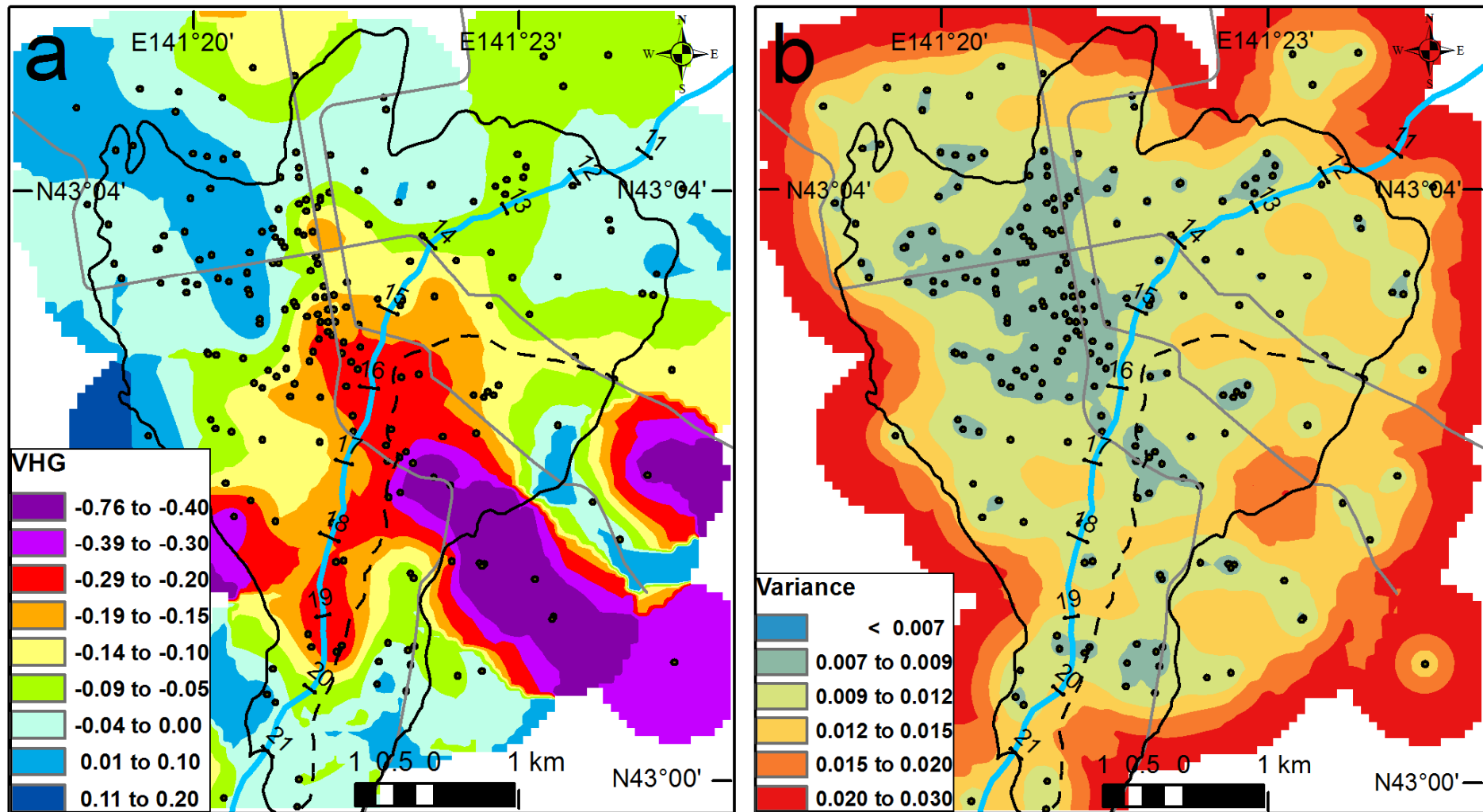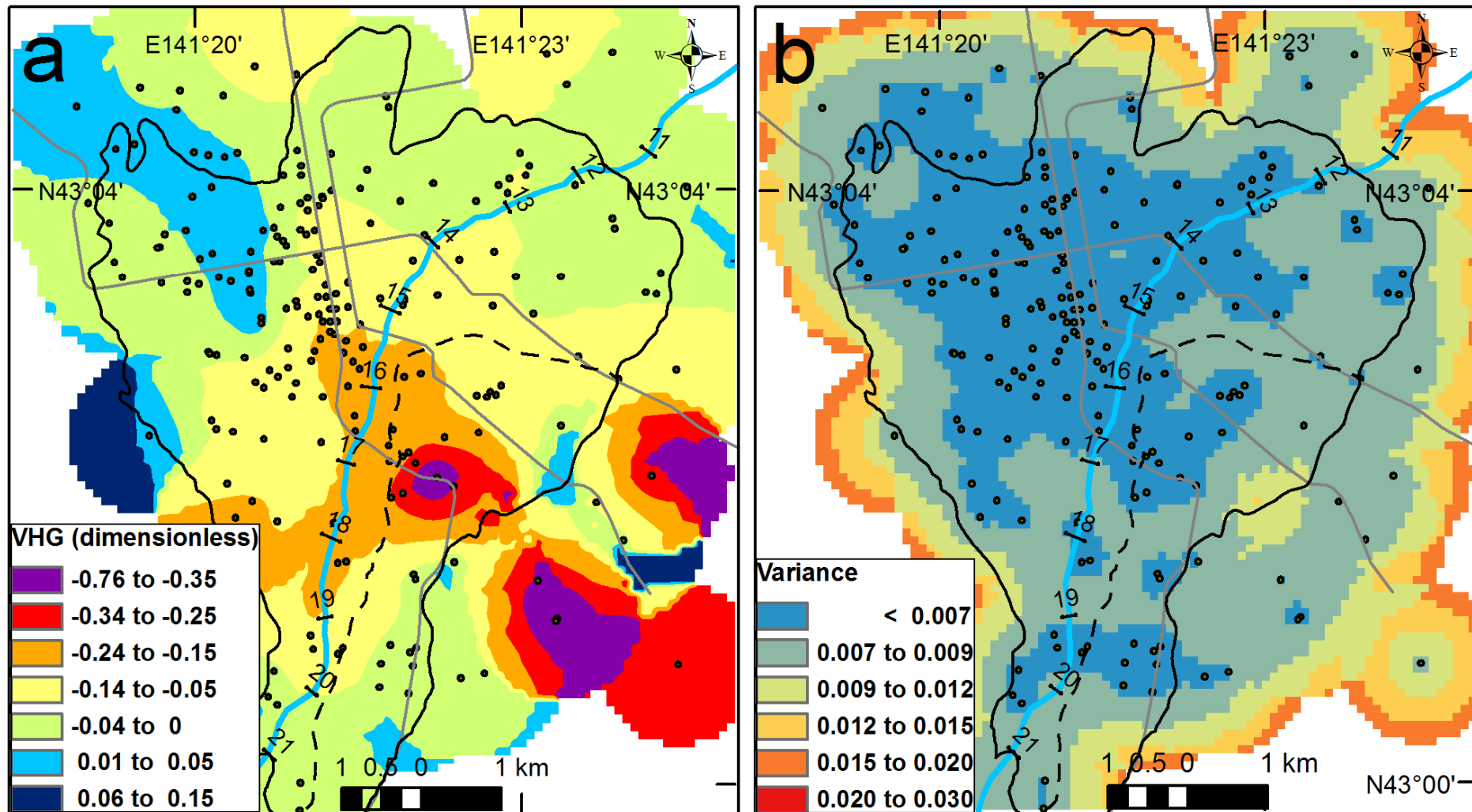
Figure 2.12 Maps of (a) VHG and (b) VHG variance in the Toyohira River alluvial fan. The elevations of bottom screens in the deep wells (circles) are used for individual VHG values. The cross-validation (Table 2.3) shows the maps are more valid than Figure 2.10 and Figure 2.11

2.4 Conclusions and future works

Mapping of vertical hydraulic gradient has rarely been attempted on the regional scale because of the lack of piezometer nests and the uncertainty in conventional well data. This study generalized the concept of the traditional plot method, and performed mapping of GTE and VHG by kriging interpolation of conventional well data. The case study site was the Toyohira River alluvial fan, Sapporo, Japan. A large number of water levels were observed by appropriate filtering. The long-term variations in water level and box plots of its fluctuations in 30 observation wells were produced, and nonparametric trend analysis was performed. Annual mean variation indicated that construction of subway lines induced significant dewatering before 1988. Thereafter, the daily fluctuations and the long-term variations ranged within a few meters. Water well data from 1988 were divided into those for shallow wells of up to 20 m deep, and deep wells of over 20 m deep. First, the GTE was mapped by adding the topographic drift to the residuals, which were interpolated by ordinary kriging. The drift was formulated as a linear relation between water levels in the shallow wells and the ground surface elevation by ordinary least squares. Next, individual VHG values in the deep wells were calculated by using its top, middle, or bottom elevations of screen depth, respectively. VHG and its variance maps were also generated by using ordinary kriging with a search radius fixed (moving neighborhood kriging). The cross-validation indicated the validity of the GTE map and the VHG map of the bottom screen depths. The other VHG maps of the top and middle screen depths could not be satisfactorily cross-validated. The VHG map, over a wide area, visually reveals the magnitude and extent of recharge and discharge in the fan. The downward flows are predominantly distributed over the fan due to the basement depression at the head, the seepage loss from the river in the middle, and the artificial dewatering in the distal part.

The proposed incorporation of VHG and GTE maps provides a quasi-3D representation, under the assumption that VHG at any location is invariable from the groundwater table to the bottom of the aquifer; The assumption is not realistic. Several recent studies have currently challenged three-dimensional mapping (Tonkin 2002; Rivest 2008). A 3D-representation of groundwater head remains in future work.

3 Quantification of gravel-bed river discharge and leakage by synoptic survey

3.1 Introduction

Groundwater recharge is the entry into the saturated zone across the water table surface, and information about both recharge area and rate is critical to determine water balances and capacities of aquifers (Bower 1978). Groundwater recharge is also important as upper boundary conditions in numerical models of groundwater flow. For many regional groundwater studies, however, insufficient attention is paid to recharge estimation (de Vries and Simmers 2002; Ruston 2003). This is because groundwater recharge generally varies in space and time, depending on both systematic and random fashions. Hence, estimation of recharge is most problematic in groundwater modeling study as geologic heterogeneity.

A variety of techniques for recharge estimation are developed on different time- and space- scales (e.g. Gee and Hillel 1988; Scanlon et al. 2002; Healy 2010). Most methods are fundamentally based on the water-budget equation, such that recharge is calculated as a residual component in precipitation from other meteorological, hydrological, and hydrogeological components. Considering only measurement error, variance of recharge component is represented as a sum of variances of other components. If recharge is small relative to other components, as usual there are, uncertainty of recharge component can easily exceed 100% of the true value (Gee and Hillel 1988). Thus, the validity of recharge estimation depends on accuracy of other components. However, all of various components that consist of the water-budget equation are rarely obtainable with sufficient accuracy level, especially on regional scale.

The water budget method is applicable under specific conditions that as much components as possible are negligible. Intermittent focused recharge from streams or rivers is often the dominant recharge mechanism in arid- and semi-arid regions (Healy 2010). Here, focused recharge is more localized recharge from specific bodies of water to underlying aquifer, while diffuse recharge is more regional recharge reffered from precipitation and snow melting. The rate of focused recharge is generally higher as either slope or permeability of the river-bed increases, such as in the rivers flowing on alluvial coarse aquifers. Also in such regions, river managements during low flow periods are frequently focused on how minimum discharge under the seepage loss is needed to

enhance endangered living in the river.

The focused recharge occurs based on the mechanism of interaction between surface/groundwater. A stream that receives groundwater discharge is known as a "gaining" stream, whereas a stream that loses water to, or recharges, the groundwater is known as a "losing" stream (Winter 1998). The mechanism is traditionally explained based on Darcy's law, which consists of hydraulic gradient, area normal to flow direction, and hydraulic conductivity of bed materials around the river. The former two terms are relatively easily determined by installing piezometers below the riverbed, however, gravel-bed rivers prove difficulty because of penetration through large cobbles and excessive stream velocities in the riffles. The third term is also rarely determined due to geologic heterogeneity and clogging.

Surface water budget method could directly estimate focused recharge that is integrated over the length of the reach. The method calculates the exchange between ground/surface water as the difference between total inflow and outflow measured by synoptic survey. Thus, synoptic survey is susceptible to uncertainty of inflow and outflow measurements. Weight (2008) suggested that an application of the method requires that net gains (losses) are greater than 10% of flow discharge. In Japan, for example, the influent seepage of rivers flowing through alluvial fans ranged in only 10^{-1} m^3/s/km orders of magnitude (Sasaki 1974). Therefore, the method has been limited only in small rivers of low discharge. Typically, discharge measurements in gravel-bed rivers include more uncertainty due to unsteady turbulent flow and roughness of boundary (Wiberg and Smith 1991). Accordingly, the synoptic survey has been considered to be less applicable in the gravel-bed rivers.

This dissertation advances the synoptic survey method in the context of reduction of uncertainty in the conventional flow measurement. The equation of flow uncertainty is indicated in ISO(2007), and the equation consists of various factors such as point velocity, water depth, number of verticals, and so forth. This research typically focuses two factors; point velocity and number of vertical. The velocimeter used in this thesis is a handheld acoustic Doppler velocimeter (ADV), which yields much more accurate velocities even in shallow water depth conditions. Next, proper arrangement of verticals is also designed in each transect as to minimize the uncertainty. The improved synoptic survey is applied in the Toyohira River, such that the longitudinal discharge and the leakage are quantitatively determined. This investigation also aims to reveal a relation between the river leakage

and the discharge in the Toyohira River. The relation has been reported during high discharge and rapid variation of river stage such as flood flow; bank storage effect. The relation during low and steady flow has been rarely discussed, but the previous synoptic surveys in the Toyohira River indicated the relation.

3.2 Material and methods

3.2.1 Surface-water budget methods

The water budget equation for a reach of stream can be written as (Healy 2010):

$$Q^{sw}_{out} = Q^{sw}_{in} + P - ET^{sw} - \Delta S^{sw} + R_{off} + Q_{trib} + Q_{inter} - Q_{seep} \qquad (3.1)$$

where Q^{sw}_{out} is the streamflow (discharge) at the downstream end of the reach, Q^{sw}_{in} is the streamflow (discharge) at the upstream end of the reach, P is the precipitation falling on the stream, ET^{sw} is the evaporation from the stream, ΔS^{sw} is the change in stream strage, R_{off} is the surface runoff to the stream, Q_{trib} is the flow from tributaries within the reach, Q_{inter} is the interflow from the unsaturated zone, Q_{seep} is the net gaining if negative or losing if positive as an exchange of water between the stream and the subsurface.

Q_{seep} is determined as a residual in Equation (3.1). The subsurface terms generally dominate Equation (3.1), and the measurement times are often selected so that precipitation, runoff, and interflow are approximately zero. ET^{sw} and ΔS^{sw} can be estimated independently, but for practical applications on naturally flowing streams the magnitudes of these terms are generally quite small relative to that of the surface-flow terms and often insignificant relative to measurement errors of surface flow (Healy 2010). Hence, Equation (3.1) is written as a simplified form:

$$Q_{seep} = Q^{sw}_{out} - Q_{trib} - Q^{sw}_{in} \qquad (3.2)$$

The method is traditionally conducted through synoptic discharge survey, conducting using stream gaging at several stream cross sections during a short period (Woessner 2000; Simonds and Sinclair 2002; Harte and Kiah 2009). The exchange of water, Q_{seep} can be estimated as the difference between inflow, Q^{sw}_{in} and outflow, Q^{sw}_{out}. All terms in Equation (3.2) are independently measured, and then the variance of the exchange is defined as:

$$\text{Var}[Q_{seep}] = \text{Var}[Q^{sw}_{out}] + \text{Var}[Q_{trib}] + \text{Var}[Q^{sw}_{in}] \qquad (3.3)$$

The above equation indicates that the resulting Q_{seep} needs to be substantially larger in magnitude

than the sum of right terms, Var [Q^{sw}_{out}], Var [Q_{trib}], Var [Q^{sw}_{in}], for quantitative discussion.

3.2.2 Improvement of flow measurement based on uncertainty

A method for measuring flow discharge in a river has been standardized by ISO (2007), and other methods have also been established in each country such as Japan (Public Works Research Institute 2002) and USA (Whiting 2003; Turnipseed and Sauer, 2010). Most publications commonly suggest that velocity measurement is elemental and firstly selected. The velocity method is the method that calculates flow discharge by a sum of subsectional charges which are obtained as products of river width, depth, and average velocity:

$$Q = \Sigma q_i = \Sigma b_i d_i v_i \qquad (3.4)$$

where Q is the total discharge, q_i is the subsectional discharge in the i th segment; b_i is the increment width; d_i is the representative (mean) water depth; v_i is the representative (mean) velocity. The standard uncertainty ("one standard deviation" values, level of confidence approximately 68%) of discharge is calculated by the following equation (ISO 2007) as:

$$u(Q)^2 = u_m^2 + u_s^2 + \frac{\sum_{i=1}^{m} \left(b_i d_i \overline{v}_i \right)^2 \left(u_{b,i}^2 + u_{d,i}^2 \quad u_{p,i}^2 + \left(\frac{1}{n_i} \right) \left(u_{c,i}^2 + u_{e,i}^2 \right) \right)}{\left(\sum_{i=1}^{m} \left(b_i d_i \overline{v}_i \right) \right)^2} \qquad (3.5)$$

where $u(Q)$ is the relative (percentage) combined standard uncertainty in discharge; u_m is the uncertainty due to the limited number of verticals; u_s is the uncertainty due to variable responsiveness of the current-meter (u_{cm}), width measurement instrument (u_{bm}) and depth sounding instrument (u_{ds}), u_s also corresponds to a root of sum of square of these terms. $u_{b,I}$, $u_{d,I}$, $u_{v,i}$ are the relative (percentage) standard uncertainty in the width, depth and mean velocity measured at i th vertical, $u_{p,i}^2$ is the uncertainty in mean velocity v_i due to the limited number of depths at which velocity measurements are made at i th vertical, n_i is the numbers of depths in the i th vertical at which velocity measurements are made, $u_{c,i}$ is the uncertainty in the velocity at a particular measuring point in i th vertical due to lack of repeatability of the current-meter, $u_{e,i}$ is the uncertainty in point velocity at a particular depth in i th vertical due to velocity fluctuations in the stream during the exposure time of the current-meter. This research aims to improve the method of flow measurement to reduce as much uncertainty as possible under the flow

conditions of gravel-bed river such as in the Toyohira River.

(1) Handheld Acoustic Doppler Velocimeter

The right side in Equation (3.5) consists of three terms, and the first term is that due to measurement instruments for width, depth and mean velocity. Among these terms, velocity is highly variable and uncertain value, which especially depends on accuracy of velocimeters (current profilers). The point velocity is conventionally measured by using acoustic velocity current profilers. The traditional velocimeter requires regular maintenance, but the accuracy of the current meters, $u(v_i)$, are considered to be no less than about 5% (Public Works Research Institute 2002; Weight 2010). In addition, the size of the traditional velocimeters is often relatively large in shallow water depths so that the whole of meter is not submerged in several measurement points. In addition, the current meters measure water velocities along flow paths, i.e. maximum of velocity, however equation (3.4) needs velocities normal to tag line. If the flow paths are not uniform along the river channel, the calculated discharges are often overestimated. In gravel-bed rivers, water depths is often less than 10 cm, and turbulent flow vectors non-orthogonally cross the transects.

This investigation applied handheld- acoustic Doppler current velocimeter (ADC), "FlowTracker ADV®" (Sontek/YSI), instead of the conventional velocimeters. The handheld-ADV operates at an acoustic frequency of 10 MHz and measures the phase change caused by the Doppler shift in acoustic frequency reflected to particle movements in the flow. The point velocities obtained by this ADV were statistically equal to those by the propeller current meter (Rehmel 2007). In addition, the FlowTracker can be used in water depths as shallow as 3 cm and in velocities ranged between 0.1 and 450 cm/ s with an accuracy of ±1%. The flow tracker measures not only magnitude of the flow, but also angle of the flow to the tag line, therefore the flow velocity normal to the tag line are exactly obtained. The FlowTracker also has several unique requirements for data-processing, i.e., standard deviation of velocity during measurement time, records the signal-to-noise (S/N ratio), number of filtered velocity spikes, etc.
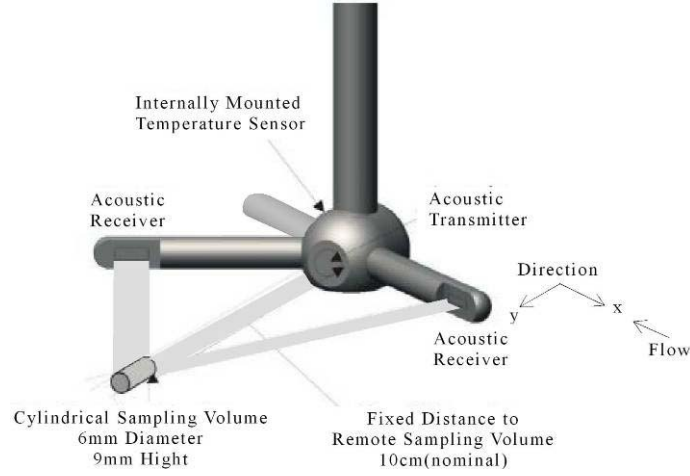
Figure 3.1 Current meters and Handheld ADV Diagram of the FlowTracker probe.

a   b
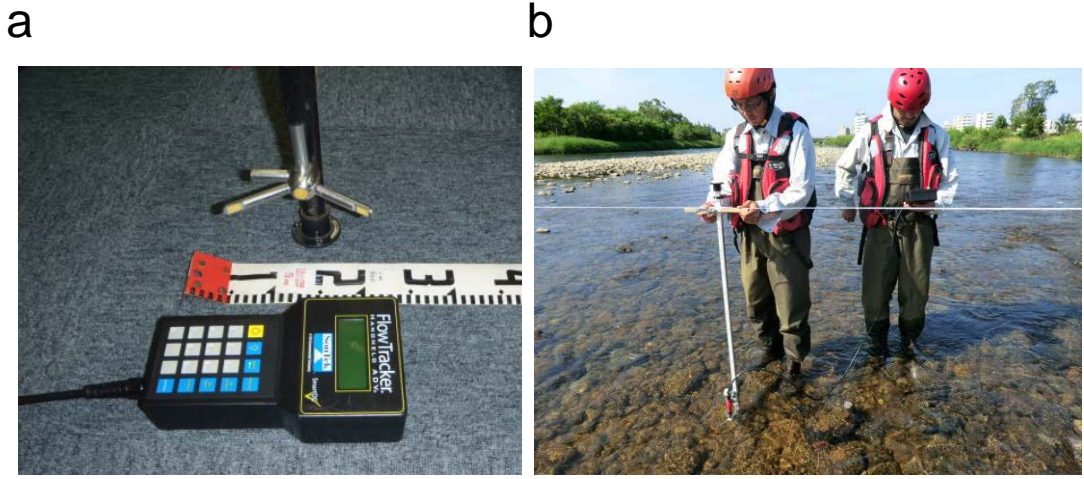
Figure 3.2 Photograph of handheld acoustic Doppler velocimeter "Flow Tracker"

(2) Arrangements of verticals of velocity and water depths

The second term in the right side of Equation (3.5), i.e., u_{m}, depends on number of verticals, m. A relation between the number of vertical and the uncertainty is indicated by ISO (2007). For example, u_{m}, is 4.5 % at $m= 10$, of which value is conventionally applied in Japan. The uncertainty decreases as the number of verticals increases, and converges to 1.0 % when the number of verticals is equal and larger than 35.

The third term, $(\sum_{i=1}^{m}(b_i d_i \bar{v}_i)^2 \Big/ \left(\sum_{i=1}^{m}(b_i d_i \bar{v}_i)\right)^2$, is ideally minimized to $1/m$ if all of the subsectional

discharges, $q_{\mathrm{i}}=b_{\mathrm{i}} d_{\mathrm{i}} v_{\mathrm{i}}$ are equal. This is known as the statement of the Cauchy- Sharwtz inequality. Additionally if m is enough large, the third term is ignored. However, it is impossible to design verticals

to satisfy the ideal statement because detailed discharge distribution in gravel-bed river is never predictable before measurement. This dissertation suggest that verticals of velocity in each transect are arranged as ratio of each subsectional discharge to total discharge, i.e. $b_i d_i \bar{v}_i \Big/ \sum\limits_{i=1}^{m}\left(b_i d_i \bar{v}_i\right)$, are no more than 0.1 (relative percentage: 10%), and number of verticals, m is enough large ($m > 20$). This criterion is expected to reduce as much uncertainty of the third term as possible.

The verticals of water depth measurement are arranged at the same location with those of water velocity (ISO 2007). Another way is that number of verticals for measuring water depth is double that of verticals the number of measurement by adding the verticals of depth at the middle points between the adjacent verticals (Public Works Research Institute 2002). In gravel-bed rivers, adjacent water depths are often variable, and the profiles of water depth have large fluctuations as shown in Figure 3.3. Measuring water depth are more effortless than velocity measurements, so this dissertation conducts 5-point means depth measurements; each subsections are equally divided into five points, next water depths at 5-point are measured in turn, and the averages of five measurements are calculated as a representative water depth in the subsection (Figure 3.3).
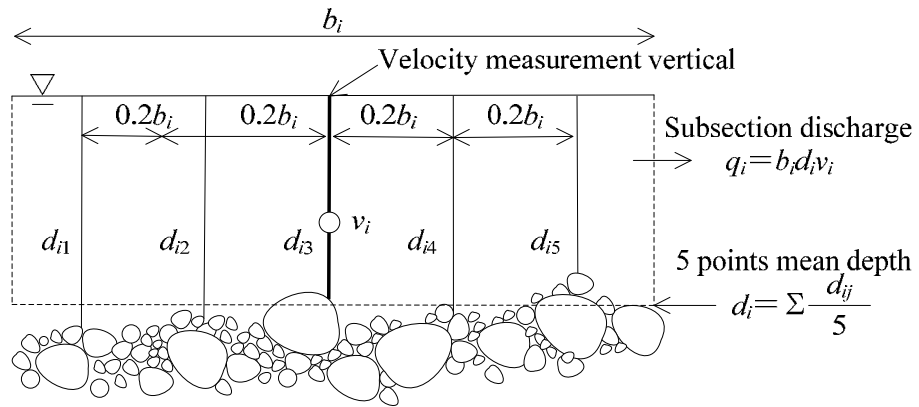

Figure 3.3 Diagram of 5-point mean depth measurements

The number of depths in the i th vertical at which velocity measurements made, n_i, affects on the term in the right side of Equation (3.3), $u^2_{p,i}(\dfrac{1}{n_i})(u^2_{c,i} + u^2_{e,i})$. The uncertainty in the mean velocity at a vertical u_{pi} depends on the number of points velocity in each vertical, and varies ranged

between 0.5 % and 7.5 %. However, velocity measurement is time consuming, and the number of point velocity in each vertical directly increases the total time of synoptic survey. Synoptic survey is needed to perform during a short time (ideally at the same time) as discharges at upstream and downstream points are invariable if no exchange along the reach. By arranging sufficient number of verticals m, the right term including the uncertainty u_{pi} is expected to be neglected. For this reason, in this dissertation, the number of point velocity n_i are determined as the conventional method (Turnipseed and Sauer 2010): $v_i = 0.5v_{0.2} + 0.5v_{0.8}$, if D > 0.45 m (two point method); Vi = $v_{0.6}$, if D <= 0.45m (one point method); Vi = $0.25v_{0.2} + 0.5v_{0.6} + 0.25v_{0.8}$, if the difference between $v_{0.2}$ and $v_{0.8}$ in each vertical exceeds to either half of v_{2i} or that of v_{8i} (three point method), where $v_{0.2}$, $v_{0.6}$, $v_{0.8}$ are the point velocity on each vertical at 0.2, 0.6, 0.8 of the depth below the surface.

3.2.3　Observation transects

The synoptic surveys were conducted during wadeable conditions of the Toyohira River at four events: 1) 14–15 September, 2010; 2) 24–25 September, 2010; 3) 8–9 October, 2010; 4) 2–4 February, 2011.

10 observation transects (St. 1 to 10) were located from the confluence of the Yamahana River to the gaging station, "Kariki" at the distal part. The observation transects are shown in Figure 3.4 . The transect (St. 9) beneath the Azuma Bridge was added in the latter measurements on October and February to identify change from losing to gaining. The transect (St. 6) was shifted 250m upstream (St. 6') to obtain more validity of the measurements on February. The measurements at transects (St. 3 and St. 7) were also performed for quantifying losing rate on 23 December, 2010 and 31 May, 2011. The water intake to the Sousei River is automatically recorded per hour by the Hokkaido Regional Development Bureau, and the averaged value during each period of synoptic survey was used for calculating Equation (3.2). The discharges in the tributary, the Shojin River was no more than 0.1 m^3/s, and the error in relatively small value are negligible. This research measured the tributary discharge by the conventional method using the current profiler meter.
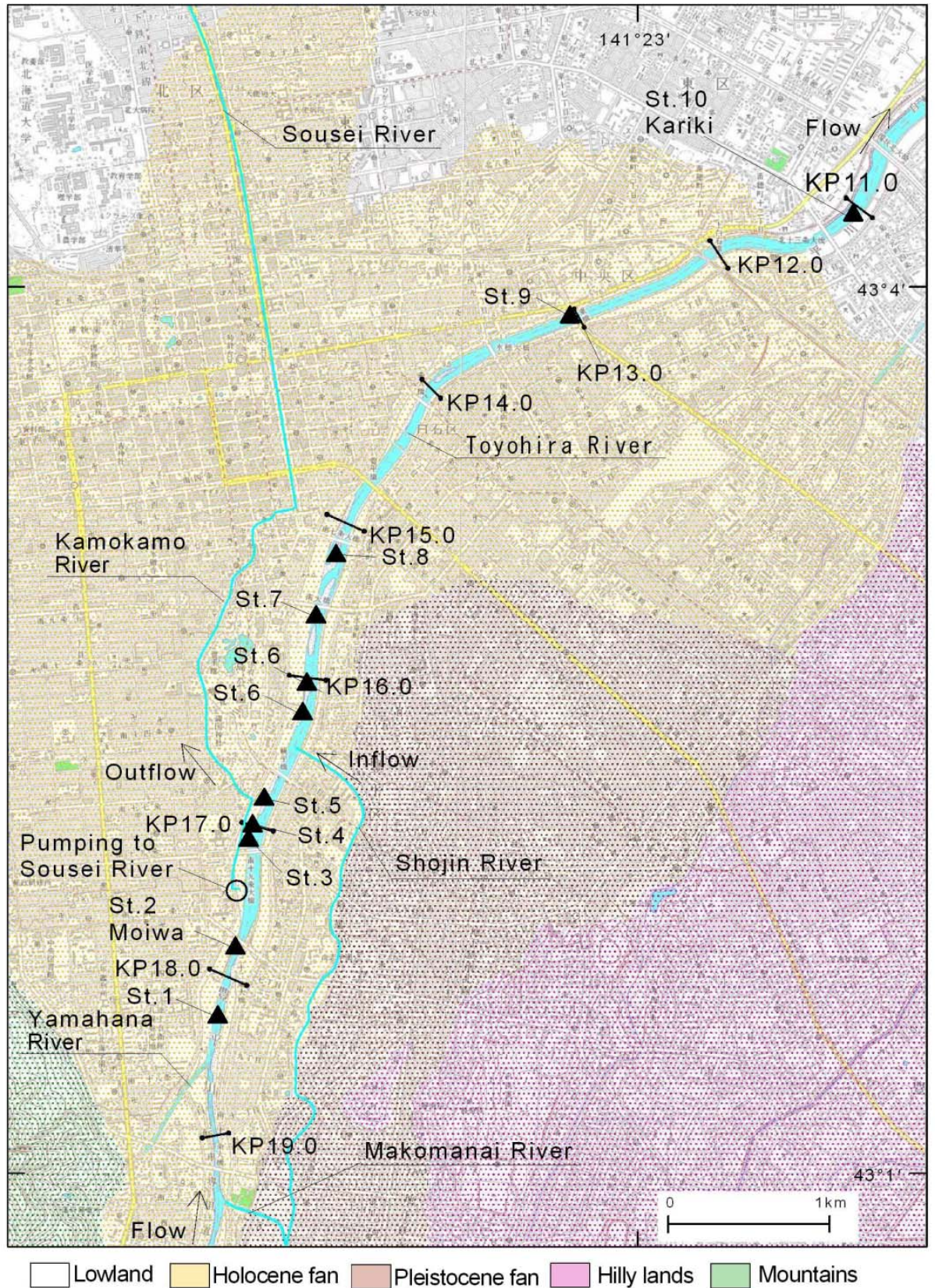
Figure 3.4 Map of Toyohira alluvial fan and gaging stations for synoptic surveys

3.2.4   Comparison with other methods

(1) Conventional method

Hokkaido Regional Development Bureau, the administrator of the Toyohira River, has conducted discharge measurements at the gaging stations, "Kariki" (St.10) and "Moiwa" (St.2), regularly one or more times per month for over half a centrury. The measurements are performed by the conventional method in the Public Works Research Institute, Japan (2002). The velocimeter used is rotating-element mechanical meter, "Sanei Type 1-P," produced by Sanei, co., Ltd., Japan. The height of propeller of the current meter is 90 mm, such that the velocimeter is not often submerged in shallow water depths, which often exhibits in the river during low flow periods. The velocimeter also provides only maximum velocity along the flow path at each point, whether the point velocity is normal to the tag lines or not (Figure 3.5b). In unsteady turbulent flows, therefore, measurement errors are inevitably derived. The number of velocity verticals used is consistently 10 in any flow condition.

This research measured flow discharges at both the stations using the proposed method (ADV measurements) at the same time (24 December, 2010) with the conventional measurements for comparison.

a   b
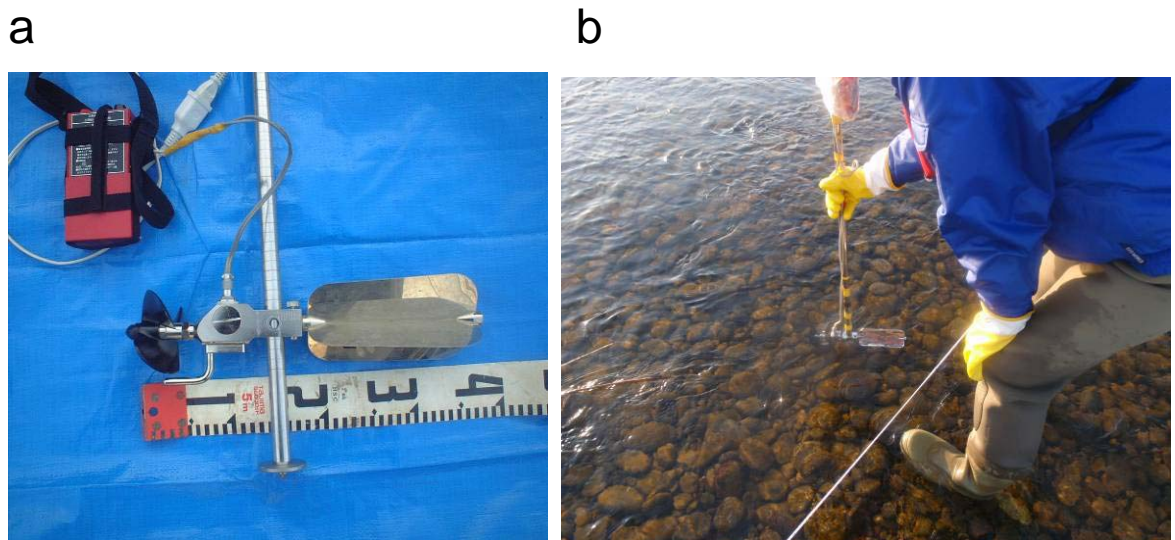
Figure 3.5 Photos of current propeller "Sanei Type 1-P"

(2) Acoustic Doppler current profiler

Acoustic Doppler Current Profiler (ADCP) provides high resolution profile of both velocity magnitudes and directions using the Doppler shift with short time. The feature of ADCP has greater advantage for synoptic survey than any other equipment (e.g., Tebakari 2010). In this dissertation, ADCP measurements were also conducted at 7 stations (St.2, 3, 5, 6, 7, 9, 10) on 3 February 2011, and the results were compared with the ADV measurements during 2–4 February 2011. Especially at the "Kariki (St.10)" gaging station, ADV and ADCP measurements were performed at the same time for more accurate comparison. The ADCP used in this research was "StreamPro®" (Teledyne RD InStruments, Inc). The ADCP was developed specifically for the shallow depth condition (<= 2m). The transducer assembly consisted of three transducers that operate at a fixed, ultrasonic frequency of 2MHz. Such high frequency resulted in more accurate profile of velocity and water depths, and the extrapolated top and bottom subsections were smaller than the other ADCP. Previous study succeeded to obtain accurate velocity profiles and discharges using the ADCP (Toyoda et al. 2010). The ADCP measurements were performed twice at each transect, i.e. from the left-side to the right-side, and from the right-side to the left-side.

a

b

Figure 3.6 Photos of acoustic Doppler current profiler, "Stream Pro"

3.3 Results and discussion

3.3.1 Discharge and uncertainty

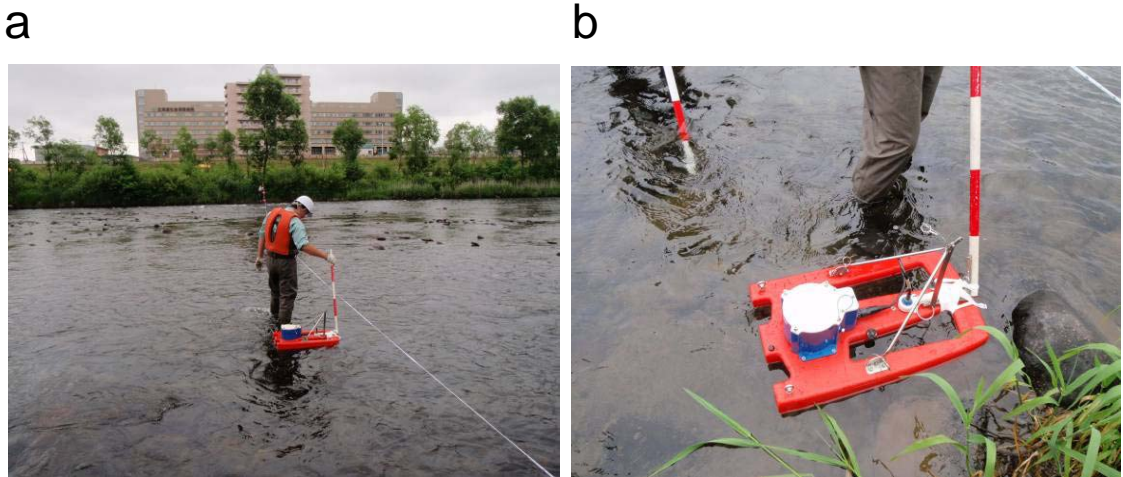The measurement results (date, number of verticals, total width, total area, mean depth, velocity (mean and maximum) total discharge ISO uncertainty (relative percentage and discharge)) are summarized in Table 3.1. The variations of river stages at the "Kariki" and "Moiwa" gaging stations at any surveys were within 0.01 m, and the variations of groundwater level at the observation wells, BW3 and BW5, were also within 0.01–0.03 m. The small fluctuation of river stage and groundwater level indicated the validation of quasi-steady condition ($\Delta S^{sw} \approx 0$). The number of verticals m in each transects were 22–40, which were double to four times than that in the conventional method (m= 10). As a result, ISO uncertainty values obtained were only 2–3 %. The accuracy was obtained owing to incorporation of the handheld-ADV (u_s= 1 %) and the detailed arrangement of verticals (u_m=1–2.5 %).

One example at the "Kariki" gaging station (St.10) at 3 February, 2011 is shown in Figure 3.7. The profile of water depths indicated that the water depths were highly variable between 0 and 0.83 m, and that the differences of water depth are often over 0.1 m even in the pairs of adjacent points. Figure 3.7 shows that the profile of averaged water depths (open triangles) almost corresponds to the profile of moving average of 0.1m interval measurements (red line). The agreement indicates that the 5-point mean depth measurement method is sufficiently applicable for measuring water depths in the gravel-bed river. The verticals of velocity measurements were located with the interval of 1 m in the left-side (distance of 23–36 m), of 4 m in the middle (distance 36–50 m), and of 0.5m in the right-side (distance of 50–61 m). The total number of verticals m of 40 was given. The measured point velocities largely varied in the range from 0.18 m/s (minimum) in the middle of the channel to maximum 1.05 m/s (maximum) in the right side. The contour map of velocity is seen as continuous and smooth, indicating the velocity distribution was well obtained. The slight disturbance in 0.8 depth velocities was recognized only in the right-side. The ratios of sub-sectional discharge q_i to the total discharge ranged between 0.4 and 5.3 %; mostly less than the target value (5%). Consequently, the total discharge was 8.49 m^3/s, and the uncertainty was only 1.9 %, which corresponded only to 0.16 m^3/s.

Table 3.1 Measurement results by synoptic surveys using ADV in the Toyohira River

| St.	Date	Number of Verticals	Total Width(m)	Total Area(m^2)	Mean Depth (m)	Velocity (m/s) Mean	Velocity (m/s) Max.	Discharge (m^3/s)	ISO Uncertainty (%)	ISO Uncertainty (m^3/s)
1	15-Sep-10	31	47	8.67	0.18	0.43	1.16	3.71	2.7	0.10
2	15-Sep-10	35	56	12.01	0.21	0.28	0.77	3.36	2.2	0.07
3	14-Sep-10	33	31	7.19	0.23	0.46	0.70	3.32	2.8	0.09
4	15-Sep-10	27	17.8	4.56	0.26	0.66	1.10	2.99	2.9	0.09
5	14-Sep-10	24	22.3	6.55	0.29	0.41	0.74	2.67	3.1	0.08
6	14-Sep-10	28	26	8.98	0.35	0.31	0.52	2.81	2.5	0.07
7	14-Sep-10	25	34.4	23.45	0.68	0.12	0.17	2.78	2.4	0.07
8	14-Sep-10	25	21.9	11.14	0.51	0.26	0.41	2.85	2.6	0.07
10	15-Sep-10	33	38.2	9.89	0.26	0.29	0.59	2.87	2.7	0.08
1	24-Sep-10	37	47	8.80	0.19	0.34	1.08	3.03	2.5	0.08
2	24-Sep-10	37	56.2	10.92	0.19	0.28	0.72	3.08	2.5	0.08
3	25-Sep-10	34	32.3	7.91	0.25	0.39	0.66	3.10	2.5	0.08
4	25-Sep-10	27	18.2	4.11	0.23	0.71	1.11	2.92	2.9	0.08
5	25-Sep-10	23	22.2	6.47	0.29	0.43	0.73	2.79	3.1	0.09
6	25-Sep-10	27	25.3	9.20	0.36	0.30	0.50	2.80	2.6	0.07
7	24-Sep-10	26	34.4	23.14	0.67	0.11	0.17	2.62	2.4	0.06
8	24-Sep-10	25	22	11.02	0.50	0.23	0.37	2.51	2.6	0.07
10	24-Sep-10	33	38.1	9.76	0.26	0.27	0.55	2.66	2.7	0.07
1	8-Oct-10	38	47.4	11.43	0.24	0.46	1.16	5.29	2.3	0.12
2	9-Oct-10	40	56.2	13.61	0.24	0.35	0.82	4.75	2.0	0.09
3	9-Oct-10	32	32.8	10.34	0.32	0.48	0.78	4.99	2.5	0.12
4	9-Oct-10	26	18.7	5.82	0.31	0.76	1.35	4.44	2.6	0.12
5	9-Oct-10	31	24.5	8.23	0.34	0.49	0.76	4.06	2.6	0.11
6	9-Oct-10	30	26.6	10.85	0.41	0.39	0.67	4.22	2.3	0.10
7	8-Oct-10	25	34.5	25.38	0.74	0.16	0.24	4.08	2.4	0.10
8	8-Oct-10	25	22.5	12.96	0.58	0.31	0.54	3.99	2.5	0.10
9	9-Oct-10	22	34.6	21.91	0.63	0.18	0.26	4.04	2.7	0.11
10	8-Oct-10	34	38.3	11.65	0.30	0.39	0.66	4.49	2.4	0.11
2	24-Dec-10	33	56.80	23.60	0.42	0.61	1.18	14.38	2.2	0.32
3	23-Dec-10	36	34.30	17.33	0.51	0.79	1.26	13.61	1.9	0.26
7	23-Dec-10	27	52.10	30.86	0.59	0.42	0.65	12.90	2.3	0.30
10	24-Dec-10	32	43.70	19.11	0.44	0.74	1.35	14.07	2.1	0.30
1	4-Feb-11	30	36.9	15.52	0.42	0.57	1.12	8.91	2.4	0.21
2	4-Feb-11	35	57.1	18.83	0.33	0.47	1.07	8.80	2.1	0.18
3	2-Feb-11	38	33.3	13.91	0.42	0.65	1.09	9.10	2.0	0.18
5	2-Feb-11	30	34.6	13.88	0.40	0.63	1.02	8.70	2.3	0.20
6'	4-Feb-11	33	49.2	21.56	0.44	0.40	0.65	8.52	2.1	0.18
7	2-Feb-11	22	35.3	32.29	0.92	0.25	0.36	7.94	2.7	0.21
8	4-Feb-11	26	23.3	14.96	0.64	0.54	0.78	8.08	2.4	0.19
9	4-Feb-11	30	44.7	35.39	0.79	0.22	0.33	7.84	2.1	0.16
10	3-Feb-11	39	43.8	15.37	0.35	0.55	1.05	8.49	1.9	0.16
3	31-Mar-11	36	33.7	14.66	0.44	0.67	1.18	9.82	2.0	0.20
7	31-Mar-11	28	34.5	31.34	0.91	0.28	0.40	8.88	2.2	0.20
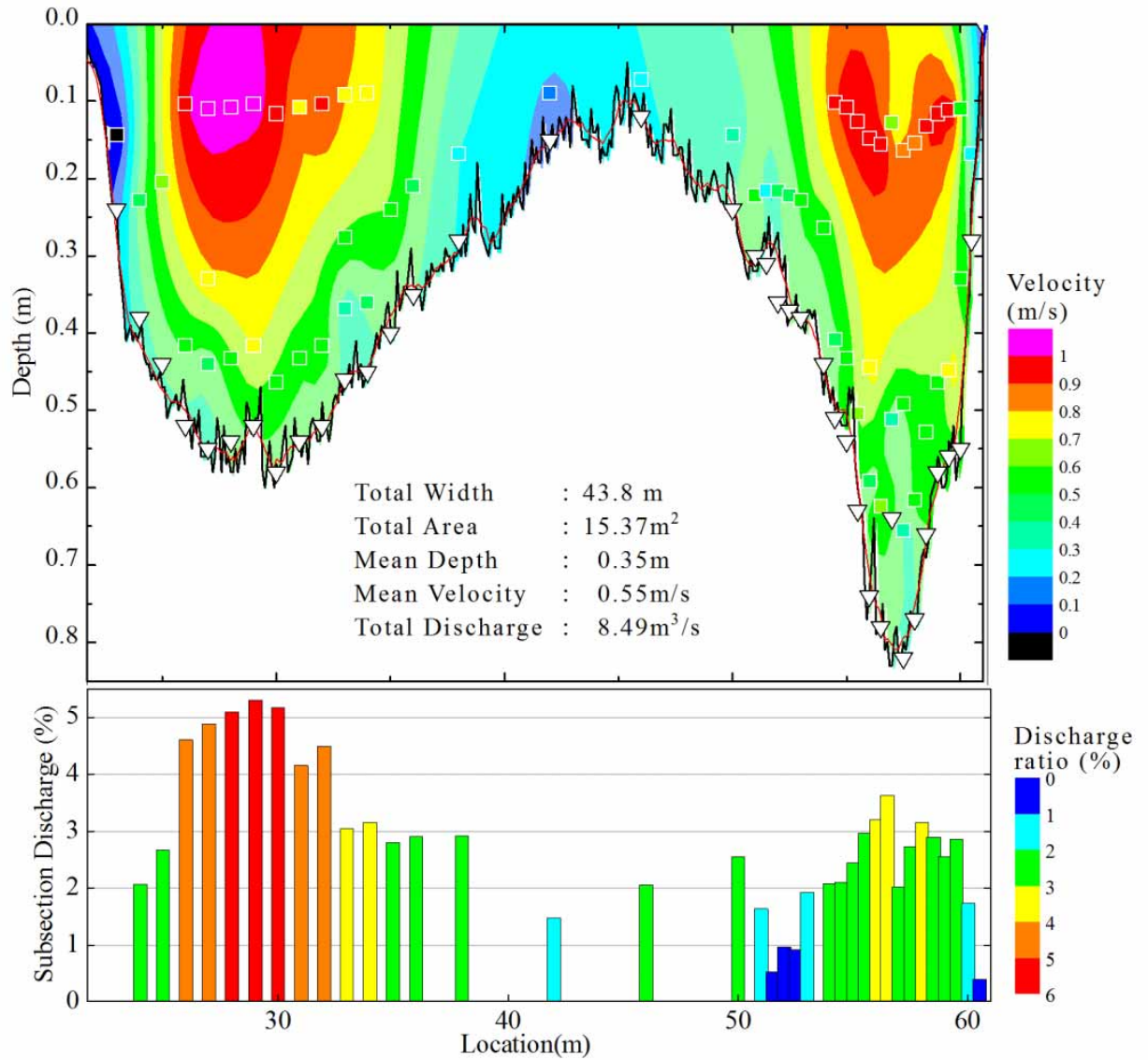
Figure 3.7 Example of measurement results of the Kariki Station (St.10) for 3 February 2011. Upper shows water depths; black line is 0.1 m interval: red line is 1 m moving average: inverse open triangles are 5-point mean, and velocity contours with squares obtained by ADV. Lower shows each subsection discharge ratio to the total discharge (8.49 m^3/s) at each vertical

3.3.2 Longitudinal discharge variation

The longitudinal discharge distributions from St. 1 to St. 10 are shown in Figure 3.8. All of the profiles indicated the same trends although the magnitudes of discharges were different among the surveys: 1) In the upper reach, the discharges slightly varied between St. 1 and St. 3, and the water intake (0.3–0.4 m^3/s) to the Sousei River are relatively negligible; 2) In the middle reach, the discharge currently decreased from St. 3 to St. 7. The inflow of the Shoujin River (KP16.5　about 0.1 m^3/s) was

also ignored. The discharges between St. 7 and St. 8 were almost constant, and so the distinct losing section of the River is determined as the reach from St. 3 to St. 7 (i.e. total length of about 1.5 km). The distinct losing section was relatively short as compared with the total length of the river through the fan (about 10 km). The river leakage occurred in the typical conditions to balance hydraulic gradient and hydraulic conductivity in the riverbed.

; 3) In the lower reach, the discharges are nearly constant between St.7 to St. 9, indicating less interaction between surface/groundwater. However, the discharges slightly increased between St. 9 to St. 10, and the lowermost reach was identified as the gaining section, although this increase was observed only twice.
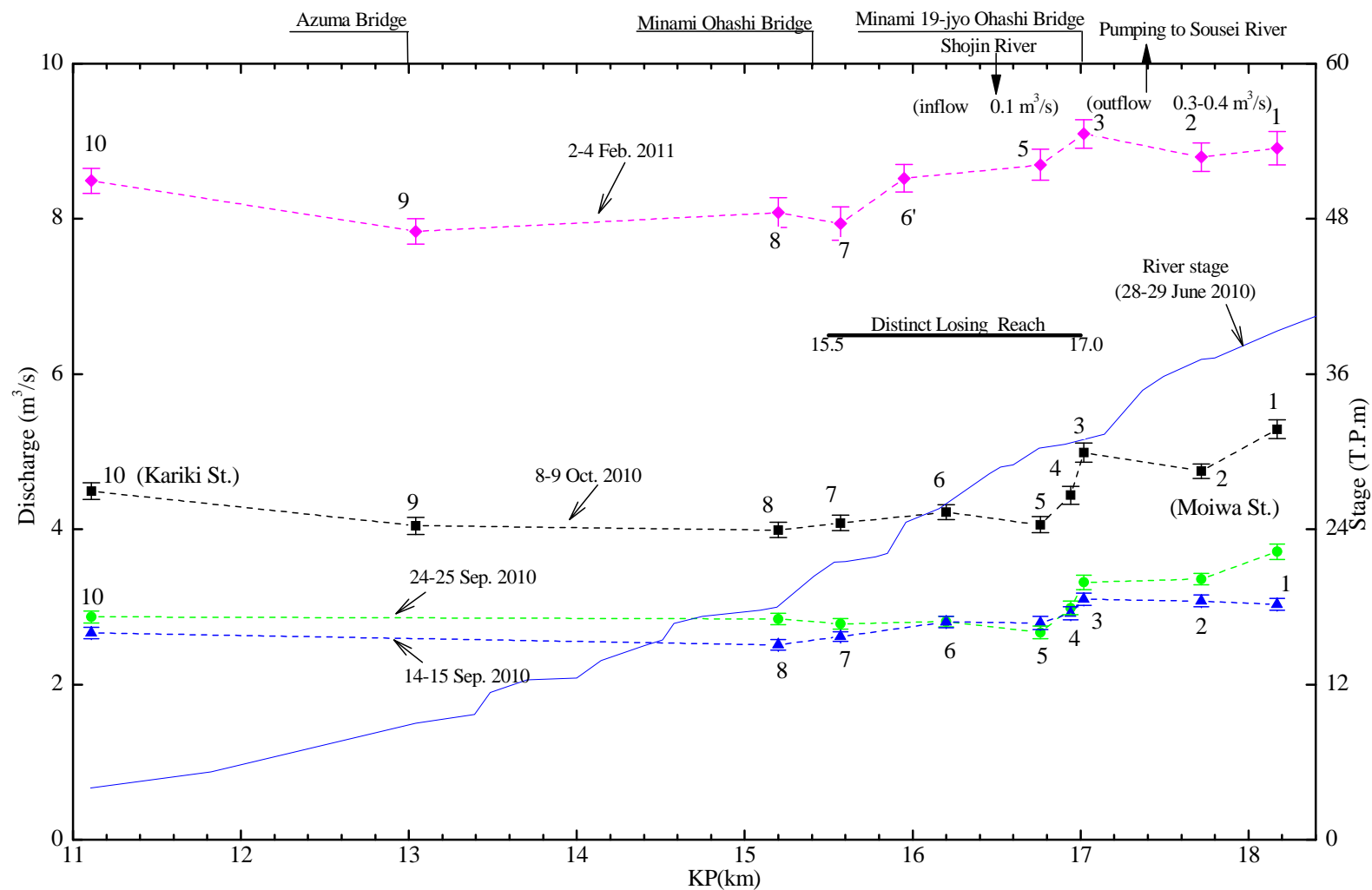
Figure 3.8 Synoptic survey results; longitudinal discharge distributions of the Toyohira River. KP is the distance from the confluence of the Toyohira and the Ishikari Rivers. Error bar represents the discharge uncertainty calculated using the ISO method. Solid blue line is the river stages in 28–29 June 2010.

3.3.3 Exchange between Surface/Groundwater

Exchange of water between the river and the subsurface was determined by Equation (3.2). In this case, two tributaries, the Sousei River and the Shojin River, were considered for calculation as:

$$dQ_{i \text{ to } j} = Q_i - Q_j - Q_{\text{Sousei}} + Q_{\text{Shojin}} \qquad (3.6)$$

where $dQ_{i \text{ to } j}$ is the exchange of water between the upper and the lower transects. Positive values indicated losing, and negative values indicated gaining. Q_i and Q_j were the discharges at the upper and the lower transect, respectively. Index i and j corresponded to the station numbers as shown in Table 3.1. Q_{Sousei} was the water intake into the Sousei River, and the term is ignored if $i >= 3$ or $j <= 2$. Q_{Shojin} was the inflow discharge from the Shojin River, and the term was ignored if $i >= 6$ or $j <= 5$. The uncertainty of $dQ_{i \text{ to } j}$ was also calculated by using the upper and the lower discharges and their uncertainty, as shown in Equation (3.3):

$$U_{i \text{ to } j} = \frac{\sqrt{(U_i \cdot Q_i)^2 + (U_j \cdot Q_j)^2}}{dQ_{itoj}} \times 100 \qquad (3.7)$$

The calculation of exchange were performed between the three sections: the overall section between the Moiwa (St. 2) and the Kariki (St. 10) gaging stations; the distinct losing section between the Minami- 19 jyo Ohashi Bridge (St. 3) and the Minami- Ohashi Bridge (St. 7); the gaining section between Azuma Bridge (St. 9) and the Kariki station (St. 10).

The estimated values and uncertainty are summarized in Table 3.2. Total exchanges through the fan, dQ_{2to10}, were commonly less than 0.15 m^3/s, because that there are different reaches through the overall section; losing section in the upper reach and gaining section in the lower reach. In such case that exchanges of losing and gaining are close to each other, total exchange has difficulty to estimate by using even this improved survey, and detailed measurements are needed by separating the long reach into several sub-sections.

The exchange values of the distinct losing section, dQ_{3to7} were constantly positive, indicating the losing. The scattered plots of the exchange values are shown in Figure 3.9. The leakage varied ranged between 0.53 and 1.27 m^3/s, and the variation was primarily attributable to the relative uncertainty. Note that the two exchange values in the low flow conditions (<5 m^3/s) were obviously smaller than the other values during the relatively large flow conditions. This probably indicated the decrease in permeability of the riverbed materials during the low flow conditions, and several factors were

considered in the literature, for example clogging on the riverbed (Katakai et al. 2006; Goldschneider et al. 2007) and unsaturated zone between the surface water and the groundwater table (Woessner 2000). However, the assumption was not valid only in the results, because the small values become close to the other values if the relative uncertainty expands, for example, the confidence interval changes from 68% interval to 95% interval. In the large discharge condition (>5 m^3/s), a typical relation between the leakage and the discharge was not found in Figure 3.9. The average values of dQ_{3to7} are 0.88 m^3/s from the all values, and 1.04 m^3/s from those except for the two small values, respectively. The two average values are not significantly different, and it is valid that the representative value of exchange in the distinct losing section, dQ_{3to7}, was about 1m^3/s, as well as the previous surveys between the 1960' and the 1990'. The similarity with the previous surveys indicates that the river leakage might be almost invariable for over half a century. In addition, the amount corresponds to about 80% of the total pumping rate (about 100,000m^3/s) of groundwater throughout Sapporo City. This means that the focused recharge plays an important role in maintaining the groundwater reservoir, although the distinct losing section is only about one tenth of the total reach through the fan.

The exchange of the third section, dQ_{9to10}, obtained was only two values, but these values were commonly estimated at about −0.5 m^3/s. This means that the surface water was gaining between the Azuma Bridge and the Kariki gaging station. The gaining forms springs in the riverbed, and the springs are valuable for contributing to the spawning of salmon (Okamoto 2000).
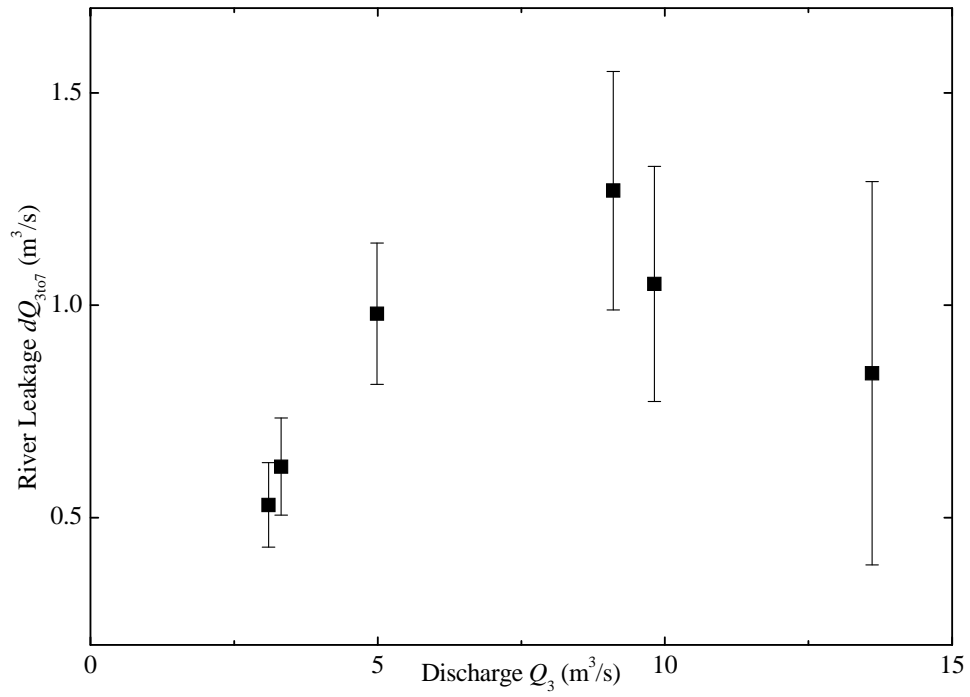
Figure 3.9 Relation between river discharge and leakage. Q_3 and dQ_{3to7} are discharge at St.3 and leakage between St.3 and St.7. Error bars are the estimated standard deviation of leakage.

Table 3.2 River leakage calculated using the stream water budget method with measurement results of the synoptic survey, positive value at water losing and negative value at gaining. Q, U, dQ, and $dQ \cdot U$ respectively denote discharge, ISO uncertainty, rate of leakage, and uncertainty of leakage

date	Measurement Results										Tributary Discharge		River Leakage					
	St.2 Moiwa		St.3 Minami 19-jyo Ohashi		St.7 Minami Ohashi		St.9 Azuma		St.10 Kariki		Pumping to Sousei River (outflow)	Shojin River (inflow)	St.2 to St.10 (losing)		St.3 to St.7 (distinct losing)		St.9 to St.10 (gaining)	
	Q_2	U_2	Q_3	U_3	Q_7	U_7	Q_9	U_9	Q_{10}	U_{10}	Q_{Sousei}	Q_{shoujin}	$dQ_{\text{2to10}} dQ$	U	$dQ_{\text{3to7}} dQ$	U	$dQ_{\text{9to10}} dQ$	U
14-15 Sep. 2010	3.36	0.07	3.32	0.09	2.78	0.07			2.87	0.08	0.42	0.08	0.15	0.11	0.62	0.11		
24-25 Sep. 2010	3.08	0.08	3.10	0.08	2.62	0.06			2.66	0.07	0.38	0.05	0.09	0.11	0.53	0.10		
8 - 9 Oct. 2010	4.75	0.10	4.99	0.12	4.08	0.11	4.04	0.11	4.49	0.11	0.33	0.07	0.00	0.14	0.98	0.17	-0.45	0.15
23 Dec. 2010			13.61	0.34	12.90	0.30					0.29	0.13			0.84	0.45		
24 Dec. 2010	14.38	0.32							14.07	0.30	0.29	0.13	0.15	0.43				
2 - 4 Feb. 2011	8.80	0.18	9.10	0.18	7.94	0.21	7.84	0.16	8.49	0.16	0.28	0.11	0.14	0.25	1.27	0.28	-0.65	0.23
31 May. 2011			9.82	0.20	8.88	0.20					0.37	0.11			1.05	0.28		

unit m^3/s

3.3.4 Comparison with other methods

(1) Conventional method

The conventional method (Public Works Research Institute 2002) has been used for the regular measurements by the Hokkaido Regional Development Bureau (HRDB) at the "Moiwa (St. 2)" and "Kariki (St. 10)" gaging stations. The measurements were compared with the synoptic survey results which were performed at the same time. Table 3.3 shows a comparison of the measurements with their uncertainty between the synoptic survey and the conventional method. The uncertainty in the measurements obtained by conventional method was similarly calculated according to Equation (3.2) with the assumption that the uncertainty of the propeller-type current meter u_s was constant at 5 %. Table 3.3 shows that the discharge values by the synoptic survey were consistently larger than those by the conventional method at both stations, because both water depth and velocity obtained by the conventional method were commonly larger than those by the synoptic survey. The relative discrepancy corresponded nearly to 10–20 %, probably due to measurement error in the conventional measurements. If the water depth at the vertical of velocity was shallower than the propeller-type current meter was workable, the conventional method often removed the vertical to the adjacent location that had sufficiently deep water depth for the current meter, such that both the velocity and the water depth were excessively measured at the arbitrary verticals. In addition, the conventional current meter provided the maximum velocity along the flow paths, not the values normal to the tag lines. The measurement error in velocity increased with the flow discharge. The conventional method had another inferiority in the number of vertical in each transect. The number in the conventional method were 7 to 10, that were about half to one-third to that in the synoptic survey. As a result, the uncertainty of the conventional method reached no less than 7–9 %, that was about twice or three times in the synoptic survey.

The previous synoptic surveys (e.g., Ozaki et al. 1965; Tanaka et al. 2010) commonly suggested the positive relations between the leakage and the discharge, but the relation was not found in this research in the previous chapter. At this time, it is probable that there is little relation between the leakage and the discharge at least during the wadeble flow condition, because of the large uncertainty in the conventional method. The quantitative discussion about the relation is needed through further survey employing this proposed method.

Table 3.3 Comparison between results of synoptic surveys by ADV and conventional measurements by propeller at the Moiwa (St.2) and Kariki (St.10) stations

St.	Date	Synoptic Surveys by ADV					Conventional Measurements by Propeller					Discharge Ratio Q_{Pro}/Q_{ADV}
		Number of Verticals	Total Area(m^2)	Mean Velocity(m/s)	Discharge $Q_{ADV}(m^3/s)$	Uncertainty U_{ADV}(%)	Number of Verticals	Total Area(m^2)	Mean Velocity(m/s)	Discharge $Q_{Pro}(m^3/s)$	Uncertainty U_{Pro}(%)	
Moiwa	15-Sep-10	35	12.01	0.280	3.36	2.2	12	12.03	0.33	4.02	8.1	1.20
(St.2)	24-Sep-10	37	10.92	0.282	3.08	2.5	12	11.30	0.33	3.71	8.1	1.21
	24-Dec-10	33	23.60	0.610	14.38	2.2	12	24.63	0.61	15.05	7.2	1.05
Kariki	15-Sep-10	33	9.89	0.290	2.87	2.7	9	12.52	0.25	3.16	8.9	1.10
(St.10)	24-Sep-10	33	9.76	0.273	2.66	2.7	9	12.69	0.35	3.30	8.8	1.24
	8-Oct-10	34	11.65	0.386	4.49	2.3	9	11.29	0.44	4.95	8.9	1.10
	24-Dec-10	32	19.11	0.736	14.07	2.1	11	20.06	0.62	15.25	7.4	1.08
	3-Feb-11	39	15.37	0.553	8.49	1.9	9	16.12	0.64	9.48	8.5	1.12

(2) Acoustic Doppler current profiler

Figure 3.10 showed the ADCP measurement results, showing the profiles of both water depth and velocity at the "Kariki" gaging station. The ADCP in this dissertation had limitation in extremely shallow depths less than 0.3m, and the measurement results were lacked around the middle (distance of 40.5–47.5m of the transect. The velocity contour obtained by the ADCP has much higher resolution and disturbance than that by the synoptic survey (Figure 3.7). The disturbances were reflected from the turbulent and unsteady flows, but the fluctuation might increase the uncertainty (Turnipseed and Sauer 2010). Another reason for the disturbances was the relative largeness of the ADCP on the shallow water depths. These noises in the gravel-bed rivers might reduce the effectiveness of ADCP (Stone and Hotchkiss 2007).

Figure 3.10 indicates the total discharge at the first turn, 7.78 m^3/s, that was a sum of the left-side (4.31 m^3/s) and the right-side discharges (3.47 m^3/s). The total discharge at the second turn, 7.77 m^3/s, was in agreement with the first value, indicating good repeatability of the ADCP measurements. However, the values were lower than that by the ADV, 8.49 m^3/s (Figure 3.7). The lack of discharge, 0.72 m^3/s, was that around the middle section, where the equipment was less appropriable due to the shallow water depth. On the other hand, the agreement of discharge except the middle section proved the superiority of the ADV measurement in this flow condition.

Figure 3.11 shows the longitudinal discharge variations by the ADV and the ADCP at the same period. The ADCP performed the measurements twice at each station, and the measurements were almost equal; the discrepancy was only 2-4% of each measurement. The longitudinal discharge variation by the ADCP indicated the similar trend with that by the ADV; the river discharges decreased between the "Moiwa" (St.2) gaging station and the Azuma Bridge (St.9), and increased between the Azuma Bridge (St. 9) and the "Kariki" (St.10) gaging station. The variation by the ADCP, however, was plotted below the variation by the ADV in whole. This was because the lack of the discharge by the ADCP were inevitable in the sections of water depth shallower than the ADCP's specification.
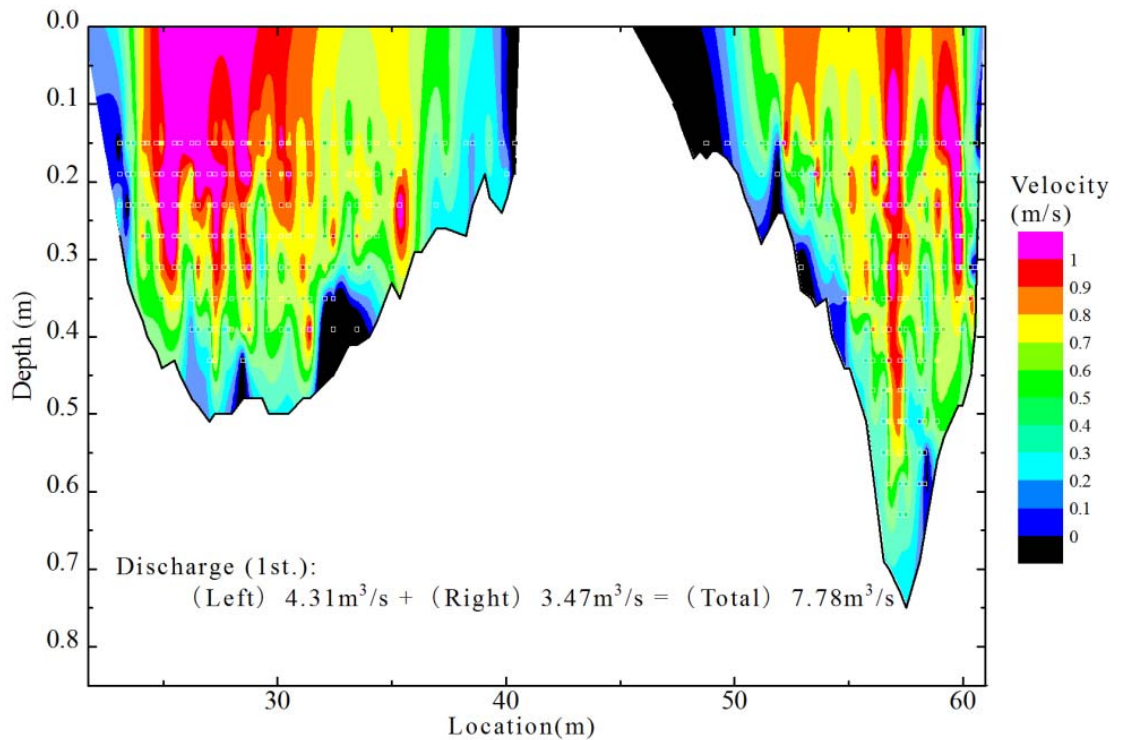
Figure 3.10 Example of measurement results obtained using ADCP, at the "Kariki" gaging station (St. 10) on 3 February, 2011. The result is the first among the twice measurements at the same time of the ADV measurements (Figure 3.10). Open squares are the measurement of velocity normal to the tag line, and the color contour was made by interpolating the point velocities. Lack of contour in the location of 41-50m is due to the shallow water depth for ADCP.
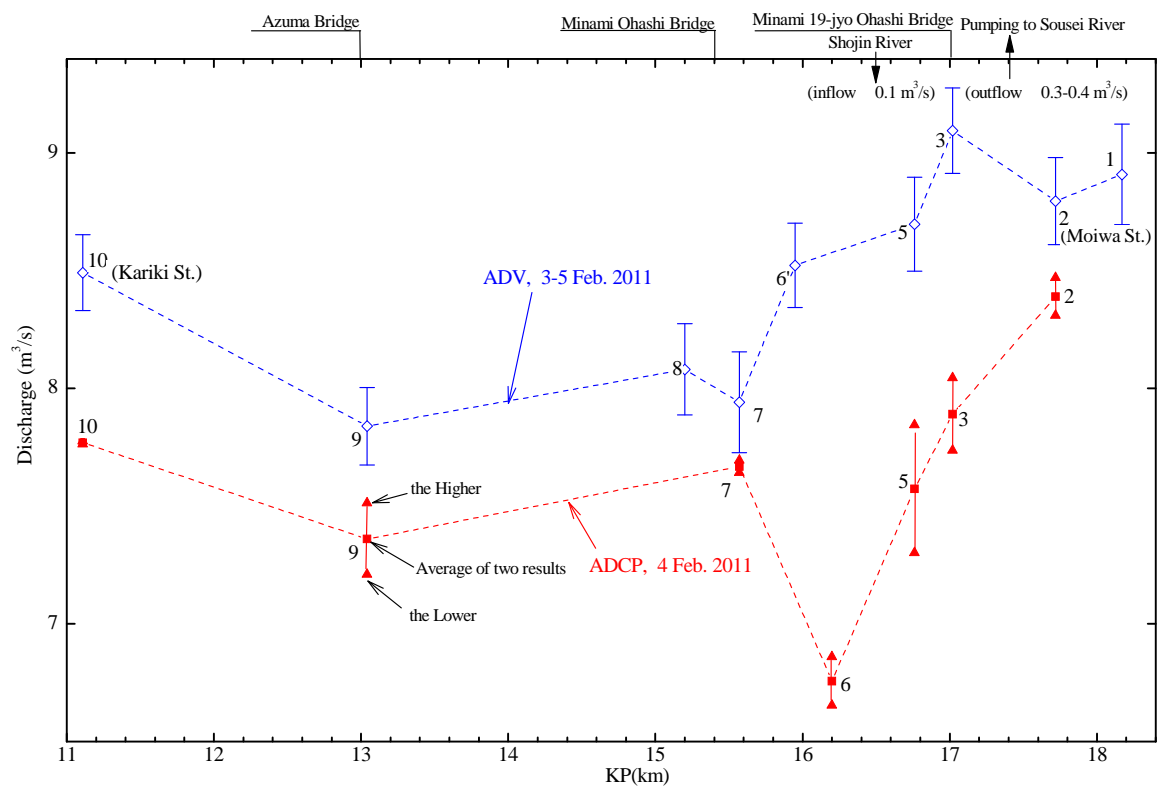
Figure 3.11 Comparison of ADV and ADCP results. Open diamonds are the results by ADV, and the error bar is the estimated standard deviation, open triangles are the twice results by ADCP, and open squares are the averages of the twice measurements.

3.4 Conclusions

A synoptic survey of the river flow was performed to quantify the focused recharge from the Toyohira River. The complexity and variation of water depth and velocity distributions in the gravel-bed river frequently caused unacceptable uncertainty due to the unsteady turbulent flow and rough boundaries. For reducing the uncertainty as much as possible, this dissertation proposed the two following improvements; 1) an application of a handheld acoustic doppler velocimeter (ADV) and 2) detailed arrangements of verticals measurements of flow and depth. Applied to the river, continuous measurements were taken at 4–6 stations each day, yielding ISO uncertainty of discharge of approximately 2–3%, that were reduced as much as possible. The synoptic survey showed its required accuracy and practical availability. It revealed the longitudinal river discharge and leakage of the Toyohira River. The distinct losing reach was only about 1.5 km between the Minami 19-jyo Ohashi Bridge (St. 3) and the Minami Ohashi Bridge (St. 7). The mean leakage was estimated at about 1 m^3/s. The total budget between the upper and lower gaging stations, "Moiwa" and "Kariki," was too little to be observed because of a change in a river-leakage pattern from loss to gain around the Azuma Bridge. Compared with the consistent flow conditions, the measurements using the conventional method with the propeller-type current meter included higher uncertainty of no less than 7–9%. Thus, the conventional method was not appropriate in quantifying the interaction between surface- and groundwater in the river. Measurements obtained using the ADCP showed good agreements with the measurements obtained using ADV in deep water conditions: depth greater than 0.3 m. In the low discharge condition of the Toyohira River, however, the total discharge by the ADCP was lower in each section because of the shallow water limitation of the instrument.

This proposed methodology contributes to yield more reliable estimates of exchange of water in gravel-bed rivers than the conventional method. However, the accuracy is not enough, and the exchange is even susceptible to the uncertainty. There are several points for addressing the uncertainty; a repeat of flow measurements at the same flow conditions, statistical analysis, subdivision of a long reach that is unknown whether gaining or losing. This method is applied only in the low-flow and wadeable condition, but flood events are also of importance as a result of bank storage and additional infiltration areas (Engeler 2011). The measurements of the exchange in the high-stage, for example early spring with snowmelt, would be performed in a future work.

4 Permeability modeling of packing level in undisturbed gravel core

4.1 Introduction

Hydraulic conductivity (K) is most critical among various hydraulic parameters in groundwater modeling because the parameter straight influences the groundwater flow fluxes according to Darcy's law. Even in a "homogeneous" aquifer, K is several orders of magnitude different among even closely-separated points. The large variability of K in space depends on geologic heterogeneity attributable to grain size, porosity, sorting, packing and so forth. Geologic heterogeneity also has scale-dependence, and K varies on microscale (cores), mezoscale (facies), and macroscale (sequences). Therefore, aquifer characterization in groundwater modeling studies almost coincides with a description of spatial images of K in the analysis domain.

In situ measurements of K are directly obtained by various methods such as multiple pumping tests, slug tests, flow meter tests and permeameter tests (Fetter 2001). However, the number of measurements by in-situ methods was limited because of economical reasons. The measurements are also inevitably affected on various degrees of uncertainty such as measurement error and scale-dependence. Geostatistical approach was powerful to address the scarcity and uncertainty in such regionalized variable (Dagan 1997; Eaton 2006; Lee et al. 2007). The approach assumes that the spatial variability is not purely random, and that there is some kind of correlation in the spatial variability. The approach also requires statistical assumptions, i.e. stationarity and ergodicity. Stationarity indicates that statistical properties such as mean and variance are constant over the space, but the assumption is not apparent in geologic materials at most scales (Anderson 1989).

Trending heterogeneity (Freeze and Cherry 1979) is also typically recognized in alluvial coarse deposits with both enormous aggradation and steep land-slope. A downward decreasing trend of K is widely known as a global trend in most fluvial terrains. Especially in alluvial fans, another humped heterogeneity is generally observed (Cehrs 1979; Neton et al. 1994), where transmissivity reached at highest values in the mid-fan area as a result of sorting trends. There are also coarsening/thickening or fining/thinning sequences, which might indicate the correlation of K profiles (Neton et al. 1994).

The dependence of permeability on depth in consolidated and unconsolidated sediments is mainly due to decreasing porosity because of compaction and other physical or chemical effects. Vertical

permeability variations in each aquifer are key information for quantifying groundwater flow and solute transport. For example, the typical information aids in realizing geological heterogeneity in geostatistical methods, which often require a fundamental assumption of stationarity (de Marsily 1986; Koltermann and Gorelick 1996; Wackernagel 2003). Analytical and numerical solutions indicate the importance of depth-dependent hydraulic conductivity K in groundwater systems of various scales (Saar and Manga 2004; Marion et al. 2008; Jiang et al. 2009; Cardenas and Jiang 2010; Zlotnik et al. 2011). A systematic decreasing trend in either porous media or fractured media is can also be understood by using semi-empirical models based on simplifications and well-established relations among permeability, porosity, fracture aperture, and effective stress (Jiang et al. 2010).

In contrast to many theoretical approaches, semi-empirical approaches rarely give a unique depth dependence of K at a particular site, especially in alluvial shallow aquifers, because geologic heterogeneity prevents detection of a specific trend from a large variability in K. Another reason is a lack of knowledge about the process of porosity structure development under various sedimentary environments. In addition, the numbers of measurements and samples are limited in the majority of practical cases. Vertical sequences in alluvial aquifers generally consist of various facies (e.g., Miall 1992), for which there are a variety of physical and chemical effects on the permeability variations with depth. Characterization has proved especially difficult in a complex alluvial fan system. The stratigraphic sequences exhibit unique sedimentary textures on different scales due to various proportions of fluvial flow, debris/mud flow, sheet flood, and sieve deposition (Einsele 2000). Coarsening- and fining-upward trends are also typically seen in alluvial fans as a result of interactions of progradation, retrogradation, and basin subsidence (Neton 1994). The vertical trend of grain size may positively correlate to the depth dependence of K. However, grain size distributions alone are insufficient for determining the vertical trend because K in the coarse sediment mixtures is a complex function of various geologic factors. An additional problem is uncertainty in grain size analysis using gravel cores of small diameter less than the maximum grain size. Groundwater flow or transport modeling in gravelly aquifers is thus often conducted under the assumption that K is approximately invariant in the vertical direction.

The depth dependence of K in unconsolidated gravel deposits has rarely been discussed because porosity reduction by compaction is of less importance in clean coarse sediments than in fine sediments, and determined relations between porosity and K are seldom adhered to in natural coarse sediments

(Morin 2006; Kresic 2007). Previous studies on the depth dependence of K were performed mainly for consolidated rocks because diagenetic and metamorphic affects occur only at depths on the kilometer scale. The results of those studies were commonly that K exponentially or logarithmically decreased with depth, and that decay exponents varied on the order of 1×10^{-2} to 1×10^{-4} m^{-1} at specific sites (Manning and Ingebritsen 1999; Saar and Manga 2004; Ingebritsen et al. 2006; Jiang et al. 2009; Wang et al. 2009; Luo et al. 2011). K in unconsolidated gravel deposits varies greatly even under a slight change in porosity. The fractional packing model (Koltermann and Gorelick 1995; Kamann et al. 2007), which represents K in sediment mixtures as a function of the porosity and volume fraction of each component, indicates that K ranges over several orders of magnitude by these factors. Major (1997; 2000) performed triaxial compression and permeability tests on various poorly sorted debris flow sediments, and reported that the permeability of debris flow mixtures varies exponentially with porosity, and that changes in porosity of as little as a few percent could cause greater than 10-fold changes in permeability. Matsumoto and Yamaguchi (1991) found that in situ measurements of K in Holocene gravelly deposits decreased by about one order of magnitude for test fills of less than 7 m in height. They also conducted laboratory tests using undisturbed gravelly samples, and proposed that the relations between permeability and effective stress reflected the connectivity and compaction of the open pores. As another example, Chen (2011) investigated channel sediments in the Platte River, USA, and hypothesized that a decreasing trend in vertical K with depth resulted from hyporheic processes that moved fine grained sediments from shallow parts of the channel to deeper parts. All of those studies concluded that K is highly dependent on depth in unconsolidated gravel deposits. However, the trends were usually shown only graphically, and more quantitative characteristics about the trends (e.g., the decay exponents) were not typically determined.

The sedimentary or permeability correlation length in the vertical direction is within only a few meters or even decimeters (Hess et al. 1992; Jussel et al. 1994; Rubin 2003; Falivene et al. 2007); thus, a number of measurements are required to distinguish the vertical trend of geological heterogeneity. As an alternative, indirect methods using empirical equations of grain size, porosity or other factors in samples, give K values that approximately agree with measurements taken at the same depth (e.g., Vukovic and Soro 1992; Cheong et al. 2008; Song et al. 2009; Vienken and Dietrich 2011). Discrepancies in indirect methods are considered to be caused by the simplification of equations to only a few variables (or even a single variable, for example, effective grain size diameter).

Undisturbed core sampling of gravel deposits is applied to investigate properties in the deep zone. Undisturbed sampling of gravel deposits is challenging even today. In situ freezing of samples is commonly employed, but the number of samples is restricted with this method due to its high economic cost. In contrast, several nonfreezing sampling techniques have been developed (e.g., McElwee et al. 1991). Unique to Japan, various tube samplers have been improved for high-quality sampling of gravel deposits. Tanaka et al. (1990) indicated the similarity between measured physical and mechanical properties of gravelly samples obtained by these improved tube samplers and by in situ sample freezing. The diameters of undisturbed samplings are usually less than 1 m, and are not enough to evaluate the true distributions of grain size. ASTM determines that grain size analysis needs the sample of diameter larger than several times of maximum grain size. The gravel core of small diameter is also used to determine sedimentary structures related to hydro-facies in gravel deposits. However, the small undisturbed cores keep how fine sediments are packed between the gravel grains.

This dissertation suggested that when applying an indirect method for unconsolidated gravel deposits, other variables are needed that reflect the packing in openings between the gravel grains. Consequently, an additional "*matrix packing level*" index was proposed using relatively undisturbed gravel cores obtained from the Toyohira River alluvial fan, Sapporo, Japan. A distinct difference is found in the undisturbed cores obtained by the samplers in terms of the packing of fine sediments in pore spaces between gravels. The packing in undisturbed cores is qualitatively categorized into four typical levels, and the length fraction of each packing level was measured. The equivalent horizontal value of K per unit depth was then formulated by using the grain size diameter and length fraction of each packing level. Next, an additional grain size analysis is performed on past core samples, and profiles of the grain size diameter are found for three sampling points, two in the mid-fan and one in the fan-toe. Secondly, the previously determined relation is applied to convert the core property profiles into those of the estimated conductivity. To eliminate errors during this process, the moving averages of log-conductivities are calculated and the decay exponent of K with depth is estimated through a linear regression analysis. Finally, a longitudinal cross section is then generated from the profiles such that the boundaries of the gravelly aquifer structure are determined.

4.2　Material and methods

4.2.1　Sampling and tests

(1)　Undisturbed sampling

An improved double core-tube sampler used was developed and patent by ACE Shisui Co., Ltd., Japan. The sampler was based on standard double core-tube samplers, but was equipped with innovative features to avoid disturbances to the gravel cores. As shown in Figure 4.1, the head of the bit tube was characterized by a circular step below the ports to facilitate water discharge and avoid flush fluids flowing onto the cutting surface. Furthermore, the cutting head was constructed of a special alloy of diamond and tungsten, and required little drilling water to cut relatively hard gravels and cobbles. Various other features such as a core-lifter were also equipped on the sampler.

Undisturbed cores sampling are conducted at seven points near the river throughout the fan, BW1−7 as shown in Figure 4.1.
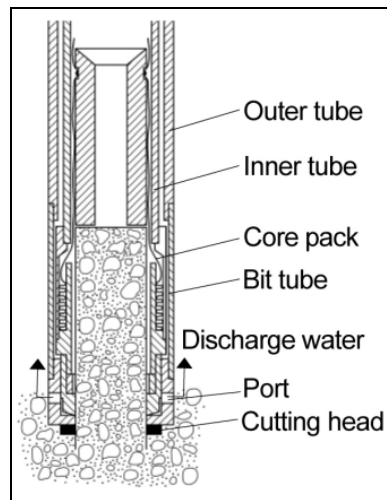
Figure 4.1 Schematic of improved double core-tube sampler used in this study
(ACE Shisui, Co., Ltd., Japan)
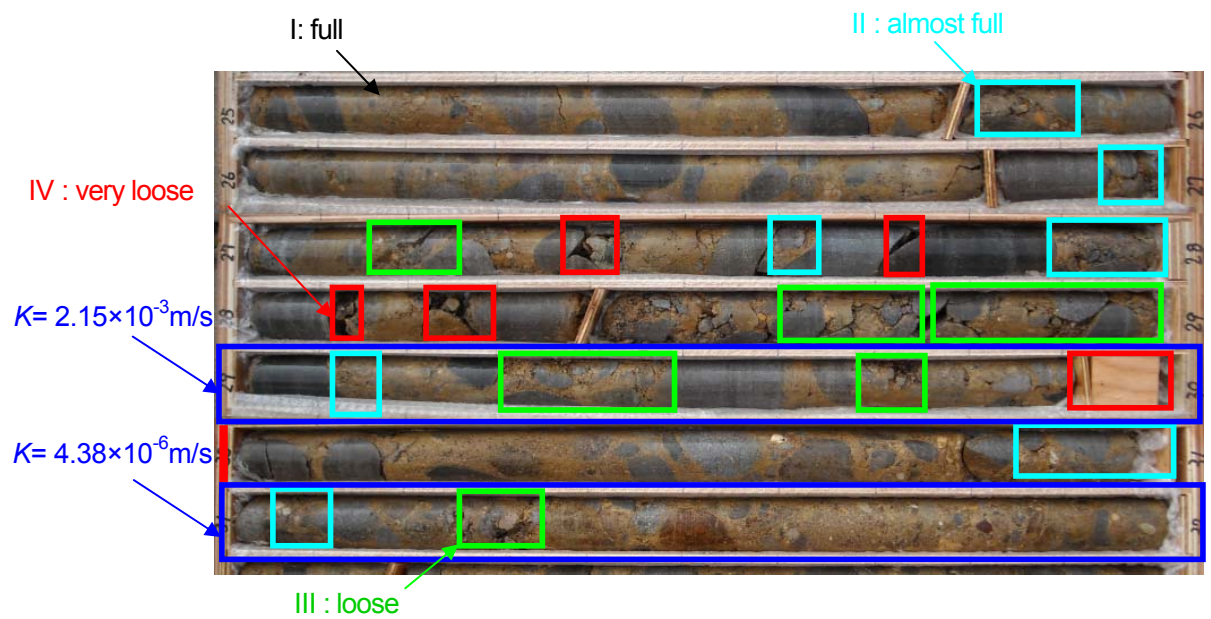
Figure 4.2 Relatively undisturbed cores, obtained at BW03 between 25 and 30 meter in depth, showing examples of matrix packing level and slug test result
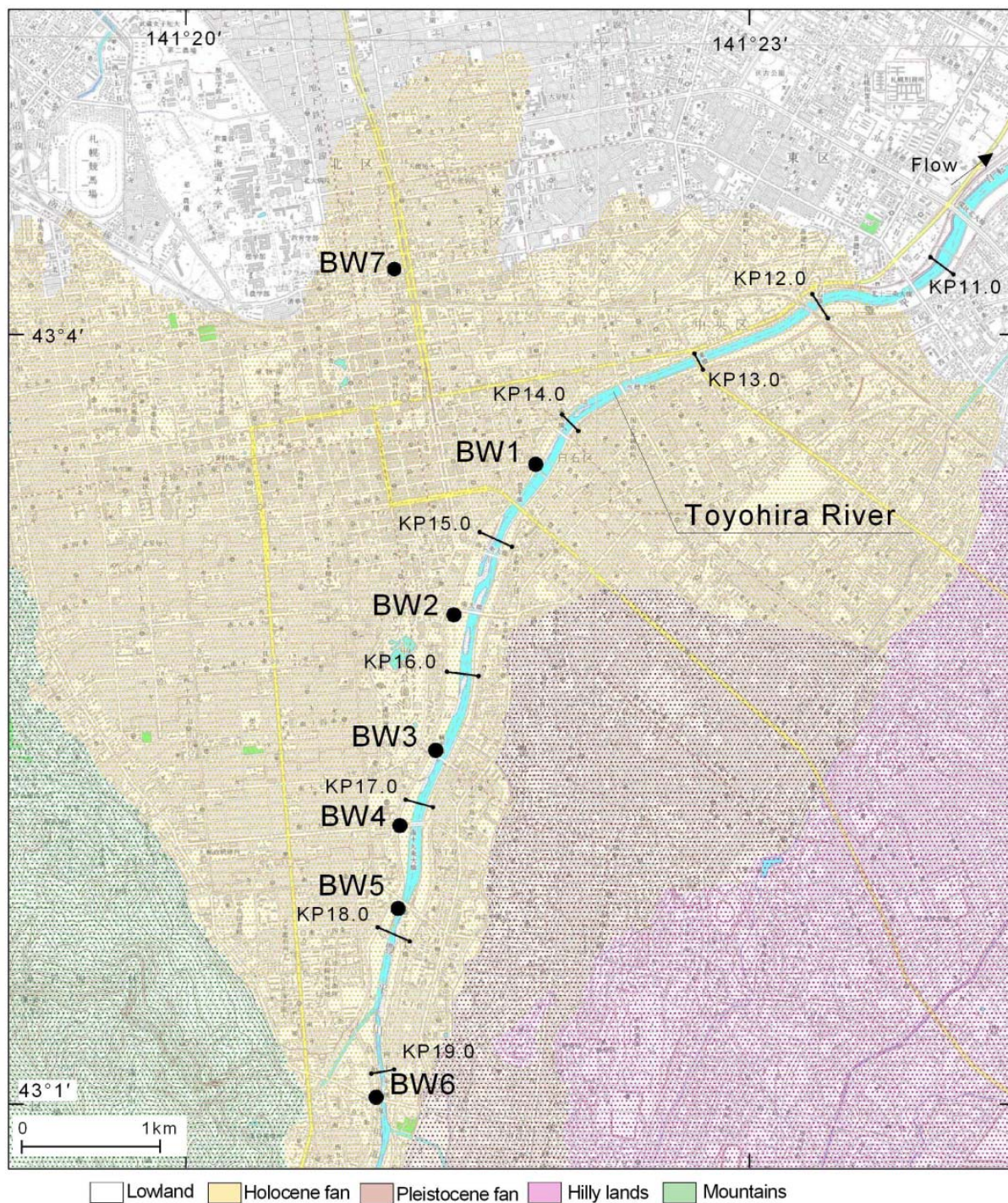
Figure 4.3 Location maps and geologic features of the study area; the Toyohira River alluvial fan. Solid circles represent undisturbed sampling points; BW1–7; dashed lines denote water surface contours with elevation values (in meter above sea level) measured in June 2010; KP values denote the distance (in km) along the river channel upward from the confluence of the Ishikari River

(2) Slug tests

A total of 32 slug tests were performed on the undisturbed samples. The tests were conducted using the Japanese Geotechnical Society (JGS) method (JGS 2004), which originated from the conventional Hvorslev method (Hvorslev 1951). The (JGS) method is divided into an unsteady method and a quasi-steady method according to the permeability of the test section. If the water level variation in a borehole can be measured manually at appropriate time intervals while the water level rises toward the static water level, the value of K is calculated by the following equation:

$$K = D_e^2 / 8H \cdot \log(\alpha H / D + \sqrt{1 + (\alpha H / D)^2}) \cdot \log(s_1 / s_2) / (t_2 - t_1), \qquad (4.1)$$

where K is the radial or horizontal hydraulic conductivity, D_e is the effective radius of the well casing, D is the test depth diameter, K_z is the vertical hydraulic conductivity, $\alpha = \sqrt{K/K_z}$ is the conductivity ratio representing the anisotropy, H is the test screen length and s_1 (s_2) is the drawdown at time t_1 (t_2). Conversely, if the water level variation is too rapid to be measured manually due to high permeability in the test section, a pumping test is instead conducted in the borehole, and the pumping discharge rate and drawdown from the static level in the borehole are measured under the pseudo-steady state. In this case, K is calculated as:

$$K = Q / 2\pi s H \cdot \log(\alpha H / D + \sqrt{1 + (\alpha H / D)^2}), \qquad (4.2)$$

where s is the drawdown under the pseudo-steady state and Q is the pumping discharge rate. In all tests, the value of H was consistent at unit depth. The water temperatures during each test were measured by transducers. The temperature was in the 5–12 °C range, and was related to the infiltration near the river. Figure 4.4 shows a relation between slug test results and test depths, indicating depth-dependence in the gravel deposits.
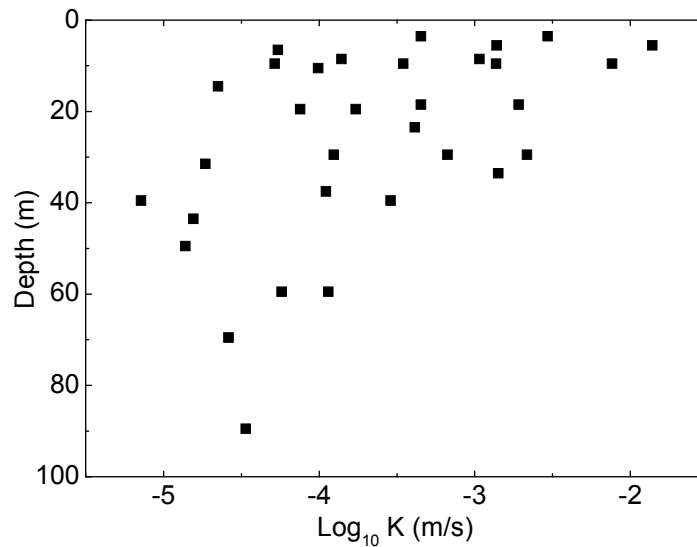
Figure 4.4 Relation between previous results of slug test and mid-depths of the
test screens in the fan

(3) Matrix packing level

The relatively undisturbed cores consisted of coarse grain frameworks with openings between the grain components. The majority of these openings were adequately filled with a detritus of fine gravel, sand and silt. However, the openings were typically not completely packed, and the amount of finer sediments in the openings differed even though the drilling conditions (e.g., the swivel rotation and drilling fluid pressure) were kept almost constant. Therefore, the packing in the gravel cores is considered to be related to the sampling depth, and the obvious absence of fine sediment corresponds to the natural openings that form water passages.

This study proposes to designate this packing difference as the matrix packing level, and packing was qualitatively categorized into four levels (Figure 4.5): level I (full), level II (almost full), level III (loose) and level IV (very loose). For level I, the openings between the gravel grains are fully packed with a fine filling, and the appearance of the core is similar to that of a conglomerate; for level II, the majority of the openings are filled, but fine sediment is dispersedly seen to be missing on the centimeter scale; for level III, an absence of fine sediments is frequently found throughout the sample such that several openings are connected and form empty belts across the core; and for level IV, the fine fillings are almost nonexistent, and so only the gravel framework is seen. Photographs of representative example cores with each packing level were shown in the previous paper. A core section with packing level I or II was further called the "*high packing part*," and that with packing level III or IV the "*low packing part*." The length of each packing level

was individually measured to the nearest centimeter.

Such measurements were conducted throughout each of the cores except for those consisting mainly of finer sediments. All researchers observed the cores simultaneously to obtain consistent results, because assigning the packing level, especially for levels II or III, was sometimes challenging. After taking the measurements, the values were recorded in terms of unit depth (i.e., the length fraction of each packing level, which were denoted L_1–L_4 (m/m).

Statistics of the length fraction measurements for the low packing parts, L_3 and L_4, are summarized in Figure 4.6. L_3 is relative larger than L_4 at the same depth, and occasionally is >0.1 m/m. However, the vertical trend of L_3 is unclear. In contrast, L_4 is usually of the order of 1×10^{-2} m/m, but sometimes exceeds 0.1 m/m near the surface. L_4 has an obvious decreasing trend such that it almost vanishes below a depth of ~30 m.
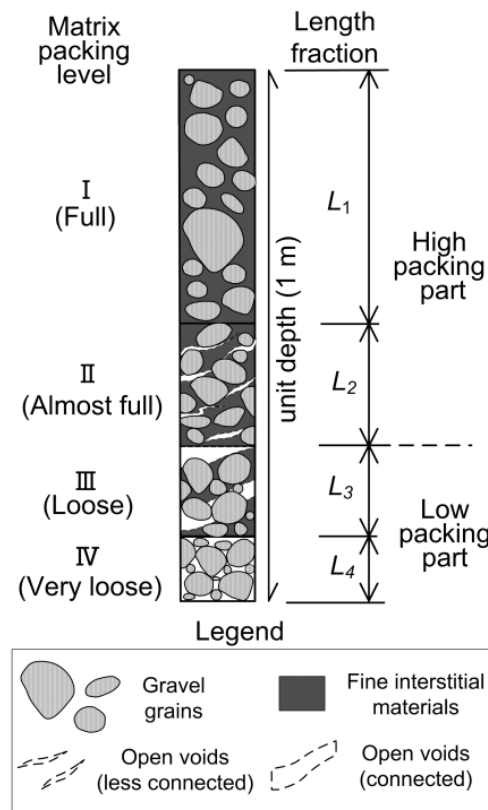
Figure 4.5 Classification of gravel core according to matrix packing level. Open granular squares in the column denote gravels, small dots denote fine sediments in openings between gravel grains and black shadows denote losses of fine sediments. Packing levels I and II (III and IV) at unit depth are grouped as the high (low packing part)

Table 4.1 Core samples and features of matrix packing level I to IV

Matrix packing level	Core sample	Feature
I: full	Depth= 49.0- 49.5 m in BW3	All pore spaces between gravel grain are fully packed by fine sediments. No cracks are identified througout the core.
II: almost full	Depth= 59.5- 60.0 m in BW3	Almost pore spaces are fully packed, but a lack of fine sediments are partially recognized around a few gravel grains.
III: loose	Depth= 56.0- 56.5m in BW3	A lack of fine sediments are frequently recognized around gravel grains, such that gravel and matrix are loosely packed.
IV: very loose	Depth= 2.5- 3.0m in BW3	There are little fine sediments around gravel grains. Pore spaces around gravel grains are easily recognized, and overall core are very loose.
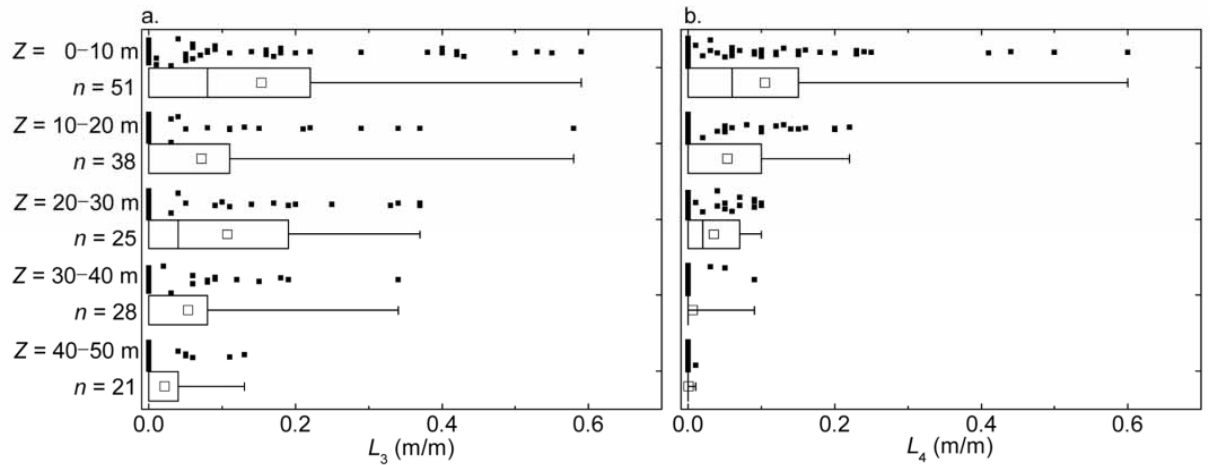
Figure 4.6 Box and whisker plots showing the vertical statistics of length fractions of low packing parts **a.** L_3 and **b.** L_4. Summaries are given at 10 m intervals. Solid squares above each box denote measurements at BW1-7, the left- and right-hand side bars of the boxes respectively denote the 25th and 75th percentiles, the bars within the boxes denote the medians, the bars at the left and right ends of the whiskers respectively denote the minimum and maximum values and open squares in the boxes denote the averages

(4) Grain size analysis

The grain size analysis was conducted using relatively undisturbed cores taken from the same depth as that used in the slug tests. Additionally, the analysis was conducted to obtain vertical profiles of the effective grain size diameter at two sampling points in the mid-fan, BW5 and BW3, and one in the fan-toe, BW7. The reasons for choosing these wells were as follows: the gravel deposits at BW5 were the thickest among the wells; BW3 was located about 1 km downstream from BW5, and was the midpoint of the losing section of the river described above; and BW7 was located near the lower edge of the fan, where finer sediments overlaid the gravel deposits and low packing parts were less observed. The total depths at BW5, BW3 and BW7 were 100, 64 and 44 m, respectively. The depths at which sandy gravel cores were analyzed per unit depth were 1−72 and 81−92 m at BW5 (82 samples); 2−40, 41−50 and 52−63 m at BW3 (58 samples); and 6−19, 21−24, 27−38 and 43−44 m at BW7 (28 samples).

4.2.2   Permeability model with matrix packing level

The following relations between the 32 slug test results and core properties at the same depth are established. (1) The K value of the high packing part (i.e., packing levels I and II) in the core is assumed to be that of a conventional porous medium. The fundamental formula for K in porous media is generally represented as a composite of the medium's fluid properties, porosity function or coefficient, and grain size (e.g., Freeze and Cherry 1979; Todd and Mays 2005):

$$K = \frac{\rho g}{\mu} C d^2, \qquad (4.3)$$

where ρ is the density of the fluid; g is the acceleration due to gravity; μ is the kinematic coefficient of viscosity; C is a dimensionless coefficient, which is dependent on the porosity, sorting, packing and other factors; and d is the effective grain size diameter. d_{10} is commonly used for d (Fetter 2001); however, Shepherd (1989) suggested that the mean diameter better represents the effective grain size diameter, and the exponent ranges from 1.5 to 2 according to the sedimentary textural maturity. In the current study, the obtained grain size distributions are noted as being different from those in nature because of sampling limitations; namely, the sampler was of small diameter and the small sample volume were used for sieving. Therefore, a more general exponential equation was applied to determine K in the high packing part:

$$K_{HP} = C_{HP} d^m, \quad (4.4)$$

where K_{HP} is the hydraulic conductivity of the high packing part, constant C_{HP} is a dimensionless proportionality coefficient and m is the exponent for effective grain size diameter d. Note that C_{HP} corresponds to the product of the fluid properties at a constant temperature of 25 °C and the coefficient C in Equation (4.3).

(2) The low packing part (i.e., packing levels III and IV) in the core is considered to form preferential water passages for the movement of fluid, which are similar to fractures in consolidated rock. A rock fracture's K value is proportional to the square of its aperture (Snow 1969; Domenico and Schwartz 1998; Singhal and Gupta 1999). A further assumption is that the water passage width in each unit of the low packing part is linearly related to the length fraction of each packing level. In addition, the proportionality coefficients are assumed to differ between packing levels III and IV. Consequently, the K value for the low packing part takes a simple form:

$$K_{LP} = C_i L_i^{\ 2}, \quad (4.5)$$

where K_{LP} is the hydraulic conductivity of the low packing part and C_i is a dimensionless proportionality coefficient, which takes a different value for packing level III (index $i = 3$ and level IV (index $i = 4$).

(3) An equivalent horizontal hydraulic conductivity $\overline{K}$ per unit depth, composed of a sequence of different packing levels, is estimated as a weighted arithmetic mean, specifically, the sum of the products of each packing level's individual K value and length fraction. Accordingly, $\overline{K}$ is calculated by the following equation:

$$\overline{K} = C_{HP}d^m \times L_{HP} + \sum_3^4 C_i L_i^{\ 2} \times L_i = C_{HP}d^m(L_1 + L_2) + C_3 L_3^{\ 3} + C_4 L_4^{\ 3}. \quad (4.6)$$

The constants C_{HP}, C_i, and m in Eq. (4.6) are simultaneously determined under the hypothesis that the estimated $\overline{K}$ values correspond to the slug test results at the same depth. j is the index of boundary between high packing and low packing parts. The agreement between estimated and actual K values is then assessed by using a least squares method to minimize the root mean square error ($RMSE$). The $RMSE$ value is calculated as the sum of the residuals between the common logarithms $\overline{Y}$ of $\overline{K}$ and the logarithms Y of K measured by the slug tests at the same depth:

$$RMSE = \sum^n (\log_{10}K - \log_{10}\overline{K}) = \sum^n (Y - \overline{Y}) = \sum^n ReY, \quad (4.7)$$

where ReY is the residual log-conductivity and n is the sample number ($= 32$). Logarithmic transformations

are used to avoid a few extremely permeable values from considerably affecting the *RMSE* results. A nonlinear optimization tool, the MS Excel Solver, was used to perform the optimization. Since d is not empirically known, it is determined by repeatedly optimizing using various cumulative weight diameters; $d_5, d_{10}, d_{15}, d_{20}, d_{30}, d_{40}, d_{50}, d_{60}, d_{70}, d_{80}$ and d_{90} (mm).

4.2.3 Moving average method

The core properties profiles in the sampling points, BW3, BW5 and BW7 were transformed into those of $\overline{K}$ by using Equation (4.6). However, the optimal equation (4.6) has inevitable uncertainty because the parameter optimization is conducted by log-transfomation in Equation (4.7). If the residuals between Y and $\overline{Y}$ (ReY) are only no more than one, the confidence interval of $\overline{K}$ was extended by several to 10-fold when the log transformation was inverted. The $_{Re}Y$ resulted from various factors: the sampling limitations of using small diameters and volumes, the over- or under-estimation of the packing level, the applicability of the slug test method to the test conditions, and the simplifications made to generate the relation in Eq. (4.6).

To address the uncertainty in Eq. (4.6), moving average method was applied to the profiles of $\overline{Y}$ in the sampling points. The moving average of $\overline{Y}$ ($\overline{Y}_{MA}$) is calculated through the following equation:

$$\overline{Y}_{MA} = \sum_{1}^{nMA} \overline{Y}_i = \sum_{1}^{nMA} \log_{10} \overline{K}_i, \qquad (4.8)$$

where $\overline{Y}_i$ is the common logarithm of estimated conductivity $\overline{K}_i$ for ranging from 1 to nMA. nMA is the total number of $\overline{K}$ values used for the moving average; in the present case, nMA corresponds to the average interval written in meter units, because $\overline{K}_i$ was calculated per unit depth. The average interval must be determined carefully since the uncertainty in $\overline{Y}_{MA}$ decreases when the average interval increases under a stationary condition. Conversely, $\overline{Y}_{MA}$ is influenced by a spatial trend (which is empirically unknown), when the average interval is relative larger than the trend. Here, an average interval of nMA $= 5$ m was applied. $\overline{Y}_{MA}$ was thus the average of five $\overline{Y}$ values; the $\overline{Y}$ value at target depth and two values at depths above and below the target depth. In traditional statistics, the 95% confidence interval of $\overline{Y}_{MA}$ was obtained as $[\overline{Y}_{MA} - 1.96\sigma/\sqrt{n\mathrm{MA}}, \ \overline{Y}_{MA} + 1.96\sigma/\sqrt{n\mathrm{MA}}]$ (i.e., $[\overline{Y}_{MA} - 0.35, \ \overline{Y}_{MA} + 0.35]$).

4.3 Results and discussion

4.3.1 Grain size analysis

The some results of grain size analysis are shown in Figure 4.7. All of the samples were poorly sorted as there was a wide range of grain size present. Less than 5% of the samples consisted of silt and clay, and more than 10–40% consisted of gravels. Figure 4.7 showed no obvious trend among different locations, for example a fining trend in the downward direction from the upper point (BW6) to the lower (BW1).
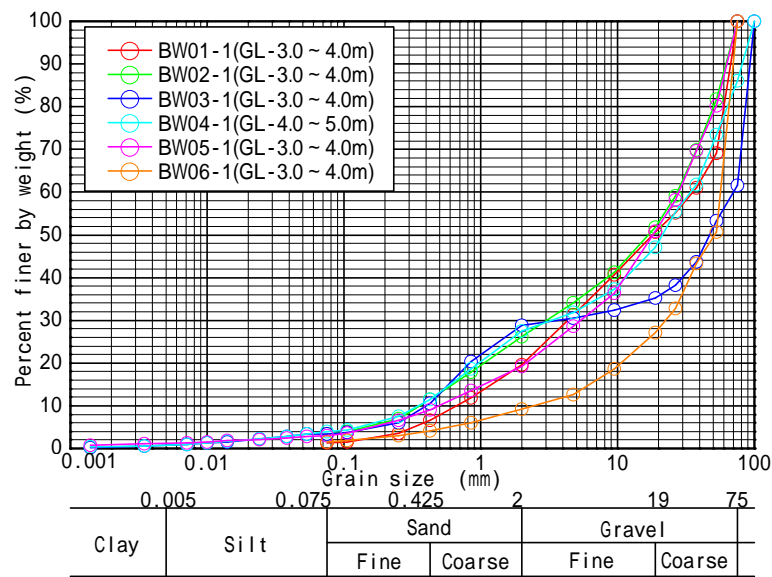

Figure 4.7 Grain size distribution curves of undisturbed cores sampled at BW1–6

Figure 4.8 shows relations between two grain sizes (d_{10} and d_{50}) and slug test results obtained in the sampling depths. There were also no obvious relations in both plots, indicating that K in the coarse gravel deposits could not be formulated only by using the traditional equations, Eq. (4.3) and (4.4). In other words, K in the coarse sediments is not a function of only total porosity; if total porosity is even small but open voids are connective between gravels, the coarse gravel deposits has high permeability. It was needed to indicate another index which reflected the open pore structures in the gravel deposits.
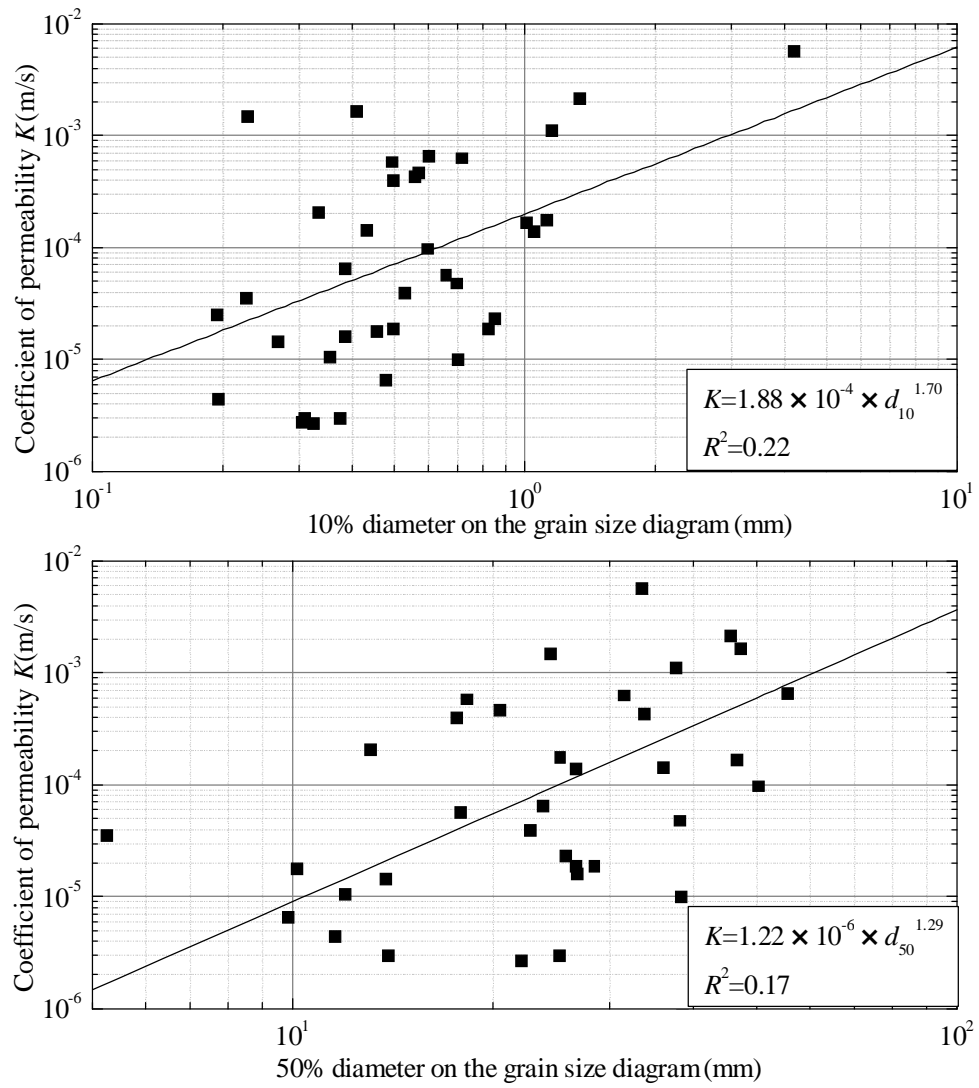
Figure 4.8 Relations between grain size (d_{10} and d_{50}) and hydraulic conductivity obtained by slug tests in the sampling depths.

4.3.2 Optimization of parameters in permeability model

The first study (Sakata et al. 2011) determined the index j (j= 1-4) and effective grain size d_e (d_e= d_5, d_{10}, d_{15}, d_{20}, d_{30}, d_{40}, d_{50}, d_{60}, d_{70}, d_{80} and d_{90}) through a comparison of $RMSE$ values obtained by Eq. (4.7). The determination was conducted employing only the data at BW1 to BW6, and the K values was not compensated to the values of constant temperature of 25 °C.

The minimum $RMSE$ value was obtained in the case of j=1 and d_e=d_{20} (Model 1 in Table 4.2), however, the case of j=2 and d_e=d_{20} (Model 2) was most optimal as followings: 1) the degree of freedom in Model 2 was smaller than that in Model 1; 2) the constant C_2 in Model 1 was enough small to be ignored, and 3) the other constants, C_3 and C_4, were almost equal in the cases.

Table 4.2 Results of parameter optimization using undisturbed cores and slug tests at BW1-6

Model 1: j=1, C_m=C_1 C_2, C_3, C_4

	d_{10}	d_{20}	d_{30}	d_{40}	d_{50}
$RMSE$	0.97	0.68	0.81	0.91	0.96
m (-)	2.9	3.2	2.2	1.5	2.5
C_m (1/m²s)	28,800	8,642	2.0	0.014	0.19
C_2 (1/m²s)	0.00048	0.00038	0.00037	0.00026	0.00030
C_3 (1/m²s)	0.010	0.010	0.011	0.012	0.012
C_4 (1/m²s)	1.1	0.65	0.71	0.78	0.75

Model 2: j=2, C_m=C_1=C_2 C_3, C_4

	d_{10}	d_{20}	d_{30}	d_{40}	d_{50}
$RMSE$	0.99	0.83	0.89	0.90	0.95
m (-)	2.3	2.2	1.6	1.5	2.4
C_m (1/m²s)	516	30	0.12	0.013	0.16
C_3 (1/m²s)	0.0098	0.0093	0.010	0.012	0.013
C_4 (1/m²s)	1.0	0.69	0.74	0.78	0.75

Model 3: j=3, C_m=C_1=C_2=C_3 C_4

	d_{10}	d_{20}	d_{30}	d_{40}	d_{50}
$RMSE$	1.35	1.24	1.29	1.30	1.37
m (-)	1.3	1.4	1.0	1.0	1.2
C_m (1/m²s)	0.86	0.40	0.012	0.0049	0.0046
C_4 (1/m²s)	1.1	0.86	0.91	0.91	0.94

Model 4: j=4, C_m=C_1=C_2=C_3=C_4

	d_{10}	d_{20}	d_{30}	d_{40}	d_{50}
$RMSE$	2.05	1.86	1.89	2.01	1.86
m (-)	0.6	1.2	1.0	0.7	2.1
C_m (1/m²s)	0.011	0.25	0.031	0.0024	0.30

Following the sampling at BW7, the next study (Sakata and Ikeda 2012b) calculated the optimal

parameters again. The analysis data and results are listed in Table 4.3. In the calculation, the K values

were converted into those at a constant temperature of 25 °C for heat transport simulation in Chapter 5.

The optimization resulted that the minimum RMSE value was obtained as:

$$\overline{K} = 6.89(d_{20}/1,000)^{1.9}(L_1 + L_2) + 0.0167L_3{}^3 + 1.87L_4{}^3. \qquad (4.9)$$

A scatter plot of estimated $\overline{K}$ versus measured K values is given in Figure 4.4. The coefficient of

determination (R^2) between $\overline{Y}$ and Y is relatively high at 0.80.
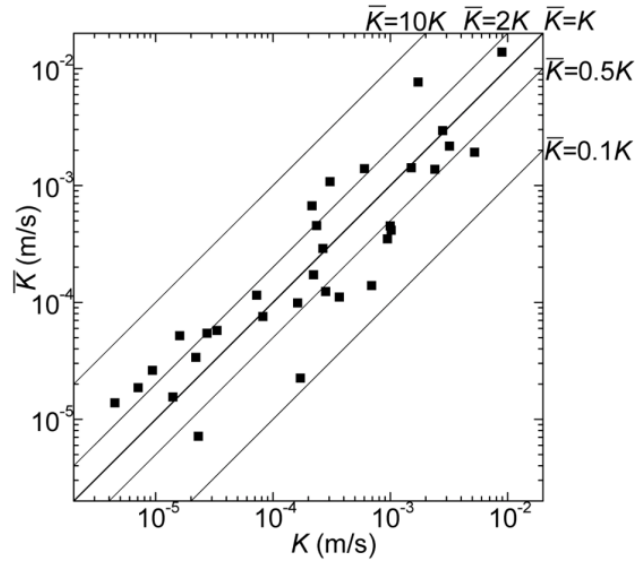
Figure 4.9 Comparison in double logarithmic scale between hydraulic
conductivities measured by slug test (K (m/s)) and estimated by Eq.
(4.9) ($\overline{K}$ (m/s)). Here, $R^2 = 0.80$

Table 4.3 Analysis data and optimization results to determine the relation between slug tests and gravel cores in the Toyohira River alluvial fan.

Sample number	Point identifier	Sampling and test depth (m)	Properties of gravel cores				Log-conductivity		
			d_{20} [a]	L_1+L_2 [b]	L_3 [b]	L_4 [b]	Y [c]	Y [d]	ReY [e]
1	BW1	9–10	0.85	0.91	0.00	0.09	-2.62	-2.86	0.24
2	BW2	5–6	12	0.29	0.53	0.18	-2.05	-1.86	-0.19
3		8–9	1.6	0.80	0.18	0.02	-3.16	-3.86	0.70
4	BW3	3–4	0.83	0.50	0.40	0.10	-2.55	-2.53	-0.02
5		9–10	3.7	0.43	0.42	0.15	-2.76	-2.12	-0.64
6		19–20	2.4	1.00	0.00	0.00	-4.09	-4.12	0.03
7		29–30	8.6	0.66	0.25	0.09	-2.50	-2.66	0.16
8		31–32	0.70	0.91	0.09	0.00	-5.15	-4.73	-0.42
9		39–40	4.2	0.81	0.19	0.00	-3.58	-3.54	-0.04
10		49–50	1.0	1.00	0.00	0.00	-5.35	-4.86	-0.49
11		59–60	3.0	1.00	0.00	0.00	-4.14	-3.94	-0.20
12	BW4	5–6	1.0	0.82	0.09	0.09	-3.22	-2.86	-0.36
13		8–9	0.63	0.60	0.40	0.00	-3.51	-2.97	-0.54
14	BW5	3–4	2.2	0.71	0.29	0.00	-3.00	-3.35	0.35
15		9–10	2.0	1.00	0.00	0.00	-4.80	-4.29	-0.51
16		19–20	3.3	0.85	0.15	0.00	-3.65	-3.77	0.12
17		29–30	1.5	0.93	0.00	0.07	-3.67	-3.18	-0.49
18		39–40	0.71	1.00	0.00	0.00	-4.64	-5.15	0.51
19		59–60	2.1	1.00	0.00	0.00	-4.48	-4.24	-0.24
20		69–70	0.86	0.90	0.10	0.00	-5.03	-4.58	-0.45
21		89–90	1.43	0.92	0.08	0.00	-4.66	-4.47	-0.19
22	BW6	6–7	2.1	1.00	0.00	0.00	-4.56	-4.26	-0.30
23		9–10	5.2	0.93	0.04	0.03	-3.03	-3.46	0.43
24		18–19	4.4	0.84	0.11	0.05	-3.63	-3.35	-0.28
25	BW7	10–11	2.8	1.00	0.00	0.00	-3.79	-4.01	0.22
26		14–15	1.3	1.00	0.00	0.00	-3.76	-4.65	0.89
27		18–19	1.0	0.77	0.13	0.10	-2.28	-2.72	0.44
28		23–24	0.81	0.94	0.00	0.06	-2.99	-3.38	0.39
29		29–30	0.55	0.96	0.00	0.04	-3.55	-3.91	0.36
30		33–34	2.2	0.88	0.03	0.09	-2.82	-2.85	0.03
31		37–38	1.1	0.82	0.18	0.00	-3.43	-3.96	0.53
32		43–44	1.1	1.00	0.00	0.00	-4.85	-4.81	-0.04
Mean									0.00
Variance									0.16

[a] Effective grain size diameter by sieving (mm)
[b] Length fraction of each packing level (m/m)
[c] Common logarithm of K (m/s) measured by slug test results (modified to a constant temperature of 25 °C)
[d] Common logarithm of $\overline{K}$ (m/s) estimated by Eq. (4.9)
[e] Residual log-conductivity between Y and $\overline{Y}$

The relation between estimated $\bar{K}$ and d_{20} for cases of L_3 and L_4 is shown in Figure 4.10. When $L_3 <$ 0.05 m/m and L_4 is rarely observed on the centimeter scale (i.e., the gravel core in effect contains only a high packing part, $\bar{K}$ varies from 5×10^{-6} to 2×10^{-3} m/s. Here, $\bar{K}$ is governed by only the grain size, and is independent of core packing level. When $L_3 > 0.5$ m/m or $L_4 > 0.1$ m/m (i.e., the occasional case that occurs near the surface (Figure 4.6)), $\bar{K}$ is of the order of 1×10^{-3} m/s for all grain sizes. Such a high conductivity regardless of the length scale for the low packing part indicates that preferential water passages may exist at the sampling depth. When $0.05 \leq L_3 \leq 0.5$ m/m and L_4 is of the order of 1×10^{-2} m/m (i.e., the intermediate case), either the grain size or length fraction of the packing levels has a strong affect on $\bar{K}$. The limit on the effective grain size that governs its effect on $\bar{K}$ is roughly $d_{20} = -2$ ($-\varphi = 4$) mm, where $-\varphi$ denotes the base-2 logarithm of grain size (mm).

Estimating $\bar{K}$ from Eq. (4.9) results in it attaining a high value even if the low packing part is fairly concentrated. This hydraulic feature corresponds to that of open framework gravel (OFG), which is usually observed in outcrops or trenches, and is considered to be the most remarkable hydro-face due to its high permeability. OFG has a distribution that is only centimeters or decimeters thick, but its K value is of the order of 1×10^{-3} to 1×10^{-2} m/s, considerably greater than the value for the surrounding layers (Jussel et al. 1994; Heinz 2003; Lunt et al. 2004; Zappa et al. 2006; Ferreira et al. 2010; dell'Arciprete et al. 2012).
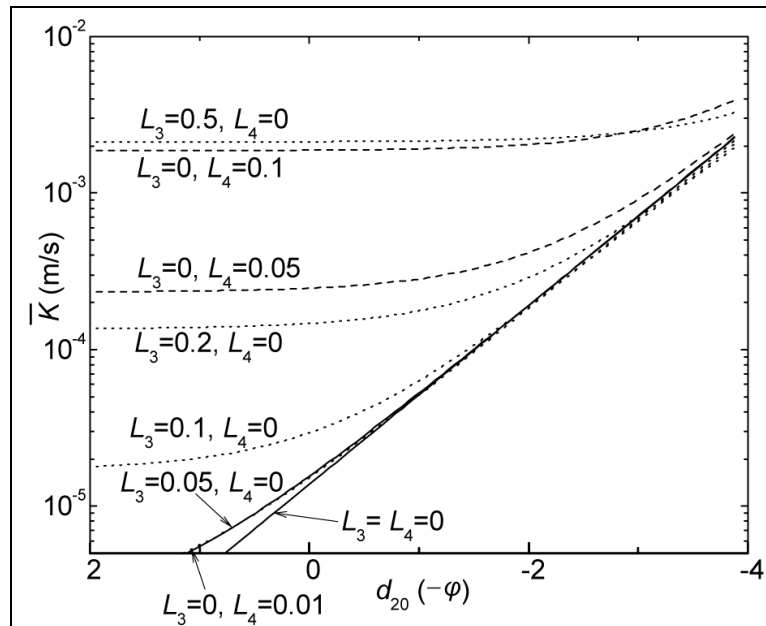
Figure 4.10 Curves relating $\bar{K}$ calculated by Eq. (4.9) and effective grain size diameter $-\varphi$ d_{20} = log$_2$ d_{20} (mm) for several length fractions of low packing part L_3 or L_4 (m/m)

ReY ranged from -0.64 to 0.89 with a variance of 0.16, as shown in Table 4.3. These statistical values of the residuals were not necessarily ignored because the confidence interval of $\overline{K}$ was extended by 3- to 10-fold or greater when the log transformation was inverted. Considering an assumptions that $\overline{Y}$ was normally distributed and $\overline{K}$ was log-normally distributed (Domenico and Schwartz 1998; ASCE 2008), and that ReY was also normally distributed with a constant variance of $\sigma^2 = 0.16$, specifically, ReY was assumed to occur randomly with no spatial correlation and with a constant variance. A 95% confidence interval for $\overline{Y}$ was obtained under the above assumptions as [$\overline{Y} - 1.96\sigma$, $\overline{Y} + 1.96\sigma$] (i.e., [$\overline{Y} - 0.78$, $\overline{Y} + 0.78$] in other words, [$\overline{K}/6.0$, $6.0\overline{K}$]. The interval is approximately equal to a single order of magnitude and so $\overline{K}$ was not quantitatively valid in this case. On the other hand, the 95% confidence interval of $\overline{Y}_{MA}$ was obtained as [$\overline{Y}_{MA} - 0.35$, $\overline{Y}_{MA} + 0.35$], and was transformed to [$\overline{K}/2.2$, $2.2\overline{K}$]. This range was considered to be sufficient for quantitative discussion of the vertical trend.

4.3.3 Vertical profiles of core properties and hydraulic conductivity

The results for BW5, BW3 and BW7 are shown in Figure 4.11. From left to right, the results for each sampling point show changes with depth of the geologic column, effective grain size diameters, length fractions of the low packing part and log-conductivities: Y measured by slug tests, $\overline{Y}$ estimated by Eq. (4.9) and $\overline{Y}_{MA}$ over 5-m intervals. Gaps in the profiles indicate data rejected or not obtained at depths where cores are composed mainly of fine sediments.

The geologic columns at BW5 and BW3 do not show migration sequences of the gravel deposits, which are generally a characteristic of alluvial fans rather than meandering river sequences. A majority of the intercalating sandy layers are ≤1 m in thickness, and are rarely seen in consecutive horizontal positions among the wells. Only monotonic gravel successions therefore show no obvious hydrogeologic boundary in the gravel aquifer (e.g., the boundary between Holocene no. II and Pleistocene no. III aquifers). In contrast, the gravel deposits at BW7 lie below an alternation of fine sediments, which corresponds to the upper edge of the Holocene no. I aquifer. Additionally, the intercalating layers in the gravel deposits are frequently distributed with even finer sediments. In particular, volcanic ashes are typically interbedded at depths of ~19–20 and 41–43 m, corresponding to the reworked deposits of Shikotsu pumice flows (~40,000 yr) before present (B.P.) and of Toya ash falls (~110,000 yr B.P.), respectively.

d_{20} varies in each well, ranging widely from -1 to 4 (-φ) (i.e., ~0.5 to 16 mm). Moreover, the deviations in adjacent data in the profiles are often greater than 1 to 2 (-φ). This large fluctuation is considered to mask the spatial trend, for example, a down-fan fining trend from the mid-fan to fan-toe. Such fluctuations probably arise from sampling errors due to various sources (as already described), as well as from sedimentary heterogeneity. Here, no distinct difference is found between the grain size variations of BW5, BW3 and BW7, but a decreasing trend with depth is observed only at BW5, although this is not obvious due to the fluctuation.

The length fractions of the low packing part, L_3 and L_4, show a clear decreasing trend with depth at BW5 and BW3. L_4, in particular, decreases rapidly with depth, and has almost vanished by a depth of ~30 m. A somewhat decreasing trend is also seen in L_3 such that its values appear to be relatively random. In contrast, a specific trend is not seen for L_3 or L_4 at BW7. The main reason for this difference in trends is that in the mid-fan, the low packing part accumulates in the gravel deposits near the surface, whereas in the fan-toe,

the late Holocene fine sediments cover the surface with a thickness of >10 m. Another reason is considered to be the development process of OFG, the hydraulic features of which are equal to those of the low packing part. Thick OFG deposits occur due to high bedforms and large amounts of aggradation (Lunt and Bridge 2007), and form in the mid-fan, but not in the fan-toe.

Y values are measured by slug tests at several points in each well. As a result, Y ranges from -2 to -6, that is, four orders of magnitude of K (m/s), by inverting the log transformation. This large range of measurements is considered as being reflective of the geological heterogeneity in the gravel deposits. However, a decreasing trend in Y is found at BW5 and BW3. Conversely, $\overline{Y}$ values in each profile fluctuate even more widely, with an amplitude of >1–2, which corresponds to one to two orders of magnitude of $\overline{K}$. The greater fluctuation in $\overline{Y}$ is probably a result of not only the heterogeneity but also the estimation errors. Therefore, $\overline{Y}$ values are not used to determine the exhibited trend. Instead, $\overline{Y}_{MA}$ values in each profile vary more smoothly, and thus reveal the changes with depth. Decreasing trends in $\overline{Y}_{MA}$ are evident at BW5 and BW3, and are observed only above depths of ~30 m, which corresponds to the maximum depth at which L_4 values are observed. Furthermore, the moving average below this depth is ≈-4, showing that an approximately stationary field may exist. In contrast, a vertical change with depth is not obvious at BW7, where trends are not observed for L_3 or L_4. Thus, the depth dependence of K in the fan is understood from the vertical distribution of the packing levels in the undisturbed cores.
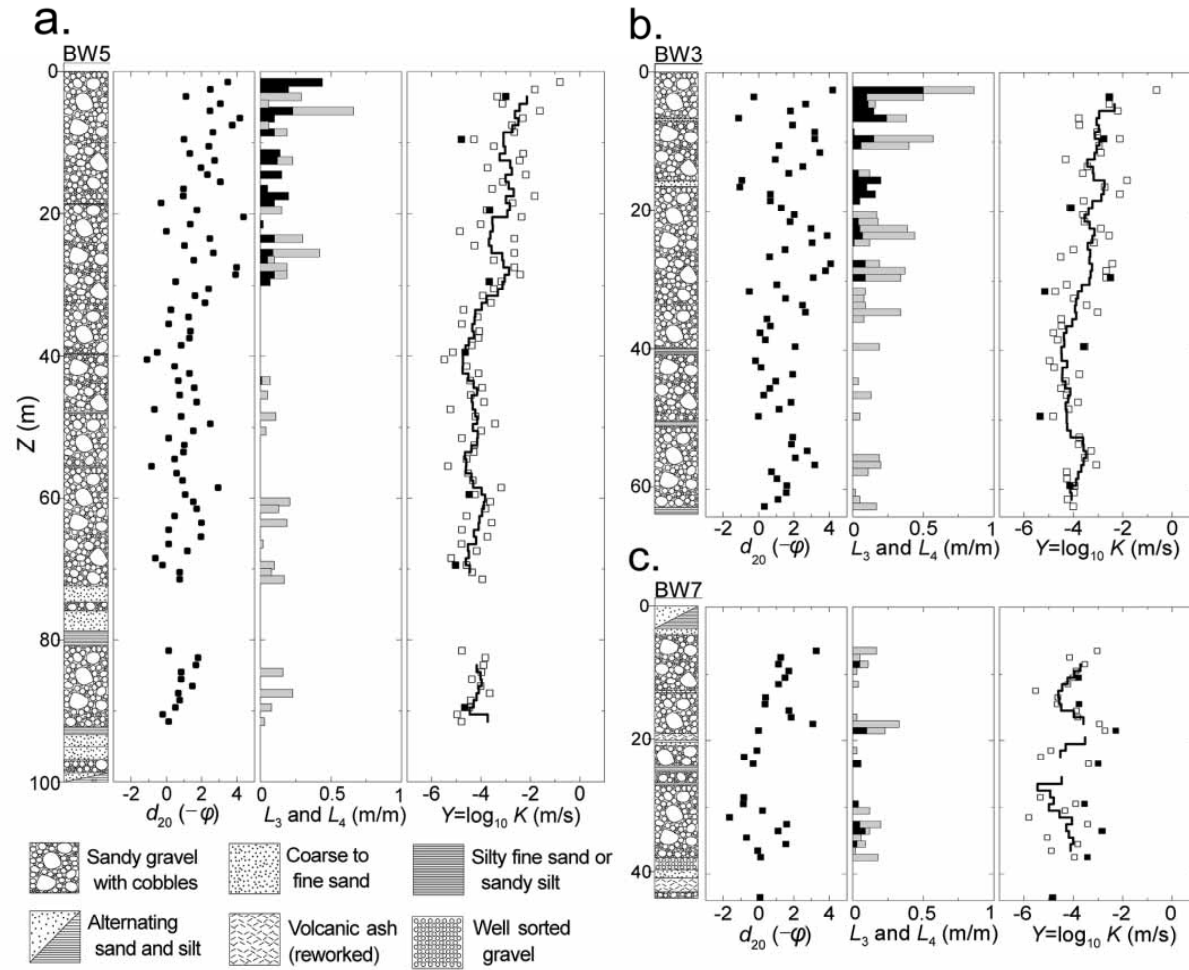
Figure 4.11 Core property and hydraulic conductivity results at **a.** BW5, **b.** BW3 and **c.** BW7. Each results contains, from left to right, the geologic column; effective grain size diameters, $-\varphi = \log_2 d_{20}$ (mm); length fractions of low packing part, L_3 (gray bars) and L_4 (dark gray bars) (m/m); and common logarithms of the hydraulic conductivity (m/s). In the log-conductivity profiles, solid circles denote Y values measured by slug tests, open squares denote $\overline{Y}$ values estimated by Eq. (4.9) and solid lines denote moving average $\overline{Y}_{MA}$ values over 5-m intervals. All data are obtained at unit depth. Gaps represent depths at which data were rejected or not obtained

4.3.4 Depth dependence of permeability

A linear regression analysis is applied between $\overline{Y}_{MA}$ and depth. Here, the depth data correspond to the midpoints of each average interval and the $\overline{Y}_{MA}$ data are taken above depths of 40 m—the maximum depth of the decreasing trend, 30 m, plus an additional 10 m. A scatter plot showing the regression results is given in Figure 4.12. The regression lines for BW3 and BW5 have approximately equal slopes and intercept values; the slopes are 0.041 and 0.052 (average: 0.047), respectively, and the intercepts are -2.5 and -2.2 (average: -2.3). In addition, R^2 values of >0.7 are obtained. A depth dependence of K is often represented as an exponential function:

$$\overline{K} = \overline{K}_0 \exp(-AZ), \quad (4.10)$$

where $\overline{K}_0$ (m/s) is the $\overline{K}$ value at the ground surface, which is equal to $1 \times 10^{-2.3}$ m/s for the current case; A (m^{-1}) is a decay exponent; and Z (m) is the depth below the surface. The decay exponent is determined by dividing the average slope of 0.047 by $\log 10 = 2.3$. Hence, $A = 0.11$ (m^{-1}). The exponent equation for the mid-fan is therefore

$$\overline{K} = \overline{K}_0 \exp(-AZ) = 10^{-2.3} \exp(-0.11Z). \quad (4.11)$$
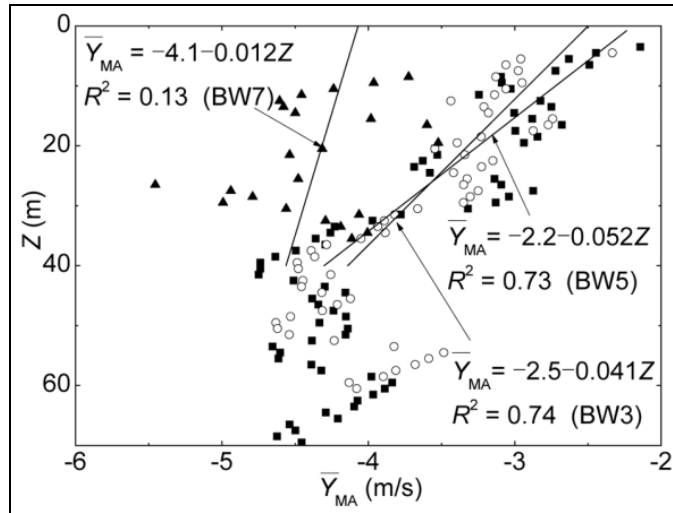
Figure 4.12 Scatter plot of $\overline{Y}_{MA}$ values at BW5, BW3 and BW7 with associated regression lines. Solid squares denote $\overline{Y}_{MA}$ values at BW5, open circles denote values at BW3 and solid triangles denote values at BW7. Averages are plotted at mid-depths of 5-m intervals. A regression analysis between $\overline{Y}_{MA}$ and depth is conducted in each well using data above a depth of 40 m

The size of the decay exponent here should be noted. For example, an increase in depth of 1 m corresponds to a ~10% decrease in K. Explicitly, K at a depth of 10 or 30 m is equivalent to approximately 1/3 or 1/25 of $\overline{K}_0$ at the ground surface. The exponents in other unconsolidated gravel deposits are regrettably not obtained in this study; thus, previous values found for various consolidated rocks are used for comparison. These values differ greatly at each site, and are of the order of 1×10^{-2} to 1×10^{-4} m^{-1}, as described before. The exponents for consolidated rocks are therefore not smaller than 1/10 to 1/1000 of the gravel deposit value. Conversely, the regression line for BW7 has an R^2 value of only 0.13. This small value implies that a vertical trend is not evident in the fan-toe (although only one profile is created). Specifically, the depth dependence of K is not common throughout the fan, but is restricted to the upper fan, where gravel deposits of the low packing part accumulate below the ground surface.

The typical characteristics in the vertical trend—the large exponent A in the mid-fan and the fan-apex, and the lack of a trend in the fan-toe—are considered as follows. One simple and most probable argument is that the depth dependence at BW5 and BW3 is a unique stratigraphic trend (i.e., coarsening-upward trend) due to progradation in the Holocene fan. Stationarity below a depth of ~30 m may indicate different (lower energy and slower) depositional environments such as braided river system. The lack of a trend at BW7 indicates that the location is adjacent to, but not in, the alluvial fan depositional system. However, the interpretation based on only stratigraphic sequences remains slightly problematic. The low packing parts in the gravel cores are rarely observed at deep depths, although the grain sizes at deep depths are often large, no smaller than those in at shallow depths. Another argument is specific post-depositional processes in shallow alluvial deposits, other than the often discussed diagenetic and metamorphic processes. In shallow burial, crushing probably has a small effect on the porosity reduction, and cementation such as groundwater calcretization is not seen in the cores. An understanding of the post-depositional processes in the shallow gravel deposits is most likely needed to obtain other information such as the stability of fine sediments in the openings between framework components. If the gravel deposits are loosely packed and the fine sediments are unstable, the open pore structures that correspond to the low packing parts in the cores are theoretically more densely filled due to the movement of the fine interstitial sediments through increased fluid pressure with buried depth. To our knowledge, the mechanism of the post-depositional transition from loose to high packing in alluvial coarse mixtures has not been examined. Although the factor in the trend, whether depositional or post-depositional processes, has not been determined, this field

investigation reveals a unique vertical trend in the investigated alluvial fan, and the depth dependence is well-formulated as the exponential model used for the analysis and numerical modeling of groundwater systems.

4.3.5   Aquifer structure

A longitudinal cross section is generated by using the geologic columns and $\overline{Y}_{MA}$ profiles, as shown in Figure 4.13. This cross section extends from the fan-apex 2-km upstream of BW5 to the fan-toe at BW7. The two dotted lines are the boundaries determined from only the stratigraphic information. The lower dotted line is related to the boundary between Pleistocene nos. III and IV aquifers, which is distributed throughout the cross section at an elevation of around -50 meters above sea level (m asl) according to Hu et al. (2010). The upper dotted line represents the boundary between Holocene nos. I and II aquifers, which is determined to be ~10 m asl at BW7. These dotted lines are relatively distinguishable because of the sudden stratigraphic change between the gravel fan deposits and the fine fluvial deposits. However, other boundaries of the gravel deposits such as between Holocene no. II and Pleistocene no. III aquifers are hard to specify among the monotonic stratigraphic columns.

Two $\overline{Y}_{MA}$ boundaries are also traceable among the profiles: a lower broken line with $\overline{Y}_{MA} = -4$ and an upper broken line with $\overline{Y}_{MA} = -3$. The lower boundary is below a depth of ~30 m from the ground surface, and is at the same elevation as the hydrogeologic boundary between Holocene no. II and Pleistocene no. III aquifers (Hu et al. 2010b). This correspondence indicates that the Pleistocene no. III aquifer has only weak K depth dependence, and the permeability in the aquifer is assumed to be stationary at around the expectation of $\overline{K} = 10^{-4}$ m/s. In contrast, the upper boundary of $\overline{Y}_{MA}$ divides the Holocene no. II aquifer into two further aquifers: nos. IIa (upper) and IIb (lower). The Holocene no. IIa aquifer is ~10 m thick near the surface, and $\overline{Y}_{MA} > -3$ here (i.e., $\overline{K} = 1 \times 10^{-3}$ m/s). Such high values of $\overline{K}$ are similar to those found in previous pumping test results: pumping tests were conducted in shallow wells near BW5 and BW3, and obtained an average hydraulic conductivity of $K \approx 2 \times 10^{-3}$ m/s (Hokkaido Regional Development Bureau 2008). The Holocene no. IIa aquifer is directly connected to the river bed, and the surface water is actively infiltrated through the aquifer due to its high permeability and vertical hydraulic gradients. Thus, the Holocene no. IIa aquifer along the river is of importance as an infiltrative aquifer. However, if the aquifer is at a distance of several hundred meters from the river, it is almost unsaturated since the groundwater

surface slopes downward.

In the Holocene no. IIb aquifer, the permeability takes a wide ranges of values, from $\overline{K} = 1 \times 10^{-5}$ to 1×10^{-2} m/s. This range is affected by the sedimentary texture at each depth. Conversely, the average permeability decreases with depth according to the exponent equation (4.11). As a result, the groundwater flows horizontally and vertically through the water passages, which are formed and affected by the geological heterogeneity and depth-dependent effects. Three-dimensional groundwater flows also influence the solute transport. For example, the temperature profiles at BW5 and BW3 suggest the existence of large envelopes and a deepening of the isothermal layer. Typical temperature distributions around the losing river are explained by the presence of large heterogeneity, as well the depth dependence of the permeability, through a simulation that couples groundwater flow and heat transport in chapter 5.
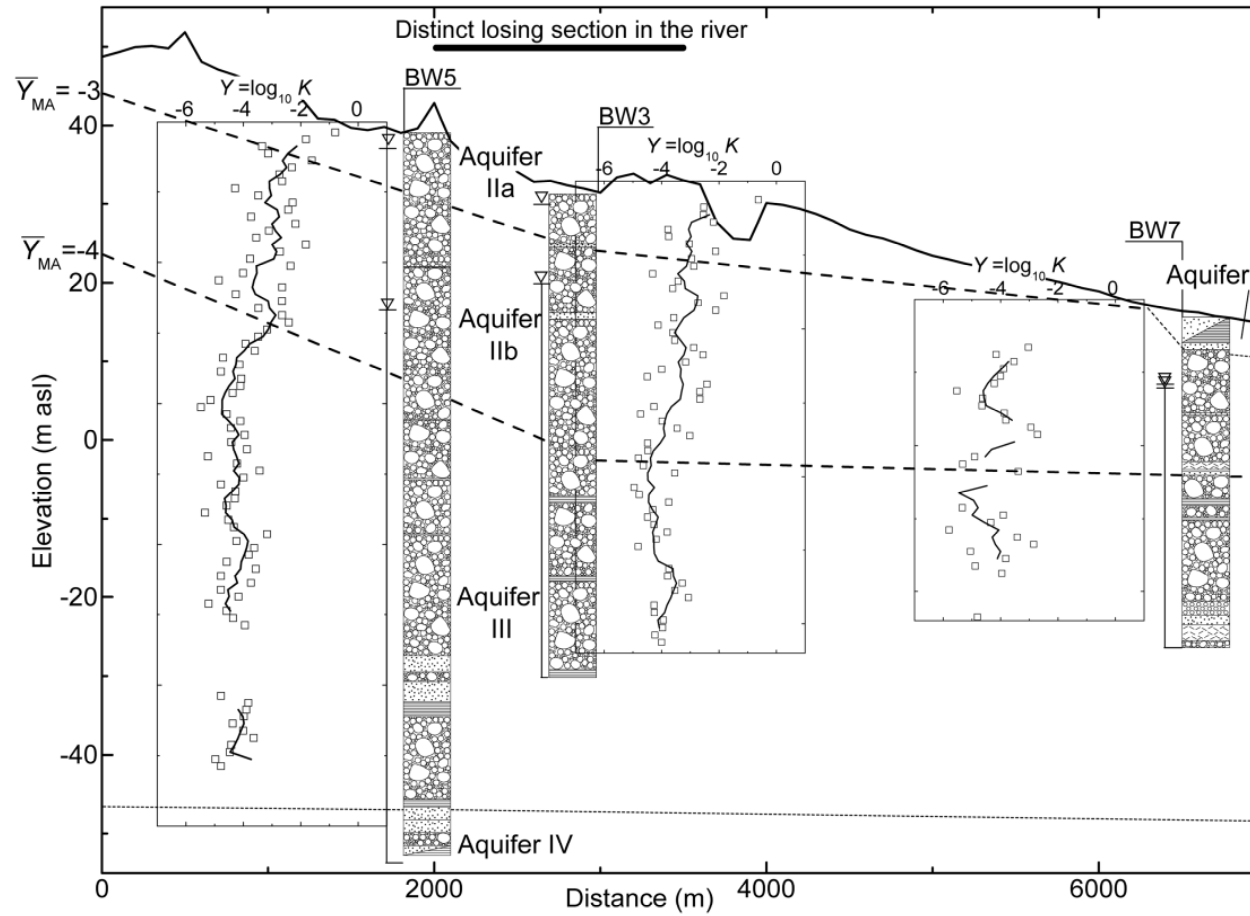
Figure 4.13 Longitudinal cross section showing hydrogeologic boundaries in the fan. The columns and profiles for BW5, BW3 and BW7 are the same as those Fig. 7. Inverted open triangles beside each column denote groundwater heads measured during drilling at the first (upper) and last (lower) depths, and indicate vertical hydraulic gradients in the mid-fan at BW5 and BW3. Dashed lines denote $\overline{Y}_{MA}$ boundaries inferred from the profiles: $\overline{Y}_{MA}$ = -3 (upper) and $\overline{Y}_{MA}$ = -4 (lower). Dotted lines are boundaries inferred from geologic columns and Hu et al. (2010). Classification of aquifers, nos. I, II, III and IV, are taken from Hu et al. (2010b). Aquifer no. II is further subdivided into nos. IIa and IIb.

4.4 Conclusions

The depth dependence of the hydraulic conductivity K in the Toyohira River alluvial fan was determined, and the trend was represented by an empirical exponential equation. The proposed method consisted of the following steps.

(1) Relatively undisturbed and sequential gravel cores were sampled by using improved tube samplers.

(2) The packing in gravel cores was categorized qualitatively into four levels, and then the length fraction of each packing level was measured per unit depth. After these measurements, the effective grain size (in the current case this was d20) was obtained by sieving.

(3) The relation between the slug tests and core properties was established through optimization.

(4) Core properties profiles were transformed into those of the estimated hydraulic conductivity $\overline{K}$ by using the established relation.

(5) A moving average method was applied to eliminate errors. In the present case, an average interval of 5 m was used.

(6) A linear regression analysis revealed the depth dependence of K in the mid-fan, and the decay exponent was estimated.

The depth dependence of K was shown at the sampling points BW5 and BW3, and the decreasing trend had a decay exponent of A = 0.11 (m-1), which is 10- to 1000-fold that for consolidated rock in the literature. Conversely, at BW7 in the fan-toe, a vertical trend was not observed. A longitudinal cross section was further generated by using the moving average profiles. Moving average boundaries of $\overline{Y}_{MA}$ = -4 and $\overline{Y}_{MA}$ = -3 classified the gravel aquifer without migration succession. As a result, the hydrogeologic structures were understood as a high infiltrative aquifer (Holocene no. IIa), a depth-dependent and heterogeneous aquifer (Holocene no. IIb) and a stationary permeable aquifer (Pleistocene no. III).

Several problems remained unsolved in this study. The relation between the slug tests and core properties has not been sufficiently verified either theoretically or experimentally. Moreover, the obtained relation was applied only in the fan, and individual relations must be established at each site. The sampling error of the sampler has not been assessed experimentally (e.g., by comparison with bulk sampling). The scale at which permeability was observed in this study (i.e., unit depth is not necessarily

appropriate at other sites), and the employed scale must be discussed in terms of each hydrogeologic unit (Anderson 1989). Furthermore, the proposed method provided only vertical information at the sampling points. Thus, for three-dimensional groundwater modeling, horizontal information must be acquired by other methods such as outcrop analyses, geophysics surveys or deterministic depositional models. In spite of these issues, the proposed field method is expected to be useful for gaining greater quantitative insight into the depth dependence of the permeability in unconsolidated gravel deposits.

5 Stochastic Simulation of Groundwater-Flow and Heat-Transport

5.1 Introduction

Any analytical methods to solve the governing equation of groundwater are limited to particular problems in which all of the region of flow, boundary conditions, and geologic configuration are simple and regular. Numerical modeling and simulation are versatile for such complex and actual conditions in the geologic settings. Geostatistical approaches also contribute to realize spatial variability of hydraulic properties such as hydraulic conductivity K. However, the approaches need typical information about global trends in trending heterogeneity of the alluvial coarse deposits. The previous chapter indicates the depth-dependence of K in the fan-gravel deposits as the exponential function, of which exponent decay is 10- to 1000- orders of magnitude larger than that in consolidated rocks. This chapter currently realizes trending heterogeneity in the gravel deposits by incorporating the global trend and stochastic simulation, and allows assessment of its importance in groundwater modeling.

Hydraulic conductivity K in the gravel deposits is represented as a sum of a global trend component and a residual component as the groundwater table elevation is mapped in Chapter 2. The global trend is divided into those in the vertical and horizontal directions. The vertical trend has been obtained as the exponential function in the previous chapter, and then the horizontal trend is estimated as a linear regression model of coordinates in this chapter. The residual component of K offers its spatial variability as an anisotropic variogram model. 100 realizations of residuals are produced using sequential Gaussian simulation, and the multiple realizations of K are obtained by summing the residual realizations with the trend values at given points in the analysis domain. 13 study cases each of which includes 100 realizations are prepared as a comparison study, i.e., stationary or trending heterogeneity, isotropy or anisotropy of each cell, River conditions (width and vertical hydraulic conductivity), spatial variability of residual, temperature-dependence of fluids or independence, upscaling affect on simulation results.

Solute transport simulation is more susceptible to geologic heterogeneity than only flow simulation is. Hydraulic head contours usually look smooth as a result of a pressure balance, while solute concentration contours have sharp fronts reflected to actual flow of groundwater, not

Darcy's flow. However, the coupled model involves more difficulties than the uncoupled flow model: 1) scarce measurements of solute concentrations, 2) higher uncertainty in parameters of fluid and aquifer (e.g., diffusivity), and 3) numerical errors associated with spatial and temporal discretization. For example, a high-resolution model (e.g., grid spacing of 1 m) is needed to obtain detailed, accurate results to solve for the solute concentration, but excessive resolution is inappropriate for larger-scale models (e.g., a three-dimensional basin model) due to computational limitations.

The first and second problems are addressed by using heat as a groundwater tracer by exploiting the similarity between temperature transport and solute transport: compared with other solute components, heat can be measured with greater ease and accuracy, and the representative values of thermal parameters are obtained from the literature.

Also, most of thermal properties in various materials and fluids are described in literature. Especially, heat has been utilized for analyzing the movement of groundwater and its interaction with surface water in many previous studies (Lapham 1989; Stonestrom and Constanz 2003; Anderson 2005; Constanz 2008; Constanz et al. 2008; Healy 2010; Anderson 2010). Temperature of surface water flowing in the open channels is variable diurnally and seasonally, while that of groundwater beneath the streambed is more invariable. Many field studies have been performed based on the difference of temporal variation between surface water and groundwater. In particular, temporal fluctuations (envelope) of groundwater temperature are often observed in the wells below the water bodies, and 1D analytical model is utilized to estimate the properties of geologic material and the velocities of vertical groundwater flow (Taniguchi 1993; Taniguchi 1999; Vandenbohede and Lebbe 2010). However, numerical simulation of heat transport in a groundwater system has been rarely performed due to the computational expensiveness. K in a geologic material consists of fluid density and viscosity in addition to intrinsic permeability, such that K is inherently dependent on groundwater temperature. In most conventional models, the effect of temperature is ignored. Recent studies, however, suggest the importance of temperature dependence with respect to solution robustness in groundwater modeling (Doppler et al. 2007; Ma and Zheng 2010; Engeler et al. 2011). If the temperature of river water varies between about zero in winter to over 20 °C in summer, the lowest K value of sediments around the river is about

a half of the highest. More rigorous solutions in groundwater flow and solute transport are obtained by using advanced models, in which density and viscosity of fluids are variable as functions of temperature (Ma and Zheng 2010; Engeler 2011). A computer program of variable density and viscosity of fluids flowing in porous media, "SEAWAT" (Guo and Bennett 1998; Guo and Langevin 2002; Langevin et al, 2003; Thorne et al. 2006), is used in this study. The program used, SEAWAT, couples the flow program "MODFLOW" (Harbaugh et al. 2000) and the solute transport program "MT3DMS" (Zheng and Wang 1999). To simulate heat transport within the text of the SEAWAT framework, one of the MT3DMS species is used to represent temperature, and the effects of changing density and viscosity can be considered (Ma and Zheng 2010). SEAWAT also calculates groundwater flow and temperature transport with greater accuracy by using iterative processes. The third problem is also addressed by using a high-resolution grid model. Previous study (Weismann and Fogg 1999; Weismann et al. 1999) suggested that a high-resolution numerical model of groundwater flow and solute transport is needed to assess the effect of complex heterogeneity in groundwater mixing and tracer concentration. In this dissertation, a high-resolution grid model of 1 m grid-spacing is designed to satisfy the criterion.

A block-averaging model consisting of 5 m square cells is also prepared for a comparison with the high-resolution model. Upscaling of a high-resolution model to a basin-scale model is a long-standing problem in groundwater modeling (Deutsch 2002; Zhang et al. 2006; Zhang et al. 2010). This is because K depends on scale, that is, microscale (e.g., drilling cores; several meters or less), mesoscale (e.g., facies; 10 to 100 m), and macroscale (basin scale, 100 m or more). The discrepancy between the different discretized models shows a direction of upscaling in groundwater modeling of alluvial coarse deposits.

5.2   Material and Methods

5.2.1   Data preparation

Hydraulic head and groundwater temperature were measured in the observation wells located along the off-stream transect near the Horohira-Bridge (KP16.6) in the distinct losing section (KP15.5−17, Chapter 3). Four observation wells of different locations and depths were installed by the Hokkaido Regional Development Bureau between March and June 2008; deep and

shallow wells near the river channel (BW3−1 and BW3−2); a shallow well leftward from the channel (BW3−4); and a shallow well rightward from the channel (BW3−5). The observation wells, BW3−1 and BW3−2, correspond to the wells, OW15D and OW 15S in Table 1.1, respectively. The details of wells are summarized in Table 5.1, and the locations are shown in Figure 5.1.

The automatically-recorded sensors of two different types, U20-001-01 HOBO pressure transducer (an accuracy of +/−0.05 cm, HOBO Inc., USA) and U22-001 HOBO thermal sensor (an accuracy of +/−0.02°C), were inserted into the observation wells. The hourly measurements were carried out from 10 June 2011. The hourly stages of river stage in the "Kariki" and "Moiwa" gaging stations were publicly available from the website "Water Information System" of the Ministry of Land, Infrastructure and Transport, Japan. The river water temperatures in the Horohira-Bridge were also given in the same website, but the measurement regrettably stopped at 21 March 2011.

Temperature logging in the deep well BW3−1 was also performed to obtain seasonal profiles of groundwater temperature in the focused recharge zone. The temperature profiles obtained were those at 9 June 2010, 9 August 2010, and 3 December 2010. The logging was performed per 0.1 m above a depth of 30 m, and per 0.5 m below the depth using a thermistor made of platinum resistance (an accuracy of +/−0.01°C).

Table 5.1 Observation wells in the off-stream transect (Figure 5.1). X denotes horizontal distance from the center of river channel: SC denotes well screen depth: H denotes groundwater head at 10 June 2011: Z denotes depth of temperature sensor(s). BW3−3 is omitted because of the same location and depth with BW3−2

Well	X	SC	H	Z
BW03-1	-62	62 - 64	20.93	15, 30, 60
BW03-2	-66	2.5 - 7.5	28.67	5
BW03-4	-140	9.5 - 11.5	28.69	11
BW03-5	50	3 - 5	28.27	5
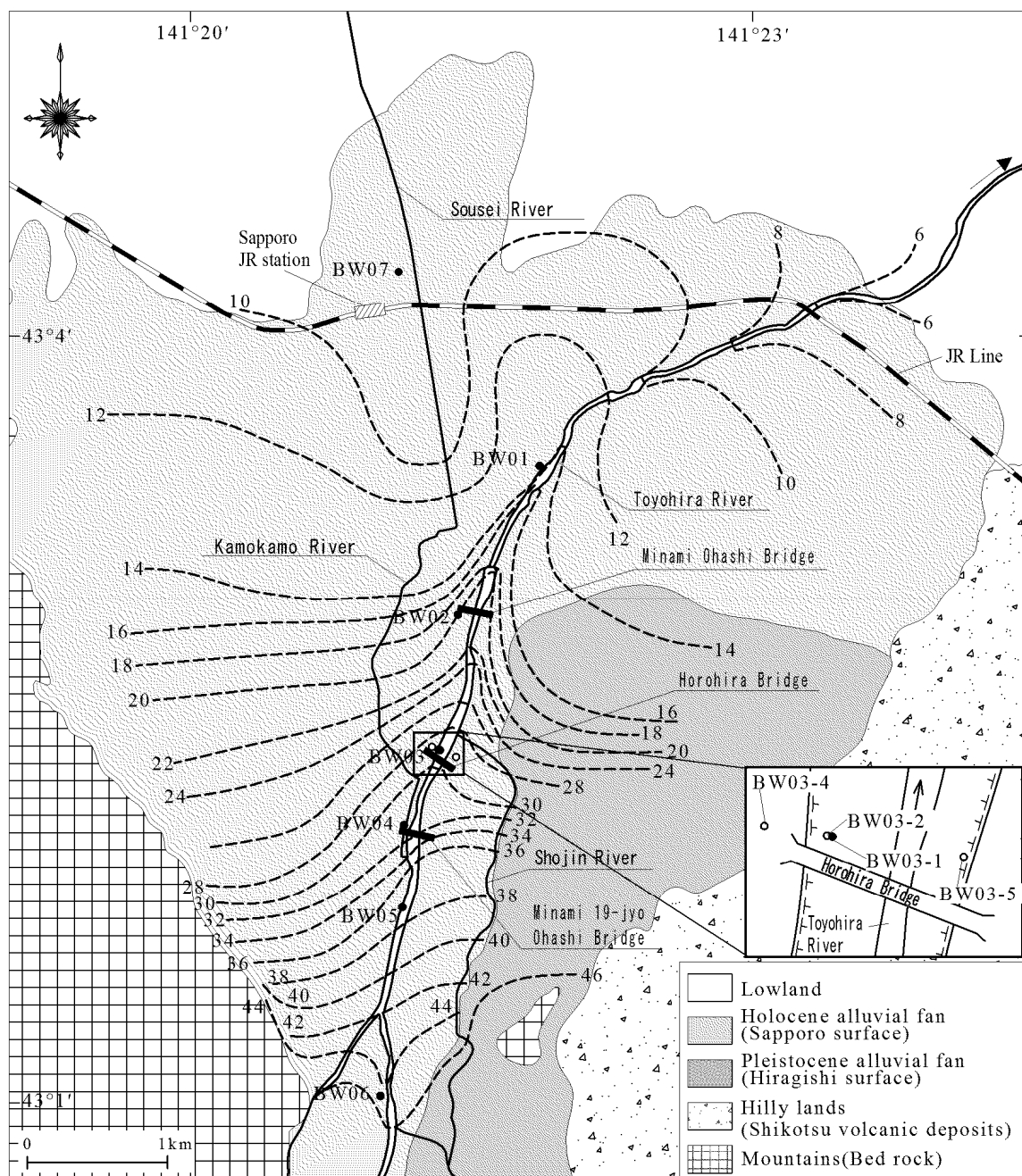
Figure 5.1 Configuration of the off-stream well transect at KP16.6 on the Toyohira River. Solid circle, open circle, and dashed line denote undisturbed sampling point, observation well, and water-table contour of each 2 m asl on June 2010, respectively
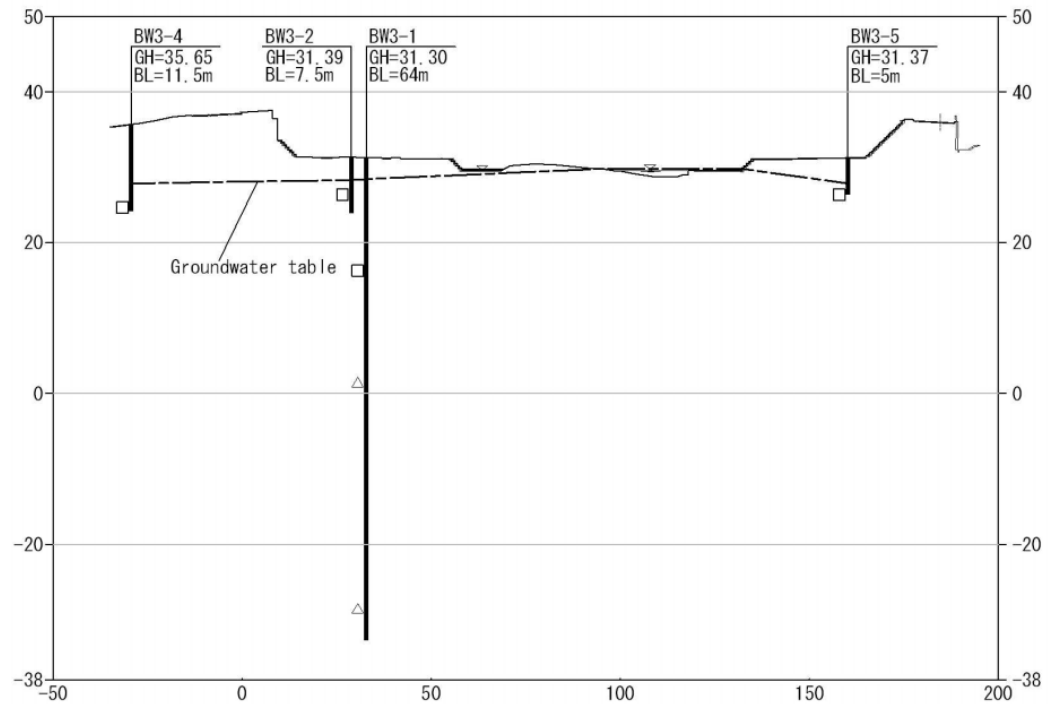
Figure 5.2 Explanatory vertical cross-section of the offset-stream transects.
Open square and triangle denote depths of pressure transducer and
the thermal sensor in the observation wells, respectively

a   b

Figure 5.3 a) pressure transducer and b) thermal sensor used for this study

5.2.2   Trend and Variogram analysis

Non stationary problem that faces geostatistical approaches in the alluvial coarse deposits was
addressed using the methodology of regression kriging (Hengel 2007), as well as the mapping of
groundwater table elevation in Chapter 2. The regression kriging process requires the assumption
that regionalized variable (hydraulic conductivity in this case) is a sum of a global component
and a residual component. The vertical trend of K was formulated as the exponential function in

Chapter 4. The logarithmic transformation is often used in groundwater study because K values are positive and relatively many small values exit compared to larger values (e.g. Freeze, 1979; Anderson 1995; Domenico and Schwartz 1998; ASCE 2008). Thus, the vertical trend of common logarithm of K is mathematically represented as:

$$\log K_0(\boldsymbol{x})_{z=0} = \log K + Az/\ln(10) \qquad \text{at } z \quad z_0 \tag{5.1}$$

$$\log K_0(\boldsymbol{x})_{z=0} = \log K + Az_0 \qquad \text{at } z > z_0 \tag{5.2}$$

where $K_0(\boldsymbol{x})_{z=0}$ is hydraulic conductivity at the ground surface (depth $z=0$) of the $\boldsymbol{x}$ position: A is the exponent decay of K with depth ($A= 0.11 \text{m}^{-1}$ in this case): z_0 is the maximum depth of the depth-dependence ($z_0= 30$ m in this case).

The horizontal trend of common logarithm of K was then estimated by formulating a linear regression model of coordinates X and Y (JGD 2000) as:

$$\log K_0(\boldsymbol{x})_{z=0} = aX + bY + c \tag{5.3}$$

K_0 at the ground surface was obtained by translating the measured $\log K$ using Equation (5.1) and (5.2). Averaged $\log K_0$ value was applied when in-situ tests were obtained at different depths in the same location. The constants a, b and c in Equation (5.3) were estimated by the straightforward linear regression method. Consequently the global trend component $M(\boldsymbol{x})$ in common logarithm of K is given as:

$$M(\boldsymbol{x}) = M_h + M_z = (aX + bY + c) + Az/\ln(10) \quad \text{at } 0 < z \quad z_0 \tag{5.4}$$

$$M(\boldsymbol{x}) = M_h + M_z = (aX + bY + c) + Az_0/\ln(10) \quad \text{at } z_0 < z \quad z_{\text{bottom}} \tag{5.5}$$

where $M(\boldsymbol{x})$ is the trend component at any points $\boldsymbol{x}$ in the domain: M_h is the horizontal trend on the ground surface,: M_z is the vertical trend: A is the exponent decay (-0.11 in this case): z_0 is the maximum depth of depth-dependence of K ($z_0 = 30$m in this study): z_{bottom} is the bottom depth of the model (e.g, $z_{\text{bottom}} = 64$ m in BW3-1).

The residual component at the measurement points $\boldsymbol{x}_i$, where i denotes the index of measurement points, were calculated as:

$$Re(\boldsymbol{x}_i) = \log K(\boldsymbol{x}_i) - M(\boldsymbol{x}_i) \tag{5.6}$$

where $Re(\boldsymbol{x}_i)$ is the residuals at the in-situ test points $\boldsymbol{x}_i$. In-situ measurements of K for this analysis were summarized in Table 5.2. Table 5.2 also shows residual $Re(\boldsymbol{x}_i)$ calculated by Eq. (5.4), (5.5), and (5.6).

5.2.3　Sequential Gaussian simulation

Sequential Gaussian simulation (SGS) is the most powerful and popular among various simulation processes for realizing geologic heterogeneity (Koltermann and Gorelick 1996; Lee et al. 2007). SGS requires an assumption that the probable density function (pdf) of target (residual in this case) attribute is Gaussian that is defined by only mean and variance. Under the assumption, the statistical hypothesis of second-ordinary stationarity is simultaneously established. In sequential Gaussian algorithms, grid nodes at which values have not yet been assigned are selected at random, and one value is drawn a random on the local conditional probability distribution. The mean and variance in local conditional probability distribution is estimated using kriging estimation (e.g., ordinary kriging) of nearby data at previously simulated grid and conditional grid. The process is repeatedly performed until simulation values at all desired nodes are determined.

This analysis produced 100 realizations of residuals, $Re(\boldsymbol{x})$, at a regular-grid of 1 m in the cross-sectional area using a free Fortran program SGSIM in GSLIB (Deutsch and Journel 1998). The theroretical variogram of $Re(\boldsymbol{x})$ required in SGS was an anisotropic spherical model as:

$$\gamma(h) \quad B \quad (C \quad B)\left[\frac{3}{2}\frac{h}{a} - \frac{1}{2}\left(\frac{h}{a}\right)^3\right] \tag{5.7}$$

where B was the nugget effect, C is the partial sill, a is the range, and h is the separation distance. The lateral- and vertical- variograms of residuals $Re(\boldsymbol{x})$ were produced from 67 in-situ measurements of K in the fan as shown in Table 5.2. In this study, the experimental and theoretical variograms of $Re(\boldsymbol{x}_i)$ were produced by using the software "Surfer" (Goldensoftware, Inc.). These parameters a, B, and C were also determined through the non-linear regression method in Surfer. The products of residuals were then translated to common logarithm of K as:

$$\log K(\boldsymbol{x}) = M(\boldsymbol{x}) + Re(\boldsymbol{x}) \tag{5.8}$$

In this analysis, the trend $M(\boldsymbol{x})$ was assumed to be function of depth z, because the trend was approximately invariable in the small analysis domain:

$$\log K(\boldsymbol{x}) = M_1(z) + Re(\boldsymbol{x}) \quad \boldsymbol{x} \quad D \tag{5.9}$$

where D is the domain of the two-dimensional model, and $M_1(z)$ is the specific trend at the observation well BW3−1. In-situ measurements of $\log K$ at BW3−1 were used as the honored data

in the conditional simulation; i.e., $\log K$ (m/s) = −2.777 (Z= 3.5 m), −2.955 (Z= 9.5 m), −4.249 (Z= 19.5 m), −2.668 (Z= 29.5 m), −5.359 (Z= 31.5 m), −3.754 (Z= 39.5 m), −5.521 (Z= 49.5 m), and −4.320 (Z= 59.5 m), respectively.

Table 5.2 In-situ measurements of hydraulic conductivity in study site

a

Well ID	Coordinates (m) Y(E-W)	X(N-S)	Test screen depth (m)		Test result (m/s) log$K$	logK_0
1	-73,307	-108,928	7.7	13.2	-3.55	-3.05
2	-72,005	-107,831	8.0	19.0	-6.37	-5.73
3	-74,506	-106,755	9.5	15.0	-3.14	-2.56
4	-72,260	-106,255	4.0	10.0	-5.70	-5.37
5	-71,196	-106,297	14.5	20.0	-4.53	-3.70
6	-74,877	-105,517	9.5	15.0	-2.62	-2.62
7	-71,939	-103,728	11.5	17.0	-2.60	-2.60
8	-70,835	-104,202	4.5	13.5	-2.65	-2.65
9	-72,351	-102,088	10.0	18.0	-3.66	-3.66
10	-73,463	-104,514	14.0	19.5	-2.97	-2.97
11	-73,637	-103,895	27.0	32.5	-3.06	-3.06
12	-72,012	-104,216	9.0	10.0	-2.82	-2.82
13	-72,603	-105,300	4.0	5.0	-4.28	-3.28
			5.0	6.0	-2.24	
			8.0	9.0	-3.33	
14	-72,734	-106,278	3.0	4.0	-2.78	-3.00
			9.0	10.0	-2.95	
			19.0	20.0	-4.25	
			29.0	30.0	-2.67	
			31.0	32.0	-5.36	
			39.0	40.0	-3.75	
			49.0	50.0	-5.52	
			59.0	60.0	-4.32	
			63.0	64.0	-5.49	
15	-72,993	-106,820	5.0	6.0	-3.39	-3.21
			8.0	9.0	-3.69	
16	-73,005	-107,418	3.0	4.0	-3.23	-3.78
			9.0	10.0	-5.00	
			19.0	20.0	-3.85	
			29.0	30.0	-3.85	
			39.0	40.0	-4.80	
			49.0	50.0	-7.26	
			59.0	60.0	-4.63	
			69.0	70.0	-5.18	
			79.5	80.0	-6.82	
			89.0	90.0	-4.81	
			99.0	100.0	-5.13	
17	-73,164	-108,782	6.0	7.0	-4.72	-3.34
			9.0	10.0	-3.18	
			18.0	19.0	-3.78	
18	-72,296	-108,936	8.0	8.5	-5.10	-4.64
			20.0	20.5	-7.42	
			21.5	22.0	-3.79	
19	-71,420	-109,347	10.0	10.5	-6.50	-4.28
			21.0	21.5	-5.23	
			28.0	28.5	-3.97	
20	-72,996	-109,079	8.0	8.5	-4.25	-4.21
			8.0	8.5		
			14.0	14.5	-5.24	
21	-72,846	-109,086	12.0	15.0	-5.72	-5.08
22	-72,019	-109,202	5.5	6.0	-2.41	-3.12
			15.0	15.5	-4.83	
23	-72,019	-109,202	13.0	13.5	-5.25	-4.32
			21.5	22.5	-5.08	
24	-71,119	-109,288	17.0	17.5	-4.74	-3.91
25	-73,262	-108,990	8.8	9.3	-4.75	-3.14
			17.5	18.0	-3.20	
			26.0	26.5	-4.01	
26	-72,150	-106,595	15.9	16.4	-5.56	-4.83
			22.0	29.8	-5.53	
			34.4	35.0	-6.06	
			53.4	61.4	-5.63	
			58.7	59.2	-7.94	
			64.0	64.5	-7.98	
			76.3	80.8	-5.84	
			86.3	87.0	-4.92	
			97.8	99.2	-6.03	
27	-69,988	-103,193	13.0	14.0	-4.90	-4.85
			18.7	19.4	-4.98	
			32.5	33.2	-4.45	
			43.0	44.5	-4.84	
			73.0	76.0	-5.07	

b

Well ID	Coordinates (m) Y(E-W)	X(N-S)	Test screen depth (m)		Test result (m/s) log$K$	logK_0
28	-74,021	-107,143	14.9	15.9	-1.36	-3.70
			35.5	36.0	-5.57	
			45.6	47.2	-4.72	
			54.7	55.2	-4.73	
			75.5	76.2	-8.26	
			78.3	78.8	-5.44	
29	-75,209	-103,982	8.9	9.4	-4.40	-4.75
			32.0	32.5	-4.19	
			51.9	52.4	-4.60	
			74.6	75.2	-5.64	
			91.0	92.6	-4.93	
30	-72,090	-110,835	11.5	12.0	-4.82	-3.95
			16.5	17.0	-4.45	
31	-73,608	-110,881	8.5	9.0	-3.35	-3.29
			16.0	17.0	-4.43	
32	-73,608	-110,881	19.5	20.0	-5.49	-4.55
33	-74,965	-110,681	5.2	5.7	-5.07	-4.81
34	-72,308	-106,653	17.4	59.5	-4.20	-2.77
35	-73,802	-105,518	34.0	72.5	-3.47	-3.47
36	-70,096	-102,729	3.5	4.5	-4.51	-5.52
			10.5	11.0	-6.52	
37	-73,557	-102,370	2.5	3.5	-5.70	
			5.0	6.0	-6.94	
38	-73,557	-102,370	2.5	6.0	-6.32	-6.32
39	-73,217	-102,634	7.0	7.5	-5.49	-5.08
			11.0	11.5	-4.67	
40	-72,738	-102,965	5.5	5.5	-5.03	-5.17
			8.5	9.0	-5.31	
41	-72,740	-103,181	5.5	5.6	-5.48	-4.84
			8.5	9.0	-4.20	
42	-72,698	-103,490	5.5	5.5	-4.42	-5.18
			8.5	9.0	-5.94	
43	-74,757	-103,530	10.0	11.0	-3.79	-3.79
44	-74,938	-103,559	10.0	11.0	-2.43	-2.43
45	-75,033	-103,897	10.0	11.0	-3.90	-3.90
46	-75,913	-105,708	7.0	7.4	-4.54	-5.29
			11.0	11.5	-7.28	
			14.5	15.4	-5.48	
			17.8	18.6	-5.88	
			24.0	25.0	-3.17	
			28.1	29.0	-5.36	
47			8.0	8.5	-3.86	-5.17
			24.0	24.5	-6.49	
			8.0	24.5	-5.17	
48	-74,052	-101,299	7.0	7.5	-5.60	-5.60
49	-73,912	-101,378	6.2	6.5	-5.02	
49	-73,912	-101,378	8.4	8.9	-5.99	
49	-73,912	-101,378	6.2	8.9	-5.50	-5.50
50	-73,840	-100,880	7.0	7.5	-5.38	-5.38
51	-67,924	-103,080	15.0	15.5	-2.71	-3.48
			19.0	19.5	-3.90	
			26.5	27.0	-3.82	
52	-71,237	-103,516	8.5	9.0	-4.49	-4.49
53	-71,261	-103,411	7.6	8.1	-5.13	-5.13
54	-72,603	-104,564	14.0	14.5	-4.09	-4.09
55	-72,642	-104,411	9.0	9.5	-4.96	-4.96
56	-72,660	-104,300	10.0	10.5	-3.06	-3.06
57	-72,683	-104,182	11.0	11.5	-5.10	-5.10
58	-72,710	-104,019	13.0	13.5	-5.01	-5.01
59	-72,732	-103,895	11.0	11.5	-5.25	-5.25
60	-72,757	-103,773	7.0	7.5	-4.65	-3.37
			15.0	15.3	-2.10	
61	-72,773	-103,646	7.0	7.5	-4.82	-4.82
62	-72,820	-103,429	9.0	9.5	-4.18	-4.18
63	-73,225	-103,339	9.5	10.0	-4.62	-4.62
64	-73,241	-103,535	9.5	10.0	-4.67	-4.67
65	-73,169	-103,599	10.5	11.0	-4.86	-4.86
66	-73,194	-103,762	10.5	11.0	-5.20	-5.20
67	-73,130	-103,900	11.0	11.5	-5.09	-5.09

5.2.4 High-resolution two-dimensional model of groundwater flow and Heat Transport coupling

A three-dimensional model is ideal for realizing actual groundwater flow and solute transport, however, its computational cost is often effortful, especially in stochastic simulation. This analysis applied a two-dimensional cross-sectional model. The simplified model provided no less accurate solutions than the three- dimensional model in the typical condition that main lateral direction of groundwater flow was only one direction. The GTE mound along the river showed that the horizontal flows of groundwater were mainly perpendicular to the channel (Chapter 2).

The two-dimensional finite-difference models are shown in Figure 5.4. A SEAWAT program was originally three-dimensional code, but this analysis utilized the program in the vertical cross-sectional model, of which width is 1 m in all cells. The two-dimensional model was thus the vertical cross sectional box, which was 190 m in length from the center of river and 64 m in height (between −35 m asl and 29 m asl). The upper boundary was constantly 29 m asl because the unsaturated zone was of insignificance in this study. The lower boundary was inclined westward as estimated by the geologic information (Figure 5.7).

Two models of different discretization were prepared for a comparison in this study; high-resolution model and block averaged model. The high-resolution model (Figure 5.4a) was mainly used in this study. The model consisted of grid cells of two different sizes: 1 m square in the lateral (x) and vertical (z) directions between the center of the river ($x = 0$ m) and the observation well BW03−1 ($x = 64$ m); 5 m in the lateral direction by 1 m in the vertical direction in the other area. The vertical sizes of cells in the bottom layer (below the elevation of −25 m) were variable adjacent to the inclination of the basement. The K values in the cells were input from the SGS realizations of 1 m regular grid, of which the hundredth place was rounded off. The K values in the cells in the lowermost layer were geometric averages over the individual values in each cell

The purpose of the fine discretization around the river was to satisfy the criterion of the Peclet number for stable solution in the conduction-convection equation. Peclet number was generally formulated in the case of heat transport as:

$$Pe = \frac{\rho_\text{w} c_\text{w} qL}{k_\text{e}} = \frac{qL}{D_\text{e}} \qquad (5.10)$$

where ρ_w is the density of fluid, c_w is the specific heat per unit volume of water, q is Darcy's specific discharge, L is a characteristic length, and k_e is the effective (bulk) thermal conductivity. Darcy's specific discharge is calculated by multiplying K by hydraulic gradient. D_e is the effective diffusivity. Considering one typical case; the hydraulic gradient was 0.1; K was 10^{-1} m/s (i.e., Darcy's flux $q=10^{-2}$ m^2/s); the grid-spacing L was 1 m; the bulk thermal diffusivity D_e 0.0083 m^2/hr, the Peclet number was 1.2, and the value was less than the criterion value from 2 (Gray and Pinder 1976) to 4 (Anderson and Woessner 1992; Zheng and Bennett, 1995). The Courant number was also utilized to determine the discretization in time, i.e., time step:

$C = vdT/L \qquad (5.11)$

where C is the Courant number, v is the average linear velocity of groundwater, which is obtained by the Darcy's velocity dividing by the effective porosity, for example 0.2 in sandy gravel. dT is the time step (1 hr in this study). If v is 10^{-2} or 10^{-3} m/s, the Courant number obtained is 0.24 or 0.024, which are less than the criterion value, 1 (Anderson and Woessner 1992).

The block-averaged model (Figure 5.4b) was used in only two study cases for a comparison with the high-resolution model. The grid size in the practical model was 5 m square throughout the domain. The K values in the cells were geometric averages of the same values of high-resolution model (i.e., SGS realizations) included in the cells.

A total calculation period for analysis was 264 days (i.e., 10 June 2010 to 28 February 2011). The initial analysis date was the start date of the well observation (9 June 2010), and the final analysis date was the end of last month when the temperature observation near the Horohira Bridge stopped (21 March 2011).
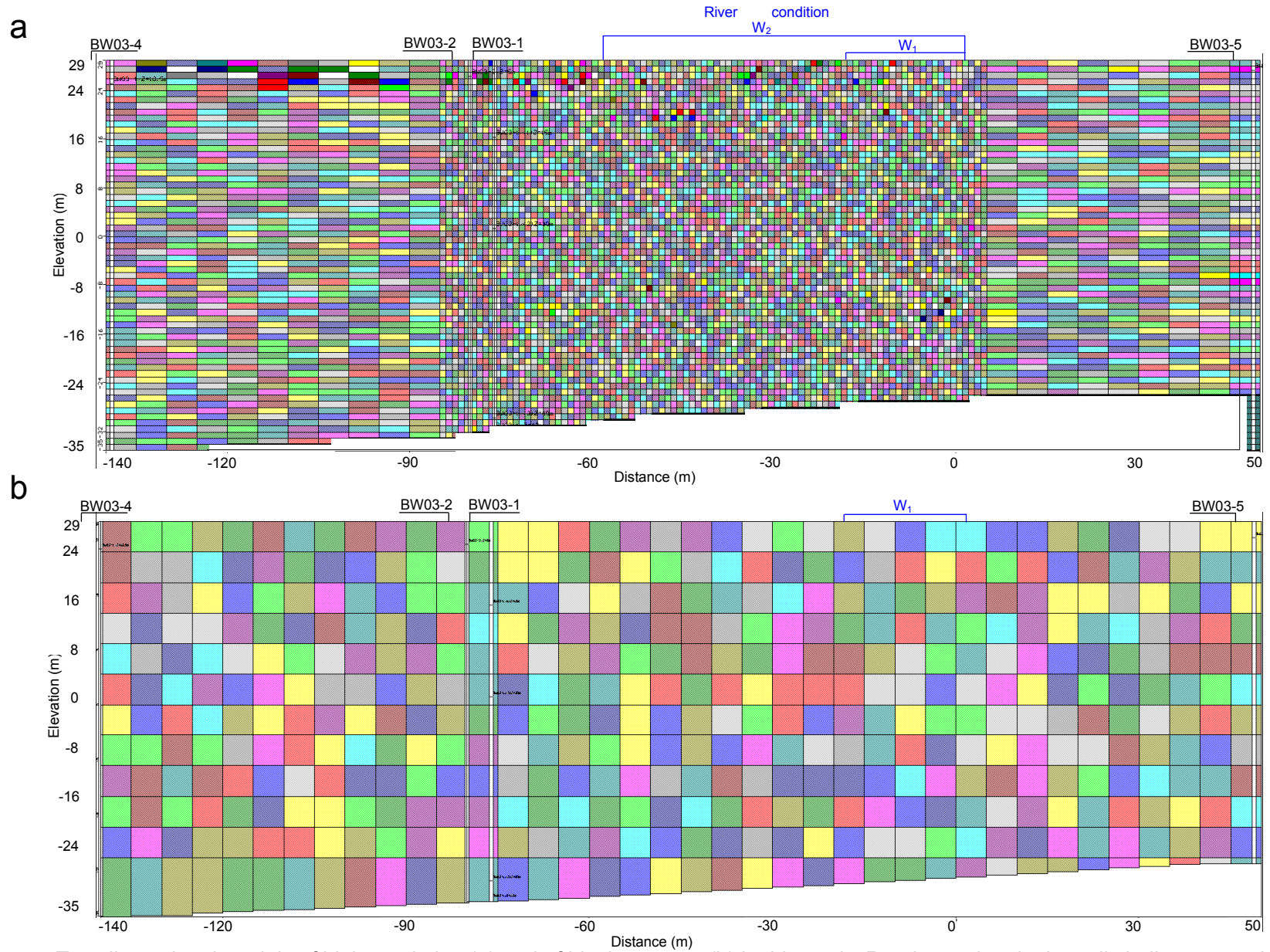
Figure 5.4 Two dimensional models of high resolution (a) and of block average (b) in this study. Random colors in the cells indicate magnitudes of *K*

5.2.5　Boundary condition and input parameters

Boundary conditions along the left and right sides of the cross-sectional model were given as the Dirichlet conditions. Under the condition, the hydraulic heads in the cells of the both sides were consistently fixed at the specified heads. The groundwater tables in the both sides were observed in BW3−4 and BW3−5. The vertical hydraulic gradient in the both sides were calculated by using the discrepancies of heads between the deep BW3−1 and the shallow BW3−2. No vertical fluxes into/from the external domain are assumed in the bottom of the model (no flux condition). River boundary condition is a typical condition in the program. The condition aims to simulate the influence of a surface water body on the groundwater flow. The MODFLOW River Package input file requires the following information for each grid cell containing a River boundary. The discharge from or to the river cells is calculated by Darcy's law as:

$$QRIV = CRIV(HRIV - h) \quad h > RBOT$$
$$QRIV = CRIV(HRIV - RBOT) \quad h \leq RBOT \qquad (5.12)$$
$$CRIV = K_r \frac{WL}{M}$$

where $QRIV$ is the rate of leakage between the river and the aquifer: $CRIV$ is the streambed conductance to account the length L, and width W of the river channel in the cell, the thickness of the bedding materials M, and their vertical hydraulic conductivity K_r: h is the heads in the $RBOT$ is the bottom of the streambed. A schematic River condition is shown in Figure 5.5. The river stages $HRIV$ were not observed around the Horohira Bridge. This study observed the river stages at the Horohira Bridge on 2010, and found the good relation with the stages at the upper "Moiwa" gaging station ($R^2 = 0.95$). Therefore, the river stages for analysis periods were estimated from the data at the upper station using the relation. The temperature of the river cells was those observed at the Horohira-Bridge. As usual, it was difficult to determine vertical conductivity K_r in the bedding materials due to its heterogeneity and widely variation in orders of magnitude (Fleckenstein et al. 2006; Doppler et al. 2007; Genereux et al. 2008; Frei et al. 2009). For its uncertainty, K_r was fixed at 100 m/d (1×10^{-3} m/s) in most study cases, and at 1×10^{-5} m/s except for Case 3. The River cells were the upper cells between $x = -10$ m to 10 m (total width 20 m) in most cases, and the cells between $x = -20$ to 20 m (40 m). The bottom of bedding material $RBOT$ was consistent at 28.5 m asl in all study cases.
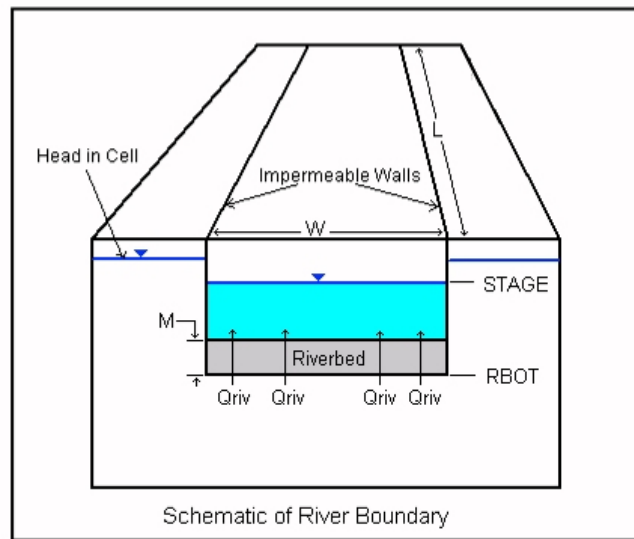
Figure 5.5 Schematic River boundary (after MODLOW manual)

Diffuse recharge flux were not given in other upper cells. The total precipitation during the analysis period was 1,152 mm, and the total volume of water in the analysis domain was 218 m^3. On the other hand, the seepage loss in the distinct losing section (1.5 km) was determined at about 1m^3/s along the (Chapter 2), and so the loss in the model (unit length) during the period was estimated at 1.5×10^{-4} m^3. The seepage loss was over 70-folds of the precipitation, such that the water volume of precipitation was enough small to be neglected in the focused recharge zone.

A list of input parameters used is summarized in Table 5.3. The storage coefficient was the results from the previous pumping results (S=0.05), and the total porosity was determined by the laboratory tests of the undistrurbed samples. The thermal properties (specific heat and thermal conductivity) were the bulk values of andesitic gravel deposits in the literature (ICE 1976; Jumikis 1977; Jessop 1990; Langevin et al. 2008). The bulk thermal diffusivity D_m was generally anisotropic, and but the detail was not unknown. In this dissertation, the vertical diffusivity D_m was one hundredth of the horizontal value.

Table 5.3 Input model and parameter values in the model

	Input parameter	Value	Units	Comments
Grid properties	Number of columns (NCOL)	190	-	12 only in case 8
	Number of rows (NROW)	1	-	Assigned
	Number of layers (NLAY)	64	-	12 only in case 8
	Δx (DELR)	1 or 5	m	Δx= 1 m only in x= 0 to 64, except for case 8
	Δy (DELC)	1	m	Assigned
	Δz (DZ)	1	m	Assigned, Δz in the bottom layer is variable at x location
Aquifer properties	Horizontal hydraulic conductivity (K_{h0})	-	m/d	variable
	Anisotropy ratio (α)	1 or 0.1 or 0.01	m/d	the ratio of vertical hydraulic conductivity to horizontal value, α=1 in case1a and 2a, α=0.01 in case1c and 2c, α=0.1 in
	Specific storage (S_s)	1.00×10^{-5}	m	
	Porosity (θ)	0.20	-	Assigned
	Longitudinal dispersivity (α_L)	10	m	Assigned
	Transverse dispersivity (α_T)	0.1 or 10	m	α_T= 10 m only in case5
	Heat capacity of the solid (C_{Psolid})	835	J/(kg)	Approximate value for calcite
	Density of the solid (ρ_s)	2,600	kg/m^3	Approximate value for calcite
	Bulk density (ρ_b)	2,080	kg/m^3	Calculated from θ and ρ_s, ρ_b= ρ_s(1- θ)
	Thermal conductivity of solid (k_{Tsolid})	2.30	W/(m)	Approximate value for Gravel and Sand
	Bulk thermal conductivity (k_{Tbulk})	1.96	W/(m)	Volumetric weighted average (20% water, 80% calcite)
	Bulk thermal diffusivity (Dm_{temp})	0.202	m^2/d	Calculated
Fluid properties	Heat capacity of the fluid (C_{Pfluid})	4,186	J/(kg)	Approximate value for water
	Thermal conductivity of water (k_{Tfluid})	0.58	W/(m)	Approximate value for water
	Distribution coefficient for temperature (K_{d_temp})	2.00×10^{-4}	m^3/kg	Calculated
	Reference density (ρ_0)	1,000	kg/m^3	Assigned
	$\delta\rho/\delta C$	0.7	-	Approximate change in density over change in salinity
	Reference concentration for density ($C_{\rho0}$)	0	kg/m^3	Assigned
	$\delta\rho/\delta T$	-0.375	kg/(m^3)	Approximate change in density over change in temperature
	Reference temperature (T_0)	25		Assigned
	Reference viscosity	0.001	kg/(m s)	Assigned
	$\delta\mu/\delta C$	1.92×10^{-6}	m^2/d	Approximate change in viscosity over change in salinity
	Reference concentration for viscosity ($C_{\mu0}$)	0	kg/m^3	Assigned
	Constants used for viscosity-temperature relation			
	A_1	2.394×10^{-5}	-	From Hughes and Sanford (2004)
	A_2	10	-	From Hughes and Sanford (2004)
	A_3	248.37	-	From Hughes and Sanford (2004)
	A_4	133.15	-	From Hughes and Sanford (2004)
	$\delta\rho/\delta l$	4.46×10^{-3}	kg/m^4	Calculated from water compressibilit

5.2.6 Study case

13 study cases were prepared for this analysis to assess the importance of modeling trending heterogeneity and of determining other uncertain parameters (Table 5.4).

Case1 was the standard case of trending heterogeneity, of which realizations of K were generated in the geostatistical methods as described in Chapter 5.2.3. Case1 consisted of three sub-cases: Case1; vertical K (K_v) is equal to horizontal K (K_h) in all cells (isotropic condition): Case1b; K_v is one tenth of K_h (anisotropic condition): Case1b; K_v is one hundredth of K_h (large anisotropic condition); the anisotropy ratio was 1 (Case1a), 0.1 (Case1b), or 0.01(Case1c).

Case2 of stationary heterogeneity was prepared for a comparison with Case1. The realizations of K in Case 2 were produced using the sane residuals $Re(\boldsymbol{x})$ with Case1, but the trend component $M(\boldsymbol{x})$ was different as:

$$\overline{M} = \frac{1}{Z_{bottom}} \int_0^{z_{bottom}} M(z)dz = \frac{1}{Z_{bottom}} \left[\int_0^{z_0} (Az/\ln(10))dz + \int_{z_0}^{z_{bottom}} (Az_0/\ln(10))dz \right] \quad (5.13)$$

$$\log K(\boldsymbol{x}) = \overline{M} + Re(\boldsymbol{x})\, \boldsymbol{x} \quad \mathrm{D} \quad\quad\quad (5.14)$$

Considering $Z_{bottom}= 64$m, $A= -0.11(\mathrm{m}^{-1})$, and $z_0= 30$m, the average trend $\overline{M}$ was -1.10 m/s. The three sub-cases (Case2a, b, and c) were also prepared as well as Case1.

Case3−7 was performed to assess sensitivities of other uncertain factors as: vertical hydraulic conductivity in the riverbed material, river width of seepage boundary, anisotropy of thermal diffusivity, spatial variability of the residual component, and temperature-dependence of fluids. The vertical hydraulic conductivity of the riverbed material, K_r, in Case3 was one-hundredth of the standard value in Case1. The river width in Case4 was twice of the standard value in Case1. The bulk thermal diffusivity in Case5 was isotropic. The lateral- and vertical- variogram ranges of the residual in case6 were one tenth of the standard values in Case1. The density and viscosity of fluid in Case7 were independent of temperature. Case8 also utilized block averaged model of 5 m square cells as shown in Figure 5.4b. Optimal realizations of K in each study case were extracted among the 100 realizations through a comparison with calculation and measurements results of groundwater temperature. Average root mean square error, $\overline{RMSE}$, and average root means square normalized error, $\overline{RMSN}$, were used for error judgment. The individual $RMSE_j$ and $RMSN_j$ in the observation points (index j) were calculated using calculated and observed temperatures, $T^*(t_i)$ and $T(t_i)$ as:

$$\overline{RMSE} = \frac{1}{6}\sum_1^6 RMSE_j \quad\quad\quad (5.15)$$

$$\overline{RMSN} = \frac{1}{6}\sum_1^6 RMSN_j \quad\quad\quad (5.16)$$

$$RMSE_j \quad \sqrt{\frac{1}{n}\sum_{i=1}^n \left(T_j(t_i) - T_j^*(t_i)\right)^2} \quad (5.17)$$

$$RMSN_j = \frac{RMSE}{(\max T_j - \min T_j)} \qquad (5.18)$$

n is the number of daily mean data (264 in this case), and j is the index of observation wells; BW3−1 at a depth of 15 m (j=1); BW3−1 at a depth of 30 m (j=2); BW3−1 at a depth of 60 m (j=3); BW3−2(j=4); BW3−4 (j=5); BW3−5 (j=6). The max T_j and min T_j are the maximum and minimum of T_j, respectively. The "good" realizations of K in each study case were extracted when $\overline{RMSE}$ and $\overline{RMSN}$ were less than 2 and 1, respectively.

Table 5.4 Description of the simulation cases

	Case1			Case2			Case3	Case4	Case5	Case6	Case7	Case8	
	a	b	c	a	b	c						a	b
Trending heterogeneity [a]	×	×	×				×	×	×	×	×		
Anisotropy [b]		×	××		×	××	×	×	×	×	×		×
K_r in riverbed [c]							×						
River width [d]								×					
Thermal diffusivity [e]									×				
Variogram [f]										×			
Temp. dependence [g]											×		
Block averaged [h]												×	×

[a]× trending heterogeneity, [b]× anisotropy ratio is 0.1 and ×× anisotropy ratio is 0.01, [c]× vertical hydraulic conductivity of bedding material is one tenth of standard value (10^{-5} m/s at 25 °C), [d]× river width is twice of standard value (20 m) , [e]× thermal diffusivity is isotropic, [f]× lateral- and vertical- variogram range of residuals are one tenth of standard value, [g]× density and viscosity of fluid are independent of temperature, [h]× blocked averaged model of 5 m square cells is used instead of high-resolution model

5.3 Results and discussion

5.3.1 Observation results

(1) Water-level and temperature variations

Figure 5.6 shows hourly variations of water- level and temperature in the river and the observation wells located along the off-stream transect. The groundwater tables in the shallow wells (BW3−2, BW3−4 and BW3−5) were consistently lower than the river stages, and the discrepancies between groundwater table and river stage were large as the distance from the river increased. The inclination of groundwater table, in other words, horizontal hydraulic gradients, was about 0.01. The groundwater table varied with the river stage, but the peaks were larger and the variations in groundwater table were smoother.

Groundwater levels measured in the deep well (BW3−1) were consistently about 21 m asl, about 7 m lower than the groundwater table. The discrepancy indicated the downward flux of groundwater due to seepage loss. The vertical hydraulic gradient was about 0.1, that was about 10-folds of the horizontal gradient in the water table. The water levels in the deep well also showed diurnal and seasonal fluctuations. The diurnal fluctuations were probably attributable to pumping rates in adjacent unknown wells. The seasonal fluctuation showed that the groundwater level in the deep part was lower on summer and winter. This was probably because the pumping rates increased for cooling in the city on summer and diffuse recharge were reduced due to snow covering. The seasonal trends were also seen in other observation wells (Fukami 2010).

The temperature of river water varied diurnally and seasonally, reaching a low of 0.5 °C and a high of 20.5 °C. The groundwater temperature was dependent on the location and depth of the observation points. The variation of temperature in BW3−5 was almost close to that in the river, indicating preferential flows from the river. The variations in BW3−2 and BW3−4 were much smoother, and the highest peak delayed in the late autumn or early winter. The decay indicated the conduction and convection process of heat mainly in the horizontal direction. On the other hand, the variations in BW3−1 at different depths showed that the groundwater temperatures became stable as the observation depth was close to the isothermal layer of around 10 °C in the city (Uchida et al. 2001).
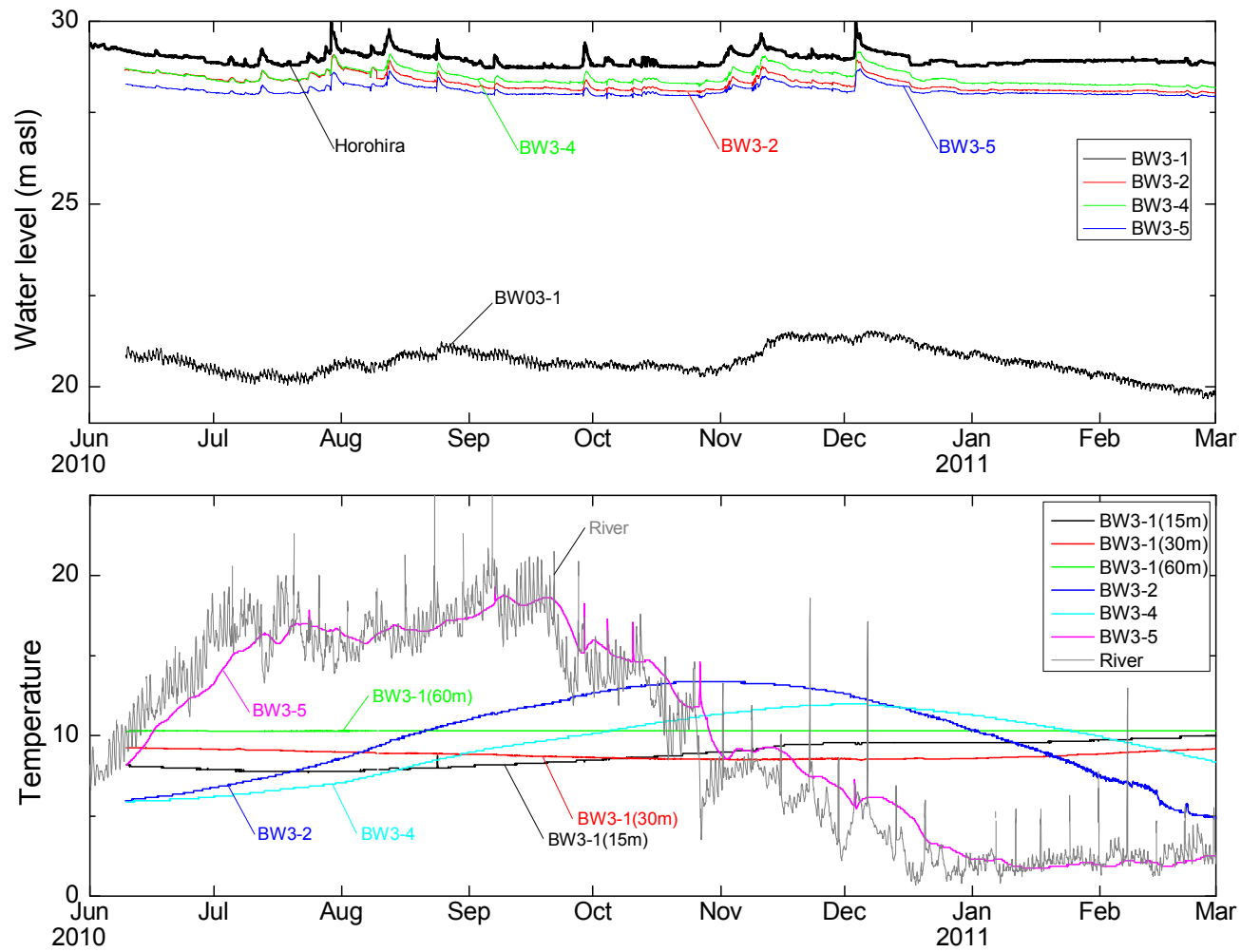
Figure 5.6 Hourly water-level and temperature variations in the river and observation wells during the analysis periods; 10 June 2010 – 28 February 2011 (264 days)
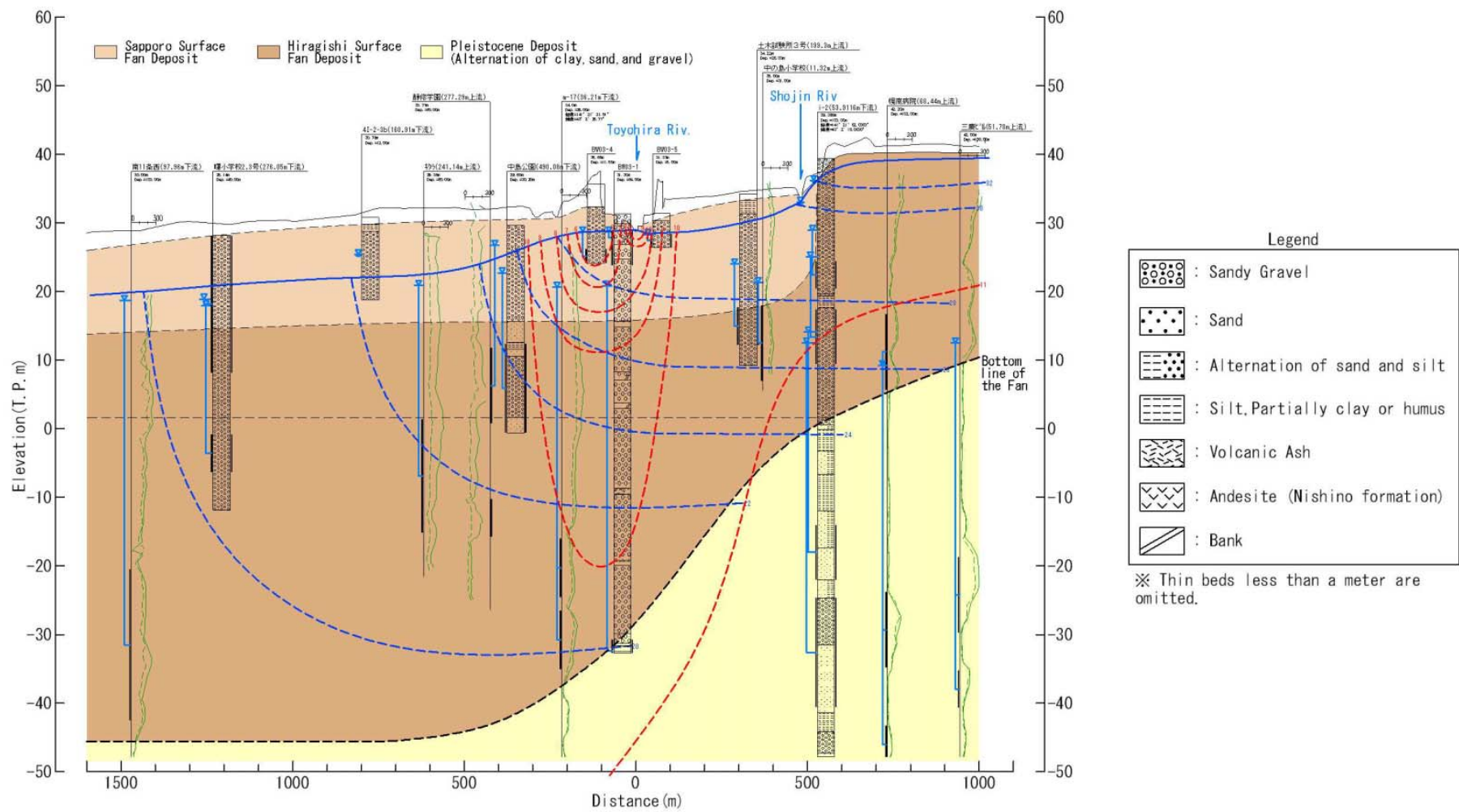
Figure 5.7 Contour maps of water level and temperature in the vertical cross section

(2) Vertical profiles of water temperature

   The vertical profiles of groundwater temperature observed in the deep well BW3−1 are shown in Figure 5.8. The seasonal envelope between 6 °C and 12 °C was recognized in the shallow zone above the depth of about 40 m, indicating the vertical heat transport system in the focused recharge zone. The groundwater temperatures in the profiles were converged to about 9.5 °C at the depth of 40m, and linearly increased with depth. The linear slope was correspondent to the geothermal gradient in the zone. Typically the groundwater temperature in the shallower zone (less than 30m) was highest on winter, not on summer. The delay was probably due to the resulting process of conduction and convection of heat under the trending heterogeneity in the gravel deposits.
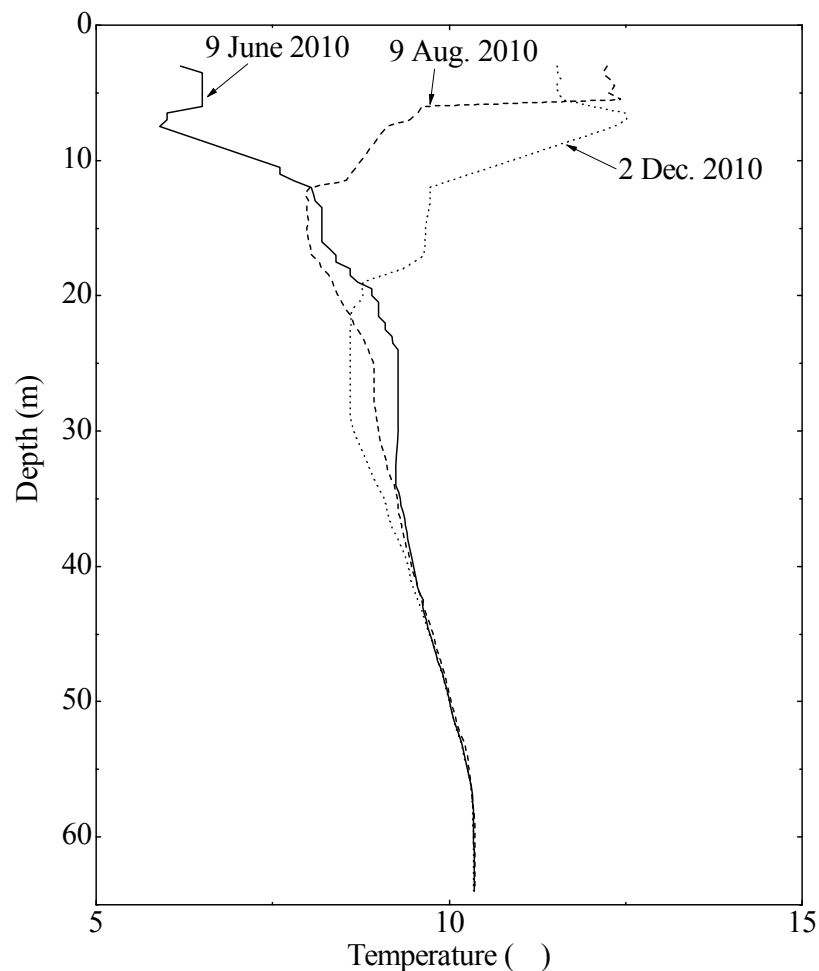
Figure 5.8 Seasonal temperature profiles in the deep well (BW3−1)

5.3.2 Horizontal trend analysis

Figure 5.9 shows relations between hydraulic conductivity at the groundsurface, $\log K_0$, and coordinates in JGD2000, X (NS direction) or Y (EW direction) coordinates. There was no obvious auto-correlation in the EW direction as shown in Figure 5.9a. The coefficient b in Eq. (5.3) was approximately zero to be neglected throughout the fan. This also indicated the validity of simplification in this analysis; the lateral trend in the two-dimensional model was assumed to be constant because the vertical cross-sectional model was amost parallel to the Y (EW) direction.

Figure 5.9b showed a certain correlation between the hydraulic conductivity and the coordinate. The coordinate was correspondent to the downward direction of the terrain, but the correlation was not uniform, and the highest values of K were obtained at the middle of the fan. Figure 5.9b probably indicated the humped trends of K as in other fans. The term "humped trend" means that the maximum K appears not in the fan-apex, but in the middle fan due to the sorting effect in depositional process. The typical hydrogeologic structure was frequently seen in alluvial fans around the world (Neton et al. 1994). The coefficient a and c of trend component $M_h(x)$ in Eq. (5.3) were determined by the linear regression analysis; a= 0.00303 (1/s) and c= 29.2 (m/s) at X< −106,000 m or a= −0.00583 1/s and c= −64.7 m/s at X> −106,000 m. In this analysis, the lateral trend in the two-dimensional model, $M_l(z)$, was constant at −3.07, that was at BW3−1 (X= −106,278 m). The expectation of K at the groundsurface was stationary at $10^{-3.07}$ m/s in the two-dimensional model, indicating extremely high permeability in the fan-deposits near the surface.
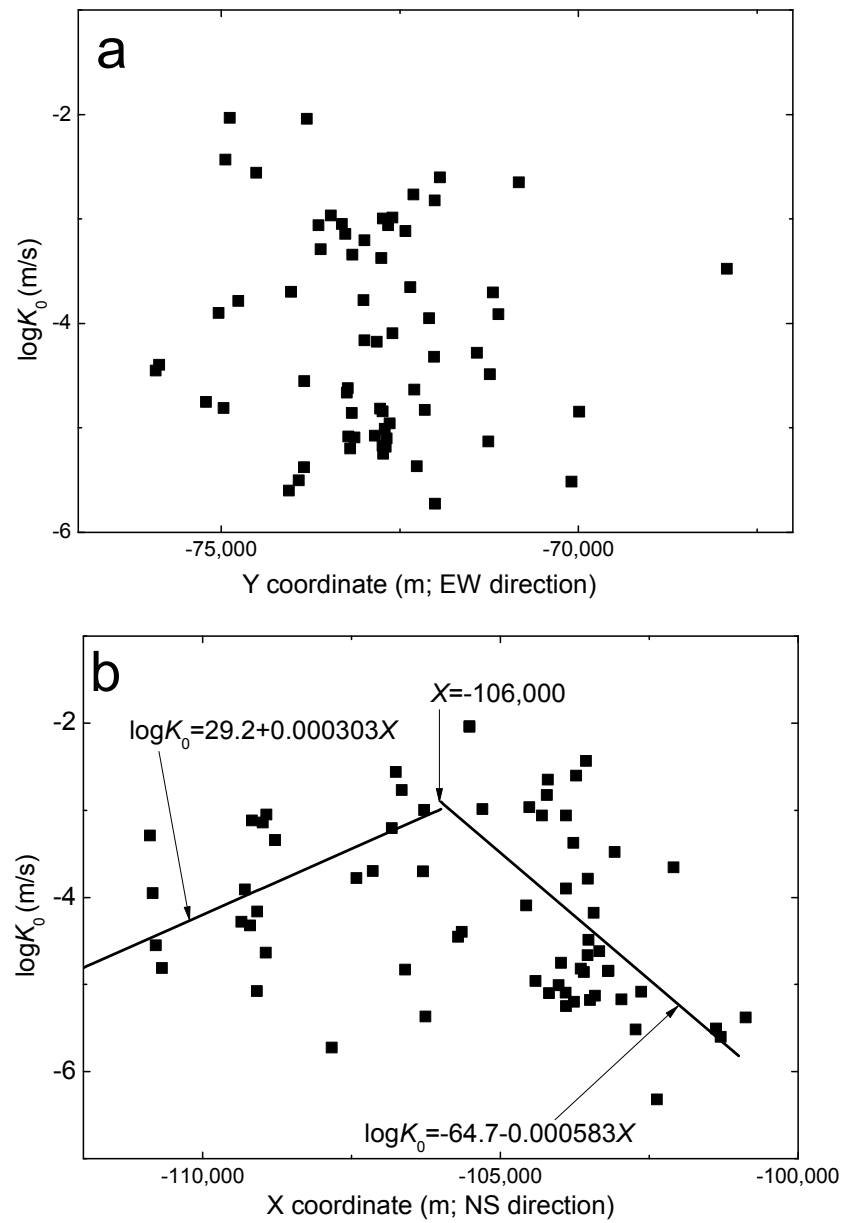
Figure 5.9 Relation between hydraulic conductivity at the ground surface, $\log K_0$, and coordinates in JGD2000; a) Y (EW) and b) X(NS) coordinates

In figure b, the labels shown are:

X=-106,000

$\log K_0$=29.2+0.000303X

$\log K_0$=-64.7-0.000583X

5.3.3   Variogram analysis

The experimental and theoretical variograms of residual are shown in Figure 5.10. The model parameters in the lateral model (a) were a= 1000 m, B= 1.15 m/s, and C= 0.5 m/s, while the parameters in the vertical model (b) were a= 20 m, B= 0.92 m/s, and C=0.5 m/s. The range a in the horizontal direction was 50-folds of that in the vertical direction. The large anisotropy was found in alluvial coarse deposits such as braided river system as shown in Deutsch (2007).
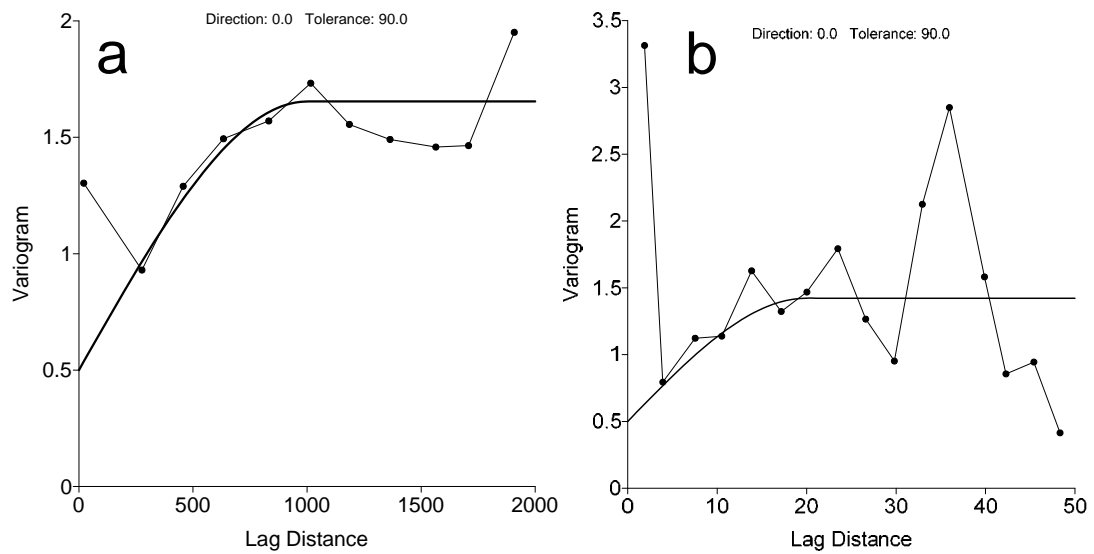
Figure 5.10 Variograms of spatial residuals of hydraulic conductivity a) in the horizontal direction and b) in the vertical direction

5.3.4 Stochastic simulation of groundwater-flow and heat-transport

The calculated values of water level and temperature in the 100 realizations of $\log K$ in 13 study cases are given in Appendix II. The optimal results are indicated in color when the results satisfy the criterions of both $\overline{RMSE}$ and $\overline{RMSN}$. Appendix III shows examples of optimal realizations in each study case at the last period (t_i= 264 day). All the results in Appendix III commonly showed that infiltrated water from the river cell widely moved toward the both sides of boundary. The directions of groundwater flows were variable, depending on the large heterogeneity, while the magnitudes were accumulated in the shallow zone because of the trending heterogeneity. As a result, the groundwater temperature contour includes sharp fronts reflected to the preferential flows, especially in the fine-spacing area, i.e., x= −63 to 0 m in distance. The block averaged models in Case8 indicates more smooth and uniform contours in hydraulic head and groundwater temperature.

(1) Comparison between trending heterogeneity, stationary heterogeneity and block averaged heterogeneity

Figure 5.11 shows simulation results of two realizations of $\log K$ (no.11 and no.33) in Case1 (trending heterogeneity), Case2 (stationary heterogeneity), and Case8 (block averaged heterogeneity). Here, no.11a (upper-left) and no.33b (lower-right) were the optimum realizations in Case1a (isotropy) and Case2 (anisotropy), respectively. The high-resolution images in Case1 and Case2 indicated large heterogeneity, reaching low values ($\log K$< −9) near the bottom and high values ($\log K$> −1) near the ground surface. The horizontal zones of low values between 15 m and 20 m in depth were less than the honored data of low $\log K$ ($\log K$= −4.249 m/s at a depth of 19.5 m and a distance of 62 m). The optimal realization was just one case in the stochastic simulation that required various assumptions and limitations, however, the realizations could provide the optimum calculations of groundwater temperature, probably due to preferential flow zone above the low-permeable thin layers

The realizations in the upper and the middle images were well-agreed below a depth of 30m, which was the maximum depth of trending heterogeneity, i.e., z_0. In the shallower depth, on the other hand, the middle realizations had a little narrower range of $\log K$. This is because of no trending stationary in Case2. The low value of logK in the shallow zone probably prevented to

obtain the optimum calculation of groundwater temperature.

The lower block averaged images indicated the same spatial trend of log$K$ with the upper and middle high-resolution images, but the averaging process translated the high-resolution image to the narrower and the smoother images. The block averaged images looked almost stationary in the domain.
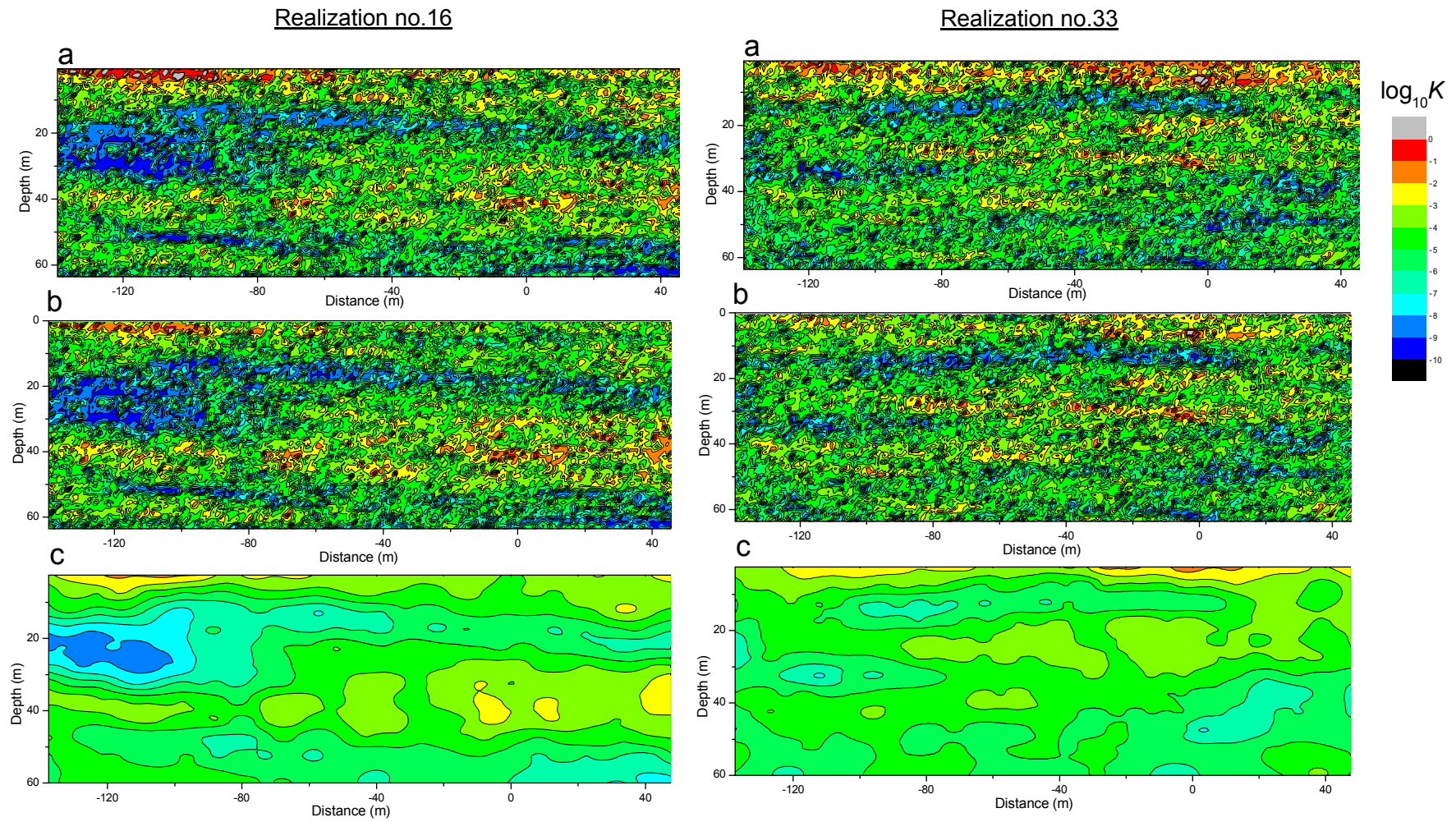
Figure 5.11 Examples of two-dimensional stochastic realizations of log*K*: the upper images (a) indicate trending heterogeneity in Case1; the middles (b) indicate stationary heterogeneity in Case2, and the lowers (c) indicate block averaged heterogeneity in Case8. The left and right images are the optimal realizations, no.11 in Case1a and no.33 in Case1b, respectively, where no. denotes individual number among 100 realizations

(2) Comparison with total number of optimal realizations of *K*

Table 5.5 summarizes total numbers of optimum realizations in each study case. The middle lines in Table 5.5 indicate the individual numbers of optimum realizations, and the lowest line indicates the total counts. The results of trending heterogeneity in Case1 obtained a few optimal realizations among the 100 realizations. The total numbers were different among the cases and the sub-cases. It is noted that the stationary heterogeneous realizations involved no optimal realizations, whether there is isotropy or anisotropy (Case2a, 2b, and 2c). The failure in stationary heterogeneity, although only 100 realizations in this study, indicated that modeling of trending heterogeneity was indispensable for a quantitative description of the groundwater flow system in the focused recharge zone.

Compared with whether there is trending or stationary heterogeneity, other uncertain factors in Case3−7 (river conditions, thermal diffusivity, the range of variograms of residuals, and temperature-dependent effects) less significantly affect the optimal solutions. On the other hand, the number of optimal realizations is larger than that of a high-resolution model, indicating the applicability of block averaging to a larger basin model.

Table 5.5 Individual (middle lines) and total numbers (bottom line) of optimum realizations in each study case (upper line)

1a	1b	1c	2a	2b	2c	3	4	5	6	7	8a	8b
16	4	13	-	-	-	4	63	4	-	7	1	1
	47							7		63	8	7
											70	8
											78	9
											92	17
												18
												25
												30
												33
												42
												44
												63
												65
												78
1	2	1	0	0	0	1	1	2	0	0	5	14

(3) Comparison with isotropy, anisotropy, and large anisotropy conditions

Figure 5.12 shows plots of calculation versus measurement in hydraulic head, river leakage, and groundwater temperature obtained by using the optimal realizations; no.16 in Case1a (isotropy condition), no.4 in Case1b (anisotropy condition), and no.13 in Case1c (large anisotropy condition). The agreements in hydraulic head, river leakage, and groundwater temperature are discussed as followings:

1) Hydraulic head

The well-agreements between calculations and measurements in the deep well (BW3−1) and the shallow well (BW3−2) were seen in the cases of trending heterogeneity, Case1a and Case1c (*RMSE*< 1m). The results in the case of Case1b are inferior to the agreement, and the *RMSE* values were about 2 m.

2) River leakage

Assuming that the river leakage was uniform in space and constant during the analysis period, the leakage value in unit length (model width) was estimated at $57.6 m^3/d$. The calculation in Case1a was highest and closest to the estimate. The calculation in Case1b and Case1c were about one-tenth of the estimate, and so these values might be too small. However, the uniform and constant leakage was based on the excessive assumption, and the validity of calculated leakage was determined in this study.

3) Groundwater temperature

The calculations in three different depths at BW3−1 were as much stable as the observations in all of the cases. Also in BW3−5, the calculations were sufficiently equal to the measurements, although the daily fluctuations measured were smooth in the calculations. In BW3−2, the calculations in Case1a and Case1b were matched with the measurements, but the calculation in Case1c was largely different from the measurement. Especially in BW3−4, only the calculation in Case1a obtained the sufficient agreement with the measurement (*RMSE*= 0.3 °C).

4) Summary

Compared with the optimal realizations in the isotropy, anisotropy, and large anisotropy conditions, the isotropic realization in Case1a was most reasonable in terms with agreement with measurements of both hydraulic head and groundwater temperature. The river leakage in the

isotropic condition was several-folds smaller than the estimate in Case1a. However, the discrepancy was of less importance because the seepage loss was determined only through the distinct losing section, and the detailed value in the local area was not unknown in this study. Figure 5.11 shows the low-permeability layer was interbedded between 15 and 20 m in depth the high-permeable gravel deposits. Information about the interbedding fine layer, instead of anisotropy in cells, was probably required for obtaining plausible realizations. The example results calculated in the isotropic condition were shown in Appendix II. The groundwater head contours were densely distributed in the thin layer, and the sharp fronts of water temperature accumulated in the shallow zone above about 15 m in depth. On the other hand, both of anisotropic cases also indicated insufficient agreements with the measurements, especially of the water temperature in the shallow wells. Consequently, information about both of trending heterogeneity and hydrogeological structure is required to obtain the plausible descriptions of complex groundwater flow and heat transport system.
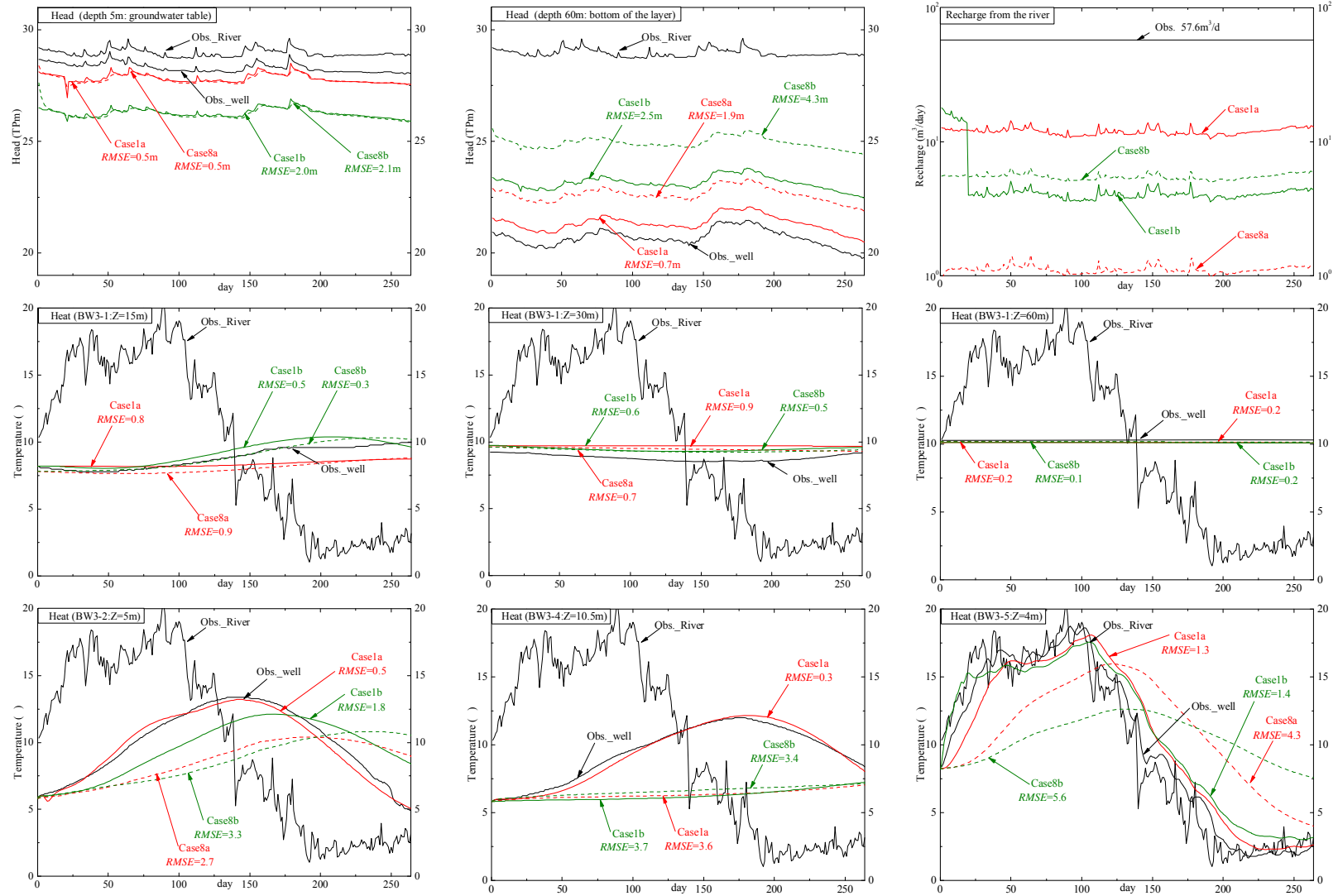
Figure 5.12 Calculations vs measurements in hydraulic head, river leakage, and groundwater temperature, in the optimum realizations no.16 in Case1a, no.4 in Case1b, and no.13 in Case1c

(4) Comparison with high-resolution and block averaged model

Figure 5.13 shows plots of calculation obtained by using the same realizations of K in the high-resolution model and the block averaged model. The isotropy results in Case1a and Case8a are compared using the optimal realization of K, no.11. The anisotropy results in Case1b and Case8b are compared using the optimal realization of K, no.4.

The groundwater level and temperature in most observation wells were largely different between the high resolution model and the block average model. The block averaged model led to less reasonable results than the high-resolution model. In particular, the groundwater temperature in BW3−4, which were most far from the river channel, was almost stable in the block averaged model. This was because the results were optimal in the high resolution model, but in the block averaged model. The geometric average and isotropy assumption in the block averaged model lost most of information about heterogeneity realized in the high resolution model. The upscaling procedure in this study might be excessively simplified in the focused recharge zone, and ideal procedure of upscaling should be conducted using a tensor of K, that is different in each cell (Zhang et al. 2006). If this can be done, more plausible realization can be expected. On the other hand, Table 5.5 shows that the numbers of optimal realizations were larger than those obtained in the high-resolution model. The superiority of the block-averaged model indicated that conventional geometric averaging was similarly effective in practice use.
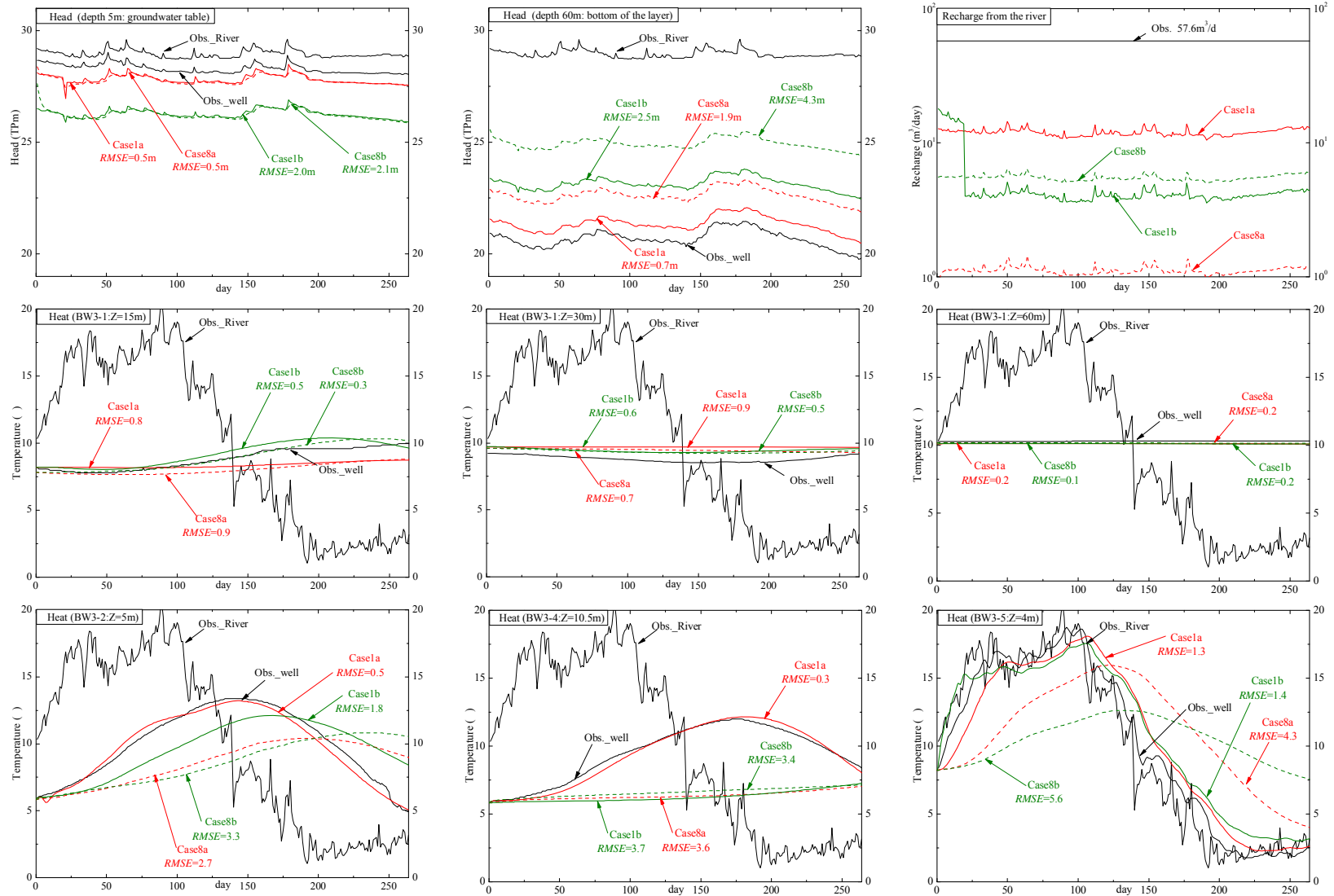
Figure 5.13 Calculations vs measurements between original and block averaged models using the same realizations of hydraulic conductivity; no.16 in Case1a and no.4 in Case1b

5.4   Conclusions and Future Work

This chapter performed stochastic simulation through an incorporation of the exponential model of K and the geostatistical method to assess the requirements for modeling trending heterogeneity in order to describe the complexity of groundwater flows and solute transport in the focused recharge zone. To obtain more rigorous solutions, the computer program "SEAWAT" was used, in which fluid properties (density and viscosity) were dependent on groundwater temperature. For the data preparation, the water levels and the temperatures were measured with piezometers along the off-stream transect in the middle of the distinct losing section. the downward vertical flows of groundwater and the conduction-convection transport of heat were typically observed in the focused recharge zone.

The horizontal trend in hydraulic conductivity was analyzed by using previously conducted in situ measurements, and variogram analysis of residuals was also performed. The trend analysis of log$K$ revealed the humped trend in the longitudinal (NS) direction as other alluvial fans indicated, while no trend in the orthogonal (EW) direction was obtained. The spatial variability in residual components of log$K$ indicated the large difference of ranges in the variogram models between in the horizontal direction and in the vertical direction. This study only used the exponent model to realize trending heterogeneity in the two-dimensional model in the assumption that the lateral trend was constant.

Sequential Gaussian simulation then produced 100 realizations of hydraulic conductivity by using the vertical trend and the variograms of residuals. This study adopted 13 study cases, respectively, of different conditions such as trending or stationary heterogeneity, isotropy or anisotropy of hydraulic conductivity, river conditions (hydraulic conductivity and width), range of the variogram, anisotropy of thermal dispersivity, temperature dependence or independence of fluid properties, and model discretization. The optimum realizations were extracted from the 100 realizations in each study case using the criterion of *RMSE* and *RMSN* values.

The high-resolution model effectively realized various complex distributions of groundwater flow vectors and temperature contours. The calculated heads and temperatures based on the plausible realization satisfactorily corresponded to the measurements in the observation wells at

different locations and depths. Several optimal realizations of K were obtained in the nonstationary condition, but no optimal realization was obtained in the stationary condition, even though the same 100 realizations of residuals were used in both conditions. This tendency was the same whether the model included isotropy, anisotropy, or large anisotropy. These simulation results indicate that modeling of trending heterogeneity was indispensable to obtain plausible descriptions of groundwater flows and solute transport in the focused recharge zone. In particular, in a comparison between isotropic, anisotropic, and highly anisotropic conditions under an assumption of nonstationary, the most plausible realizations of K were obtained in the isotropic condition. Compared with other case studies of different conditions in the high-resolution model, the numbers of optimal realizations obtained were nearly the same as in cases under the nonstationary condition. This indicated that, compared with other factors, heterogeneity, that is whether there was trending heterogeneity or stationary heterogeneity, was more significant for modeling the groundwater flow system in the focused recharge zone.

The calculation of hydraulic head, river leakage, and groundwater temperature was compared in the optimal realizations of isotropy, anisotropy, and large anisotropy cases. Only the isotropy condition yielded the reasonable calculations of hydraulic head and groundwater temperature, and other anisotropic conditions resulted in the unacceptable discrepancy of temperature in the far- and shallow- well. The most plausible realization in isotropy condition suggested the low-permeable thin layer might be interebdded in the depth of 15−20m. The detailed information about hydro-facies is also important as well as trending heterogeneity in the gravel deposits.

The block-averaged models consequently provided smoother and more uniform descriptions of the groundwater flow and heat-transport system, indicating no preferential flows. However, the numbers of optimal realizations obtained were larger than those obtained in the high-resolution model. The superiority of the block-averaged model indicated that conventional geometric averaging was similarly effective for upscaling the model of the heterogeneous alluvial gravel deposits. Upscaling such as block averaging was needed to construct more regional model in the limitation of computational power. The upscaling process has commonly faced the groundwater studies, and the last chapter discussed the future direction to address the problem. The anisotropic condition in the block cells was a typical important factor, but the anisotropy ratio was constant

in this analysis. In fact, the ratio was different from cell to cell as a result of heterogeneity. In other words, the upscaling procedure must be understood as a tensor. If this can be done, more plausible realization can be expected, and this will be pursued in future work.

This chapter applied two-dimensional vertical cross sectional model in the assumption that the major horizontal components of groundwater flow vector were perpendicular to the river channel. In more rigorous term, orthogonal flows from the upstream to the downstream affects on the groundwater flow and transport system. Alternative three-dimensional groundwater flow model is needed to discuss the importance of trending heterogeneity in more detail.

6 Conclusions and future research directions

6.1 Conclusions

Water is indispensable to living and its value is increasing, especially in arid and semi-arid regions. Among various geologic settings, alluvial coarse deposits form abundant reservoirs of groundwater around the world. However, the capacity is exhaustible because of area limitations. Furthermore, such reservoirs are susceptible to contamination and dewatering due to their high permeability. Alluvial coarse deposits consist of poorly sorted gravel deposits, and are bounded by steep land slope surfaces. Hence, the geologic heterogeneity is typically large and trending. Geostatistical approaches have been widely used as a powerful method for addressing uncertainty in the heterogeneity of various geologic settings. However, trending heterogeneity cannot be addressed by conventional geostatistical methods, which require an assumption of stationarity. Consequently, geostatistical reservoir modeling of alluvial coarse deposits has proved especially difficulty. A standard approach to nonstationary problems is to separate the attribute into a global trend component and a residual component, but the global trend has rarely been determined because of insufficient measurements of the attribute, especially in the deep parts of the reservoir.

The study area covered in this dissertation was a focused recharge zone beneath and around a losing river. In the focused recharge zone, water that infiltrated from the losing river had primarily vertical flow components, and the flow vectors varied in space and time, depending on the trending heterogeneity. If the zone has trending heterogeneity, for example, a coarsening-upward trend, the groundwater flows will accumulate in the shallower zone, and then groundwater temperature will be indicated by typical contours reflected directly from the trending heterogeneity. The representative zone was just a portion of the regional system of groundwater flows, but detailed research in the zone enabled the importance of trending heterogeneity in the groundwater flow system to be assessed by restricting various uncertain factors in groundwater models to only trending heterogeneity of the deposits.

Targeting the Toyohira River alluvial fan (Sapporo, Hokkaido, Japan), this dissertation presented well data analysis, flow measurements, permeability modeling, and stochastic simulations. First, vertical hydraulic gradient was mapped based on groundwater table elevation throughout the fan. Uncertainty of water-level data in individual wells and boreholes was addressed in this study by the

following means: data filtering based on long-term water-level variations, kriging interpolation assuming nonstationary conditions, and cross-validation.

A synoptic survey of the river flow was also performed to determine the magnitude and distribution of seepage loss from the Toyohira River. Synoptic surveys must usually contend with uncertainty in discharge measurements, especially in gravel-bed rivers with unsteady turbulent flow and rough boundaries. In this work, the uncertainty was reduced as much as possible by combining a handheld acoustic flow velocimeter and detailed arrangements of verticals for measurements of flow and depth. As a result of the improvements, the relative uncertainty of discharge measurements was only 2−4%.

This dissertation also has established the permeability model of the alluvial fan gravel deposits through the use of relatively undisturbed cores collected from the fan. The packing of fine sediments between gravel grains was qualitatively indicated by a newly defined index, the matrix packing level. The permeability model admitted a well-defined relation between slug test results and core properties at a given depth. Then, the profiles of core properties at three locations that differed in topography—the apex (BW5), the mid-fan (BW3), and the distal part (BW7)—were translated into profiles of hydraulic conductivity. The moving average method was also performed to reduce the uncertainty in the estimated values. Consequently, a common depth dependence of the permeability in the apex and the mid-fan was formulated as an exponential model of hydraulic conductivity.

Finally, stochastic simulation was performed to assess the requirements for modeling trending heterogeneity in order to describe the complexity of groundwater flows and solute transport in the focused recharge zone. To obtain more rigorous solutions, the computer program "SEAWAT" was used, in which fluid properties (density and viscosity) were dependent on groundwater temperature. For the data preparation, the water levels and the temperatures were measured with piezometers along the off-stream transect in the middle of the distinct losing section. Next, the horizontal trend in hydraulic conductivity was analyzed by using previously conducted in situ measurements, and variogram analysis of residuals was also performed. Sequential Gaussian simulation then produced 100 realizations of hydraulic conductivity by using the vertical trend and the variograms of residuals. This study adopted 13 study cases, respectively, of different conditions such as trending or stationary heterogeneity, isotropy or anisotropy of hydraulic conductivity, river conditions (hydraulic

conductivity and width), range of the variogram, anisotropy of thermal dispersivity, temperature dependence or independence of fluid properties, and model discretization.

In summary, this thesis has revealed the hydrologic and hydrogeologic characteristics of the groundwater flow system of the Toyohira River alluvial fan, particular around the focused recharge zone. The finds are summarized as follows.

1) The resulting vertical hydraulic gradient and groundwater table elevation maps indicated the hydrology of the fan featured downward groundwater flows, probably due to the effects of urbanization. The negative peak of vertical hydraulic gradient along the losing river in the mid-fan was associated with both the focused recharge and the dewatering by the subway lines crossing below the zone.

2) The distinct losing section was found to be located in the section KP 15.5−17.0 (about 1.5 km long), and the rate of water exchange was estimated at about 1 m^3/s, which corresponded to about 80% of the total pumping of groundwater throughout Sapporo City. This means that the focused recharge plays an important role in maintaining the groundwater reservoir.

3) The permeability model of the alluvial fan gravel deposits was established as a function of effective grain size (d_{20}) and length fraction of low packing levels in relatively undisturbed cores. The profiles of estimated hydraulic conductivity K indicated clear decreasing trends in the fan deposits with depth at the apex and the mid-fan, while no vertical trend was indicated in the distal part.

4) The decreasing trend of permeability was formulated as an exponential model. The exponential decay constant of 0.11 m^{-1} was 10- to 1000-fold of that of consolidated rocks reported in the literature. The primary reason for the large value was depositional processes such as progradation. Furthermore, post-depositional processes such as fine sediment infiltration might be a secondary reason.

5) The longitudinal cross section of the Toyohira River alluvial fan was generated by using profiles of moving average $\overline{Y_{MA}}$. The moving average boundaries of $\overline{Y_{MA}} = -4$ and $\overline{Y_{MA}} = -3$ revealed the hydrogeologic structures in the monotonic gravel sequences: an aquifer with a high infiltration rate (Holocene no. IIa); a depth-dependent heterogeneous aquifer (Holocene no. IIb); and a stationary permeable aquifer (Pleistocene no. III).

6) There were wide variations in hydraulic head and groundwater temperature near the losing river, depending on the location and depth of the observation well. The seasonal envelope in the groundwater temperature profiles was above a depth of about 30 m. These observations indicated that the downward flows of groundwater were largely attributable to the focused recharge zone.

7) The horizontal trend in hydraulic conductivity in the fan showed a humped trend as has been observed in other alluvial fans. Variogram analysis also revealed large anisotropy of spatial variability, and the theoretical models fitted were spherical models with a range of 1,000 m in the lateral direction and 20 m in the vertical direction.

8) The high-resolution model effectively realized various complex distributions of groundwater flow vectors and temperature contours. The calculated heads and temperatures based on the plausible realization satisfactorily corresponded to the measurements in the observation wells at different locations and depths. Several optimal realizations of K were obtained in the nonstationary condition, but no optimal realization was obtained in the stationary condition, even though the same 100 realizations of residuals were used in both conditions. This tendency was the same whether the model included isotropy, anisotropy, or large anisotropy. These simulation results indicate that modeling of trending heterogeneity was indispensable to obtain plausible descriptions of groundwater flows and solute transport in the focused recharge zone. In particular, in a comparison between isotropic, anisotropic, and highly anisotropic conditions under an assumption of nonstationary, the most plausible realizations of K were obtained in the isotropic condition.

9) Compared with other case studies of different conditions in the high-resolution model, the numbers of optimal realizations obtained were nearly the same as in cases under the nonstationary condition. This indicated that, compared with other factors, heterogeneity, that is whether there was trending heterogeneity or stationary heterogeneity, was more significant for modeling the groundwater flow system in the focused recharge zone.

10) The block-averaged models consequently provided smoother and more uniform descriptions of the groundwater flow and heat-transport system, but the numbers of optimal realizations obtained were larger than those obtained in the high-resolution model. The superiority of the block-averaged model indicated that conventional geometric averaging was similarly effective for upscaling the model of the heterogeneous alluvial gravel deposits. The anisotropic condition in the block cells was

a typical important factor, but the anisotropy ratio was constant in this analysis. In fact, the ratio was different from cell to cell as a result of heterogeneity. In other words, the upscaling procedure must be understood as a tensor. If this can be done, more plausible realization can be expected, and this will be pursued in future work.

6.2 Future research directions

The geostatistical reservoir model gave plausible realizations of the complex system of groundwater flow and heat transport in the focused recharge zone of the Toyohira River alluvial fan. However, an assumption of the vertical cross-sectional two-dimensional model was that the orthogonal flows from upstream to downstream were negligible. However, this assumption is not necessarily valid in alluvial coarse deposits because of the steep terrain in the longitudinal direction. Thus, a next study is to extend the two-dimensional cross-sectional model to a three-dimensional local model around the focused recharge zone, and to a three-dimensional basin model of the entire fan. Figure 6.1 shows a schematic three-dimensional basin model of the alluvial fan. The geostatistical process presented in this thesis also enables stochastic realizations of K to be produced throughout the fan; however, plausible realizations cannot be obtained if a number of realizations are generated without incorporating uncertain modeling factors that were assumed to be negligible in the focused recharge zone. Lastly, some research directions are discussed in terms of several modeling factors; hydrogeologic sequences, diffuse recharge, urbanization effects, and upscaling procedure.
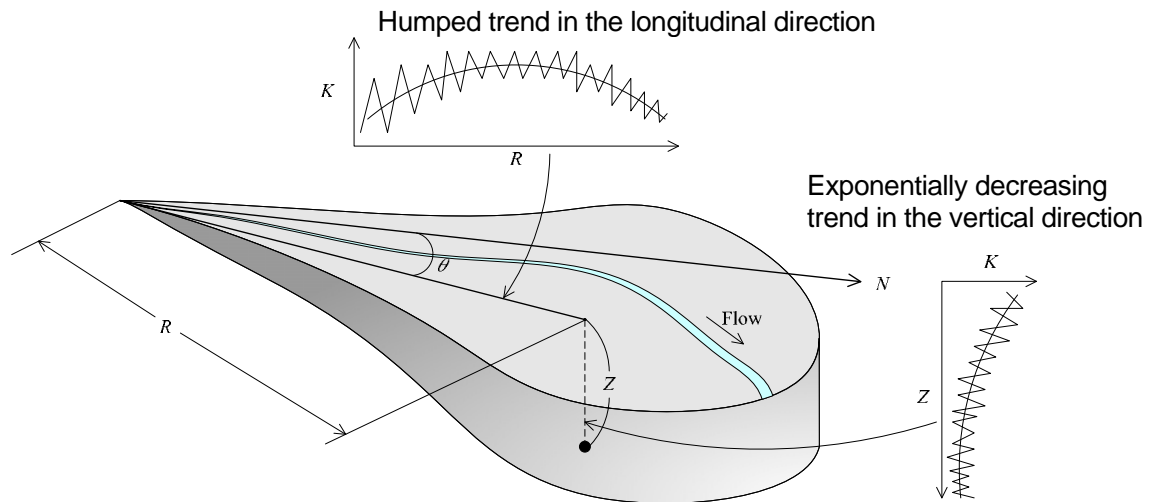
Figure 6.1 Conceptualization of three-dimensional basin model of alluvial fan

(1) Hydrogeologic sequences

In geology, sequences are generally defined as a relatively conformable succession of genetically related strata bounded by unconformities and their correlative conformities (Mitchum et al. 1977). Here, hydrogeologic sequences are those divided based typically on hydrogeologic features and hydraulic properties. This dissertation assumed that the focused recharge zone consisted of only monotonic sequences of gravel deposits, but the stochastic simulation showed that the plausible realization of K might include a thin low-permeability layer. Alluvial aquifer systems commonly consist of such mesoscopic hydrogeologic settings. For example, shallow groundwater flows in alluvial coarse deposits are generally affected by typical hydrologic and hydrogeologic zones, for example, in buried valleys that generally form preferential flows (e.g., Woessner 2000; Rossi et al. 1994). The variogram approach used in this thesis is available to quantify geologic heterogeneity, but might be overly simplified when hydrogeologic sequences of different scales are incorporated into the aquifer model. In addition, sequential Gaussian simulation is less applicable to modeling preferential pathways in analysis domains because the spatial variability and random generators lead to disorder in spatial patterns.

Alternatively, indicator methods in geostatistics are frequently used to impart a greater degree of geologic structure into models (Koltermann and Gorelick 1996; Journel et al. 1998; Proce et al. 2004; Fleckenstein et al. 2006). Other approaches are the incorporation of zonal and geostatistical approaches (Eaton 2006) and the determination of large-scale boundaries through interpolation of geologic information. Also, a Markov chain model could also be applied with a transition probability of an indicator to simulate complex alluvial depositional systems (Weissman and Fogg 1999; Ye and Khaleel 2008).

Geophysical surveys such as ground-penetrating radar (Bennett et al. 2006) and electrical measurements (Ezersky 2008) might provide useful information about hydrogeologic sequences. Moreover, deterministic depositional models of alluvial fans might be effective for determining highly permeable zones. Accordingly, future work on basin-scale reservoir modeling of alluvial coarse deposits needs to incorporate such a variety of geostatistical methods, field measurements, and depositional models.

(2) Diffuse recharge

In such a regional three-dimensional model, it is indispensable to estimate diffuse recharge from precipitation and snowmelt. However, determining diffuse recharge is generally difficult in groundwater modeling because the recharge rates vary substantially depending on elevation, geology, land surface slope, vegetation, and other factors (Lee et al. 2005). The rate also varies largely in the hydrologic cycle, and climate change also affects diffuse recharge through long-term trends. In the Toyohira River alluvial fan, for example, the season of maximum precipitation is expected to change from spring to autumn by the end of this century under global warming (Hu et al. 2010b).

Water-budget methods are general approaches to determine diffuse recharge as a residual in the water budget equation, but other components in the equation, such as evapotranspiration, are rarely estimated without uncertainty and error on a regional scale. The method has proved especially difficulty in urbanized areas, owing to complex land cover, unknown underground drainage, and the heat island effect.

Alternatively, a water-fluctuation method is more straightforward because the method is based on only the premise that groundwater levels rise in unconfined aquifers (Healy 2010). In particular, there are long-term variations of groundwater level in the observation wells throughout the Toyohira River alluvial fan. However, the method fundamentally needs the simplifying assumption that vertical flows of groundwater can be neglected; the assumption is not valid in most of alluvial fans. In the future work, theoretical or experimental improvements in the water-fluctuation method are needed so that it is applicable to even vertical flow conditions.

(3) Urbanization effect

In heavily urbanized and built-up areas such as the Toyohira River alluvial fan, a number of pumping wells and underground constructions dewater the aquifer, and a variety of contaminants harm groundwater quality (e.g., Takizawa 2008; Kasper et al. 2010). Heat is also utilized as a tracer of urbanization effect in groundwater flow system (Taniguchi and Uemura 2005). Such urbanization effects are usually seen in the groundwater flow system as negatives. Complete information about

artificial constructions and activities throughout the region is rarely available, and so large uncertainty is commonly encountered in groundwater modeling of urbanized areas. In the Toyohira River alluvial fan, there are two uncertain factors regarding urbanization: the subway lines and the pumping wells. The monthly subway drainage amounts are recorded at each station by Sapporo City, and the subway lines can be modeled as tunnel models by using the records. Modeling of numerous pumping wells is more problematic because only a portion of individual wells are characterized in terms of location, well depth, and pumping rate. Stochastic simulation of the well location and pumping program might be effective for assessing urbanization dewatering.

(4) Upscaling procedure

The permeability model in this thesis represented the core-scale permeability of gravel deposits. Such small-scale information was entered in the high-resolution two-dimensional model without modification. On the other hand, the grid-spacing in the three-dimensional basin model will need to be much larger, at least tens or hundreds of meters, due to limitations of computational power. Reconciling hydraulic data from different scales is a longstanding problem in reservoir characterization (Deutsch 2002). In this study, the block-averaged model was prepared by the conventional method where geometric averages of K in each block cell were entered, and the discrepancies between the calculations and the measurements were obtained within the acceptable levels. In more rigorous terms, however, the actual K value in each block cell is more anisotropic, as might be theoretically represented as a tensor.

The scale-up procedure is to transform a deposit-scale model to the dimensions of a sedimentary basin. Upscaling occurs when a global equivalent conductivity K* is computed for a heterogeneous deposits (Figure 6.2). Deutsch (2002) pointed out the following limitation: the upscaling procedure is applied to stationary random function models of variables that are averaged linearly and characterized by a variogram alone. Zhang et al. (2006) also suggested that equivalent conductivity for select units exhibits a scale effect and that field-scale representative elementary volume thus does not exist. The upscaling problem is probably most problematic in three-dimensional basin reservoir modeling of the alluvial fan, and this problem warrants further study in future work.
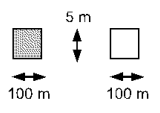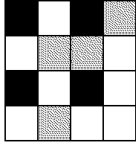
Scale	Conductivity	Simulation
Pixel scale (~100 sand grains)	not defined	none
Local scale (scaled-up pixel; local REV) 5 m, 100 m, 100 m	K (each K represents a local-scale, homogenous and isotropic porous medium)	Fully Heterogeneous Model
Global scale (a stratigraphic unit comprising of many local REV)	$K^*=\begin{bmatrix} K_{xx} & K_{xz} \\ K_{zx} & K_{zz} \end{bmatrix}$ (global K^* is an equivalent conductivity for a stratigraphic unit; global K^* arises due to heterogeneity of local K)	Hydrogeologic Framework Models

Figure 6.2 Schematic diagram illustrating the scale-up procedure and the upscaling analysis (Zhang et al. 2006)

158

Appendix A

Explanatory theory, equations, and knowledge utilized in this dissertation

A.1 Governing equation of groundwater flow

Ground water flow occurs because of the difference in energy of the water from one point to another. The flow energy of water at a given point consists of potential energy, elastic energy and kinetic energy. In general, the kinetic energy can be negligible because the ground water flow velocity is very low. The convenient way to measure the energy of the water is to measure the ground water level or hydraulic head in a piezometer (a cased well opened only over a very short section of its length). The level to which water rises in the piezometer with reference to a datum such as sea level is the hydraulic head. The hydraulic head is mathematically expressed as a sum of elevation head (potential energy per unit weight of water) and pressure head (elastic energy) :

$$h = z + \acute{Y} \qquad \text{(A.1.1)}$$

where h is the hydraulic head [L], z is the elevation head [L], $\acute{Y}$ is the pressure head [L]. The difference in hydraulic head between two points implies a hydraulic gradient. The gradient is along the direction of the lower head. The horizontal component of the hydraulic gradient in a given area can be measured by installing three or more piezometers to the same level in the ground, measuring the hydraulic head in each piezometer, and contouring these head values. It follows that the gradient is in the direction perpendicular to the hydraulic head, or equipotential contours, toward the decreasing hydraulic head. The fluid flux **q** [LT^{-1}] (often referred to as the Darcy flux) is given by Darcy's law:

$$q \quad K \quad \nabla h = \begin{bmatrix} Kx & Kxy & Kxz \\ Kyx & Ky & Kyz \\ Kzx & Kzy & Kz \end{bmatrix} \begin{pmatrix} dh/dx \\ dh/dy \\ dh/dz \end{pmatrix} \qquad \text{(A.1.2)}$$

$$K = \left(\frac{\rho g}{\mu} \right) kr \qquad \text{(A.1.3)}$$

$$q \quad \left(\frac{kkr}{\mu} \right) (\nabla p \quad \rho g) \qquad \text{(A.1.4)}$$

The formulation of the general groundwater flow equation in porous media is based on mass conservation and Darcy's law, and can be represented in three dimensions as follows (e.g. Bear 1979; Mercer and Faust 1981; de Marsily 1986):

$$\frac{\partial}{\partial x}\left(Kx \frac{\partial h}{\partial x} \right) \quad \frac{\partial}{\partial y}\left(Kx \frac{\partial h}{\partial y} \right) + \frac{\partial}{\partial z}\left(Kx \frac{\partial h}{\partial z} \right) \quad \pm R \quad S_S \frac{\partial h}{\partial t} \quad \text{(A.1.5)}$$

where K_x, K_y and K_z [LT^{-1}] are the hydraulic conductivities (or permeability) along the x, y and z coordinates, respectively, assumed to be the principal directions of anisotropy; h [L] is the hydraulic head given by $h=p/\rho g + z$, that is to say, a sum of pressure head and elevation head, p is pressure, ρ is the density of water and g is gravitational acceleration at an elevation z (i.e. the water level measured in piezometers; R' [T^{-1}] is an external volumetric flux per unit volume entering or exiting the system; and S_S [L^{-1}] is the specific storage coefficient.

The governing equation of groundwater flow indicates that conceptualization of groundwater flow system corresponds to determination of variability of hydraulic properties and recharge flux in space and time. The hydraulic properties, even though only in saturated zone, consist of hydraulic conductivity, specific storage, water contents, total and effective porosity, and others. The hydraulic conductivity is definitely most important because its magnitude proportionally affects on Darcy's flux, and the variation ranged in over 14 orders of magnitude due to various factors in geologic material (Figure A. 1). In addition, Hydraulic conductivity depends on scale, that is, microscale (e.g., drilling cores; several meters or less), mesoscale (e.g., facies; 10 to 100 m), and macroscale (basin scale, 100 m or more) as shown in Figure A. 2. The discrepancy between the different discretized models shows a direction of upscaling in groundwater modeling of alluvial coarse deposits. Thus, uncertainty in spatial variability of hydraulic conductivity faces groundwater modeling study.
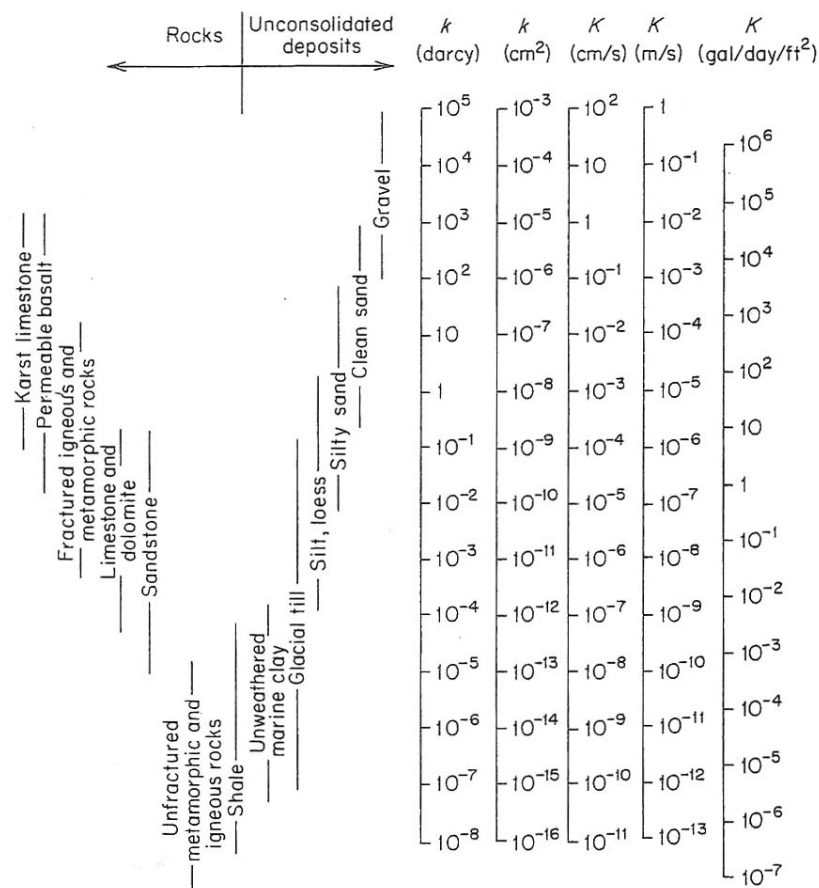
Figure A. 1 Range of Values of Hydraulic Conductivity and Permeability (Freeze and Cherry 1979)
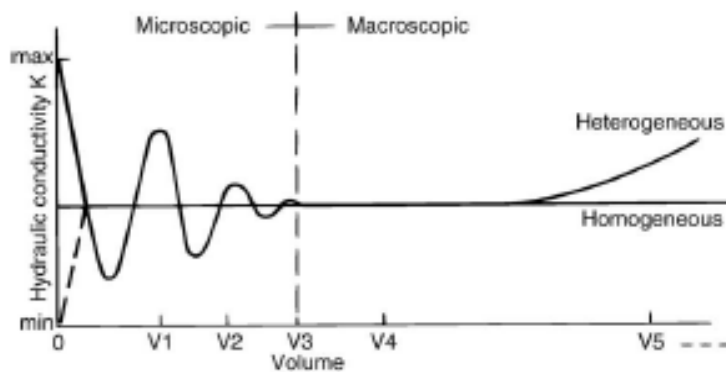
Figure A. 2 Conceptual position of a representative elementary volume (REV V3 or V4) larger than the microscopic scale, and within the macroscopic size domain (Bear 1972)

A.2 Gravitational flow system of groundwater in an alluvial fan

Hydraulic head is represented as a sum of two components: elevation head and pressure head as described in previous section. Infiltrated water in high land at precipitation has relatively high value of elevation head, and groundwater flows laterally to lower land and vertically to deeper zone. Thus, groundwater flow system is actually three dimensional. Hubbert (1940) was the first to present a graphics of a typical flow net. Tóth (2009) mathematically represented groundwater flow system by analytical solutions of boundary-value problems using Laplace's equation. Tóth (2009) also divided groundwater flow system into local, intermediate, and regional flow systems, as shown in Figure A. 3. Groundwater flow becomes more complex as the topography and geology become more complex. Local topography creates local ground water flow systems. The groundwater at a greater depth still eventually reaches the major valley through the regional groundwater system. Also, geologic structure may affect on the groundwater flow patterns. The groundwater tends to flow along high-permeable zones and across low-permeable zone.
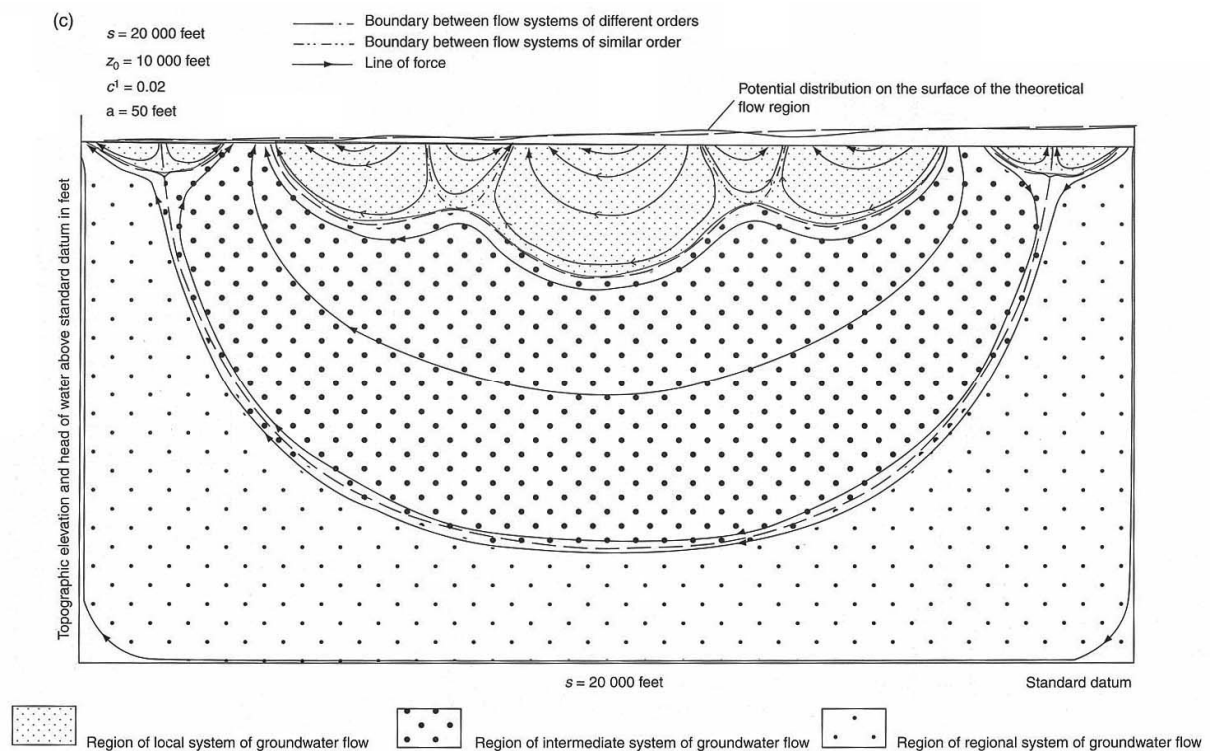
Figure A. 3 Hierarchically nestled gravity flow systems of groundwater in drainage basin with complex topography (Tóth 2009)

The mechanism of groundwater flow from apex to distal part in an alluvial fan is firstly described in Tolman (1937). An alluvial fan is hydrologically divided into four areas; I) intake area; II) Upper conduit zone; III) Lower conduit or Pressure zone; IV) Discharge zone. Intake area is shown as a belt covering the upper, where influent stream seepage is usually the chief source of supply of unconfined and confined groundwater. Upper conduit zone starts at the upper edge of a confining formation, and furnishes a less satisfactory water supply than the downstream zone due to the long distance of water table below the surface. Lower conduit or pressure zone is the zone in which the water in wells originally rose to or above the surface. Discharge Zone is the leaking portion of the pressure zone, and may play out entirely due to the constituent materials may gradually increase in fineness. Confined water moves down the conduits and is discharged by leakage to the surface throughout the entire discharge zone. On the other hand, free water moves down the water-table slope to the point where it intersects the surface, and is discharged at the upper edge of the swamp or spring.
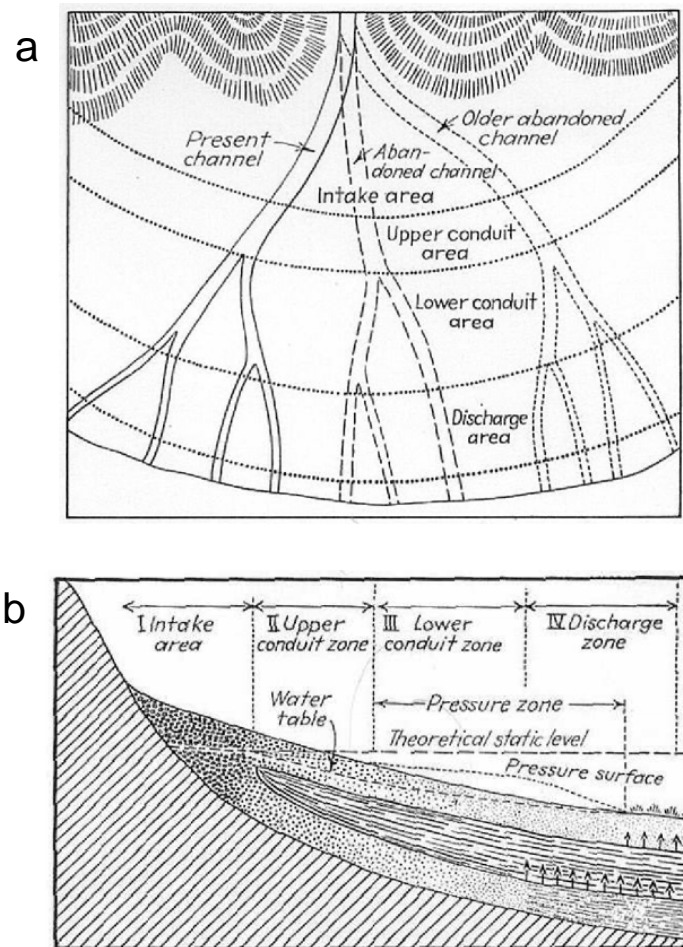
Figure A. 4 Hydrologic structure of an alluvial fan, a) planar- and b) cross- sectional explanation (Tolman 1937)

A.3 Facies model in coarse alluvial deposits

Facies model is commonly used to analysis sedimentary structure in various consolidated and unconsolidated sediments. Monotonic and no-migration sequences in alluvial coarse deposits can be subdivided as shown in Table A. 1 (Rust 1979). Among various facies, clast-supported and matrix-supported gravel are of typical importance in coarse alluvial deposits (Figure A. 5). Clast supported means the clasts in the sediments, i.e. pebbles, rocks, boulders etc., are touching each other, indicating energetic aqueous transport while sand is still carried in suspension; as flow velocity decreases, sand infiltrates into the spaces between the larger particles. Among the depositional processes, sieve deposits form as lobes of the fans which receive little sand or mud from their source areas. Open framework gravel (OFG) added into facies model is paid special attention in various studies of sedimentary and hydrology studies (Jussel et al. 1994; Heinz 2003; Lunt et al. 2004; Zappa et al. 2006; Lunt and Bridge 2007; Ferreira et al. 2010; dell'Arciprete et al. 2012). OFG includes connective and open voids between gravels, such that its hydraulic conductivity is extremely high, although OFG has a distribution that is only centimeters or decimeters thick.

Matrix-supported gravels are subdivided into two types: stratified sand matrix, and unstratified silty sand matrix. The former indicates aqueous lower transport, but at a low energy level in which sand and finer gravel particles are deposited together (Gp). The latter type of matrix support points to deposition from massive flows, which in the alluvial context are debris flow (Gms). Matrix-supported Gravel has relatively low permeability because the open spaces next to large particles are occupied by smaller particles. These facies change discontinuously laterally in cross sections and cause abrupt variations in hydraulic conductivity. Depositional and post-depositional process of high-energy flow leads to complex sequences consisting of various facies, such that geologic heterogeneity in alluvial coarse deposits is inherently large and trending.

Table A. 1 Principal facies in coarse alluvial deposits (Rust 1979)

Major facies	**Gm:**	Horizontally bedded clast-supported gravel, commonly imbricate.
	Gms:	Muddy matrix-supported gravel; lacks imbrication and internal stratification
	Gt:	Trough cross-bedded clast-supported gravel
Minor facies	**Gp:**	Planar cross-bedded gravel, transitional from clast-supported through sand matrix-supported to sand (facies Sp)
	Sh:	Horizontally stratified sand
	St:	Trough cross-stratified sand
	Sp:	Planar cross-stratified sand
	Fm:	Massive fine sandy mud or mud
	Fl:	Laminated or cross-laminated very fine sand, silt or mud.
	P:	Concretionary carbonate (pedogenic)

Figure A. 5 Schematic facies model of an alluvial fan (Rust 1979)

A.4　Spatial trend of hydrogeology in an alluvial fan

Trending heterogeneity is also recognized in coarsening/thickening or fining/thinning sequences owing to progradation, retrogradation, and basin subsidence. Consequently, hydraulic conductivity overall decreases downward with the grain size gradually decreases. This is called as trending heterogeneity (Freeze and Cherry 1979). In proximal parts the predominant facies is clast-supported coarse gravel (Gm), but in distal parts is sand matrix-supported gravel to sand (Gp to Sp). The fining-downward trend is generally recognized in an alluvial fan (Figure A. 6 A), and the downward trend of hydraulic conductivity K is corresponding (Figure A. 6 B). Another humped heterogeneity (Figure A. 6 C) is alternatively seen in the literature (Cehrs 1979). The humped heterogeneity indicates that the transmissivity reaches at highest values in the mid-fan area as a result of sorting trends, in other words, mid-fan to lower fan sheet flood and channel bar deposits (Gcsu, Gm, Smh, St, Sp) are much better sorted than upper-fan debris/mud flows (Gms, D).

Coarsening- and fining-upward trends are also typically seen in alluvial fans as a result of interactions of progradation, retrogradation, and basin subsidence (Figure A. 6 D and E). The vertical trend of grain size may positively correlate to the depth dependence of K. However, field studies rarely give a unique depth dependence of K at a particular site, especially in alluvial shallow aquifers, because geologic heterogeneity prevents detection of a specific trend from a large variability in K. In addition, the depth dependence of K in unconsolidated gravel deposits has rarely been discussed because porosity reduction by compaction is of less importance in clean coarse sediments than in fine sediments as shown in Figure A. 7. Another reason is that the relations between porosity and K are seldom adhered in natural coarse sediments (Morin 2006; Kresic 2007). Therefore, most previous studies (e.g., Hails 1976) applied the contention that little compaction occurs in clean gravels after deposition, unless great pressure in the magnitude of which is not generally known, is applied. However, K in unconsolidated gravel deposits varies greatly even under a slight change in porosity (Koltermann and Gorelick 1995; Major 1997; Major 2000; Kamann et al. 2007). All of those studies concluded that K is highly dependent on depth in unconsolidated gravel deposits. However, the trends were usually shown only graphically, and more quantitative characteristics about the trends (e.g., the decay exponents) were not typically determined.
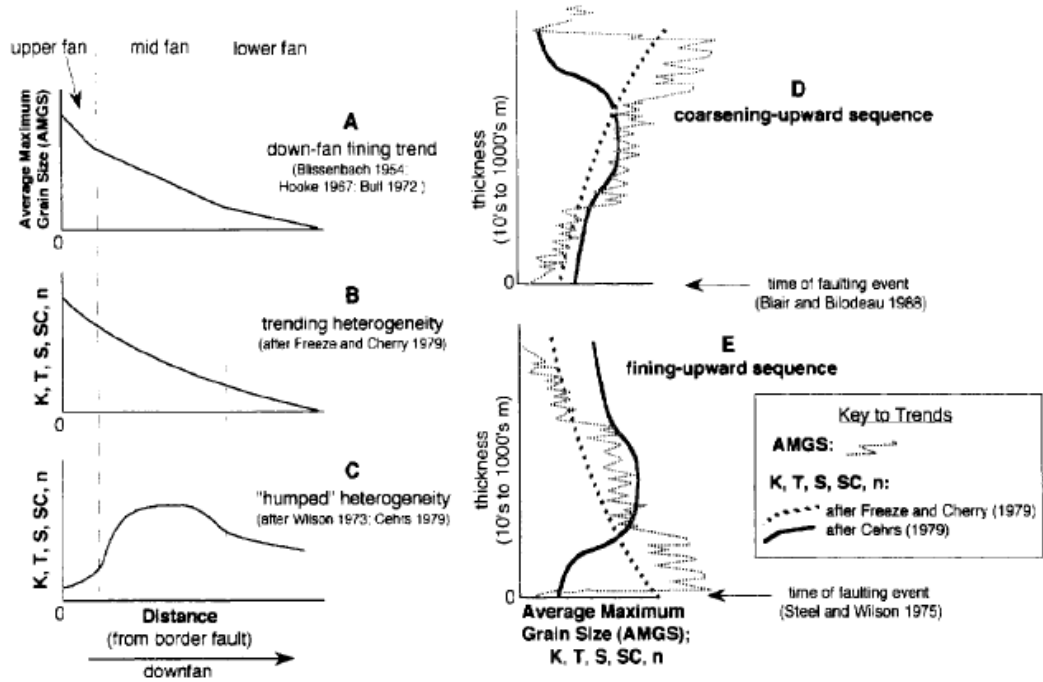
Figure A. 6 Spatial trends in grain size and aquifer parameters in alluvial fan aquifers (Neton et al. 1994)
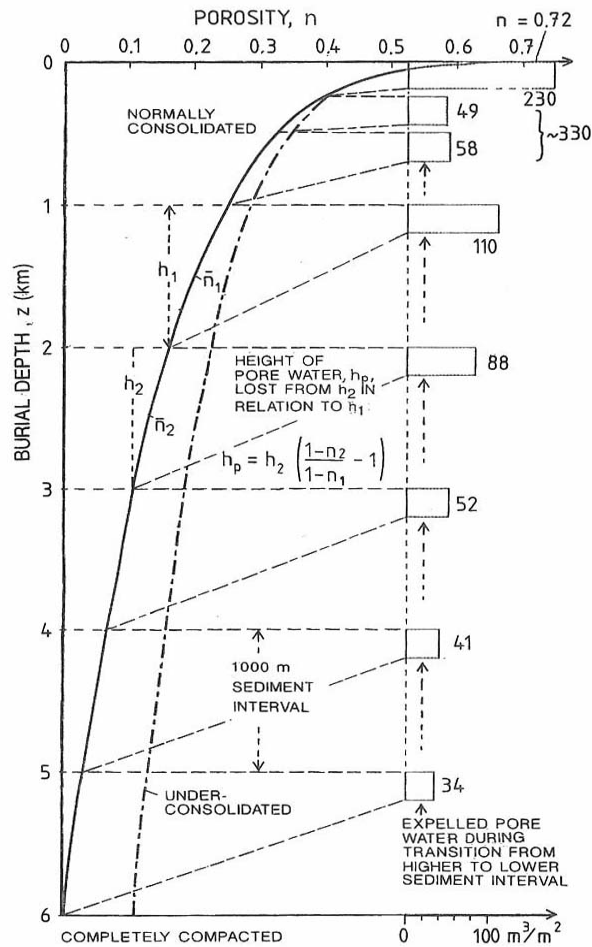
Figure A. 7   Upward-directed compaction flow calculated for a standard porosity-depth curve for normally consolidated, argillaceous sediments (Einsele 2000)

A.5   Interaction between surface water and groundwater

Direct exchanges of water between streams (or rivers) and ground water occur in three basic ways. Streams can gain water from ground-water inflow through their streambed, they can lose water through their streambed to ground water, or they may do both: gaining water in some reaches and losing it in others (Winter et al. 1998). Woessner (2000) classified four types of interactions between a stream and groundwater: (1) gaining, where the groundwater flow into the groundwater; (2) losing, where the water in the stream drains into the aquifer; (3) flow through, where the ground water flows into the stream on the one side of the channel and out of the stream on the other side of the channel; and (4) parallel, where the ground water flows in the aquifer beneath the stream and in the direction as the stream without entering or leaving the stream.
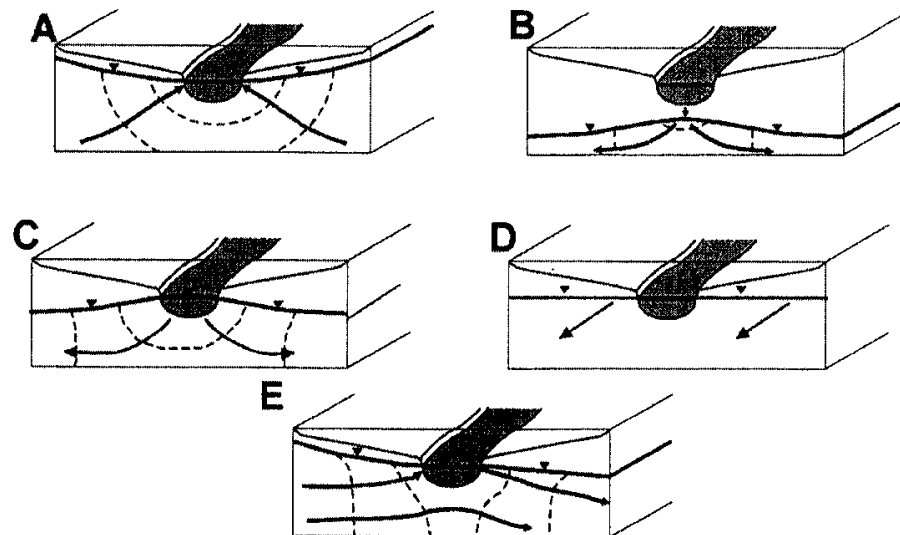
Figure A. 8 Fluvial plain water and stream channel interactions showing channel cross sections classified as: (a) gaining; (b) and (c) losing; (d) parallel-flow; (e) flow-through. The stream is shaded. The water table and stream stage (thicker lines), groundwater flow (arrows), and equipotential lines (dashed) are shown. Cross sections A, B, C, and E are constructed parallel to ground water flow; D is perpendicular to ground water flow (Woessner 2000)

A.6   A plot method for detection of recharge/discharge zone

The vertical component of hydraulic gradient at a given location can be measured by installing several piezometers to different depths and measuring the hydraulic head at each piezometer. Ground water flows in the direction of decreasing hydraulic head. The gradient direction indicates the potential for ground water flow in that direction. However, the sufficient number of piezometrers is not installed in most sites, so the information about vertical flows of groundwater actual flow direction is obtained in scattered locations. One traditional approach is to plot well depth versus depth to static water level from the groundwater table (Freeze and Cherry 1979). Under the assumption of a single topographic region, the plot determines whether the region is a recharge or discharge area. However, recharge and discharge areas in a basin are typically complex, and so it is not known a priori whether the site can be treated as a single topographic region. In the plot method, the groundwater table is a common datum surface, but the depth to the groundwater table is not uniform on such a regional scale, and varies depending on topography, geology, and other factors.
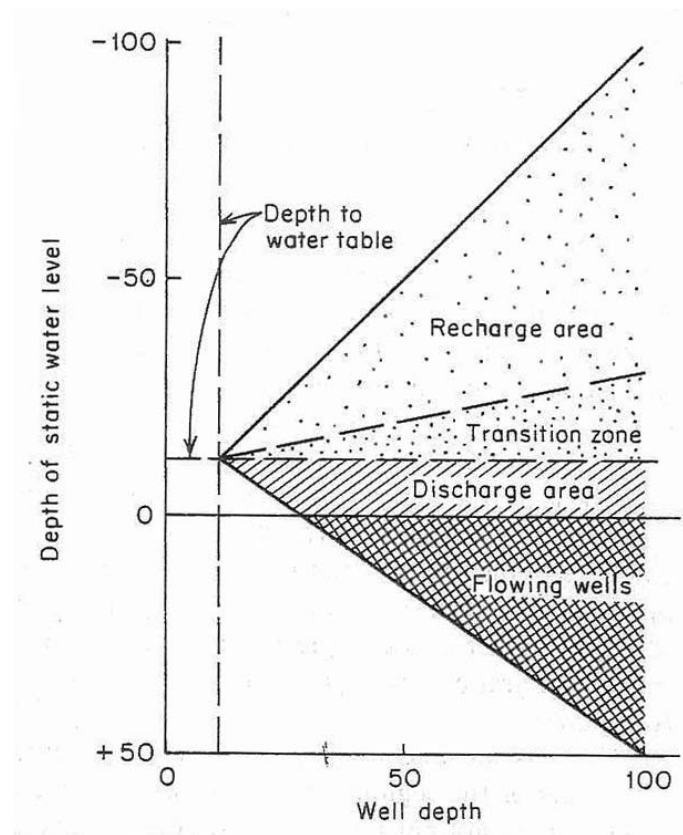
Figure A. 9 Generalized plot of well depth versus depth to static water level
(Freeze and Cherry 1979)

A.7 Mann-Kendall test and Sen's slope estimation

Mann-Kendall test (Mann 1945; Kendall 1975) and Sen's slope estimation (Sen 1968) are widely used to test for randomness against trends in ecology, hydrology and climatology (e.g., Wen and Chen 2006; Soderberg and Remy 2007). In Mann- Kendall tests, no trend or trend were e statistically tested whether the null hypothesis H_0 of no trend, i.e. the observations are randomly ordered in time, were rejected or not. Mann- Kendall test Static S value and its variance, VAR(S were respectively calculated by annual mean water levels during the analysis periods. The standard test statistic Z value is obtained as:

$$Z = \begin{cases} \dfrac{S-1}{\sqrt{VAR(S)}} & if \quad S > 0 \\ 0 & if \quad S = 0 \\ \dfrac{S+1}{\sqrt{VAR(S)}} & if \quad S < 0 \end{cases}$$

(A.7.2)

A positive (negative) value of Z indicates an upward (downward) trend. To test for either an upward or downward monotone trend (a two-tailed test) at α level of significance, H_0 was rejected if the $|Z| > Z_1 - \alpha/2$, where $Z_1 - \alpha/2$ was obtained from the standard normal cumulative distribution tables. Sen's slope was also calculated using a linear trend model, and an estimate of the slope Q_i is obtained by:

$$Q_i = \frac{x_j - x_k}{j - k}, i = 1, 2, \ldots N, j > k$$

(A.7.3)

The statistical trend analysis can be archived using a free Excel macro (Salmi et al. 2002.)

A.8   Geostatistics for groundwater modeling

(1) Zonal approach versus statistical approach

Hydraulic head are observed by piezometer, but constructing a piezometer is effortful and ineconomical. In situ measurements of hydraulic conductivity are directly obtained by various methods such as multiple pumping tests, slug tests, flow meter tests and permeameter tests. These methods commonly require boreholes, of which constructions are uneconomical and effortful. Completely three-dimensional information about hydraulic properties is never obtainable, and thus numerous methods have been developed to interpolate between data values and to use geologic, hydrologic, and geophysical information to creat images of aquifer properties (Koltermann and Gorelick 1996).

Two approaches to address such large uncertainty in hydraulic and hydrogeologic parameters are traditionally attempted; zonal (deterministic) approach and statistical (geostatstical) approach (Eaton 2006). In zonal approach, aquifer system is conceptualized as a series of layers in the term of hydrogeologic uniformity. The hydraulic properties in each homogeneous layer are only "optimum" values such as means, and parameter calibration is often conducted to obtain sufficient agreement between measurements and estimates. The zonal approach is deterministic and straightforward, so applied in most practice. The approach requires hydrogeologic boundaries that divide the target aquifer into several homogeneous layers. However, such boundaries are rarely found in monotonic gravel sequences. In addition, trending heterogeneity proves especially difficulty to advance the assumption that the gravel aquifer consists of several homogeneous layers.   Thus, zonal approach is not useless for groundwater modeling in coarse alluvial aquifer.

The stochastic approach is precisely addressing the uncertainty of regional variables in a rational, quantitative framework by using probability theory. Regionalized variable $z(x)$ is considered to be a realization of a random function $Z(x)$. The advantage in this approach is that we shall only try to characterize simple features of the random function $Z(x)$ and not those of particular realizations $z(x)$. The stochastic modeling of subsurface hydrogeology has become a subject of wide interest and intensive research (Koltermann and Gorelick 1996; Dagan 1997). The approach is also adopted by many disciplines in physics and engineering a long time ago, such as time series analysis in predicting floods and other extreme events. However, subsurface modeling of including groundwater flow deals mainly with spatial variability, the uncertainty of which is of a more

complex nature.

(2) Statistical assumptions

Stationarity and ergodicity are also necessary to make stochastic approach useful (de Marsily 1986). Stationarity assumes that any statistical property of the geologic material (e.g., mean, variance) is stationary in space, i.e. does not vary with a translation. In more rigorous terms, strong staionarity means that all the probability distribution functions (pdf) are invariant under the translation. In the case of geostatistics, week stationary is at least required where only the first two moments are staionary: expected value is constant, i.e., E $[Z(\boldsymbol{x}] = m$; covariance is not a function $\boldsymbol{x}$ but a function only of the lag h, i.e. Cov(h) = E [(Z($\boldsymbol{x} - m$) (Z($\boldsymbol{x} + \boldsymbol{h} - m$)].

Erdgodicity also implies that the unique realization available behaves in space with the same pdf as the ensemble of possible realizations. In other words, by observing the variation in space of property, it is possible to the pdf in the random function for all realizations. In most applications, it is assumed that stochastic realizations match model statistics exactly. However, the assumption is rarely achieved, nor should it. For example, multiple SGS realizations reproduce variogram, which have discrepancies with the inherent variogram model. This is called ergodicity fluctuation (Deutsch and Journel 1998). The ergodicity fluctuation depends on several factors such as simulation argorithm, the density of condinitoning data, and the size of the simulation grid. Goovearts (1997) also suggests that data that are subject to measurement error. The fluctuation of the realization variogram is generally important when the range of the variogram model is large with respect with the size of the simulated area. Furthermore, the ergodic hypothesis, i.e. the ensemble average is statistically equivalent to the spatial average of a variable in one realization, is assumed to hold (Dagan, 1997). In addition, the validity of the ergodic hypothesis has been questioned for highly heterogeneous media (Sposito 1998).

(3) Variogram analysis

Spatial variability or auto-correlation structure of regional variable, $Z(\boldsymbol{x})$, where $\boldsymbol{x}$ denotes the point in the geometric space, is often characterized by a function of only a distance vector $\boldsymbol{h} = \boldsymbol{x}_1 - \boldsymbol{x}_2$; a covariance $C(\boldsymbol{h})$ or a variogram $\gamma(\boldsymbol{h})$ as:

$$C(\boldsymbol{h}) = \mathrm{E}[Z(\boldsymbol{x} + \boldsymbol{h})\, Z(\boldsymbol{x})] - m^2 \qquad \text{(A.8.1)}$$

$$\gamma(\boldsymbol{h}) = 1/2\, \mathrm{Var}[Z(\boldsymbol{x} + \boldsymbol{h}) - Z(\boldsymbol{x})] = 1/2\, \mathrm{E}\{[Z(\boldsymbol{x} + \boldsymbol{h}) - Z(\boldsymbol{x})]^2\} \qquad \text{(A.8.2)}$$

where m denotes constant mean, i.e. $E[z(\boldsymbol{x})] = m$. In the second-order stationary hypothesis; (1) $E[z(\boldsymbol{x})] = m$ (constant mean) and (2) the function of autocovariance only depends on the distance and not on the points of reference, a relation between the covariance and the variogram is written as: $\gamma(\boldsymbol{h}) = C(0) - C(\boldsymbol{h})$. A variogram is also estimated under a less stringent hypothesis, called the "intrinsic hypothesis." Traditionally, the variogram has been used for modeling spatial variability rather than the covariance although kriging systems are more easily solved with the covariance matrices (Deutsch and Journel 1998).
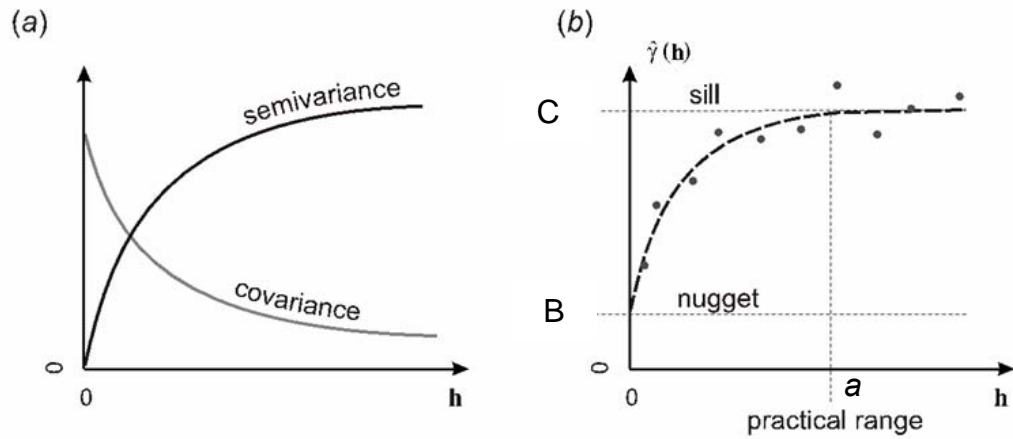
Figure A. 10 (a) the pair of covariance and variance with the same parameters, (b) parameters in variogram; is C is the sill (total variance), B is the nugget (variance of the spatially uncorrelated portion of the field) and a is the practical range that is the distance over which the field is correlated

The variogram models are determined by fitting to experimental variogram, which characterized the spatial variability of the data. Experimental variogram is defined as a half of the average squared difference between two attributed values as:

$$\gamma(d) \quad \frac{1}{2N(d)} \sum_{i=1}^{N(d)} \left[z(\boldsymbol{x}_i \quad d) \quad z(\boldsymbol{x}_i) \right]^2 \qquad \text{(A.8.3)}$$

where $N(\boldsymbol{h})$ is the number of pairs, $z(\boldsymbol{x}_i)$ is the target variable at the position $\boldsymbol{x}_i$. The separation vector $\boldsymbol{h}$ is specified with some direction and lag distance $\boldsymbol{h}$. Considering scattered measurements at scatter locations (a) as shown in Figure A. 11, variogam model is performed using as following steps: (b) all possible pairs of points are considered: (c) experimental variogram is produced by averaging over given classes of lag distances between the measurement locations: (d) theoretical variogram models are estimated through parameter optimizations to match experimental variogram. Anisotropy may

show different sensitivity with directions (Figure A. 12). This means that a large amount of measurements are required to reveal the spatial variability, and to confirm the validity of variogam model. For example, Journel und Huijbregts (1978) suggest that the number of pairs in a distance class should not be less than about 30 to 50. In aquifer characterization, the number of hydraulic properties is often unobtainable. Theoretical models are needed to satisfy statistical condition in mathematics. The spherical model, the exponential model, and the Gaussian model are, respectively, represented as:

$$\gamma(h) \begin{cases} B & ,h=0 \\ B+(C-B)\left[\dfrac{3}{2}\dfrac{h}{a}-\dfrac{1}{2}\left(\dfrac{h}{a}\right)^{3}\right] & 0<h<a \\ C & ,h\_\ge a \end{cases} \tag{A.8.4}$$

$$\gamma(h) \begin{cases} 0 & ,h=0 \\ B+(C-B)\left[1-exp\left(-\dfrac{3h}{a}\right)^{3}\right] & ,h>0 \end{cases} \tag{A.8.5}$$

$$\gamma(h) \begin{cases} 0 & ,h=0 \\ B+(C-B)\left[1-exp\left(-3\left(\dfrac{h}{a}\right)^{2}\right)\right] & ,h>0 \end{cases} \tag{A.8.6}$$

where B is the nugget effect, C is the partial sill, the range a is the practical range, h is the separated distance.
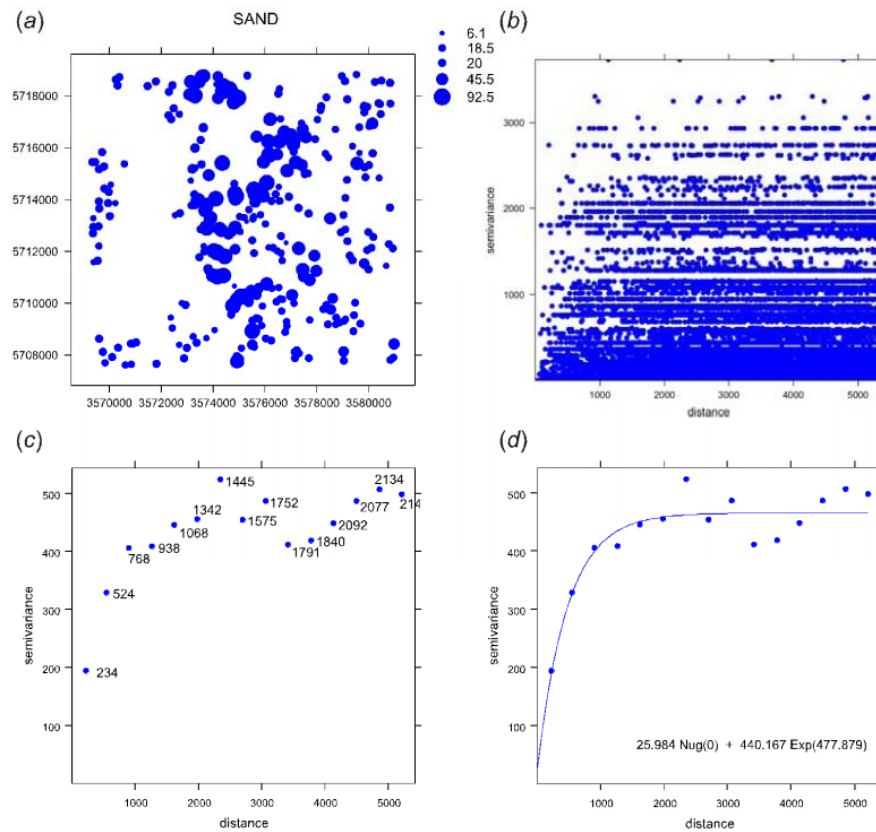
Figure A. 11 Illustrative process of variogram modeling (Hengel 2007)
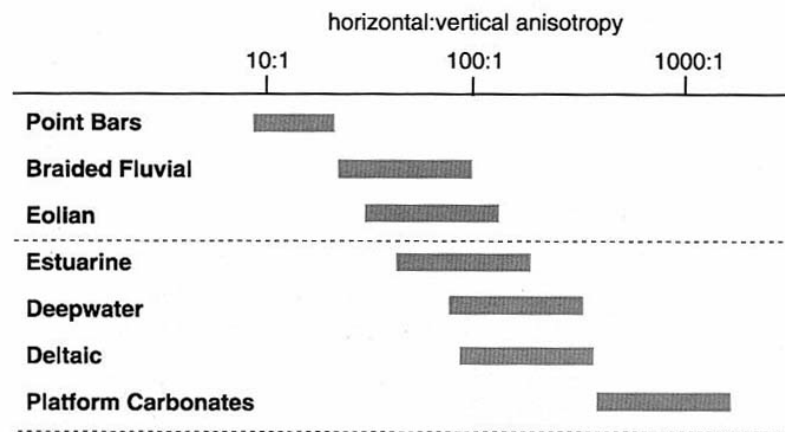
Figure A. 12 Some typical horizontal-to-vertical anisotropy ratio conceptualized from available literature and experience. Such generations can be used to verify actual calculations and supplement very sparse data (Deutsch 2007)

(4) Kriging

Kriging is an optimal interpolation procedure developed by Matheron as the "theory of regionalized variables." It was called kriging in recognition of Krige, which first proposed the origin of this method. Kriging provides best unbiased linear estimates (BLUE) at any no measurement data points, and also satisfies conditional condition, in which Kriging estimates at measurement points are exactly equal to the measurements. Kriging also infers uncertainty (i.e. variance) besides estimates at each desired points, while other deterministic estimation (e.g. IDW) cannot. In addition, linear estimation procedure is easy to theoretically understood, and input in various available software and GIS.

In geostatistics, the geological phenomenon is considered as a function of space and/or time. Let $z(x)$ represent any random function of the spatial coordinates z with measured values at N locations in space $z(x_i)$ (i 1,2,3, ... , N), and suppose that the value of the function z has to be estimated at the point x_0. Each measured value $z_1, z_2, z_3, ... , z_N$ contributes in part to the estimation of the unknown value z_0 at location x_0. Taking this into account, and assuming a linear relation between z_0 and z_i, the estimated value of z_0 can be defined as (Ahmed et al. 2010):

$$z*(x_0) \quad \lambda_1 z_1 \quad \lambda_2 z_2 \quad \lambda_3 z_3 \quad \lambda_4 z_4 \qquad \lambda_N z_N \ \text{ or } \ z*(x_0) \ \sum_{i=1}^{N} \lambda_1(x_i) \qquad (A.8.7)$$

where $z*(x_0)$ is the estimation of function $z(\mathbf{x})$ at the point x_0 and $_i$ are weighting coefficients. To ensure an unbiased and optimal predictor the following two conditions need to be satisfied:

1. The expectant difference between the estimated value and the true (unknown value (the expected value of the estimation error should be zero, i.e.

$$E[z^*(x_0) \quad z(x_0)] \quad 0 \qquad (A.8.8)$$

This unbiasedness condition is often referred to as the universality condition.

2. The condition of optimality means that the variance of the estimation error should be a minimum, i.e.

$$\sigma_K^2(x_0) \quad ver[z^*(x_0) \quad z(x_0)] \text{ is a minimum} \qquad (A.8.9)$$

Substituting Equation (8.7) into Equation (8.8) we get

$$\sum_{i=1}^{N} \lambda_i \quad 1 \qquad (A.8.10)$$

Expanding Equation (8.9) then leads to

$$\sigma_K^2(x_0) = \sum_{i=1}^{N}\lambda_i\sum_{j=1}^{N}\lambda_i E\big[z(x_i)z(x_j)\big] + E\big[z^*(x_0)^2\big] - 2\sum_{i=1}^{N}\lambda_i E\big[z(x_i)z^*(x_0)\big] \tag{A.8.11}$$

Introducing the formulae of covariance, we get

$$\sigma_K^2(x_0) = \sum_{i=1}^{N}\lambda_i\sum_{j=1}^{N}\lambda_i C(x_i,x_j) + C(0) - 2\sum_{i=1}^{N}\lambda_i C(x_i,x_j) \tag{A.8.11}$$

where $C(x_i,x_j)$ is the covariance between points x_i and x_j.

The best unbiased linear estimator is the one which minimizes $\sigma_K^2(x_0)$ under the constraint of

Equation (5.4). Thus, introducing Lagrange multipliers and adding the term $2\mu\left(1-\sum_{i=1}^{N}\lambda_i\right)$, we obtain

$$Q = \sum_{i=1}^{N}\lambda_i\sum_{j=1}^{N}\lambda_j C(x_i,x_j) + C(0) - 2\sum_{i=1}^{N}\lambda_i C(x_i,x_0) + 2\mu - 2\mu\sum_{i=1}^{N}\lambda_i \tag{A.8.12}$$

Making partial differential equations of Q with respect to λ_i and μ and equating them to zero

minimizes Equation (8.12) leading to the kriging equations:

$$C(x_i,x_0) = \mu + \sum_{j=1}^{N}\lambda_j C(x_i,x_j), i = 1,2,3...,N \tag{A.8.13}$$

$$\sum_{j=1}^{N}\lambda_j = 1 \tag{A.8.14}$$

Substituting Equation (8.13) into Equation (8.14) yields the variance of the estimation error:

$$\sigma_K^2(x_0) = C(0) + \mu - \sum_{i=1}^{N}\lambda_i C(x_i,x_0) \tag{A.8.15}$$

The square root of this equation gives the standard deviation $\sigma_K(x_0)$, which means that, with 95%

confidence, the true value will be within $z^*(x_0) \pm 2\sigma_K(x_0)$.

If the covariance cannot be defined we can apply the kriging equation:

$$\gamma(x_i,x_0) = \mu + \sum_{j=1}^{N}\lambda_j\gamma(x_i,x_j), i = 1,2,3...,N \tag{A.8.16}$$

where $\gamma(x_i,x_j)$ is the variogram between points x_i and x_j. The variance of the estimation error then

becomes

$$\sigma_K^2(x_0) = \mu + \sum_{i=1}^{N}\lambda_i\gamma(x_i,x_0) \tag{A.8.17}$$

Equation (8.16) in conjunction with (8.14) represents a set of (N + 1) linear equations with (N + 1) unknowns, which on solution yield the coefficients $_i$ Once these are known, equations (8.7), (815) and/or (8.17) can be evaluated. Compared other interpolation techniques (e.g., IDW), kriging is advantageous because it considers (Journel and Hujibregts 1978); 1) the number and spatial configuration of observation points; 2) the position of data points within the region of interest; 3) the distances between the data points with respect to the area of interest; and 4) the spatial continuity of the interpolated variable.

(5) Nonstationary problems

In nonstationary problems the mathematical expectation of z is no longer a constant: $E[z(x)] = m(x)$, and the variogram cannot be calculated directly from the data since $m(x)$ is unknown. Nonstationary problems in geostatistics have been discussed in the literature (e.g., de Marsily 1986; Goovaerts 1997; Deutsch and Journel 1998; Wackernagel 2003).

There are several procedures for solving nonstationary problems. One simple assumption is "locally stationary" as $E[z(x)] = m(s)$ s A', where A' is a certainly local field, and the variogram stays isotropic. Kriging with moving neighborhood is conducted by setting a search radius less than the distance in which the stationary assumption is satisfied.
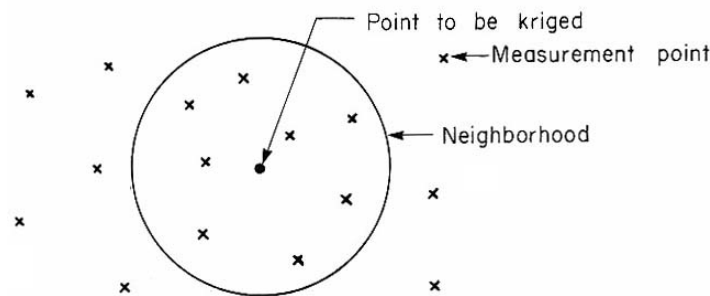
Figure A. 13 Kriging with a moving neighborhood (de Marsily 1986)

Another way is to assume that the mathematical expectation $m(x)$, i.e., global trend, is known or estimated and to krige the residuals $z(x) – m(x)$ under the assumption that the residuals are stationary. The mathematical expression might also be known for physical reasons, and then the constants of this expression may be fitted on the model. A variety of kriging techniques are developed to represent global drift using auxiliary variable, for example, porosity for hydraulic conductivity or

ground surface elevation for groundwater table elevation. The techniques are classified into co-kriging based and regression-kriging based (Hengl 2007). Cokriging is reserved for linear regression that also uses data defined on target variable and auxiliary variables. Cokriging needs auxiliary variables at not all grid nodes. This is a main advantage to use cokriging, however determination of cross-variogram is generally an effortful process. If auxiliary variables are obtained at all grid nodes, and correlated with the target variable, the latter is generally preferred over the former. In regression-kriging based approach, the regionalized variable is conceptualized as a sum of a deterministic component (drift), a spatial auto-correlation component and a purely random component as (Figure A. 14):

$$z(\boldsymbol{x}) = m(\boldsymbol{s}) + e'(\boldsymbol{s}) + e''(\boldsymbol{s}) \qquad \text{(A.8.18)}$$

where $z(\boldsymbol{x})$ is the target variable at the location $\boldsymbol{s}$, $e'(\boldsymbol{s})$ is the spatial auto-correlation component, and $e''(\boldsymbol{s})$ is the purely random component. Regression-kriging based approach is also divided into Universal kriging (UK), kriging with external drift (KED), and Regression kriging (RK), of which prediction processes are different but should give the same predictions and prediction error (Hengl 2007). Universal kriging and kriging are performed in which kriging weights and drift parameters in both kriging methods are simultaneously solved in the kriging system. The kriging system in both methods requires in advance the covariance of residuals, which are obtained by subtracting the drift by the variable, but this poses a conflict because drift parameters are determined after kriging.

Alternatively, the drift and residuals are fitted separately and then summed; this approach is applied in various techniques such as residual kriging, kriging combined with regression, and regression kriging. The applicability also has been indicated through comparison studies (e.g., Knotters et al. 1995; Hengl 2007; Nikroo et al. 2010). The formulas and parameters of drift are firstly determined by ordinary least squares (OLS). Statistically, unbiased parameters of drift are also determined by the iterative process of generalized least squares (GLS; Cressie 1993; Hengl 2007). GLS is a sophisticated but laborious process. The first OLS drift should be satisfactory but slightly inferior (Kitanidis 1993; Minasny and McBratney 2007). RK is direct and powerful method to address non-stationary problem, but discrepancies between final estimates and measurements are significantly caused if drift model is not enough satisfied. This means adequate model of drift is key point to obtain accuracy of final estimates.
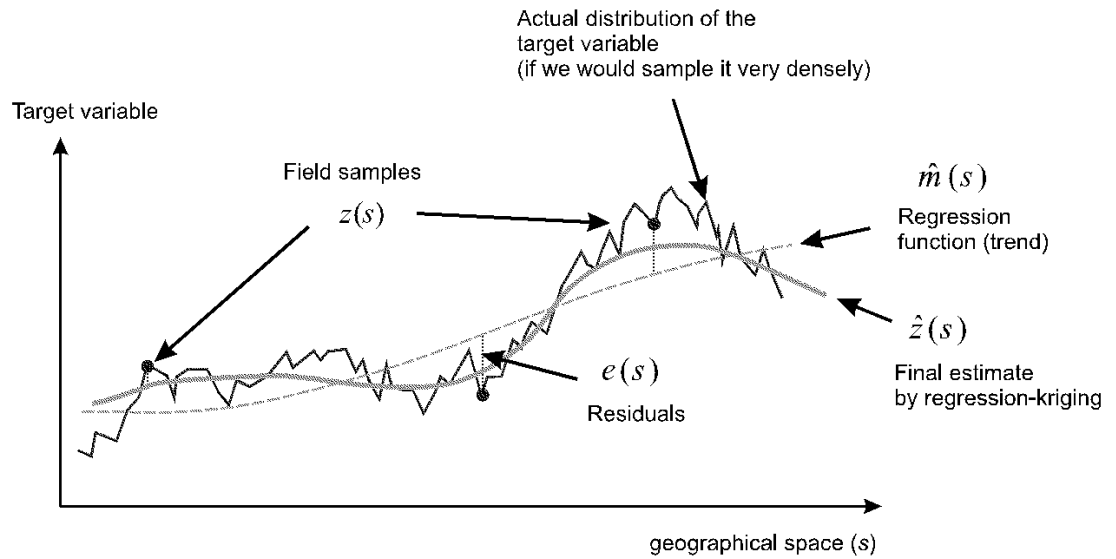
Figure A. 14 Schematic example of regionalized variables with kriging (Hengl 2007)

(6) Conditional simulation

A problem with kriging is that, while it acknowledges uncertainty, it underestimates variability - that is, kriging estimates are too smooth. This also leads to the prediction of overly smooth features far away from the points of observation (see Figure A. 15c). Often, one is not as interested in obtaining the "optimum" estimate as in reproducing spatial variability. This is squarely the objective of conditional simulation. Here, "simulation" refers to the generation of fields with the desired variability patterns, while 'conditional' refers to the constraint that any simulation should coincide with measured values at measurement point.

Algorithms include nearest neighbors, turning bands, lower-upper (LU Cholesky decomposition), spectral domain fast Fourier methods, and sequential Gaussian simulation (Koltermann and Gorelick 1996). Among these methods, sequential Gaussian simulation is the most powerful of the Gaussian random field generator algorithms. The Gaussian distribution is defined by only mean and variance of the target variables, corresponding that second-ordinary stationarity hypothesis is simultaneously established. In sequential Gaussian algorithms, grid nodes at which values have not yet been assigned are selected at random, and one value is drawn a random on the local conditional probability distribution. The mean and variance in local conditional probability distribution is estimated using kriging estimation of nearby data at previously simulated grid and conditional grid.

The process is repeatedly performed until simulation values at all desired nodes are determined. As a result, it generates conditional realizations, and can generate very large random fields at irregular grids as well as regular grids. Subsurface hydraulic conductivity frequently follows a log-normal distribution, and in other words $\log K$ is normal (e.g. Freeze and Cherry 1979; Domenico and Schwartz 1998). Sequential Gaussian simulation (SGS) is one method that seeks to overcome these problems. The underlying principle is that the error variance at each estimated point, σ_{SK}, often referred to as the kriging variance, can be calculated from

$$\sigma_{SK}(x_0) \quad Cov(0) \quad \sum_{i=1}^{k} \lambda_i Cob(x_0 \quad x_i) \qquad (A.8.19)$$

With SGS, the value estimated by Equation (8.7) is treated as the expectant. SGS then makes a stochastic estimate of the value by adding a residual sampled from a Gaussian distribution of variance, σ_{SK}^2, as obtained from Equation (8.19) (hence Gaussian simulation). This value is then added to the collection of observations (i.e. the right-hand side of Equation (8.7)). This procedure is repeated sequentially for each desired value of x_0. It should be appreciated that the matrices in the kriging equation also become increasingly larger with each estimate. Consequently, these calculations become very computationally intensive and one needs special algorithms to make them feasible (Gomez-Hernandez and Journel 1993).
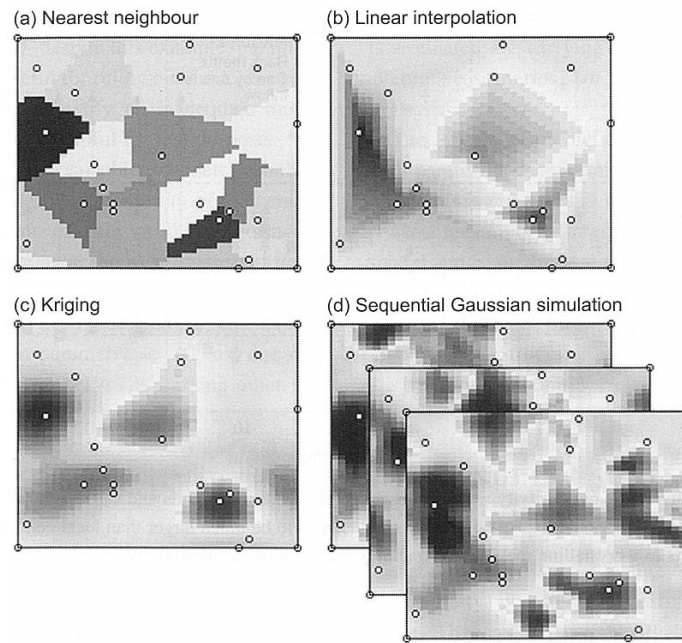
Figure A. 15 Comparison between methods to handle spatial variability (after Carrera and Mathias 2010)

A.9 Theory of heat transport in groundwater

If the properties of fluid and geologic material are independent of temperature, the three-dimensional heat transport equation under the can be written as (Domenico and Schwartz 1998):

$$\frac{k_e}{\rho c} \nabla^2 T - \frac{\rho_w c_w}{\rho c} \nabla \cdot (Tq) \quad \frac{\partial T}{\partial t} \qquad \text{(A.8.20)}$$

where T is the temperature; t is time; ρ_w and c_w are, respectively, density and specific heat of the fluid and ρ and c are, respectively, density and specific heat of the geologic material (bulk values); q is the seepage velocity or specific discharge vector; and k_e is a term that includes the effective thermal conductivity of the geologic material (bulk value).

Recent studies, however, suggest the importance of temperature dependence with respect to solution robustness in groundwater modeling (Ma and Zheng 2010; Engeler et al. 2011). SEAWAT used in this study also calculates groundwater flow and temperature transport with greater accuracy by using iterative processes. The variable-density solute-transport and ground-water flow equation (tensors and vectors shown in bold) is represented as:

$$\nabla \left[\rho \frac{\mu_0}{\mu} K_0 \left(\nabla h_0 \quad \frac{\rho \quad \rho_0}{\rho_0} \nabla z \right) \right] \quad \rho S_{s,0} \frac{\partial h_0}{\partial t} \quad \theta \frac{\partial \rho}{\partial C} \frac{\partial C}{\partial t} \quad \rho_s q_s' \quad \text{(A.8.21)}$$

where ρ_0 is the fluid density [ML^{-3}] at the reference concentration and reference temperature; μ is dynamic viscosity; K_0 is the hydraulic conductivity tensor of material saturated with the reference fluid; h_0 is the hydraulic head measured in terms of the reference fluid of a specified concentration and temperature (as the reference fluid is commonly freshwater); $S_{s,0}$ is the specific storage, defined as the volume of water released from storage per unit volume per unit decline of h_0; t is time; θ is porosity; C is salt concentration [ML^{-3}]; and q_s' is a source or sink [T^{-1}] of fluid with density ρ_s.

Equation (8.21) represents solute transport, not only heat transport under the variable condition of density and viscosity. The fluid density and viscosity can be calculated using concentrations from one or more solute species. These equations of state relate the density and viscosity terms in equation 1 to one or more of the MT3DMS species concentrations (C^k). Equation (8.21) can also be used to represent heat transport. In this case, one of the MT3DMS solute species is used to represent temperature, and the mathematical terms describing heat transport are converted into forms analogous to those used in Equation

(8.21). By allowing one or more of the MT3DMS species to affect fluid density and viscosity, variable-density ground-water flow can be coupled with simultaneous solute and heat transport. SEAWAT utilized the density function of temperature as:

$$\rho = \rho_0 + \sum_{k=1}^{NS}\frac{\partial\rho}{\partial C^k}\left(C^k - C_0^k\right) + \frac{\partial\rho}{\partial T}\left(T - T_0\right) + \frac{\partial\rho}{\partial\ell}\left(\ell - \ell_0\right) \quad \text{(A.8.22)}$$

where $\dfrac{\partial\rho}{\partial\ell}$ can be calculated from the volumetric expansion coefficient for pressure, β_P, using:

$$\frac{\partial\rho}{\partial\ell} = \rho_0^2 g\beta_P \qquad \text{(A.8.23)}$$

Dynamic viscosity is considered here to be a function of only temperature and solute concentration, which is the typical approach, and neglects the weak dependence of viscosity on fluid pressure. In SEAWAT, an alternative equation for dynamic viscosity has been implemented:

$$\mu = \mu_T(T) + \sum_{k=1}^{NS}\frac{\partial\mu}{\partial C^k}\left(C^k - C_0^k\right) = 239.4x10^{-7}\ 10^{\left(\frac{248.37}{T+133.15}\right)} \qquad \text{(A.8.24)}$$

Appendix B

Comparison between calculated and measured values of groundwater temperature in study cases as

Case1a: Trending heterogeneity and isotropy

Case1b: Trending heterogeneity and anisotropy

Case1c: Trending heterogeneity and large anisotropyisotropy

Case2a: Stationary heterogeneity and isotropy

Case2b: Stationary heterogeneity and anisotropy

Case2c: Stationary heterogeneity and large anisotropyisotropy

Case3: Case1b with tenth value in vertical hydraulic conductivity of riverbed

Case4: Case1b with twice value in river width

Case5: Case1b with isotropy condition in thermal diffusivity

Case6: Case1b with tenth value in ranges in variograms

Case7: Case1b with no-temperature dependence of fluid

Case8a: Block averaged of Case1a

Case8b: Block averaged of Case1b

Case 1a
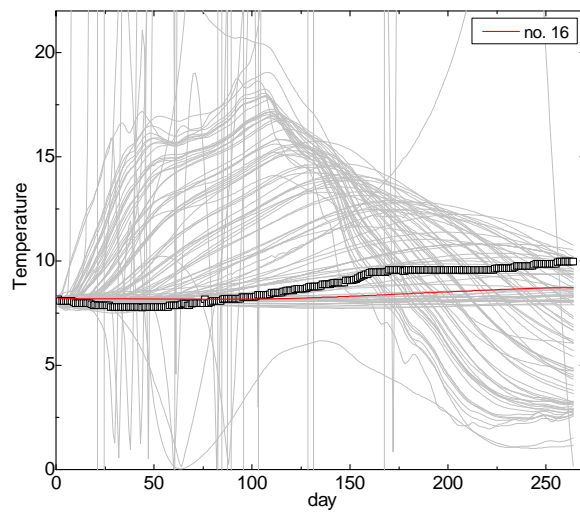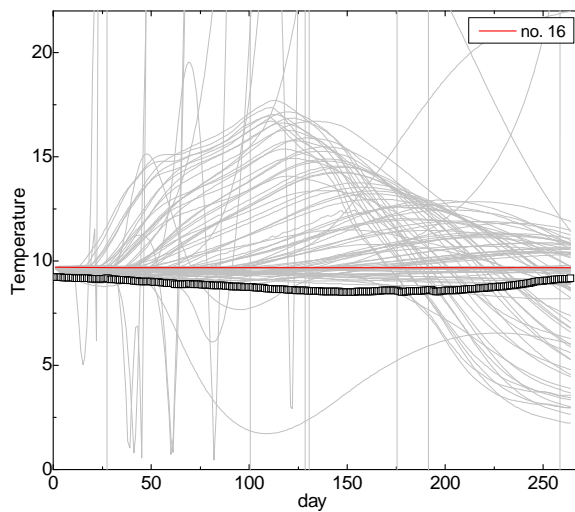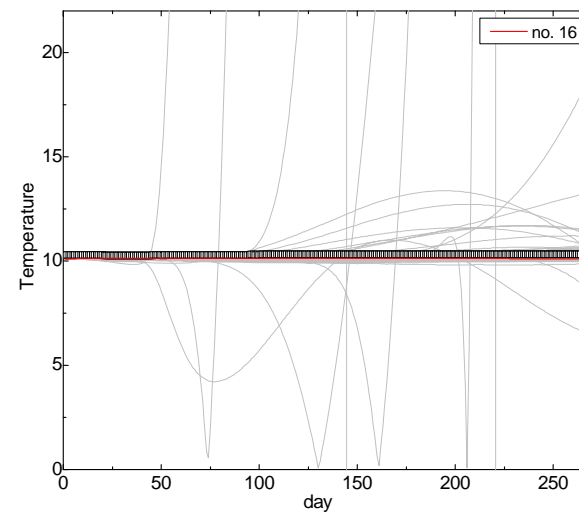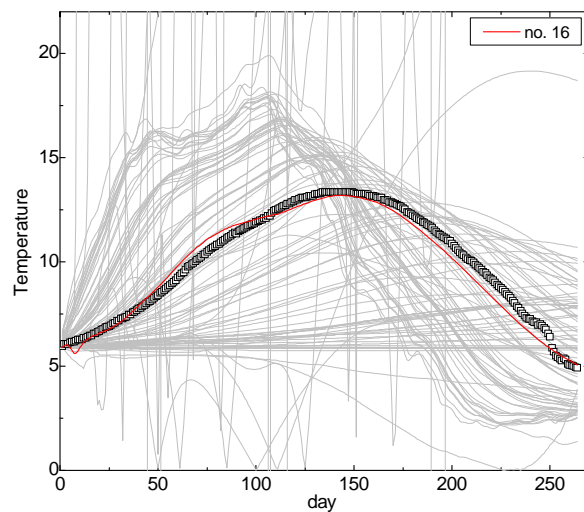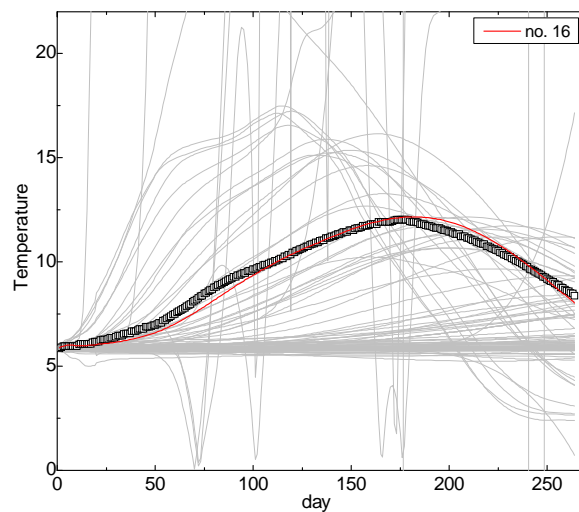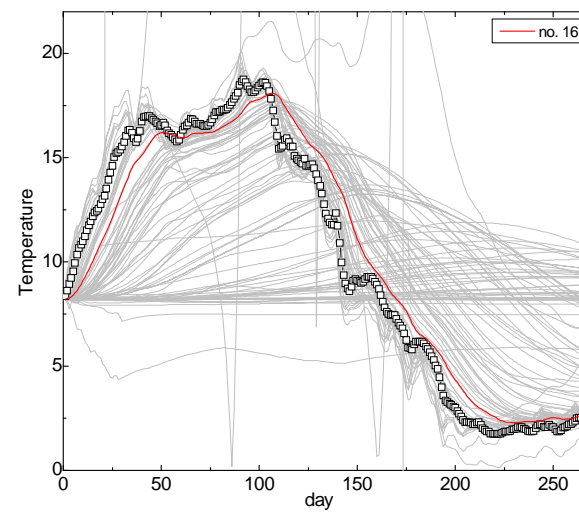
Case 1b

BW3-1: *Z*= 15m

BW3-1: *Z*= 30m

BW3-1: *Z*= 60m

BW3-2: *Z*= 5m

BW3-4: *Z*= 10.5m

BW3-5: *Z*= 4m
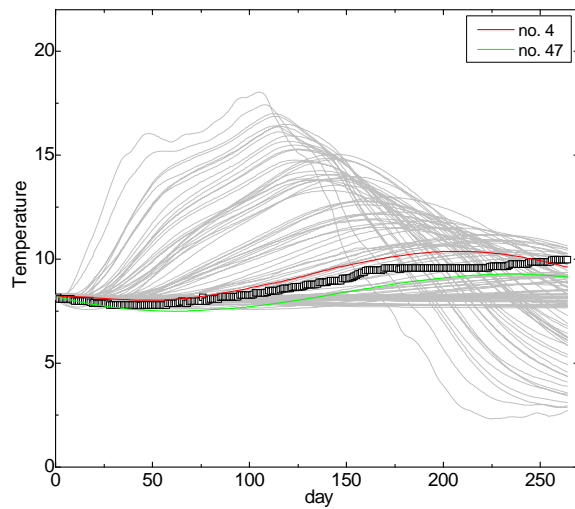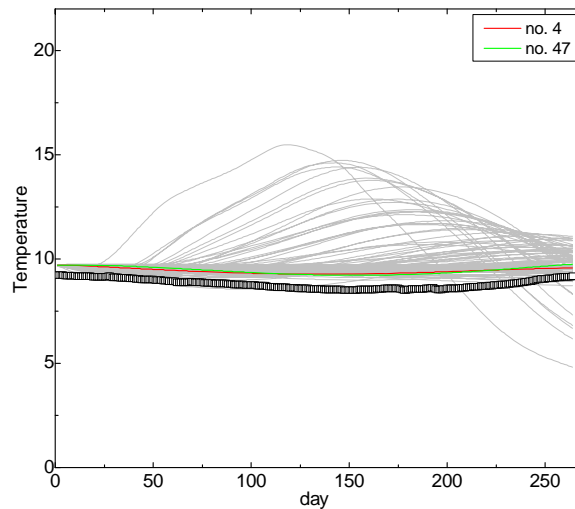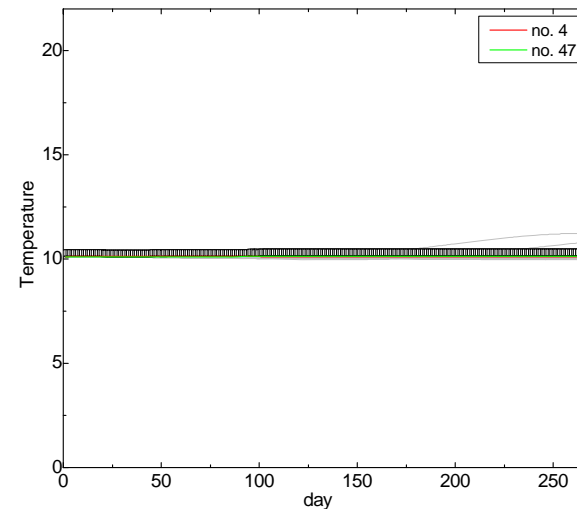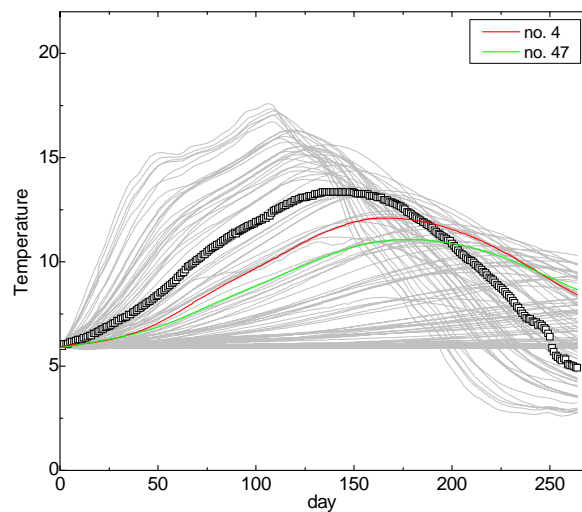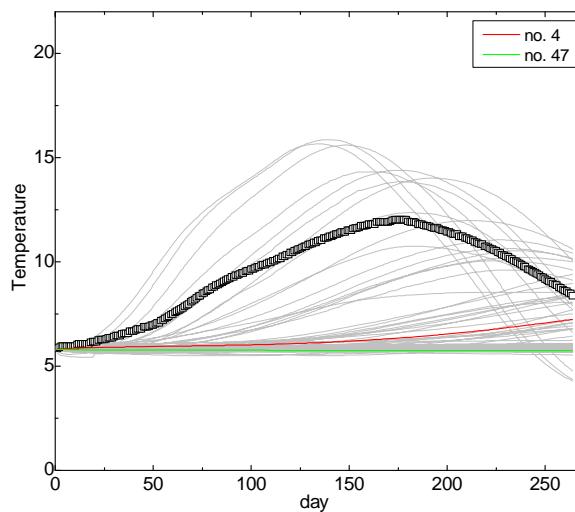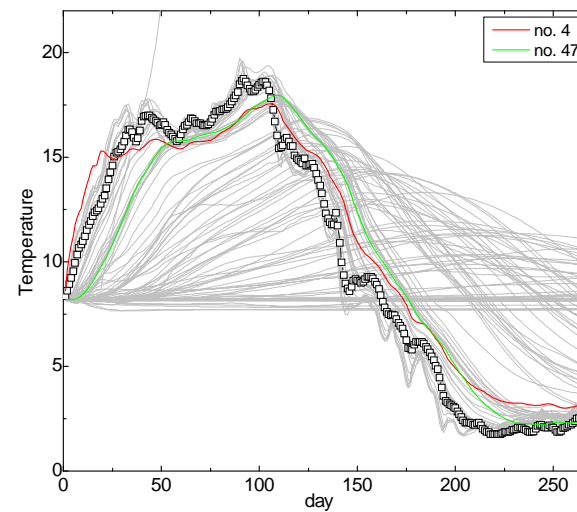
Case 1c

BW3-1: *Z*= 15m
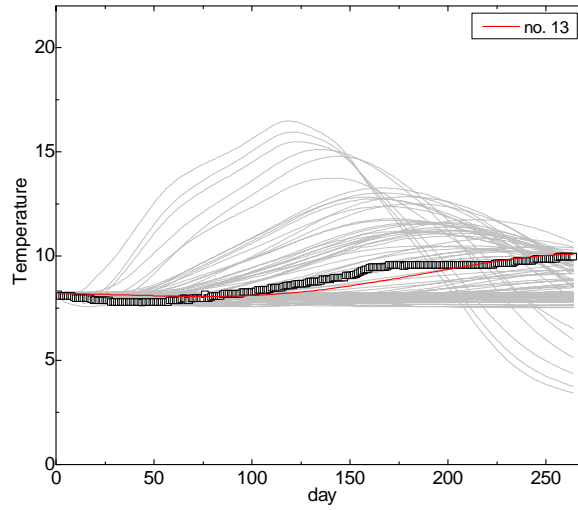
BW3-1: *Z*= 30m
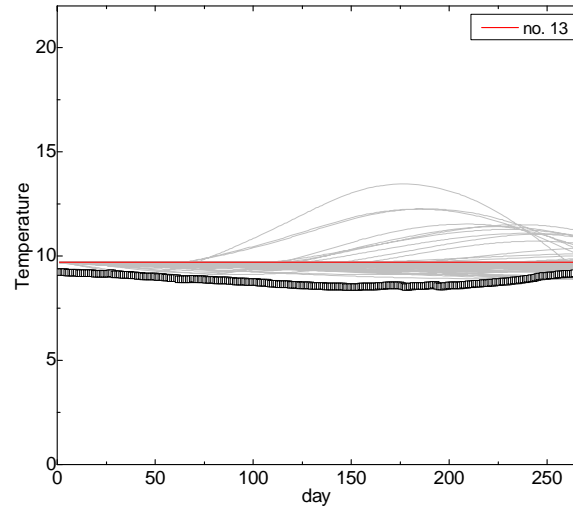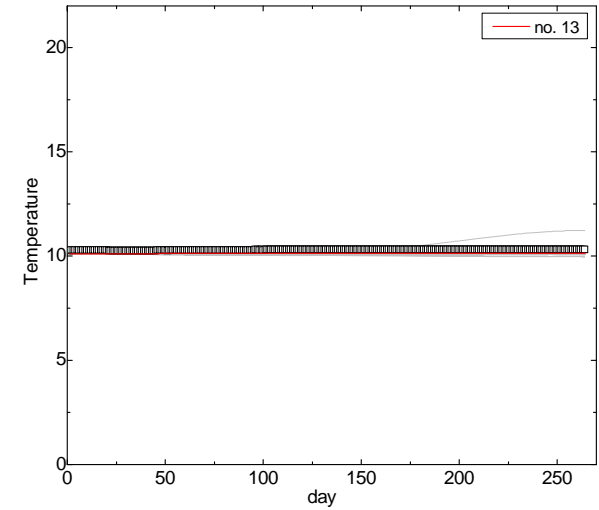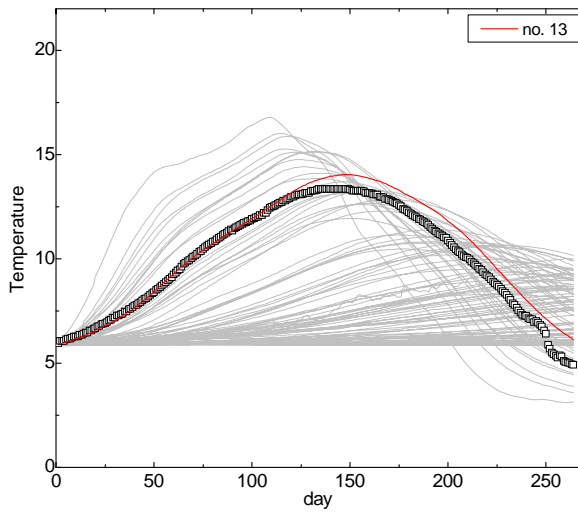
BW3-1: *Z*= 60m
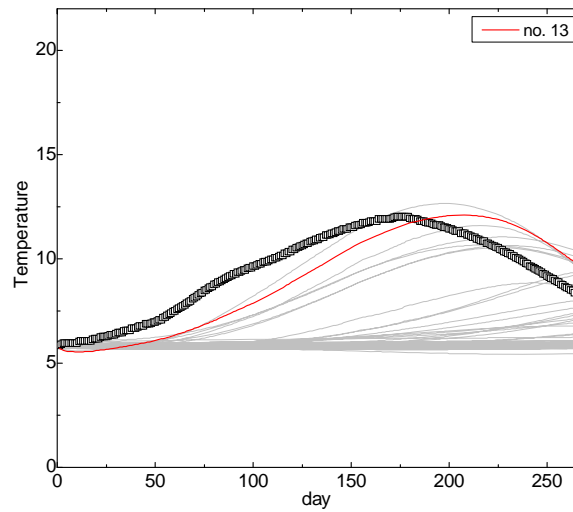
BW3-2: *Z*= 5m
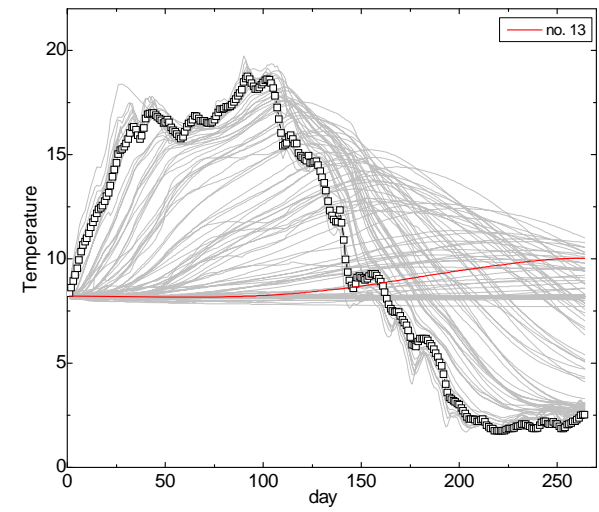
BW3-4: *Z*= 10.5m

BW3-5: *Z*= 4m

Case 2a

BW3-1: Z= 15m   BW3-1: Z= 30m   BW3-1: Z= 60m
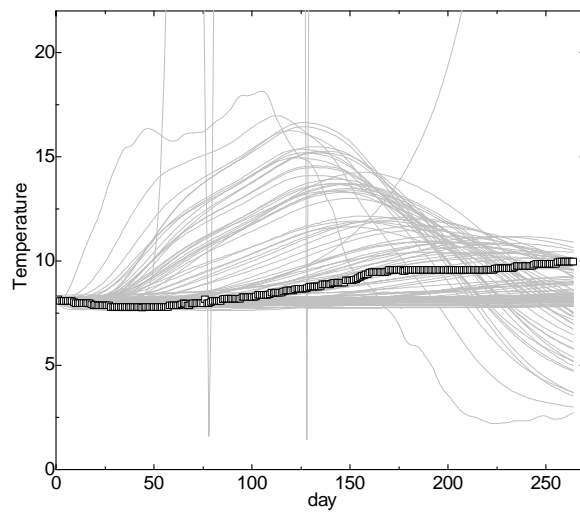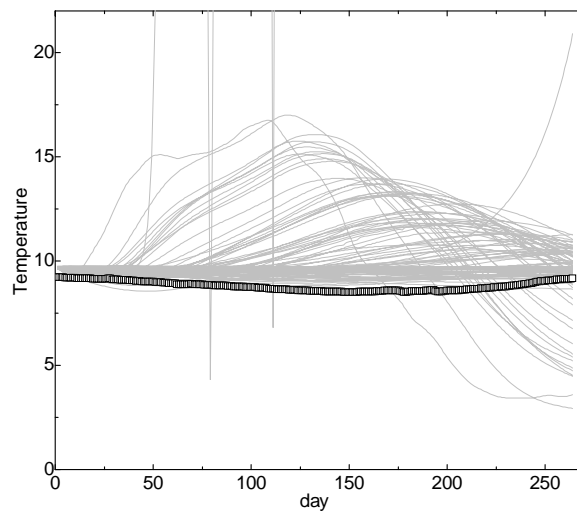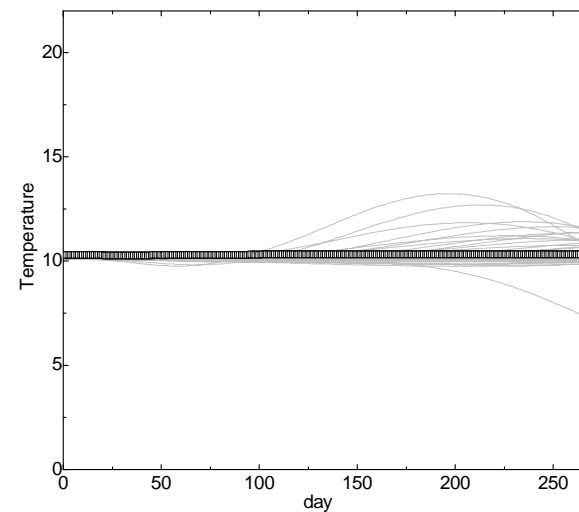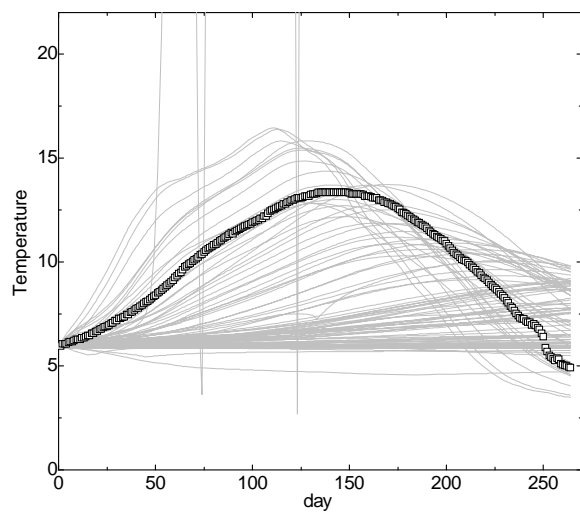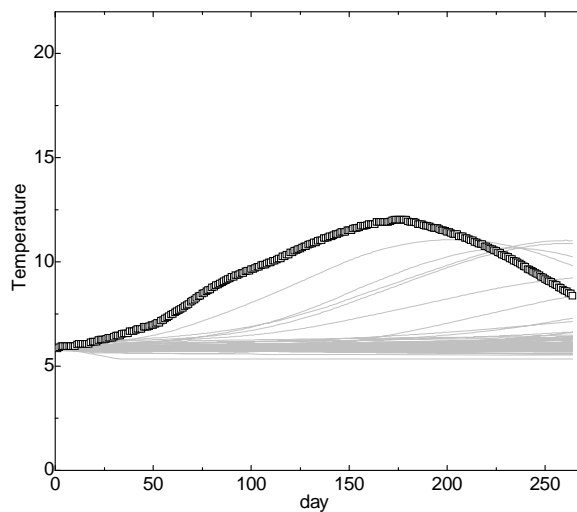
BW3-2: Z= 5m   BW3-4: Z= 10.5m   BW3-5: Z= 4m
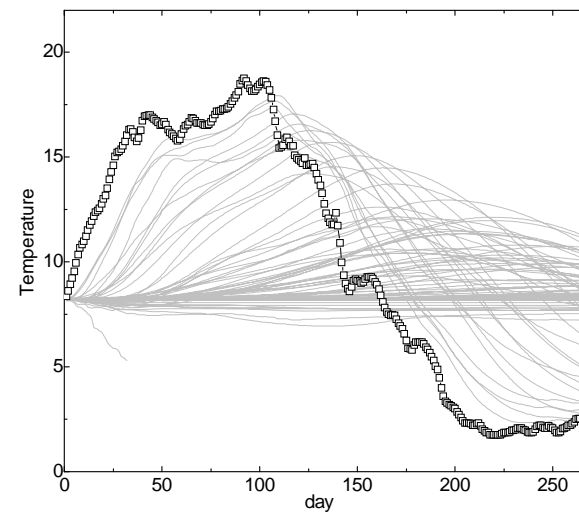
Case 2b

BW3-1: Z= 15m
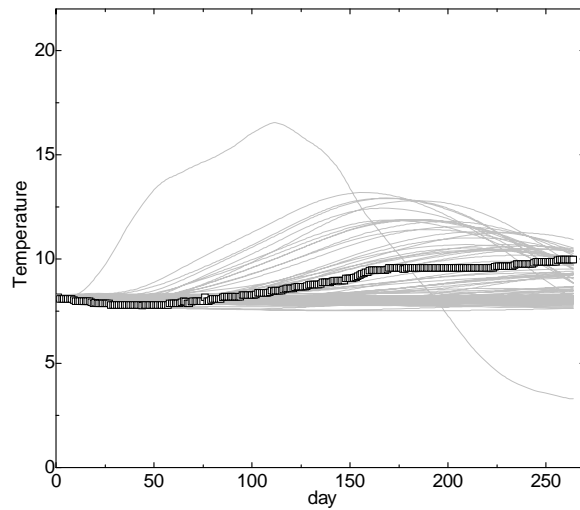
BW3-1: Z= 30m
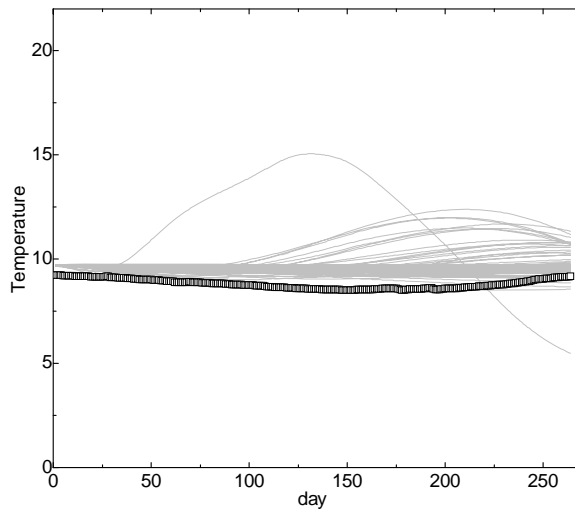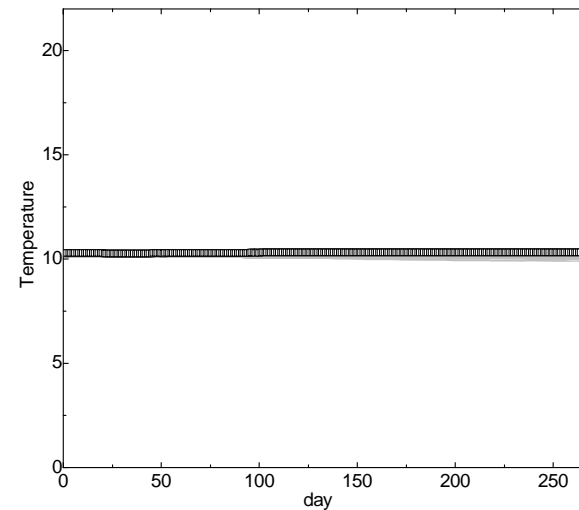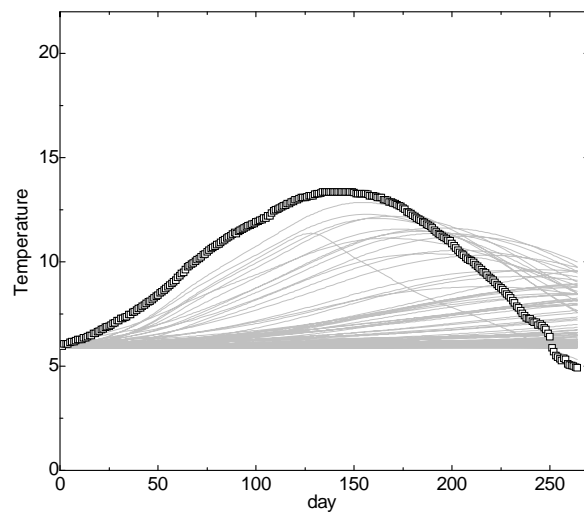
BW3-1: Z= 60m
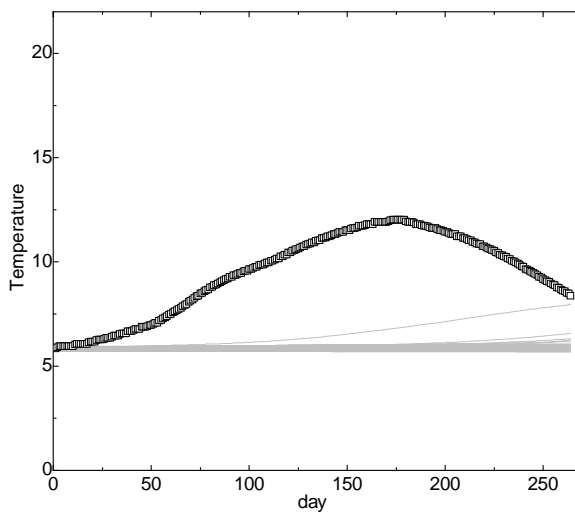
BW3-2: Z= 5m
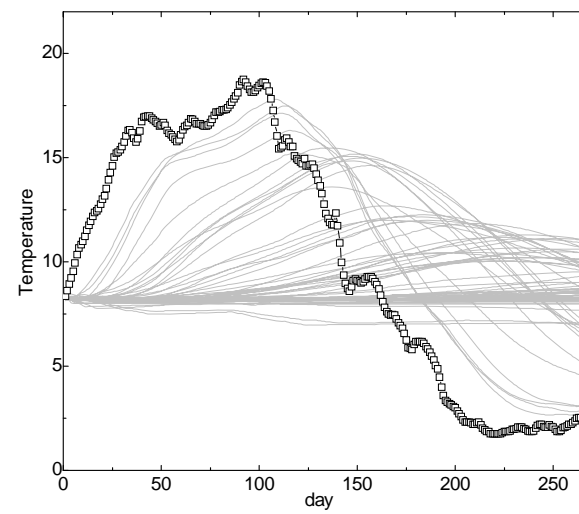
BW3-4: Z= 10.5m

BW3-5: Z= 4m

Case 2c

BW3-1: *Z*= 15m
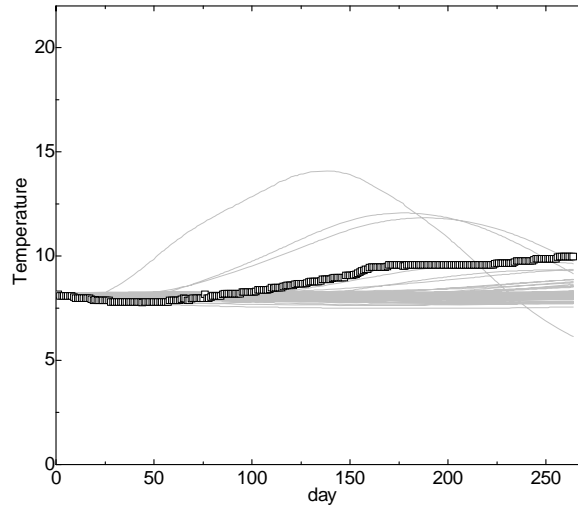
BW3-1: *Z*= 30m
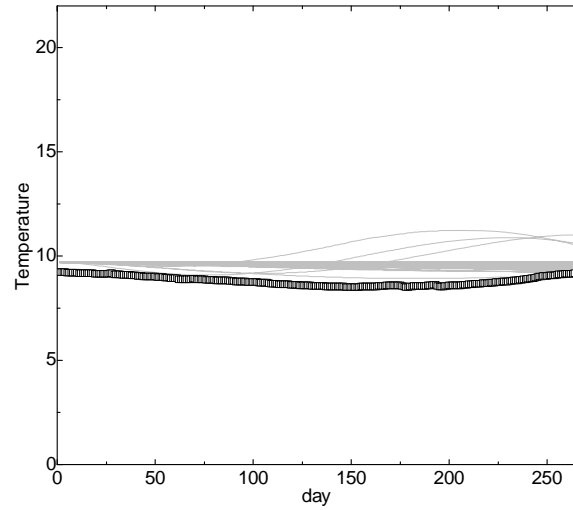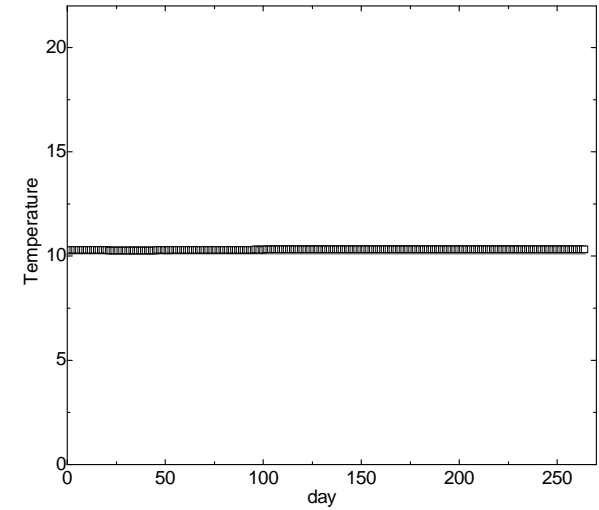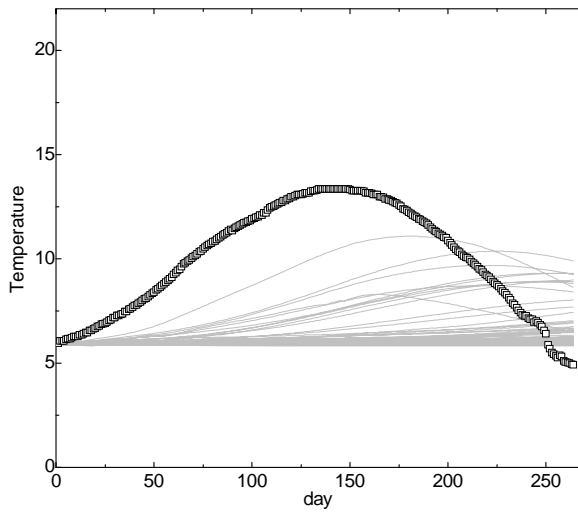
BW3-1: *Z*= 60m
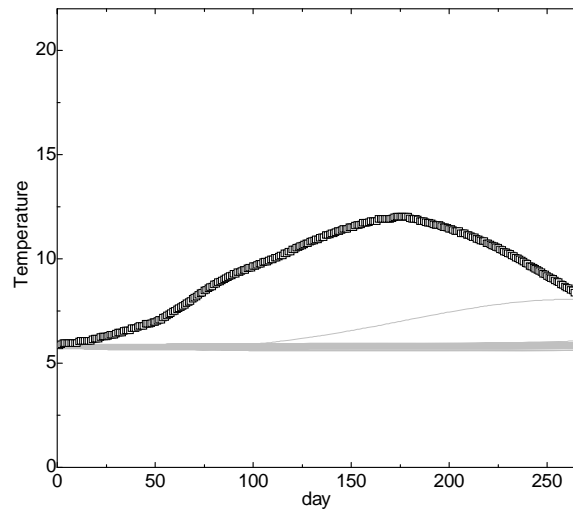
BW3-2: *Z*= 5m
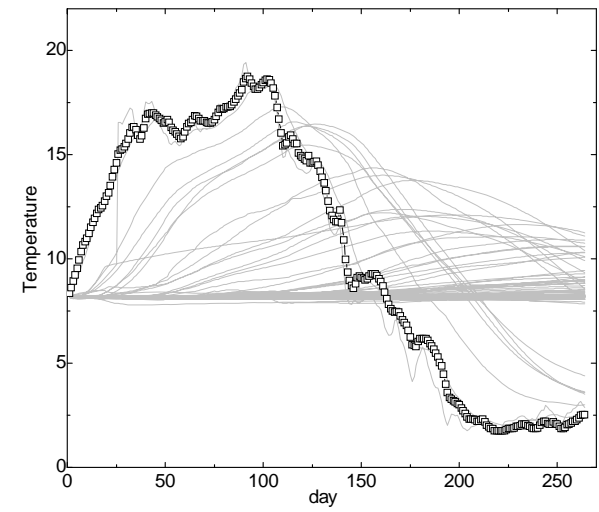
BW3-4: *Z*= 10.5m

BW3-5: *Z*= 4m

Case 3

BW3-1: Z= 15m
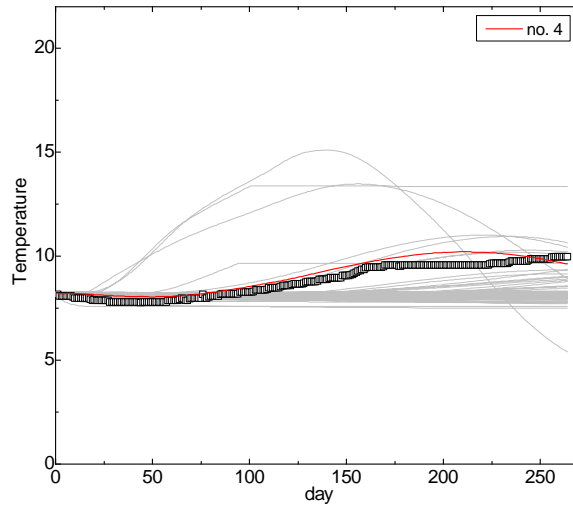
BW3-1: Z= 30m
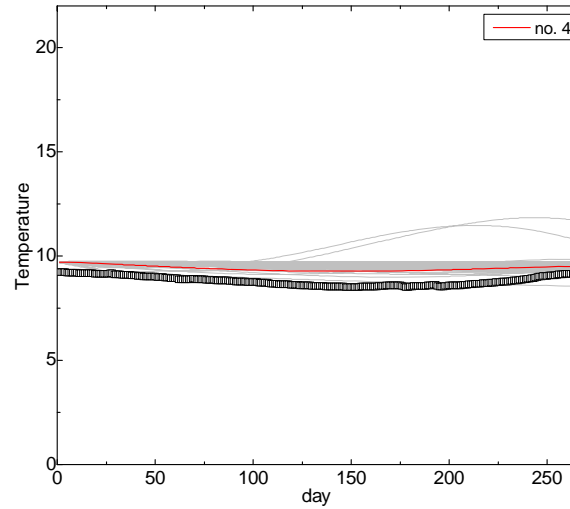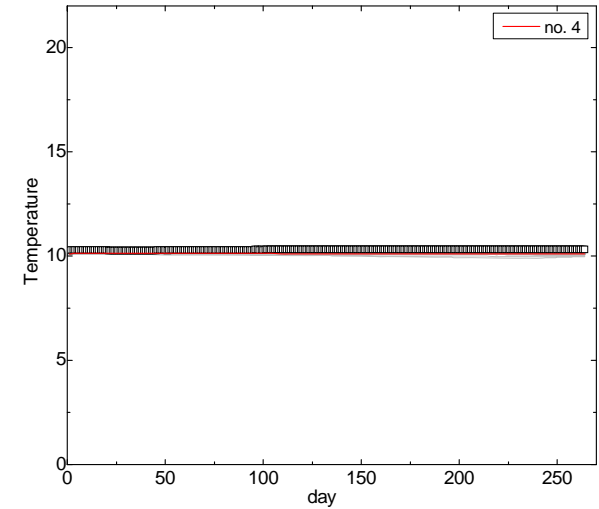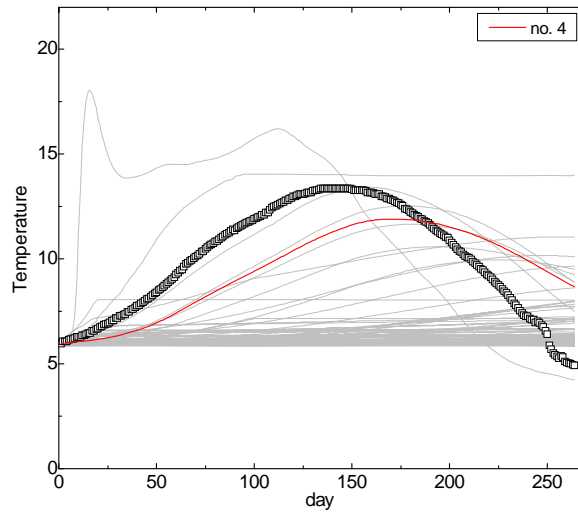
BW3-1: Z= 60m
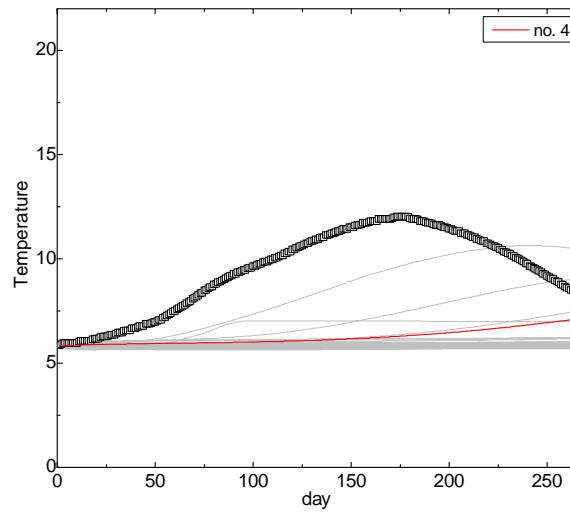
BW3-2: Z= 5m
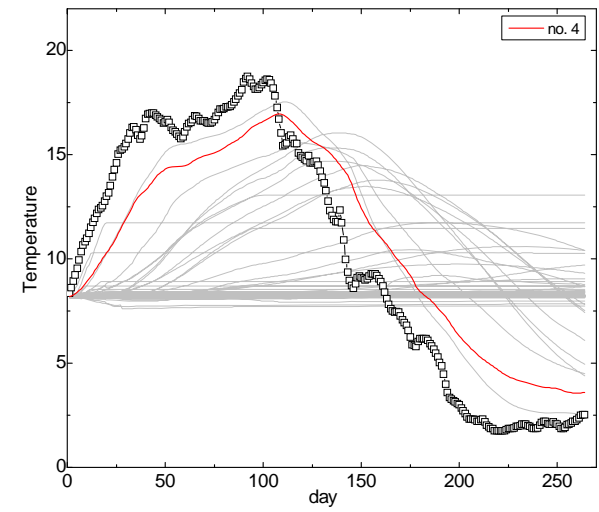
BW3-4: Z= 10.5m

BW3-5: Z= 4m

Case 4

BW3-1: Z= 15m
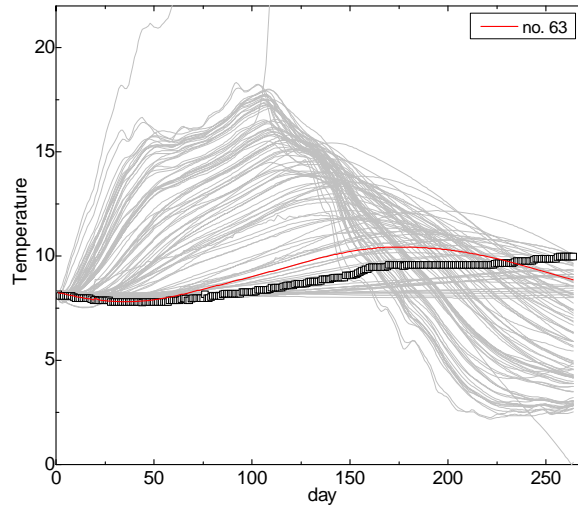
BW3-1: Z= 30m
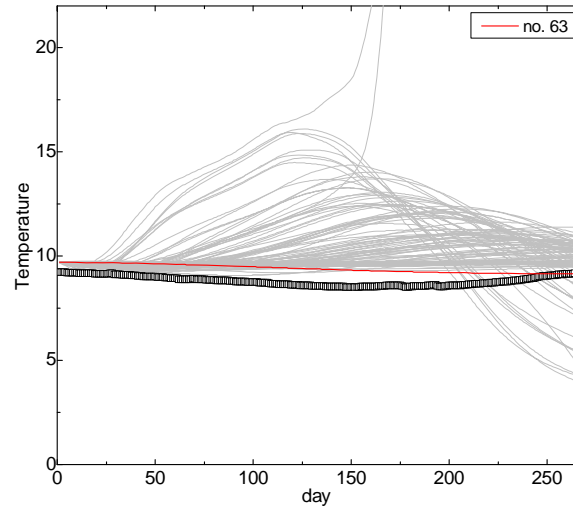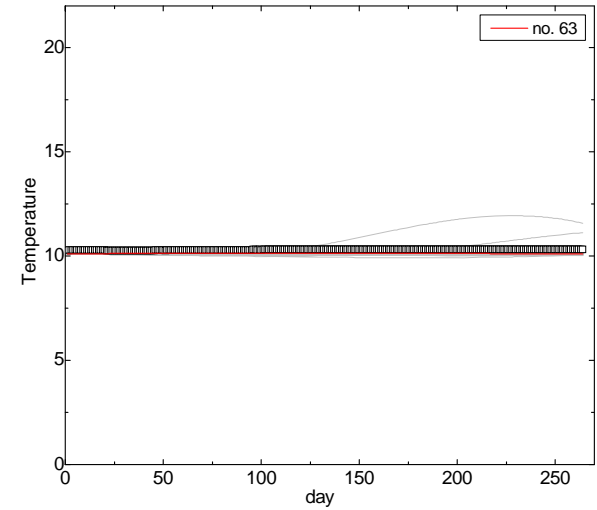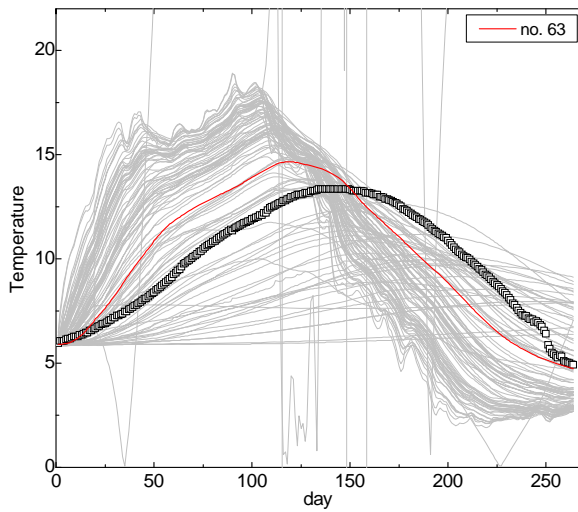
BW3-1: Z= 60m
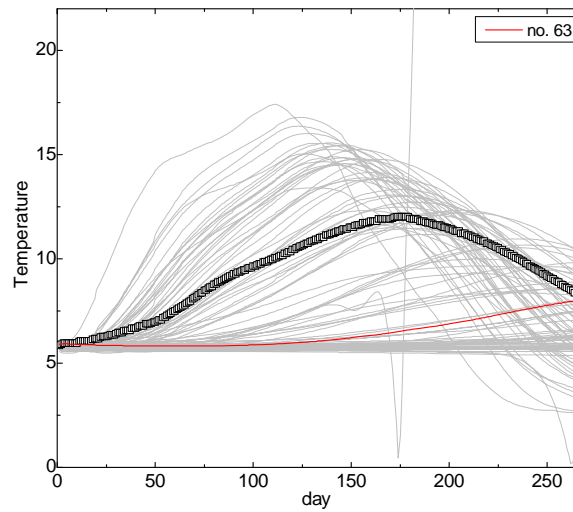
BW3-2: Z= 5m
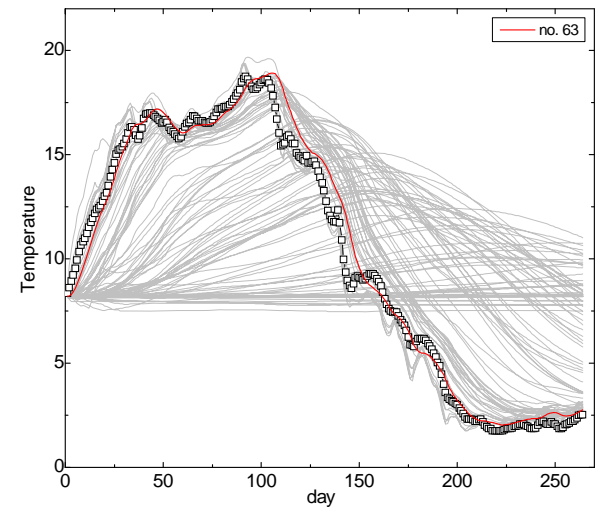
BW3-4: Z= 10.5m

BW3-5: Z= 4m

Case 5

BW3-1: Z= 15m
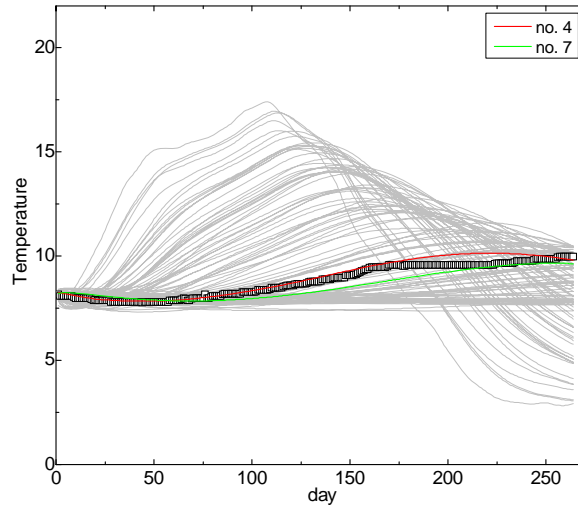
BW3-1: Z= 30m
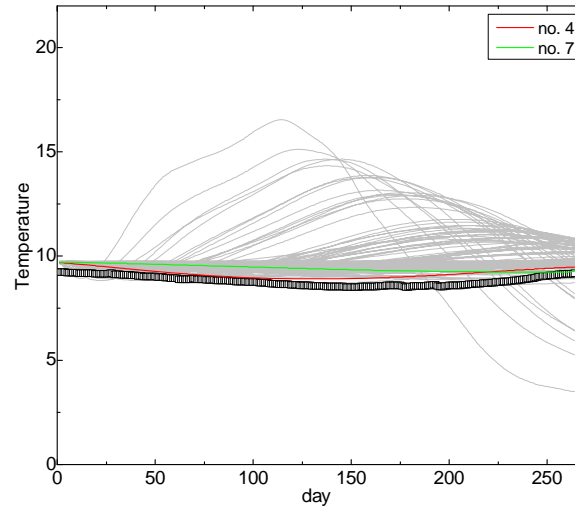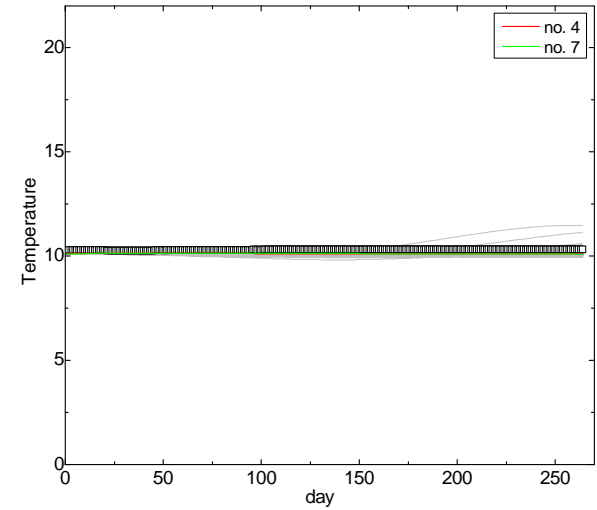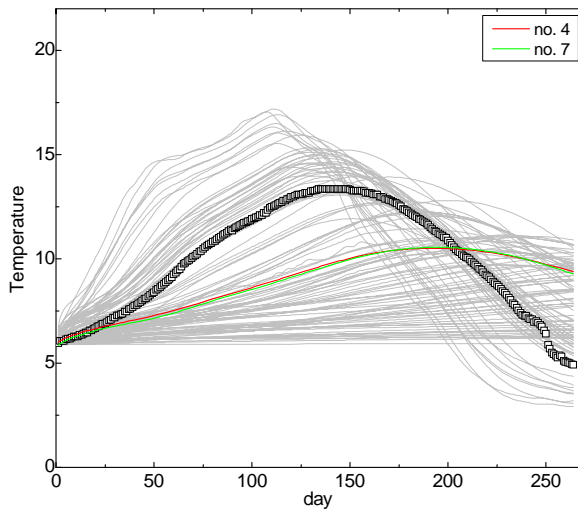
BW3-1: Z= 60m
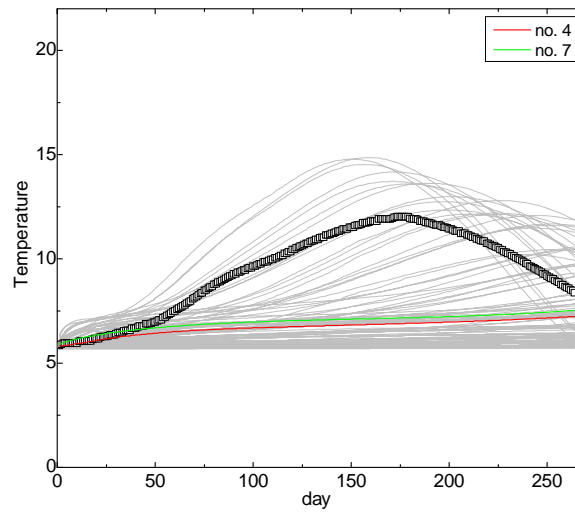
BW3-2: Z= 5m
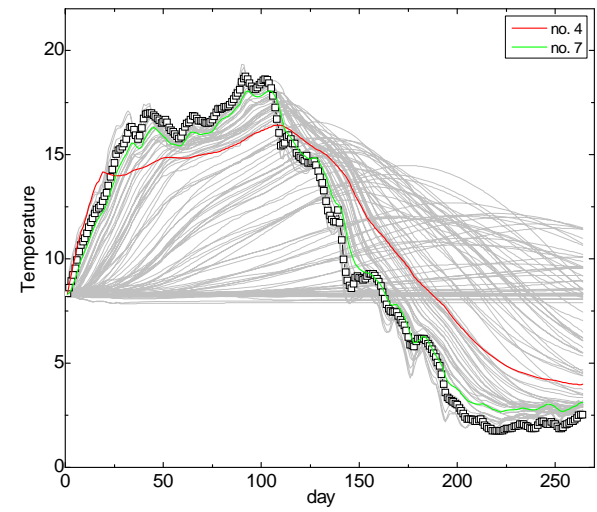
BW3-4: Z= 10.5m

BW3-5: Z= 4m

Case 6

BW3-1: Z= 15m
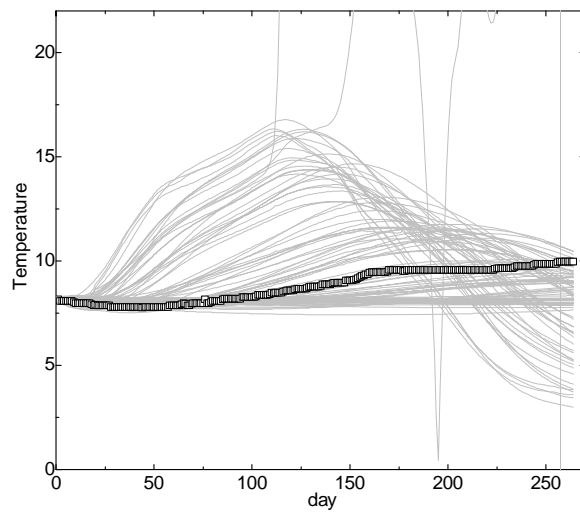
BW3-1: Z= 30m
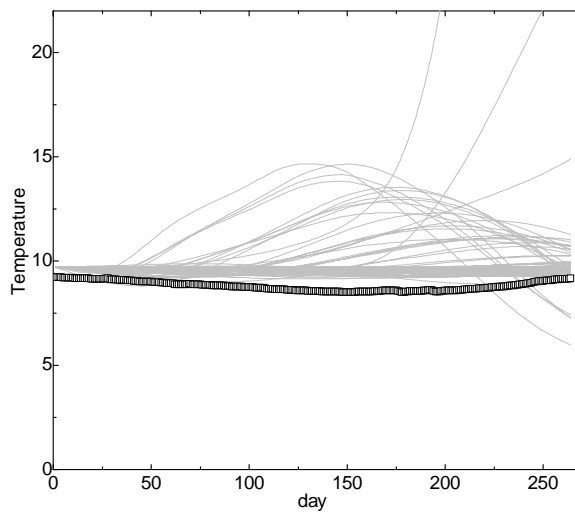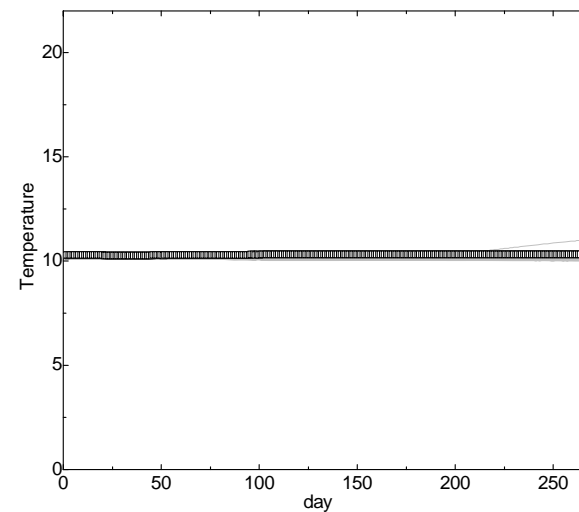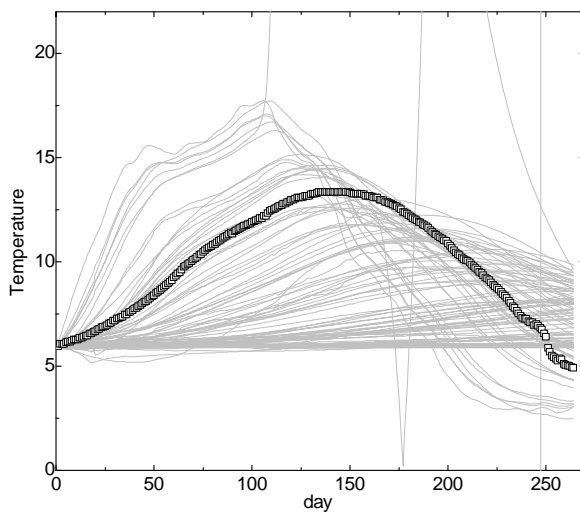
BW3-1: Z= 60m
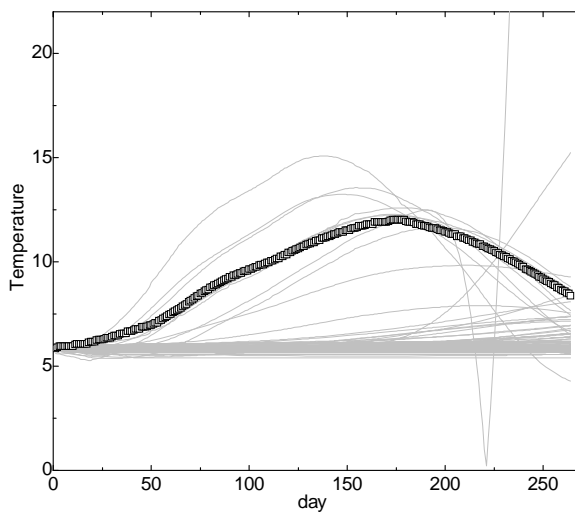
BW3-2: Z= 5m
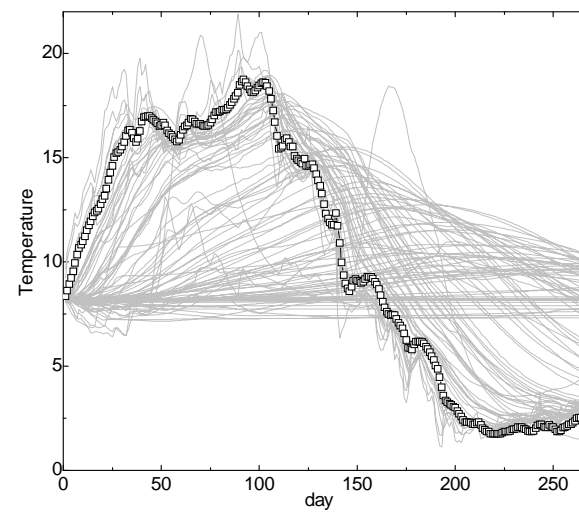
BW3-4: Z= 10.5m

BW3-5: Z= 4m

Case 7

BW3-1: *Z*= 15m
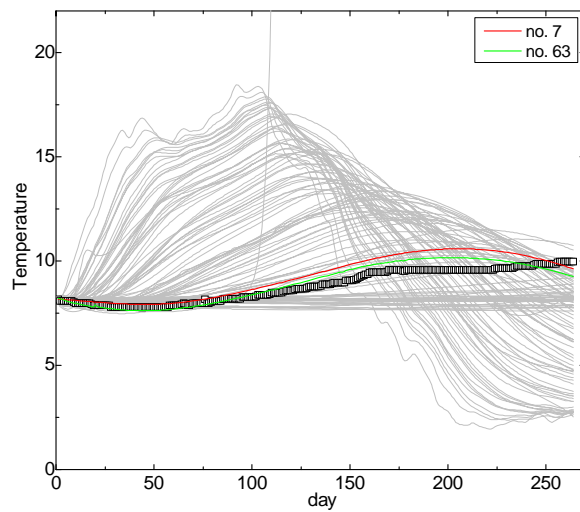
BW3-1: *Z*= 30m
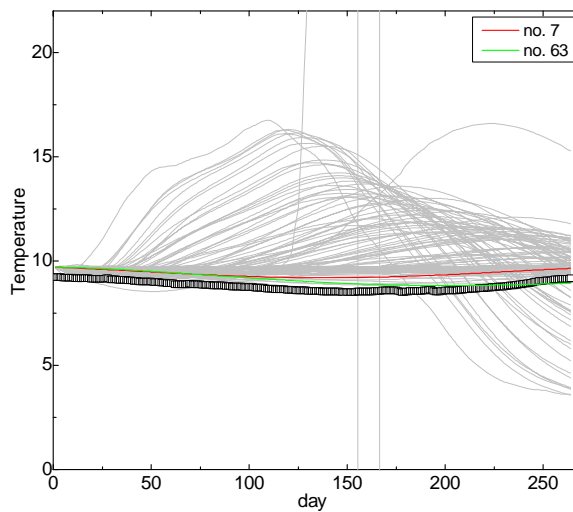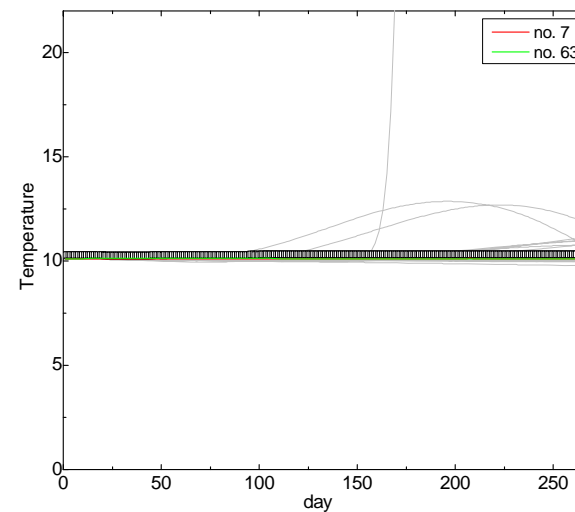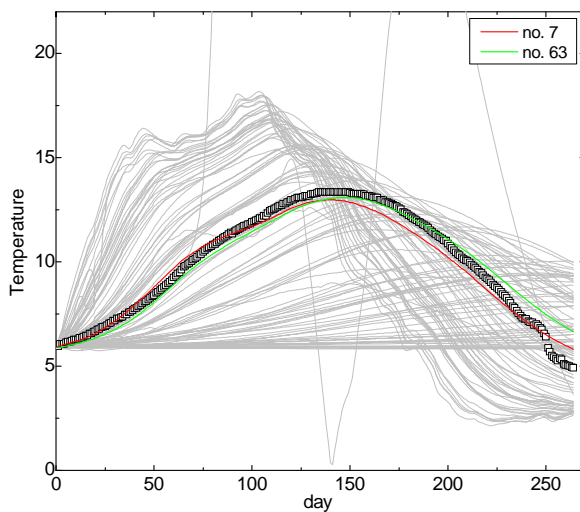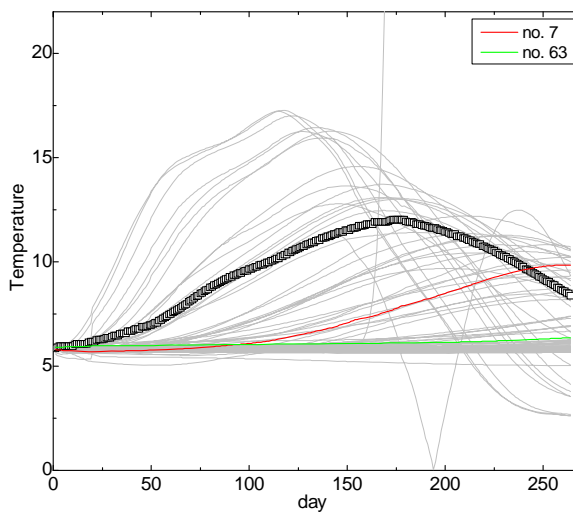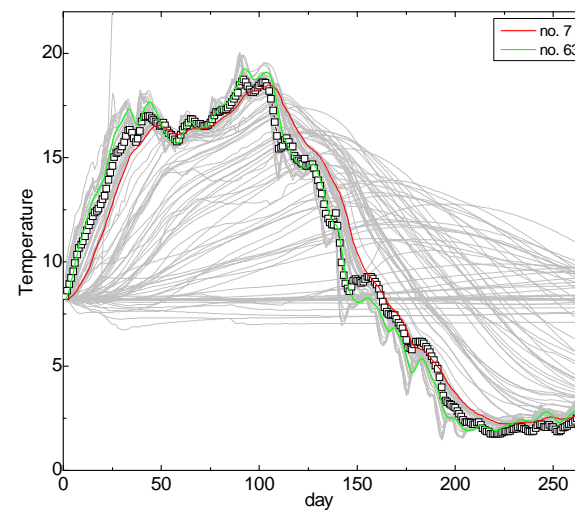
BW3-1: *Z*= 60m

BW3-2: *Z*= 5m

BW3-4: *Z*= 10.5m

BW3-5: *Z*= 4m

Case 8a
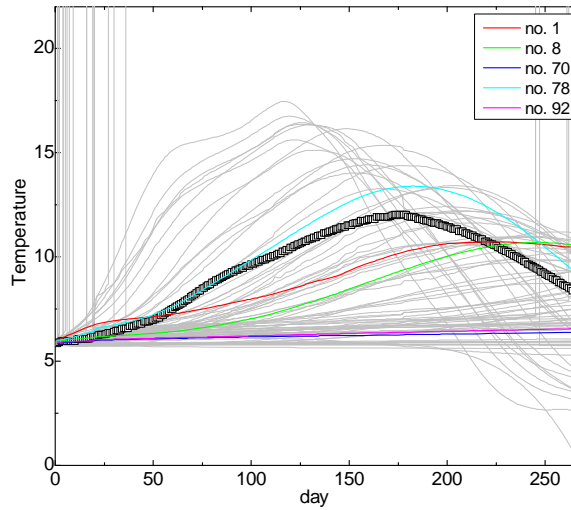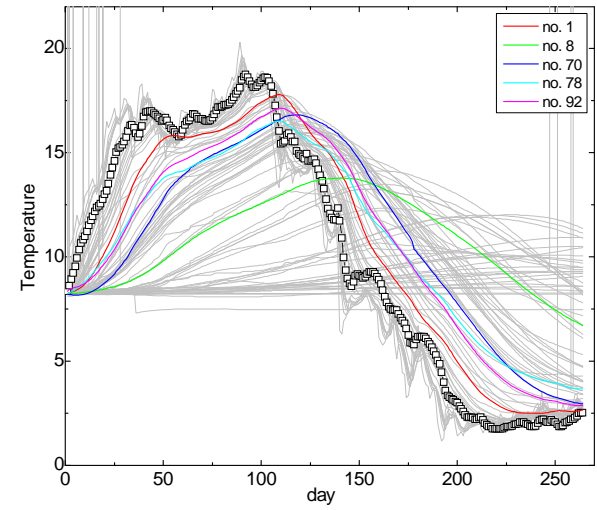
Case 8b

BW3-1: *Z*= 15m
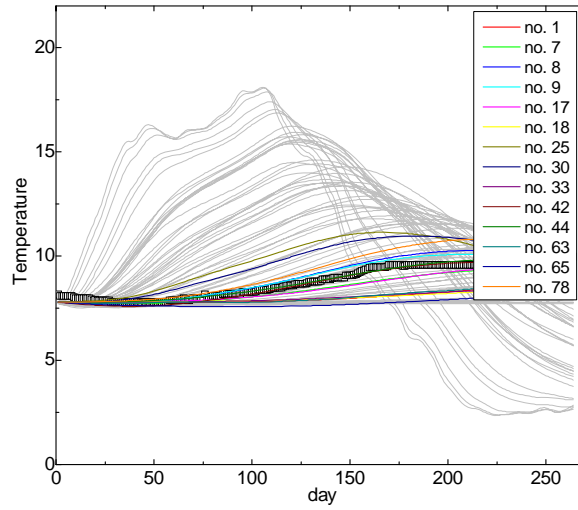
BW3-1: *Z*= 30m
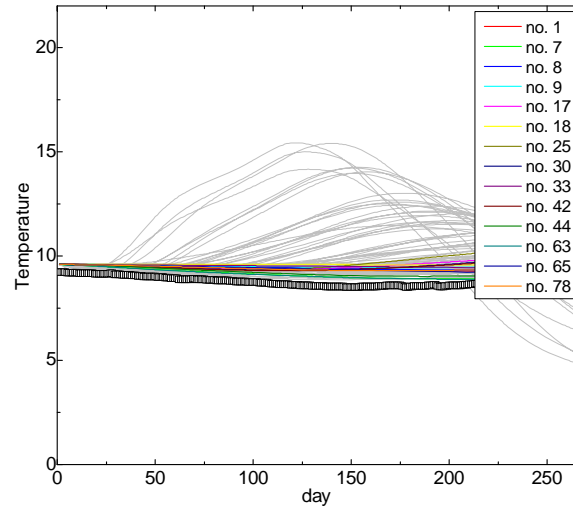
BW3-1: *Z*= 60m
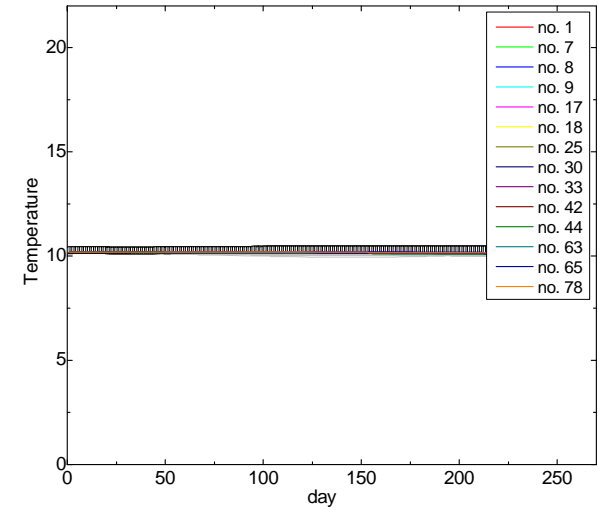
BW3-2: *Z*= 5m
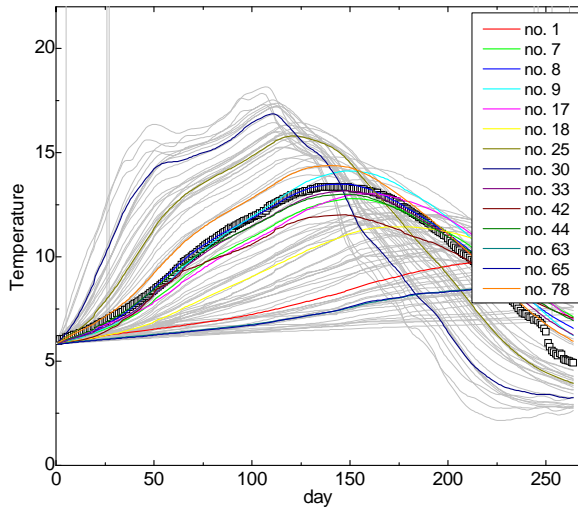
BW3-4: *Z*= 10.5m
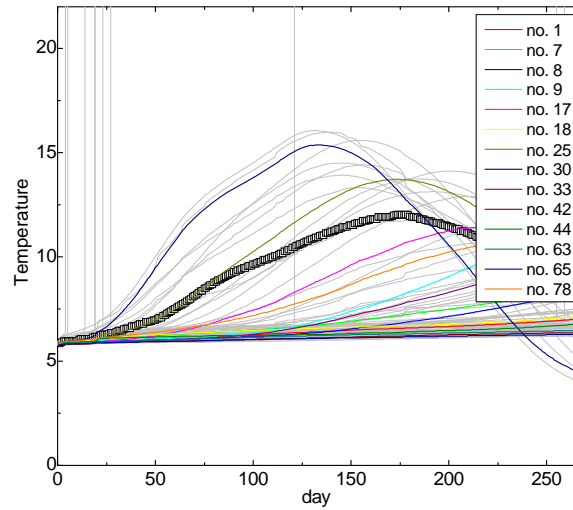
BW3-5: *Z*= 4m
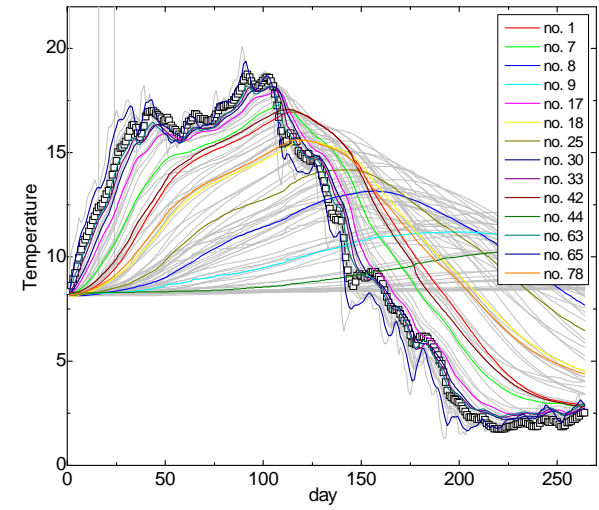
Appendix C

Simulation results of selected optimum in each study case at the last period (t_i= 264day), Blue lines, red lines, and green arrows show groundwater head contours, temperature contours, and flow velocity vectors (a: directions and b: magnitudes), respectively.
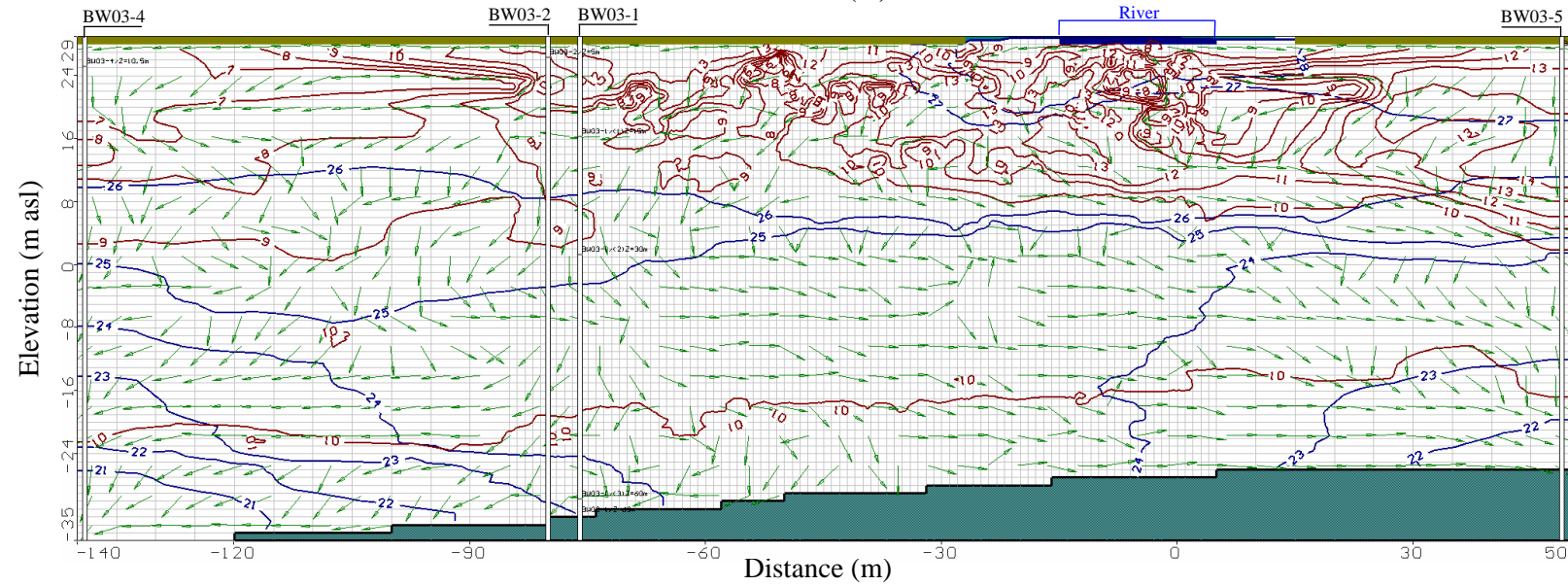
Case 1a

Realization no.16; T=50days; Maximum velocity = 260 m/d
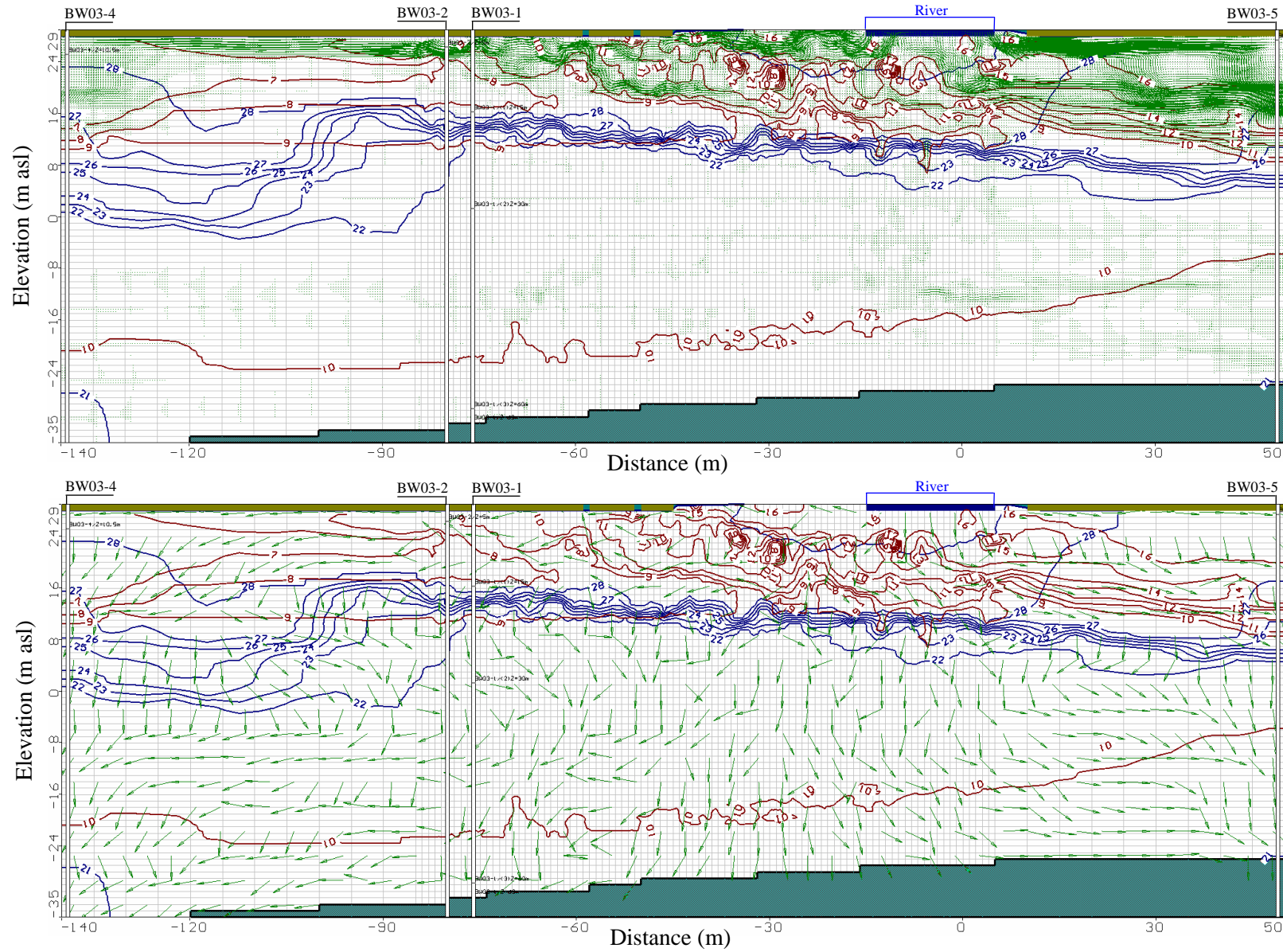
Case 1a

Realization no.16; T=150days; Maximum velocity = 240 m/d
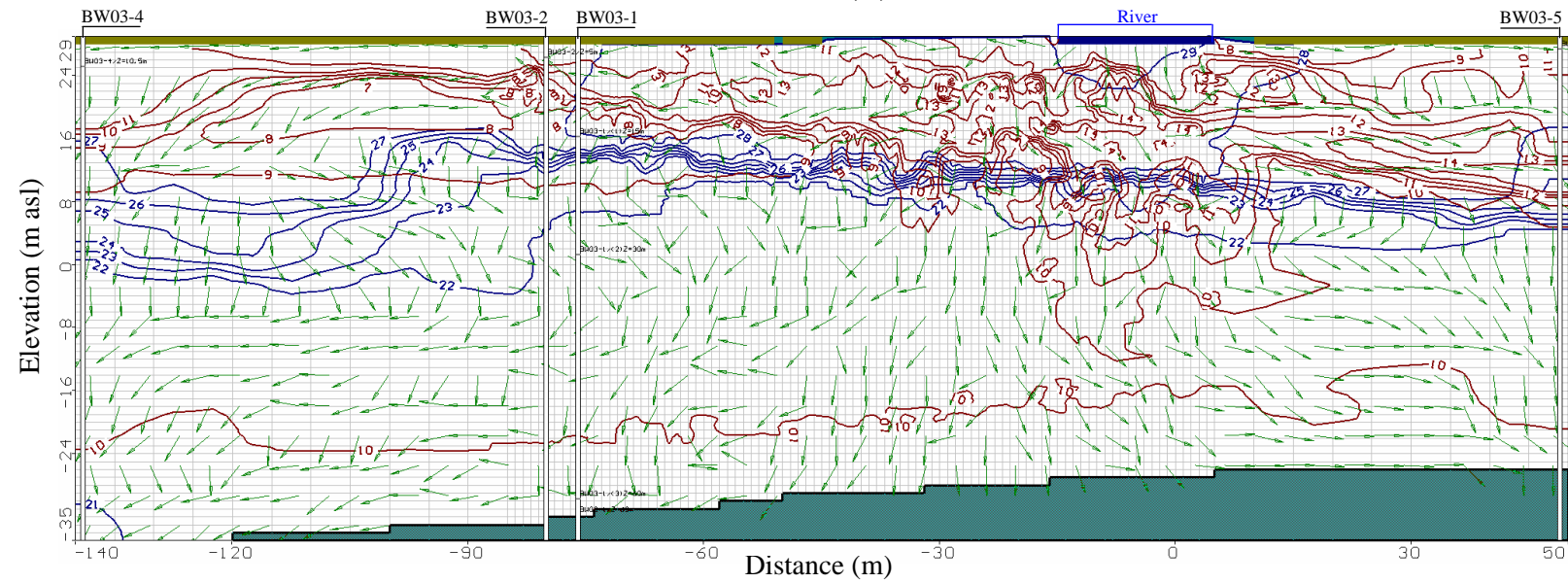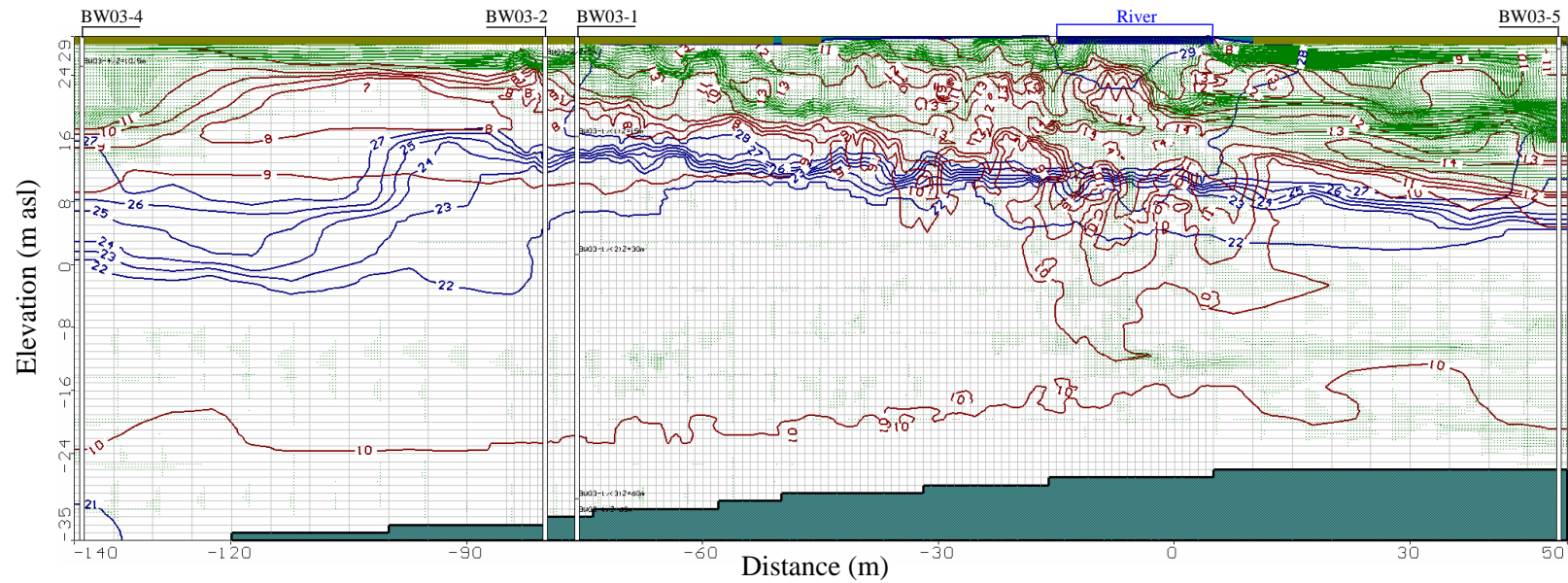
Case 1a
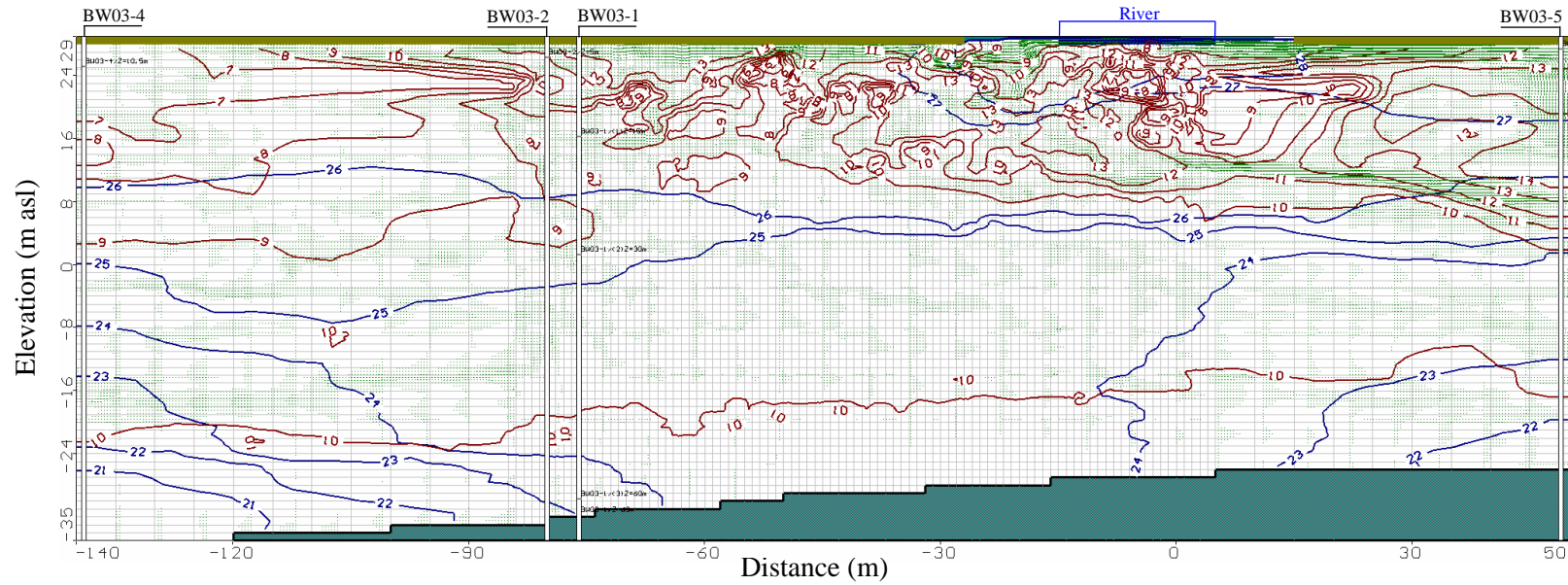
Realization no.16; T=264days; Maximum velocity = 270 m/d
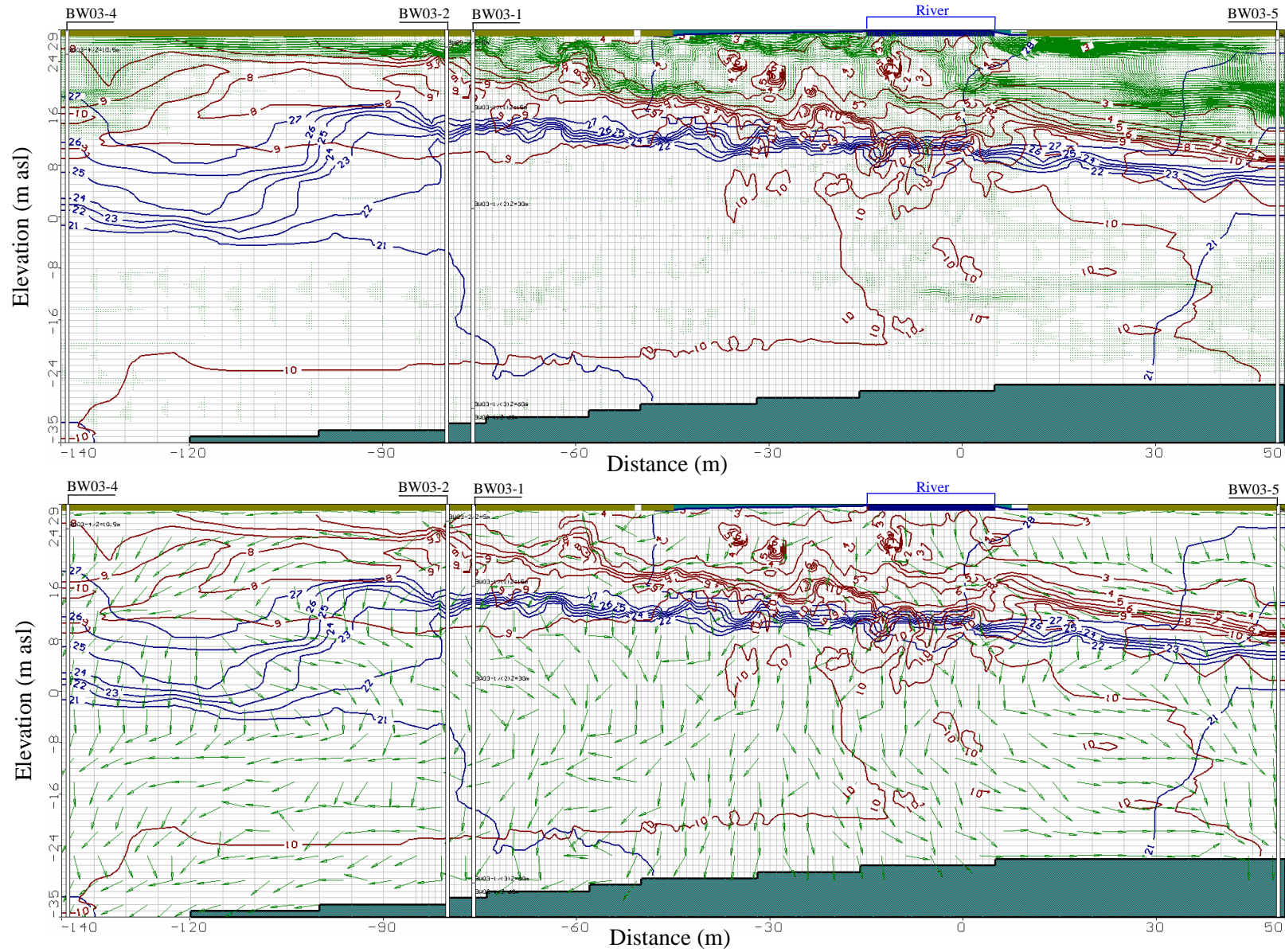
Case 1b

Realization no.4; T=50days; Maximum velocity = 130 m/d
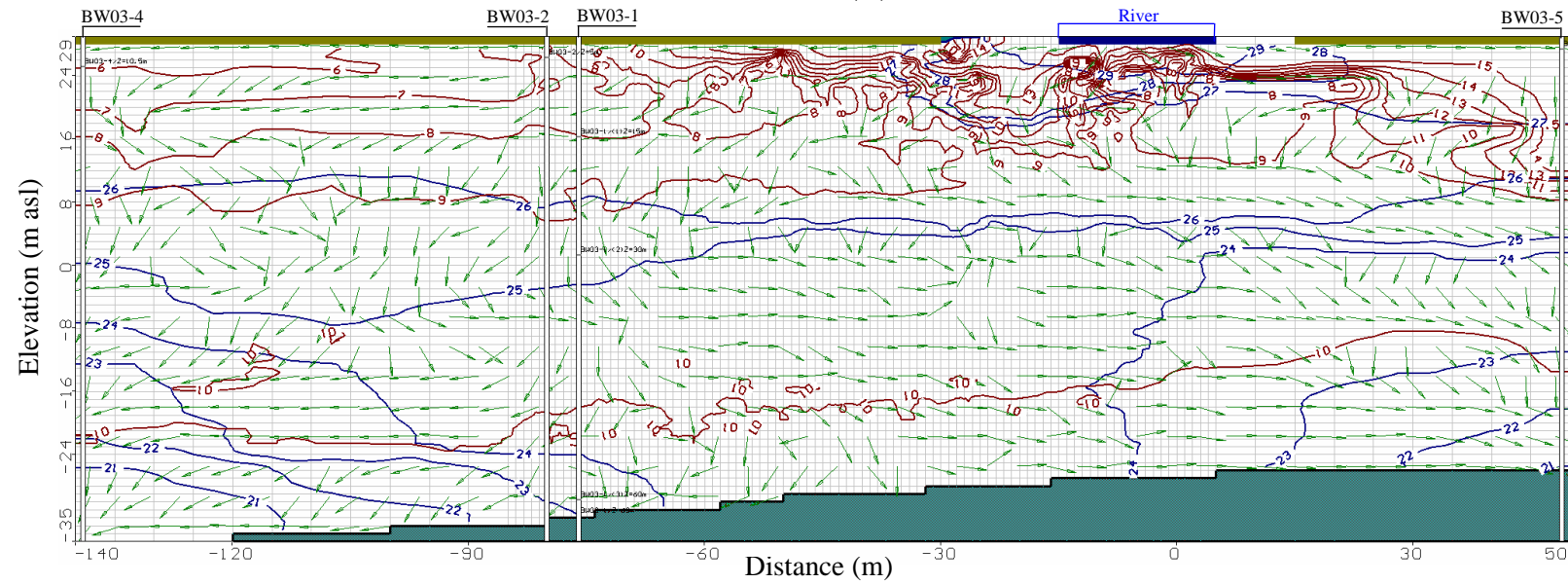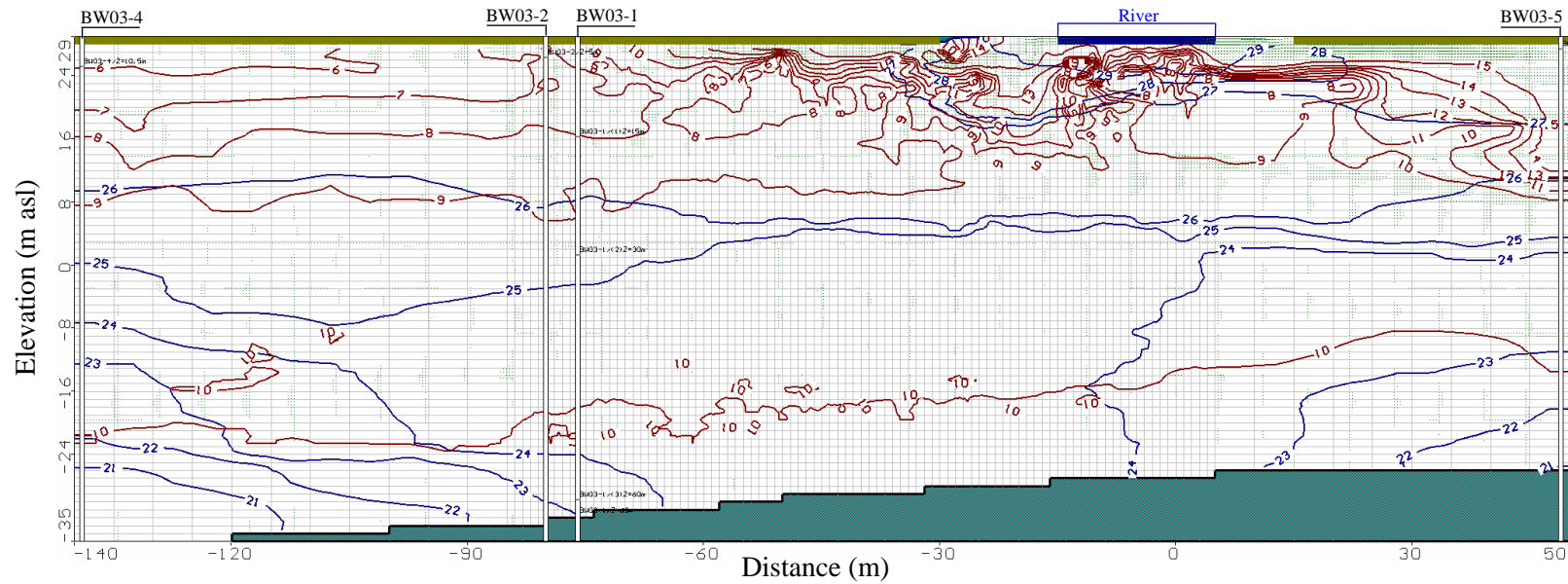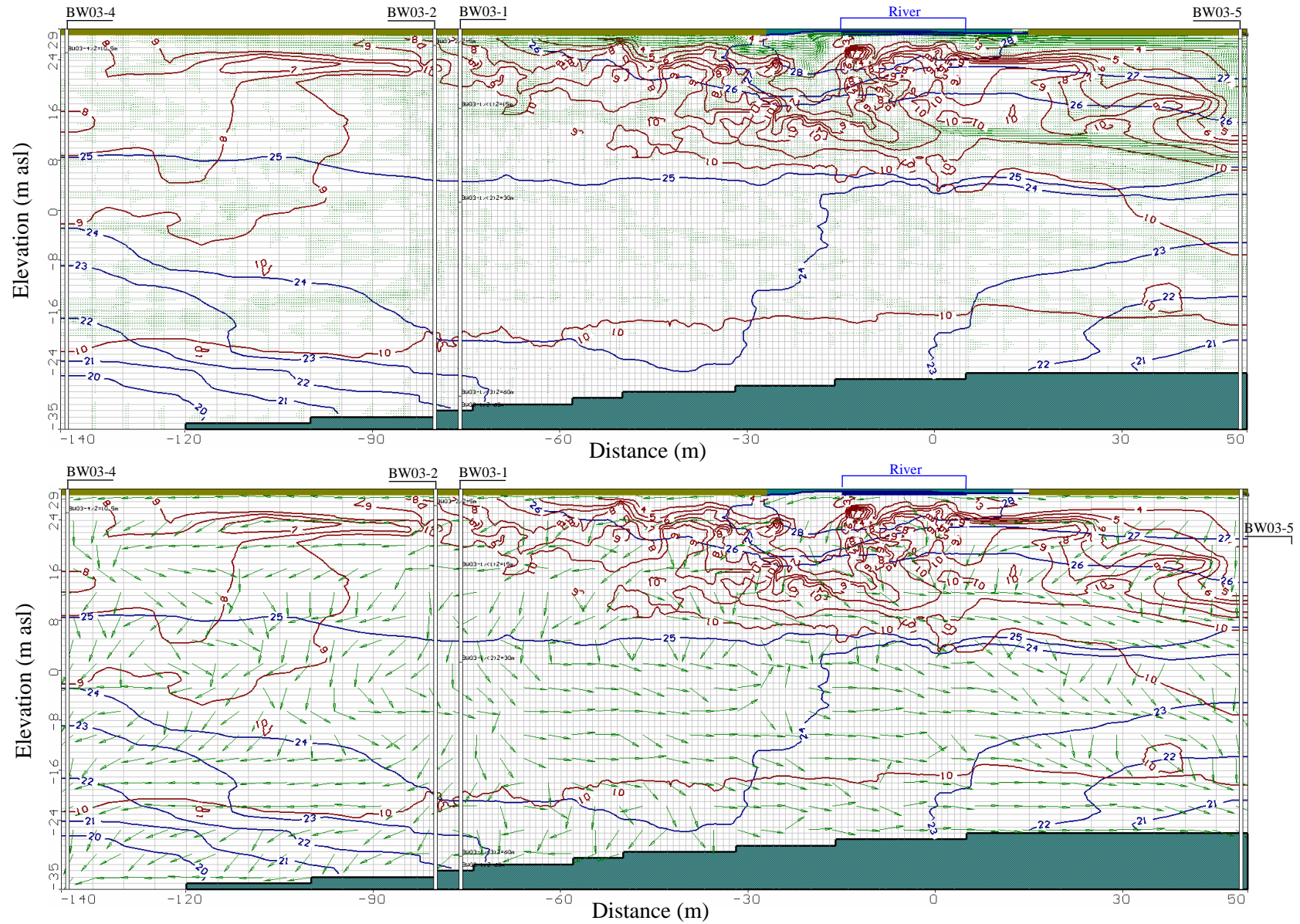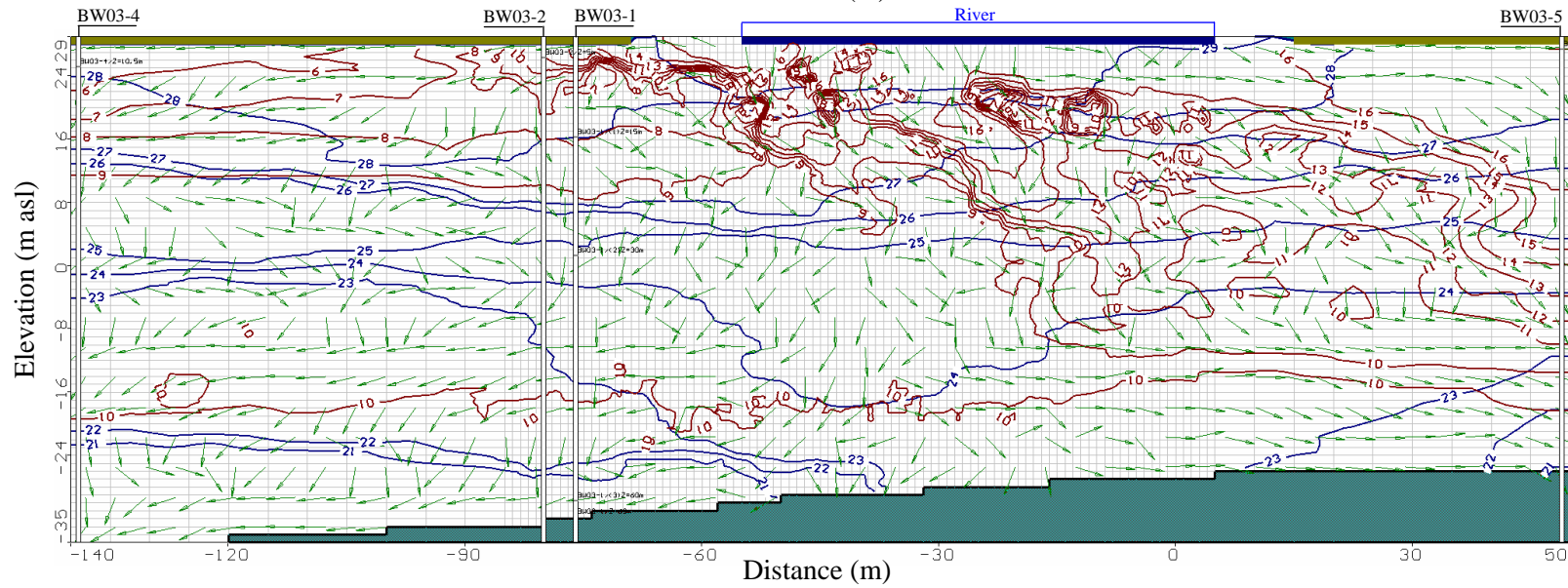
Case 1b

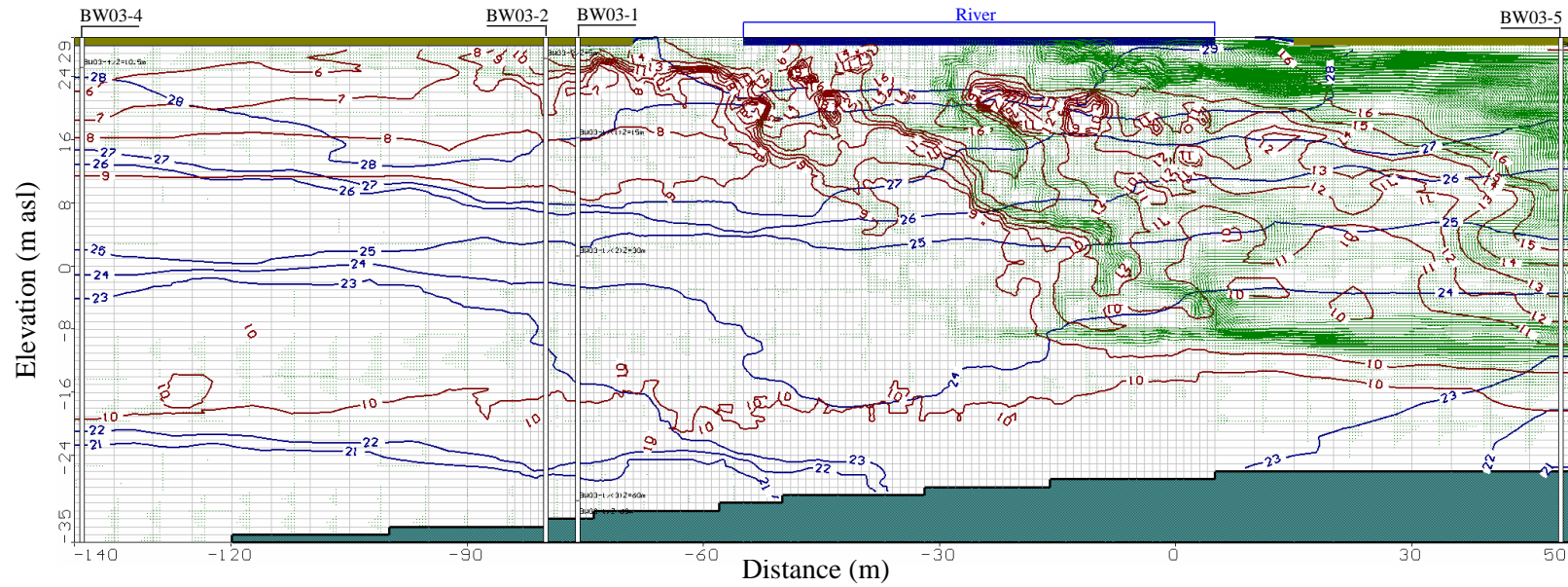## Realization no.4; T=150days; Maximum velocity = 110 m/d
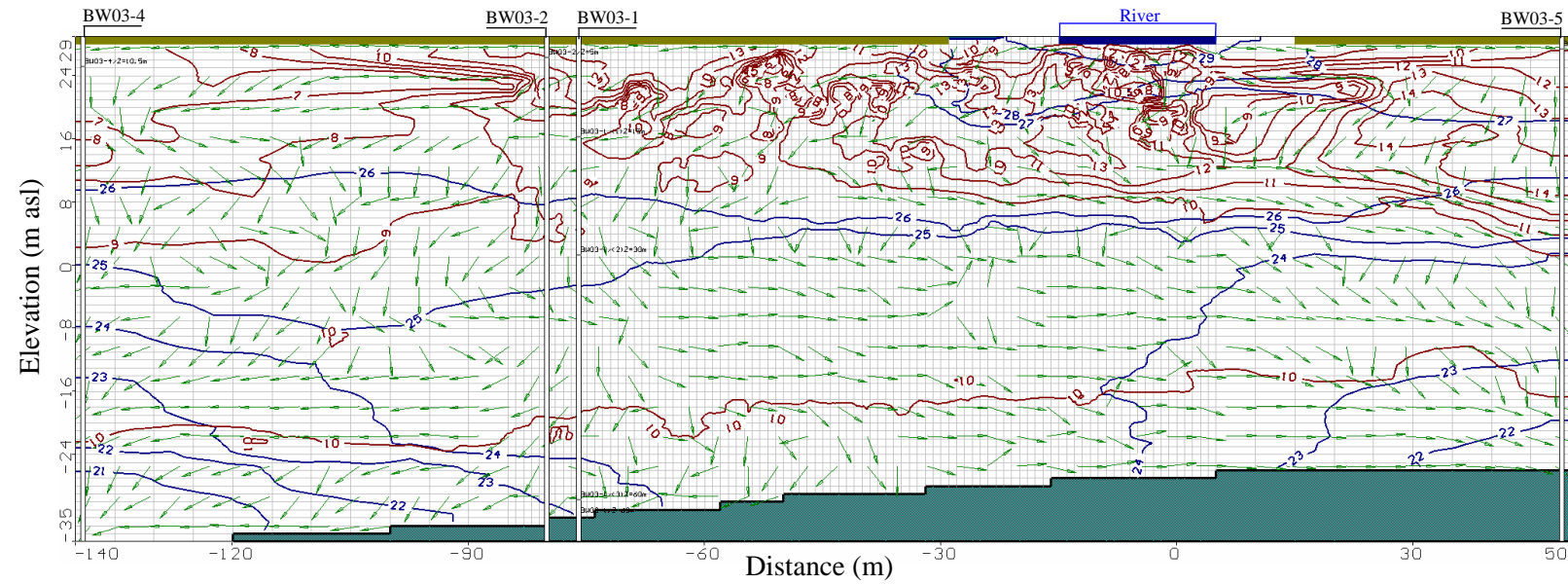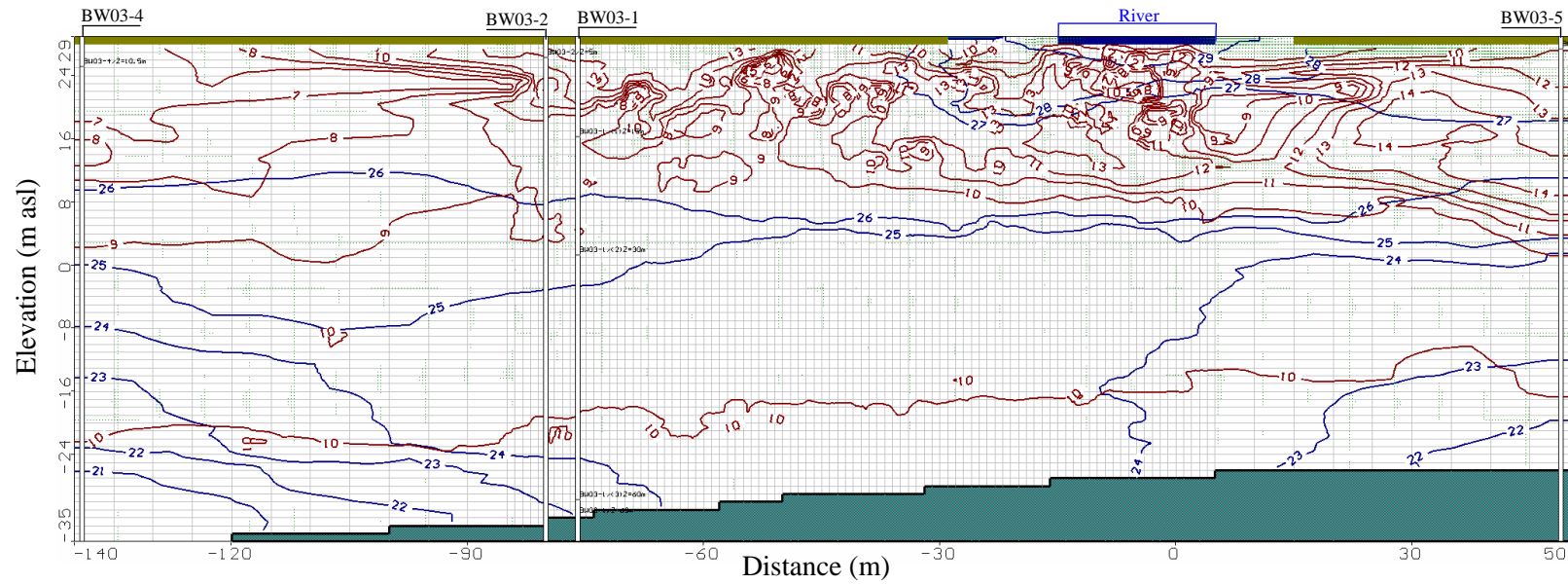
Case 1b

Realization no.4; T=264days; Maximum velocity = 140 m/d
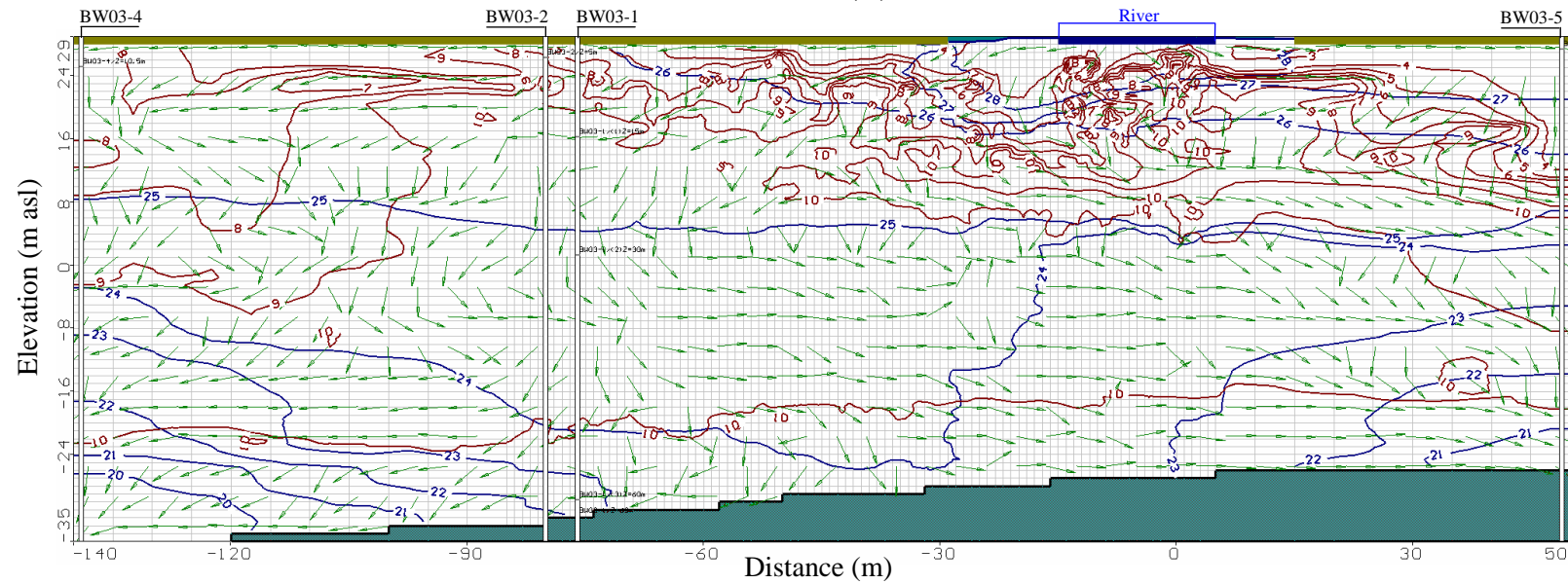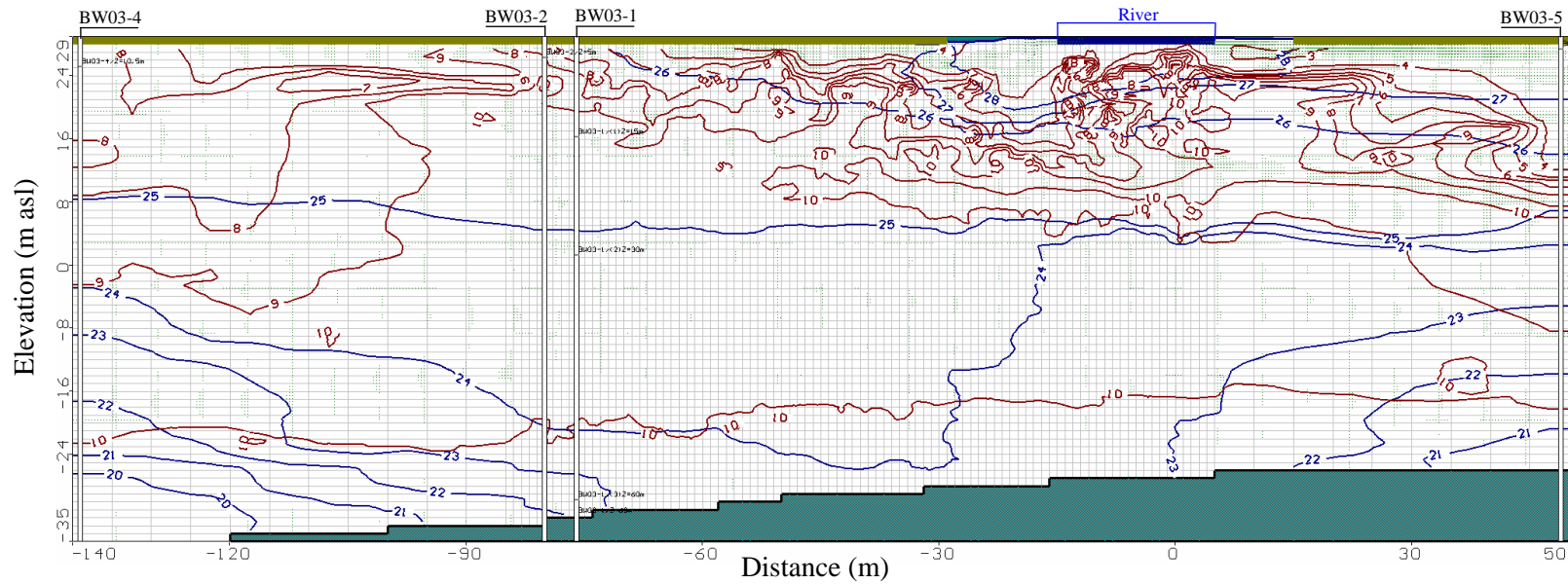
Case 1c

Realization no.13; T=50days; Maximum velocity = 68 m/d
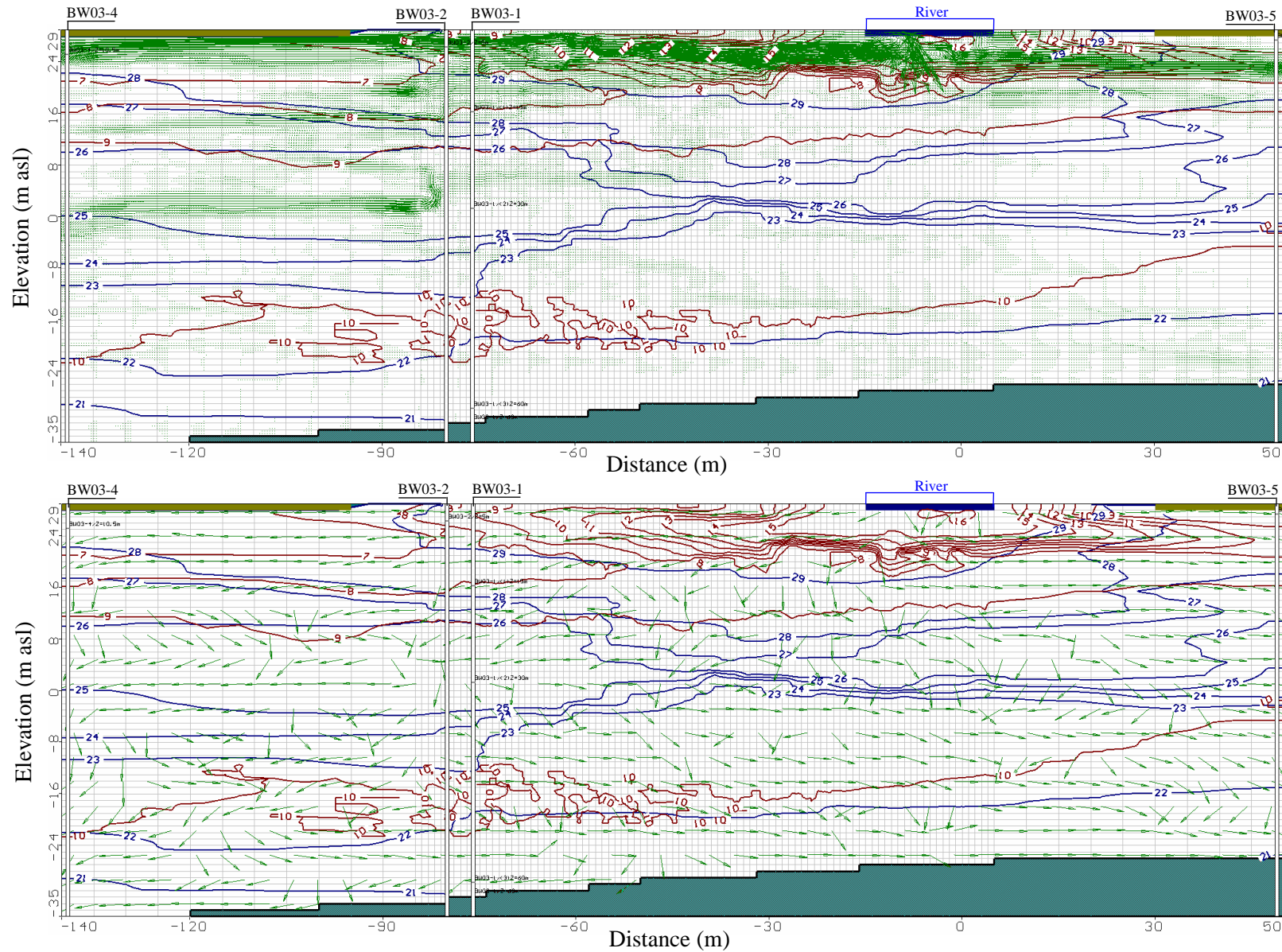
Case 1c

Realization no.13; T=150days; Maximum velocity = 55 m/d
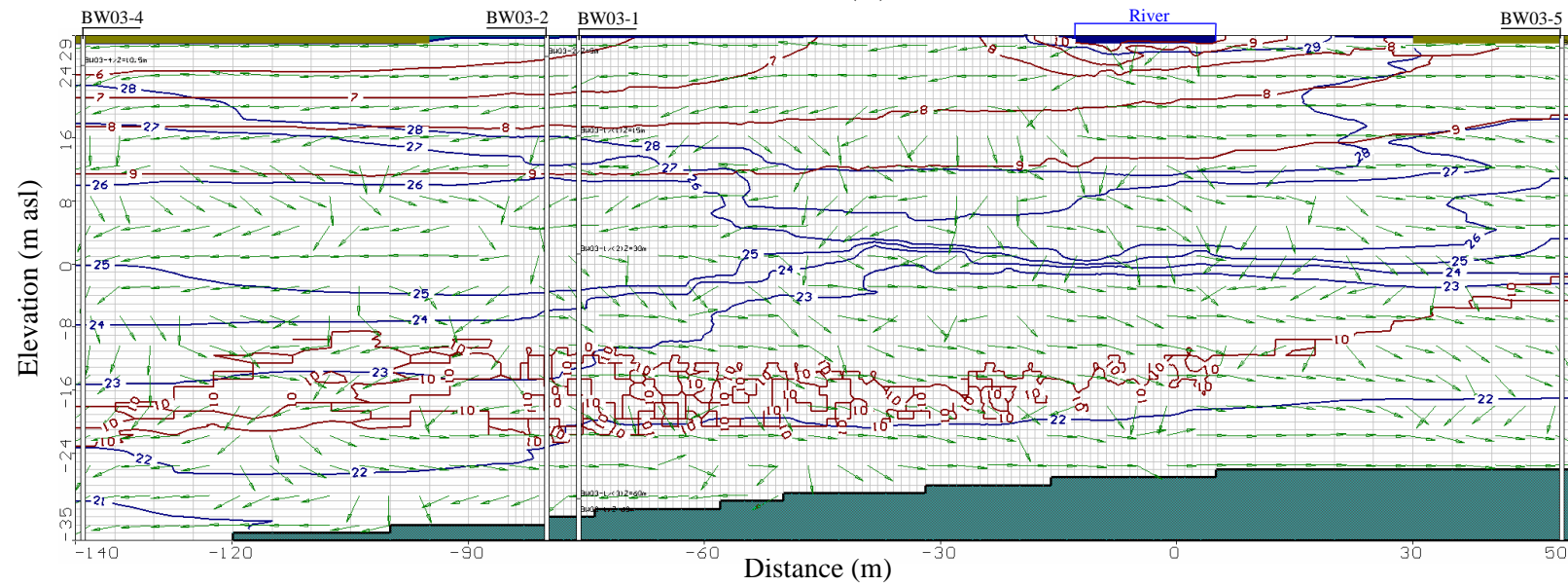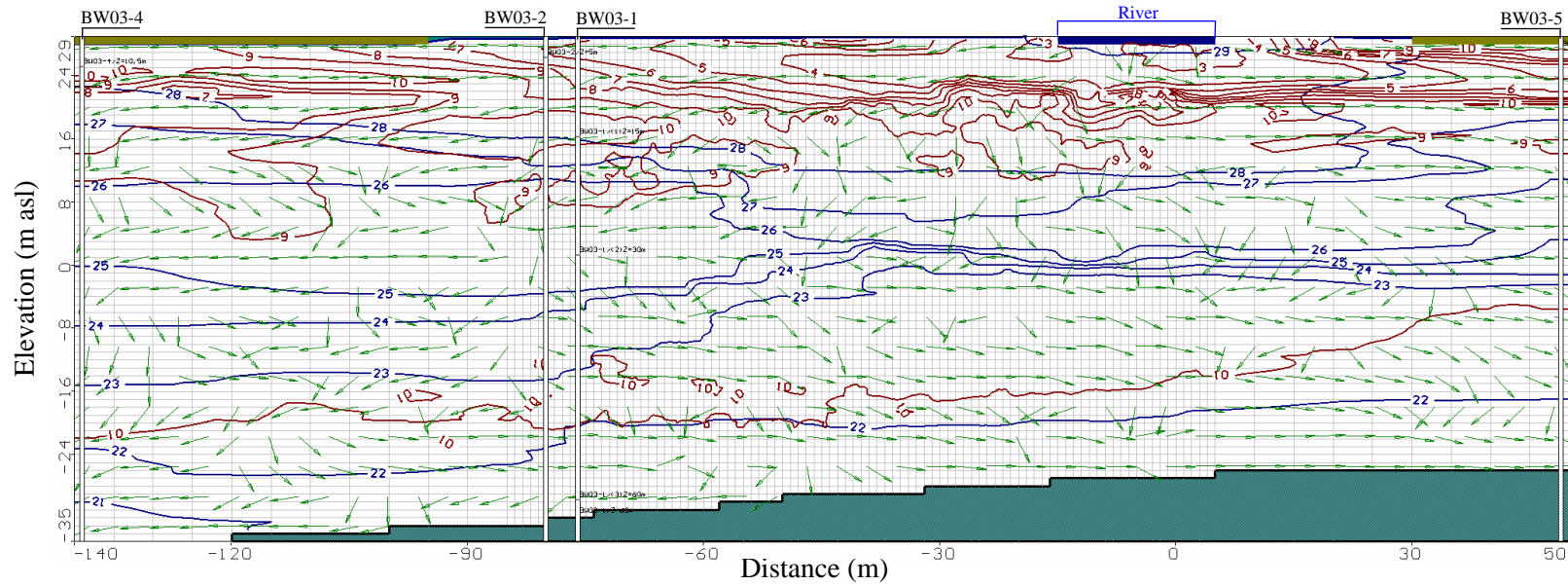
Case 1c

Realization no.13; T=264days; Maximum velocity = 63 m/d
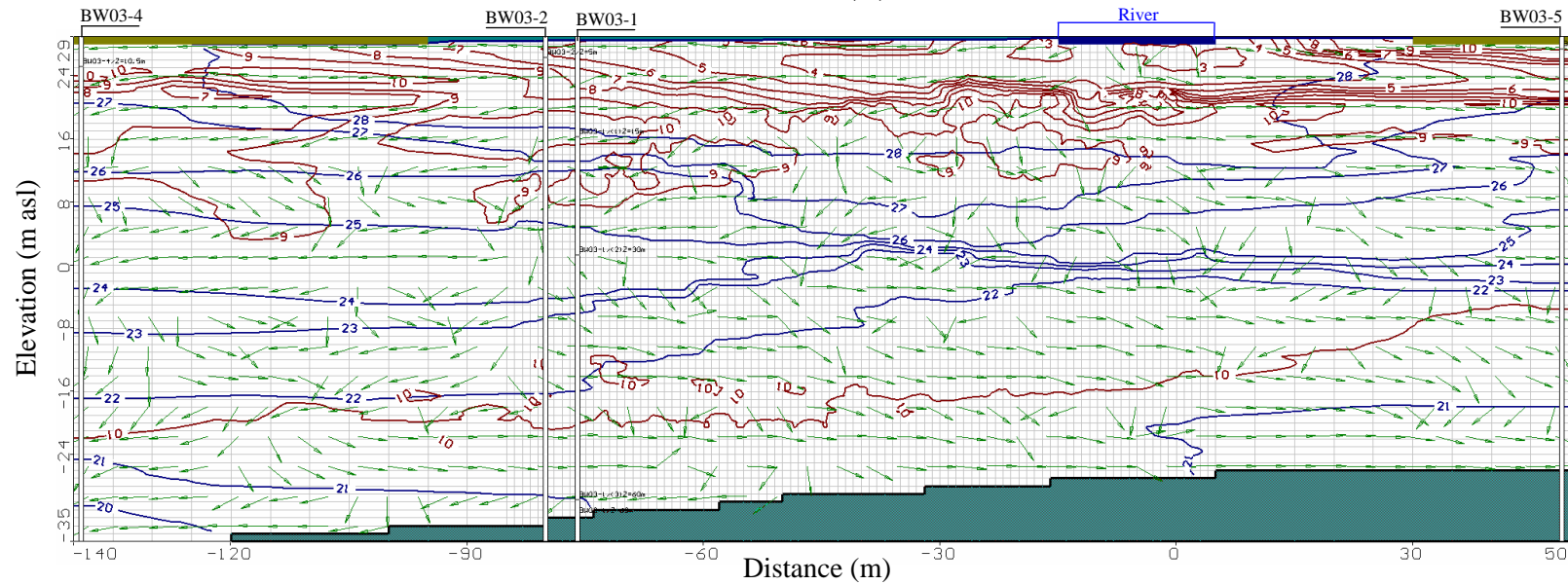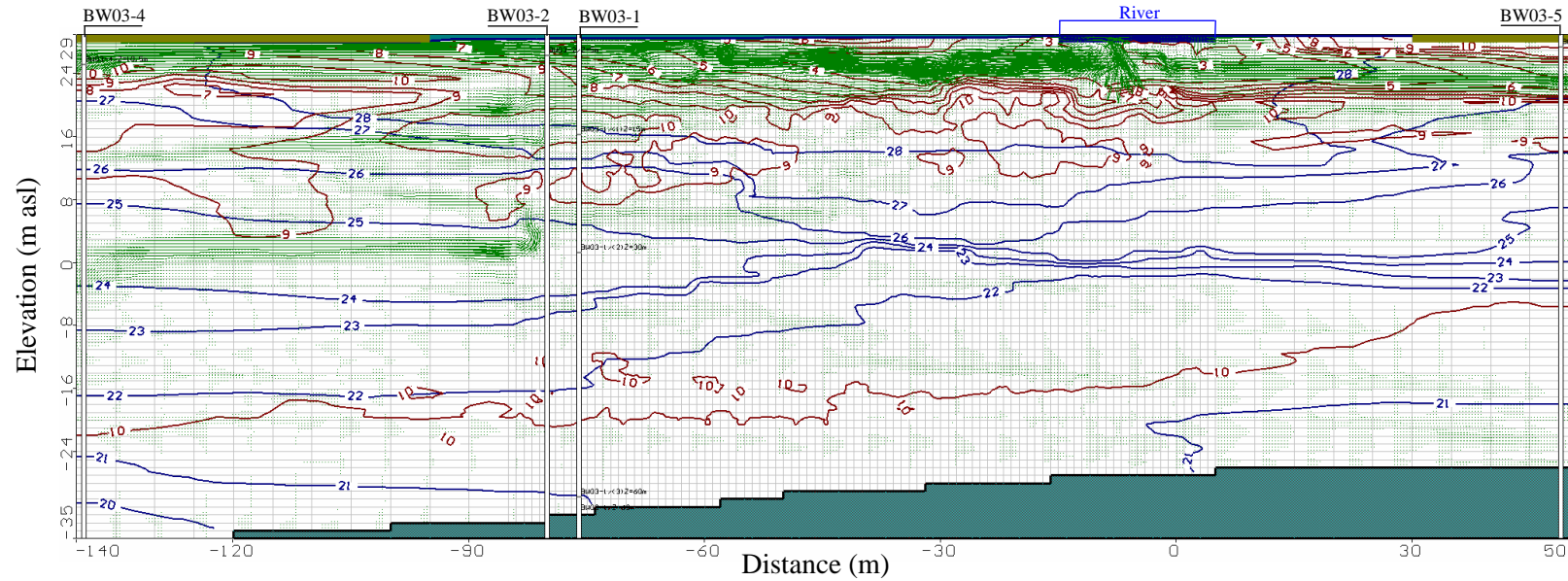
Case 3

Realization no.4; T=50days; Maximum velocity = 100 m/d
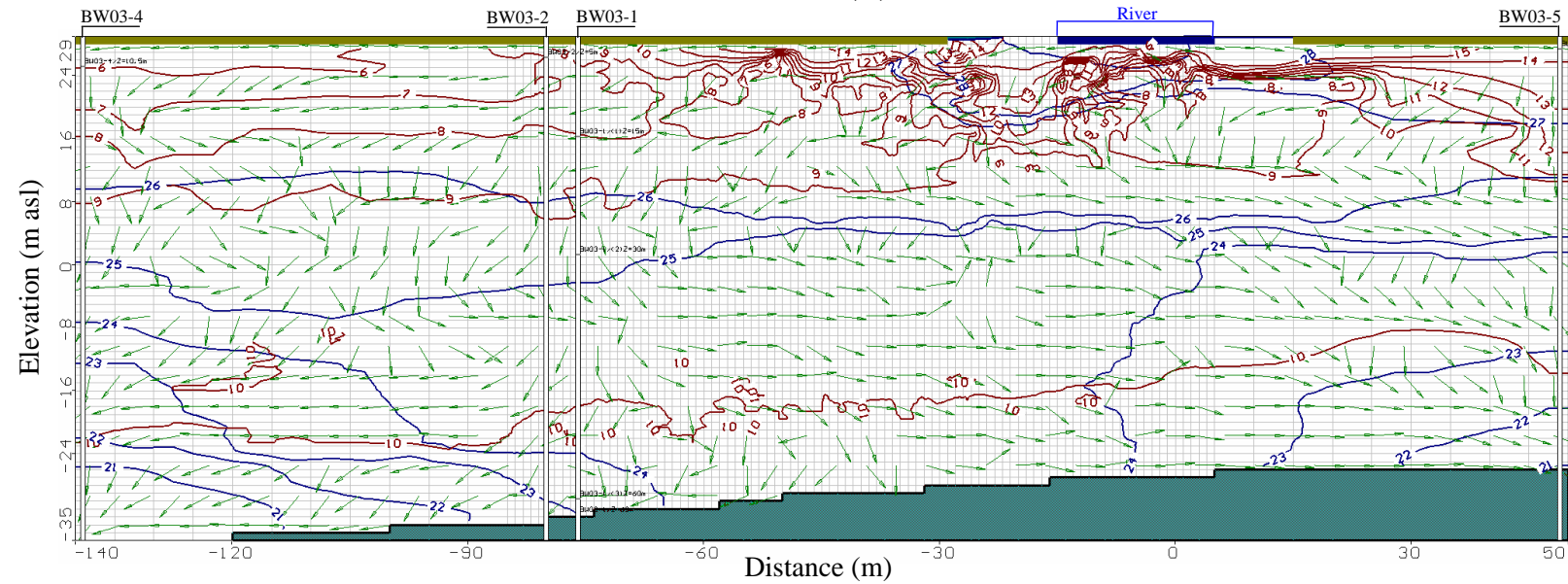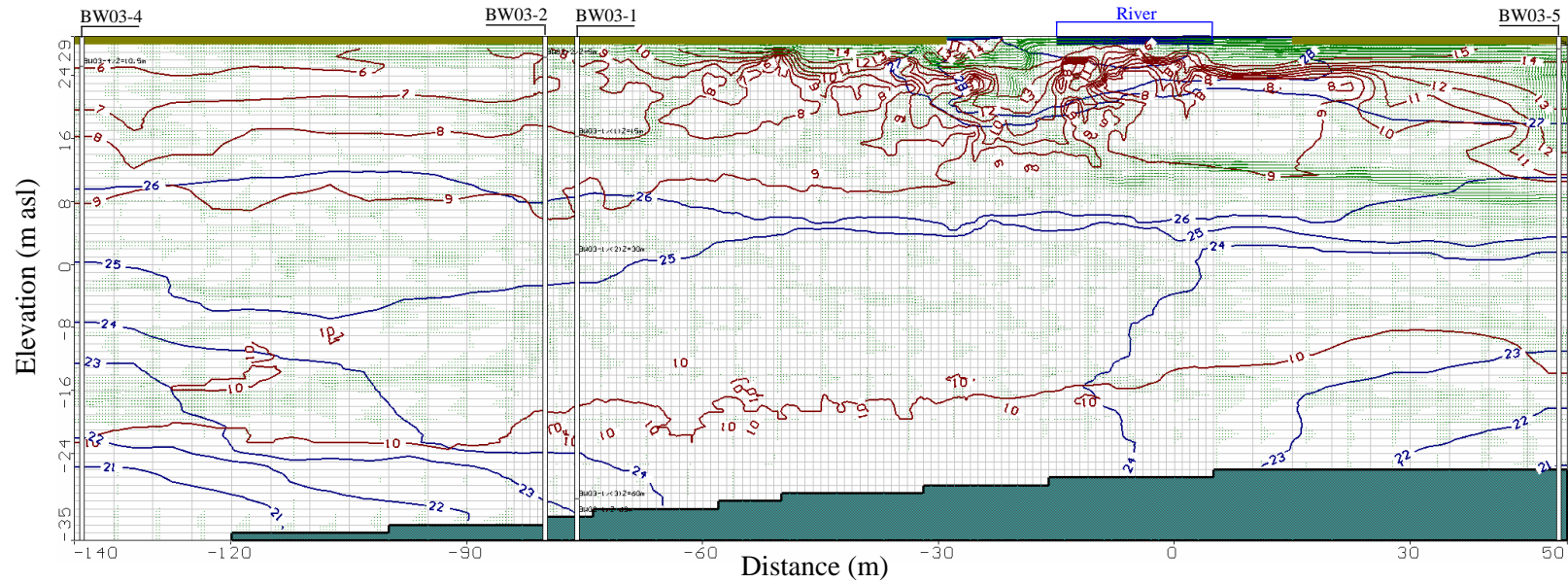
Case 3

Realization no.4; T=150days; Maximum velocity = 120 m/d

Case 3

Realization no.4; T=264days; Maximum velocity = 160 m/d
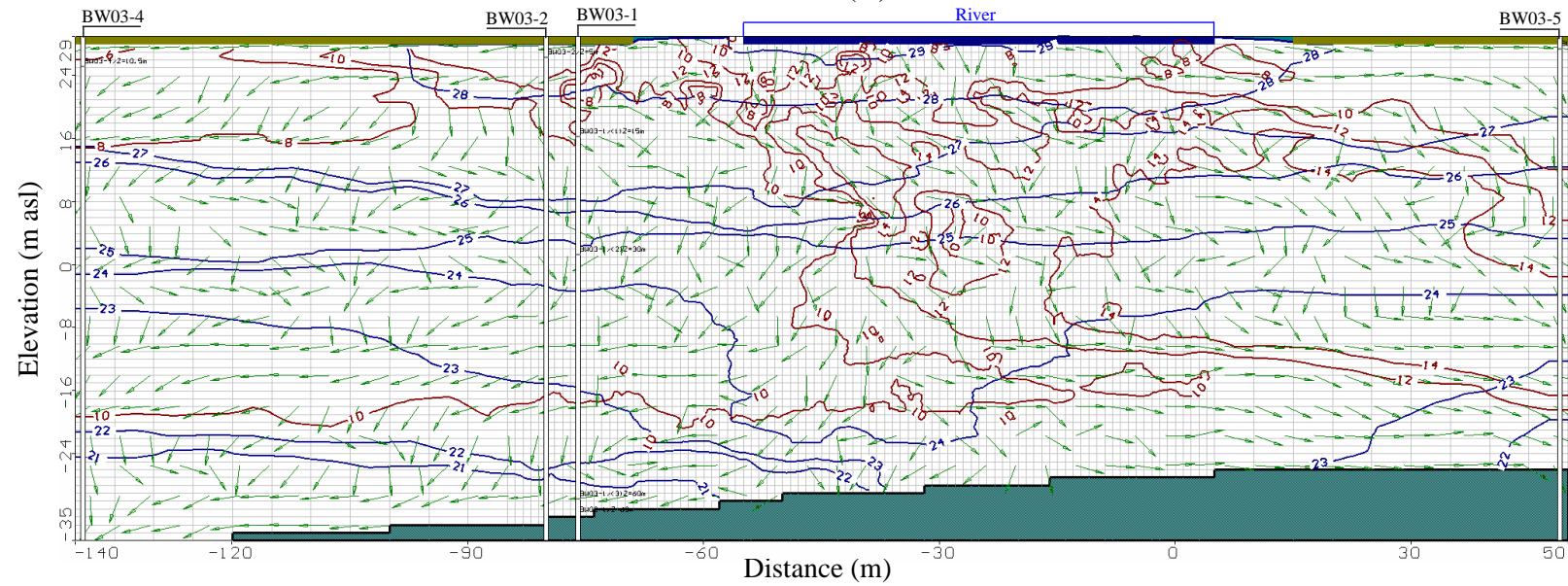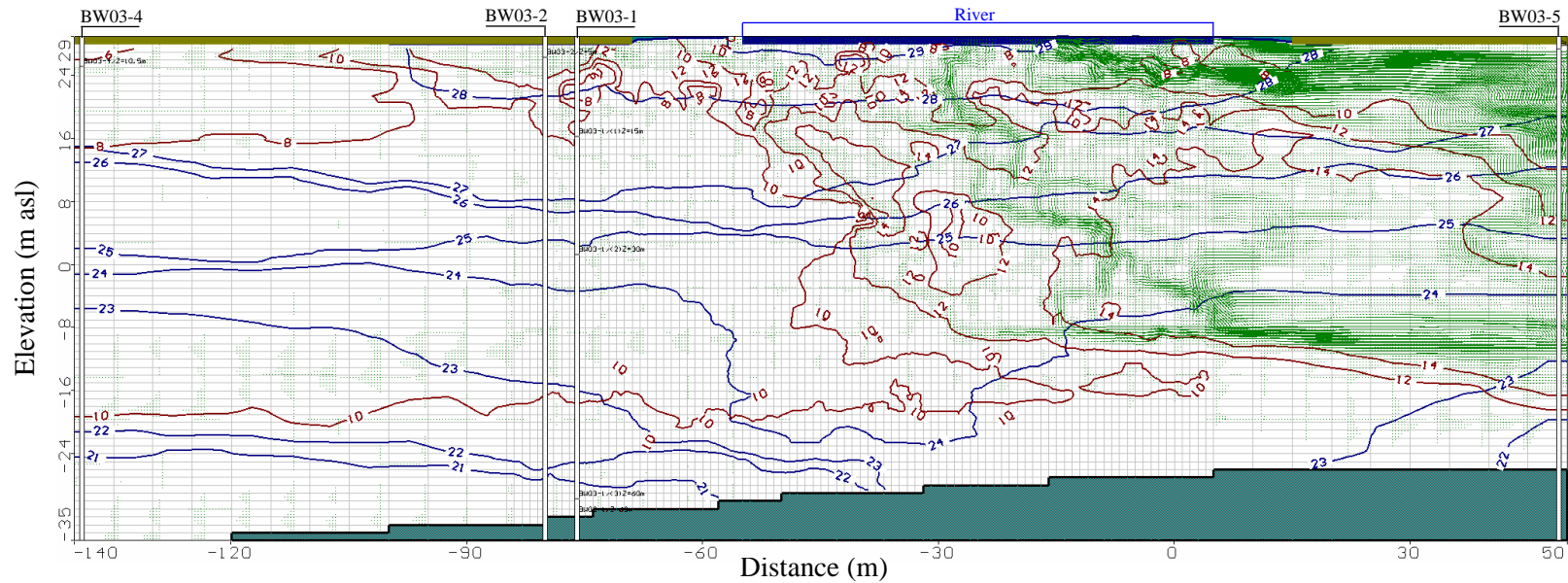
Case 4

Realization no.63; T=50days; Maximum velocity = 310 m/d

Case 4

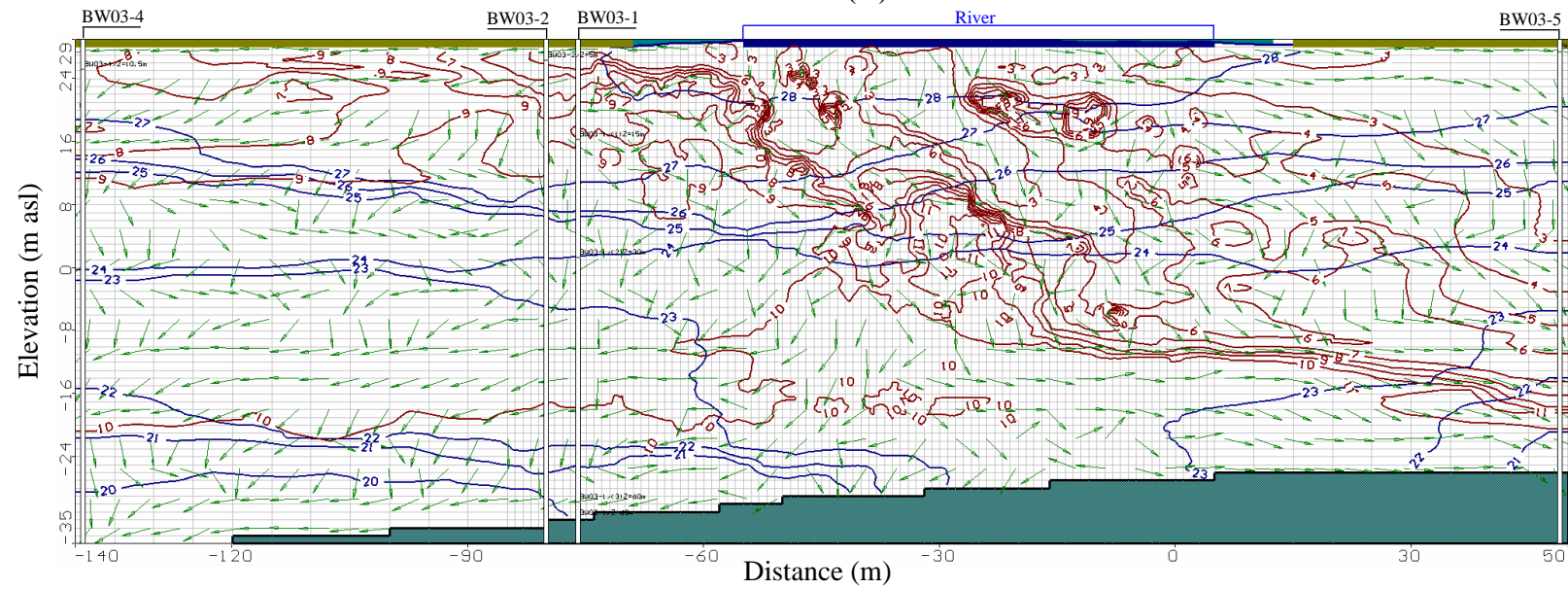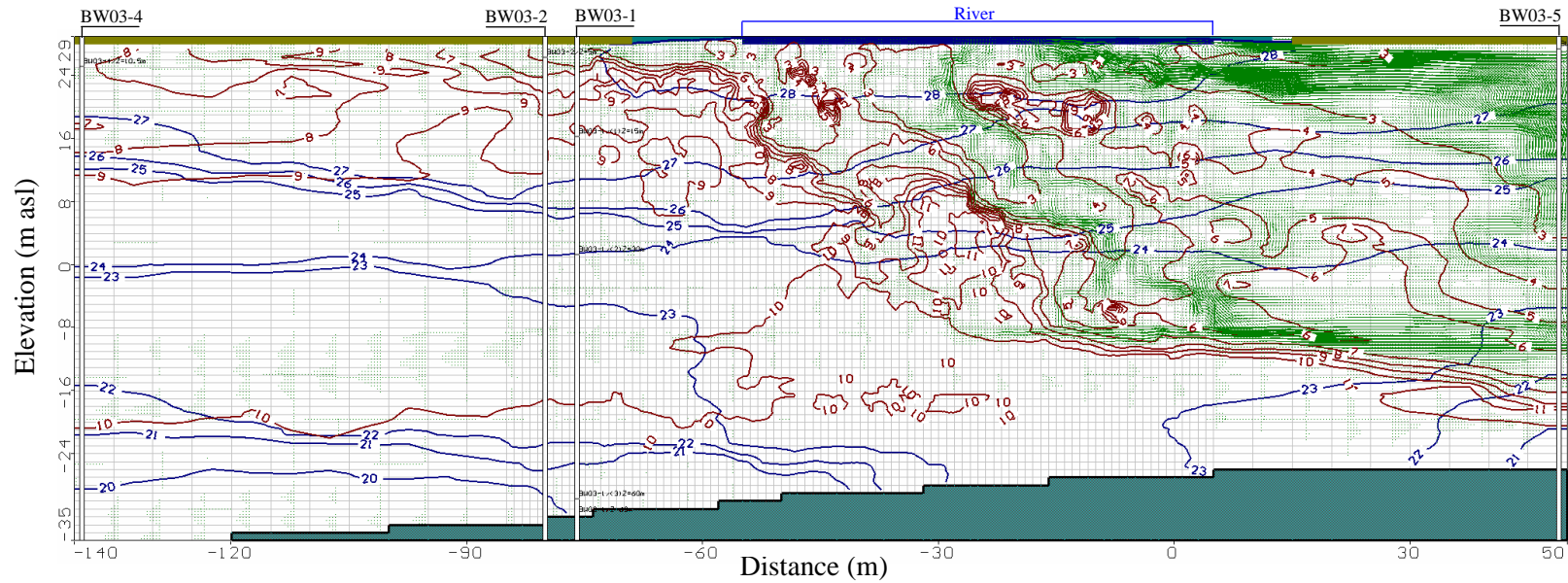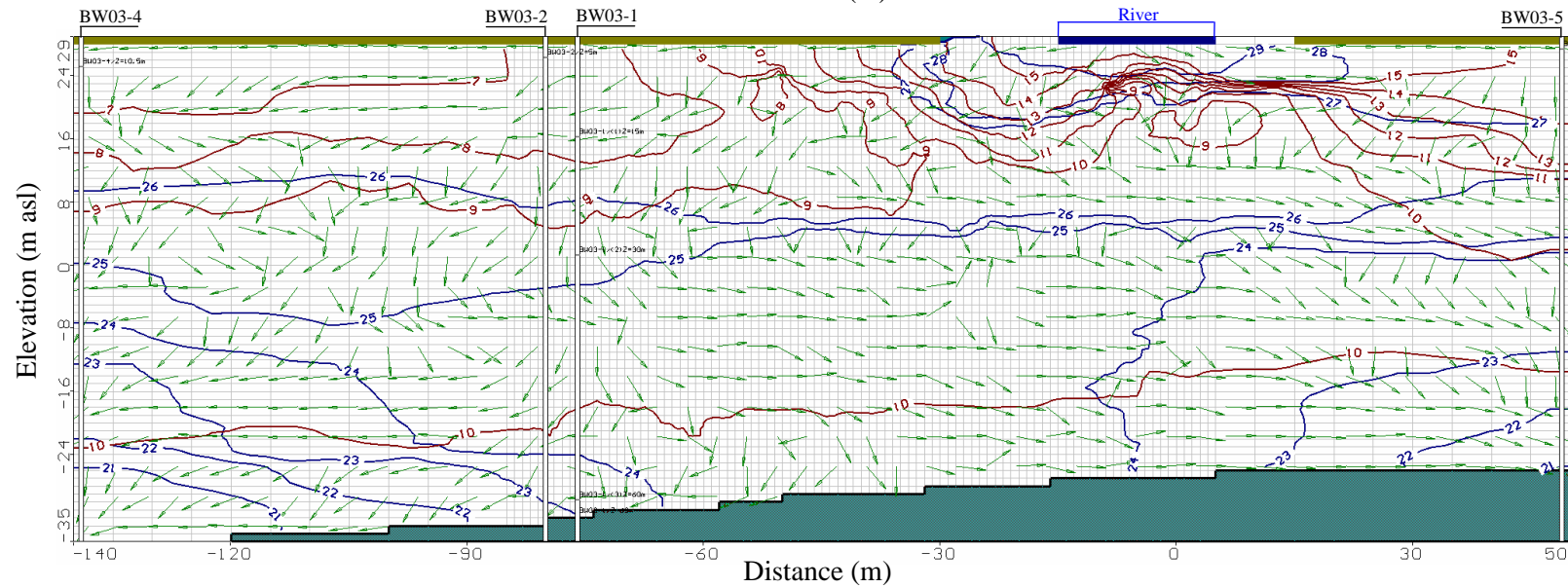## Realization no.63; T=150days; Maximum velocity = 270 m/d

Case 4

Realization no.63; T=264days; Maximum velocity = 290 m/d

Case 5

Realization no.4; T=50days; Maximum velocity = 130 m/d

Case 5

Realization no.4; T=150days; Maximum velocity = 110 m/d

Case 5

Realization no.4; T=264days; Maximum velocity = 140 m/d

Case 7

Realization no.63; T=50days; Maximum velocity = 320 m/d

Case 7

Realization no.63; T=150days; Maximum velocity = 280 m/d

Case 7

Realization no.63; T=264days; Maximum velocity = 300 m/d

Case 8a

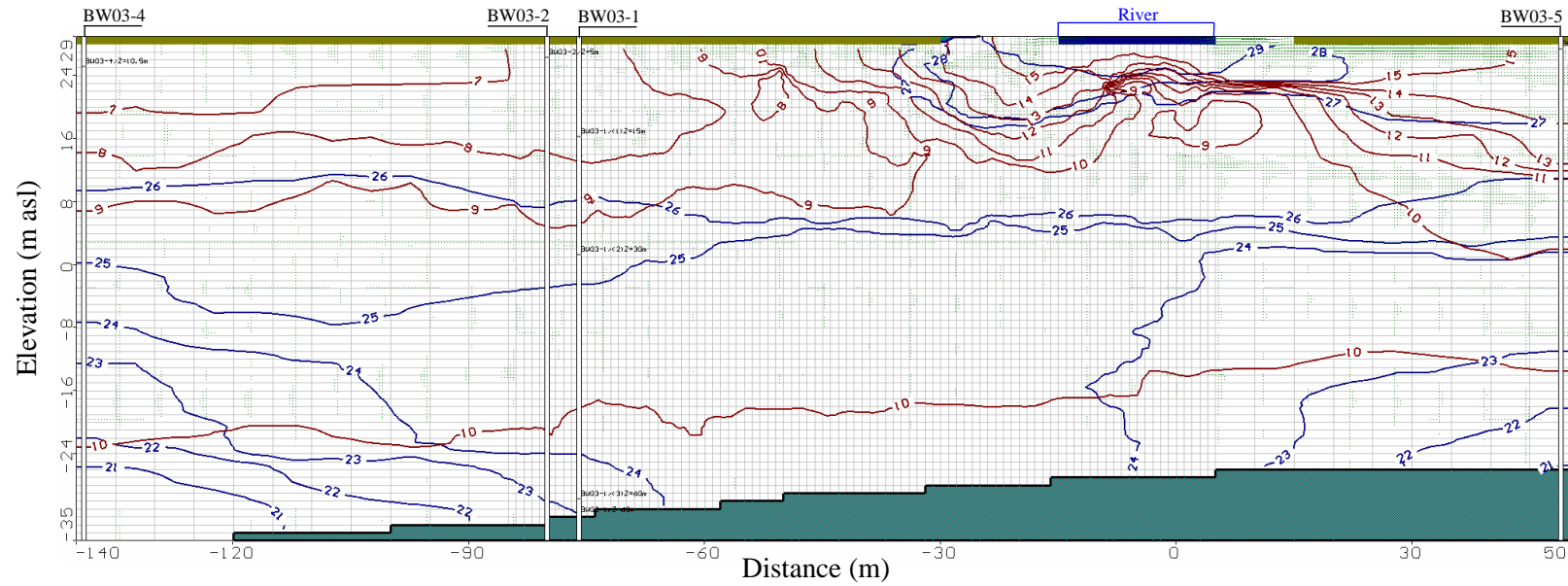## Realization no.1; T=50days; Maximum velocity = 97 m/d

Case 8a

Realization no.1; T=150days; Maximum velocity = 87 m/d

Case 8a

Realization no.1; T=264days; Maximum velocity = 100 m/d
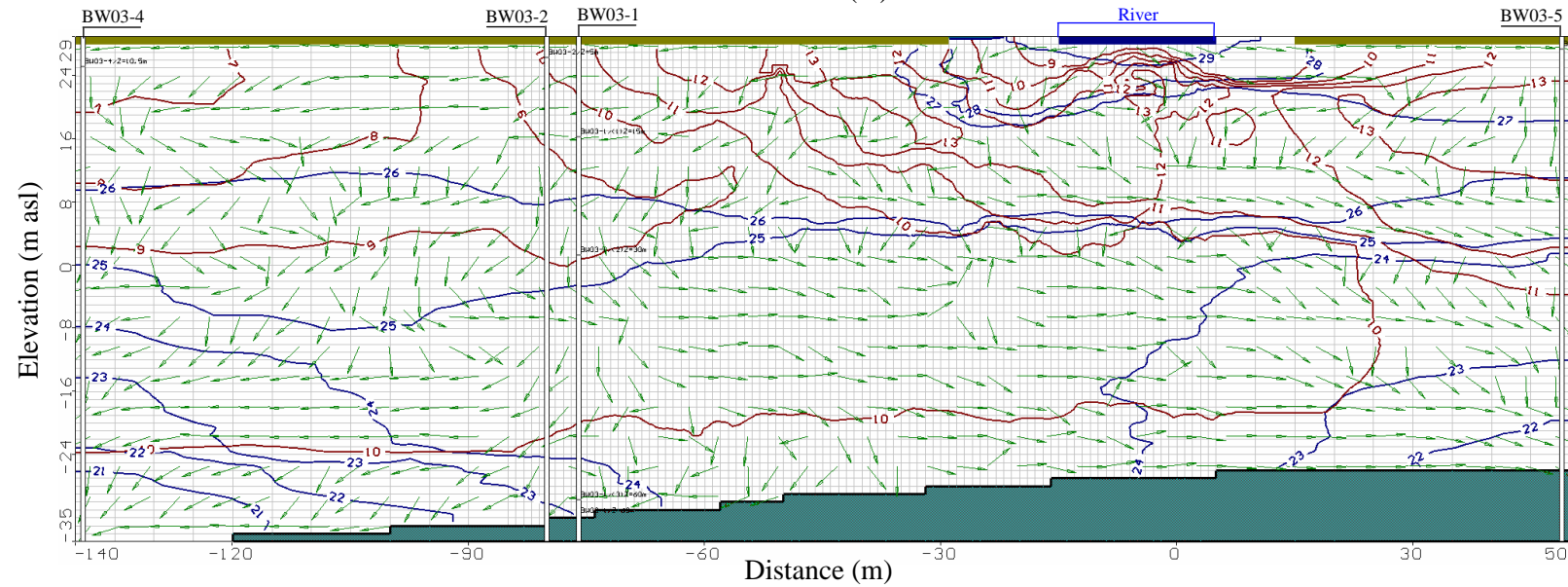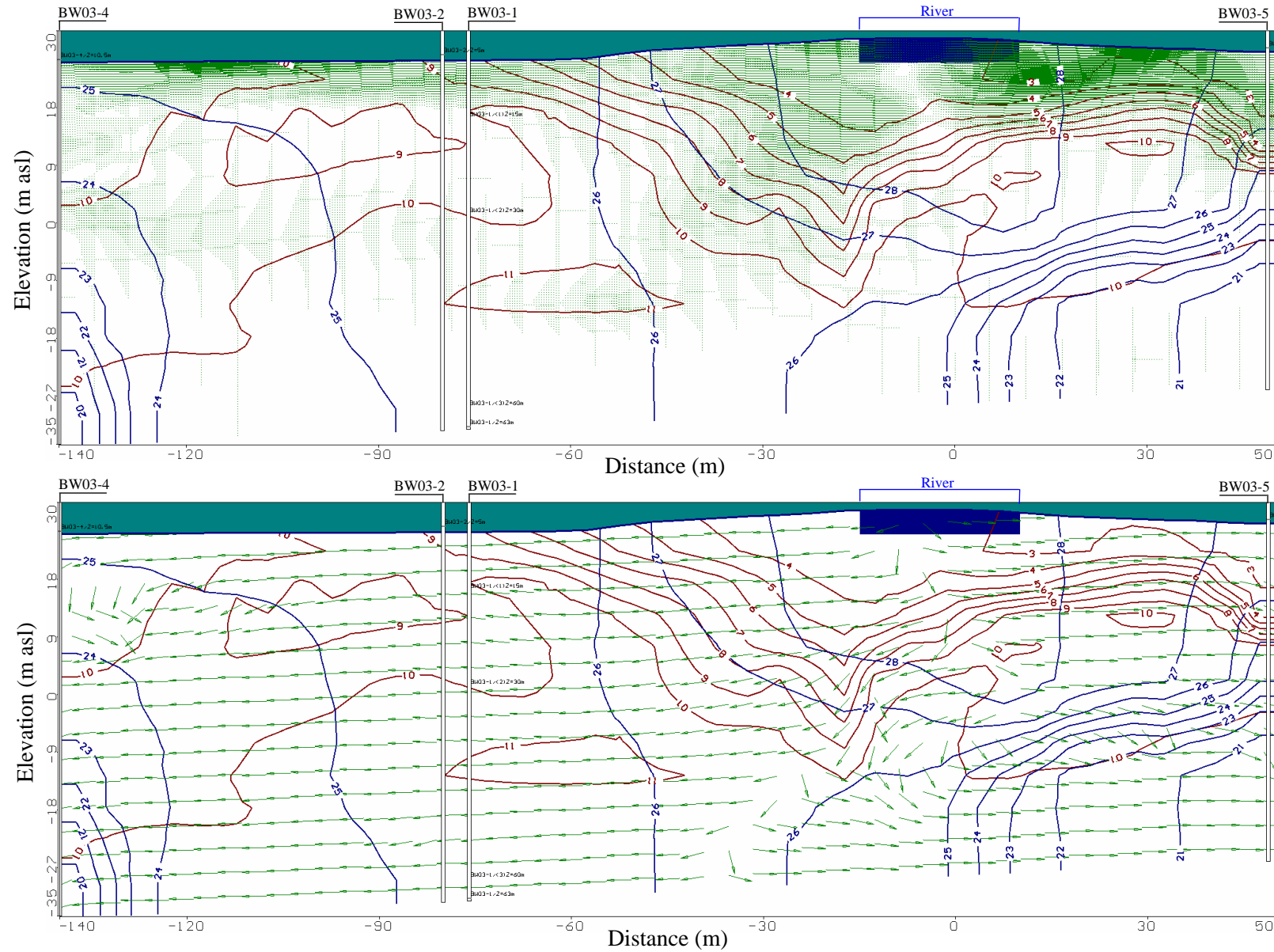
Case 8b
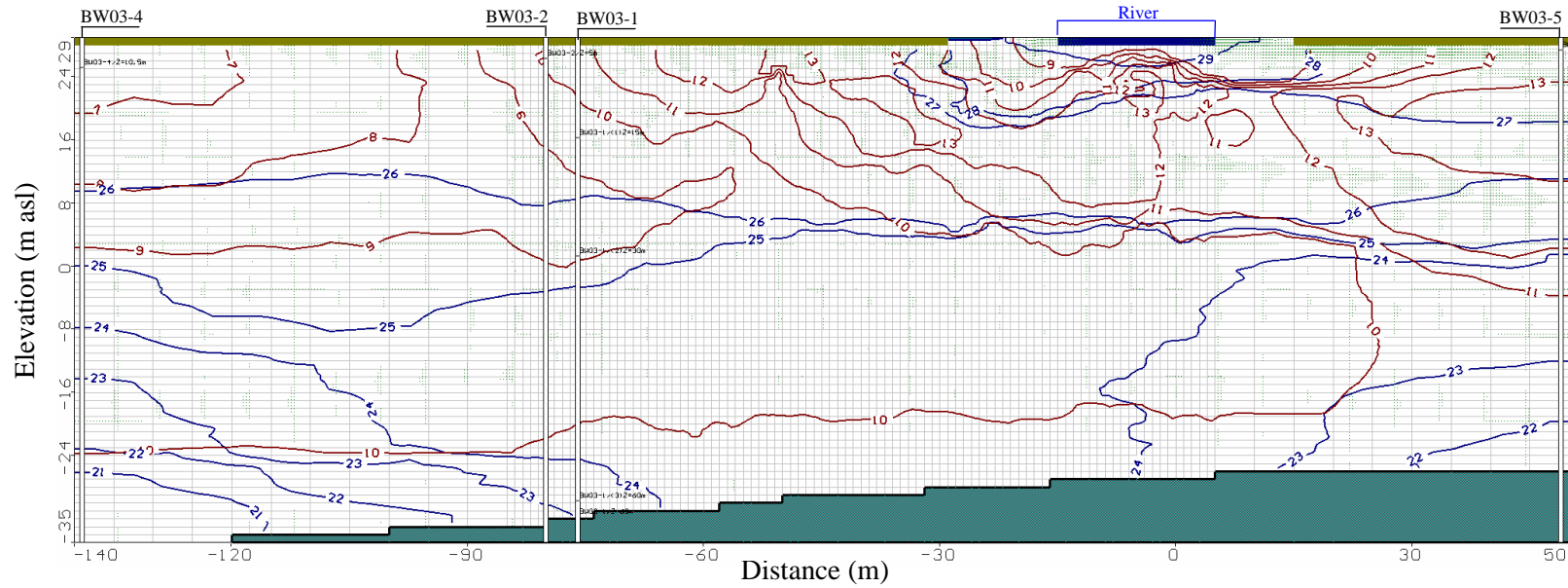
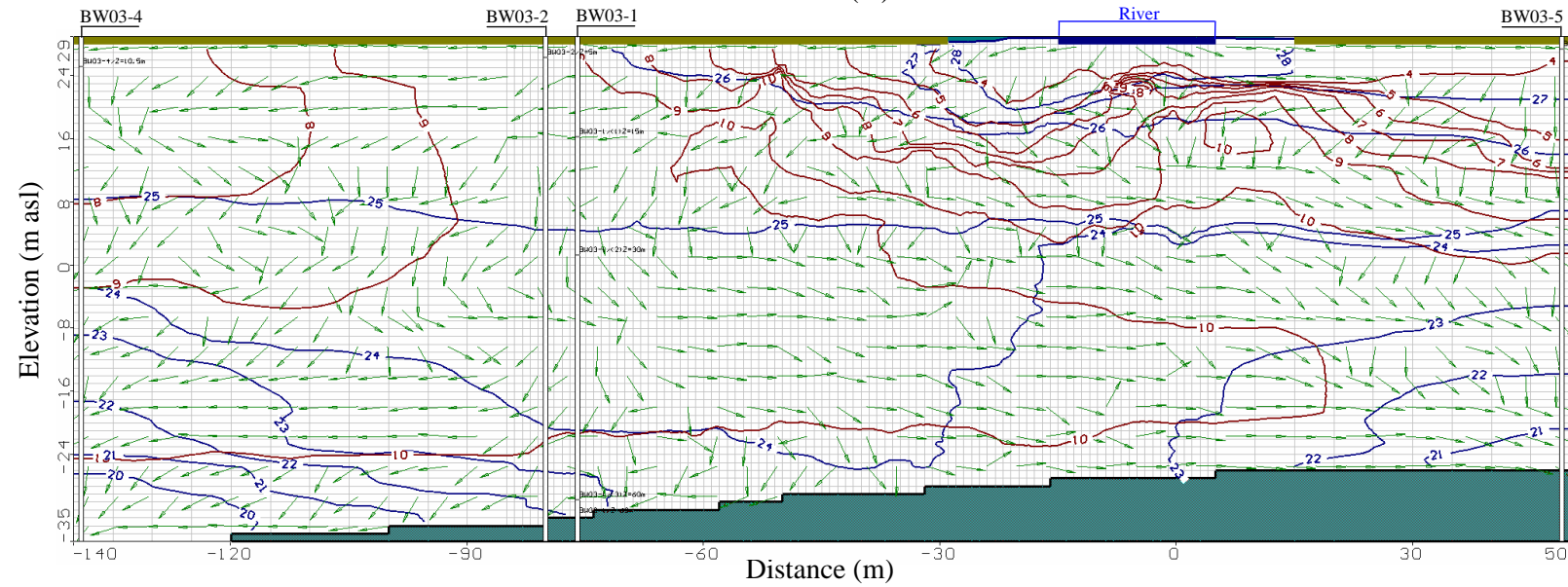## Realization no.17; T=50days; Maximum velocity = 640 m/d
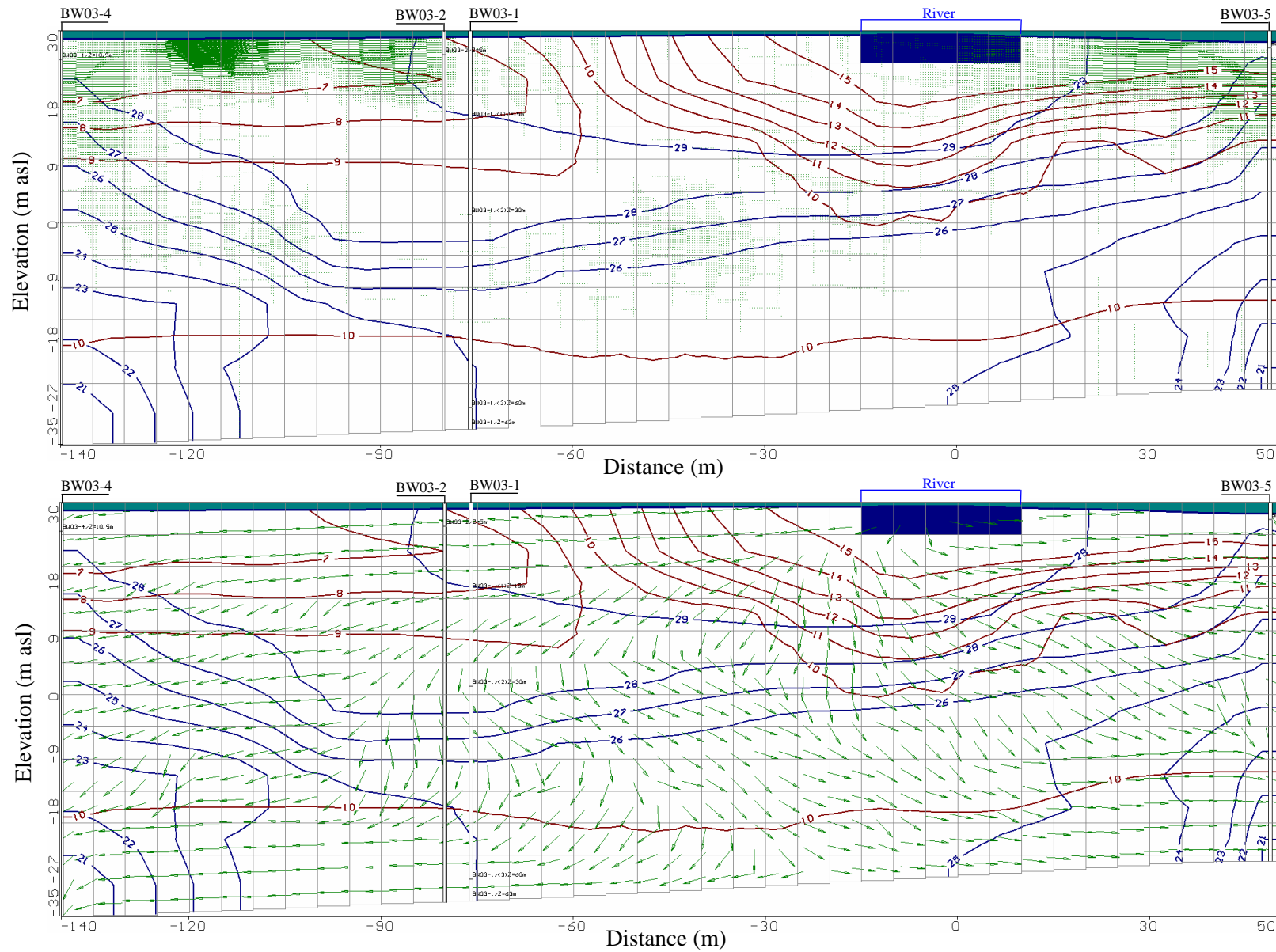
Case 8b

Realization no.17; T=150days; Maximum velocity = 390 m/d
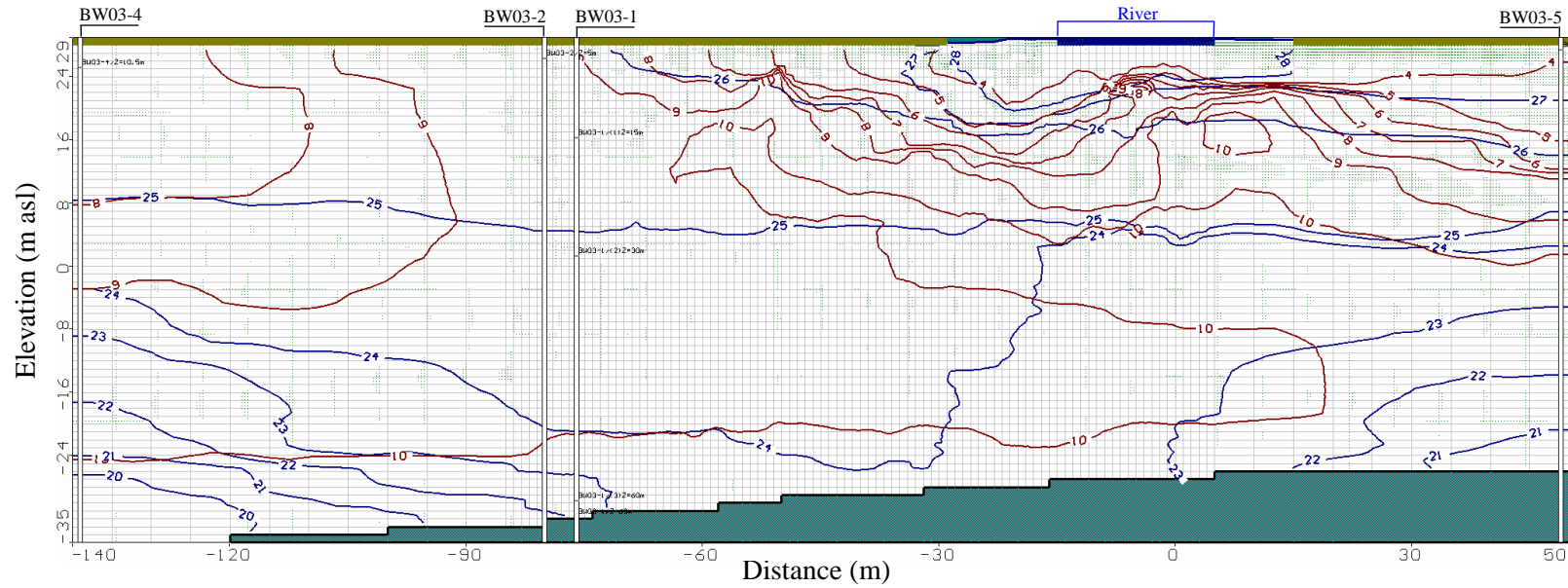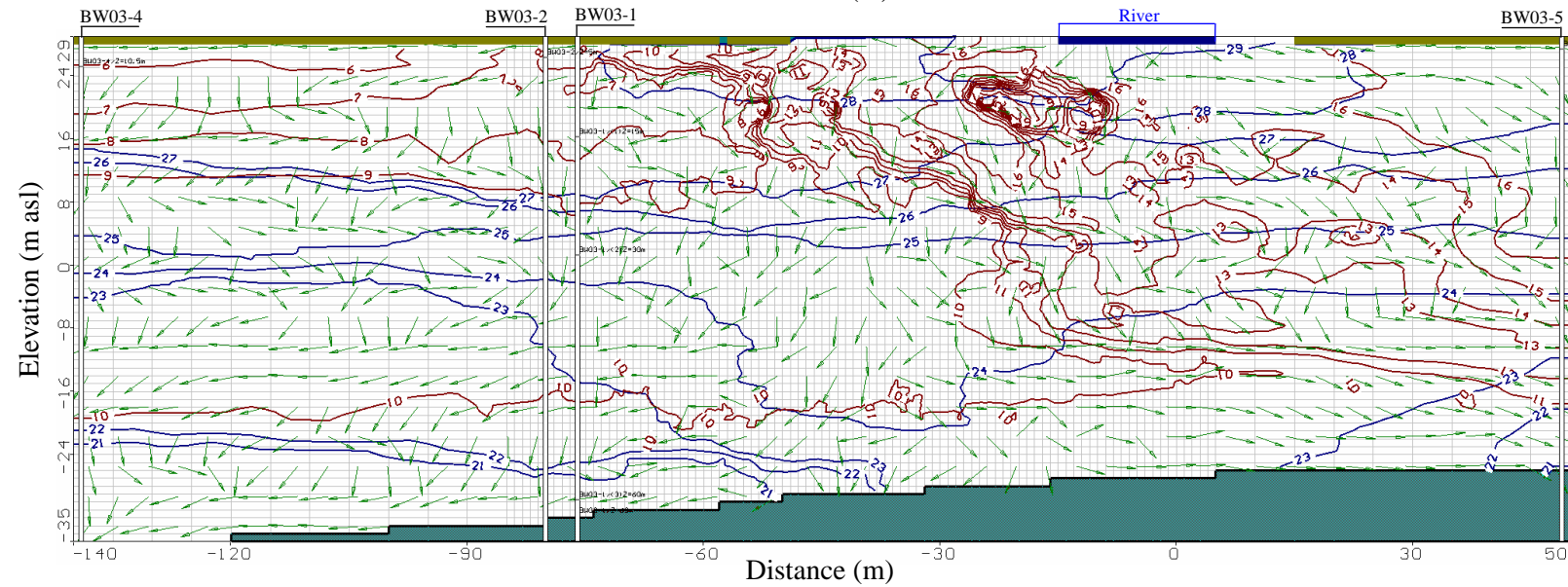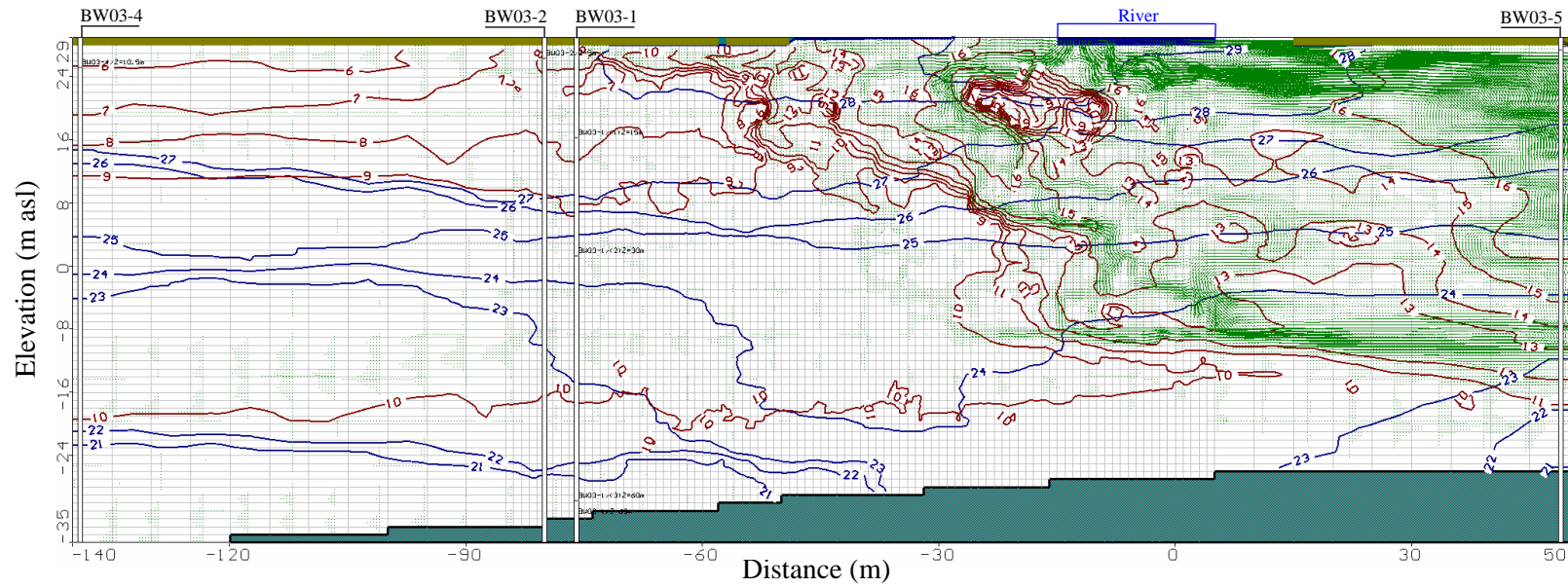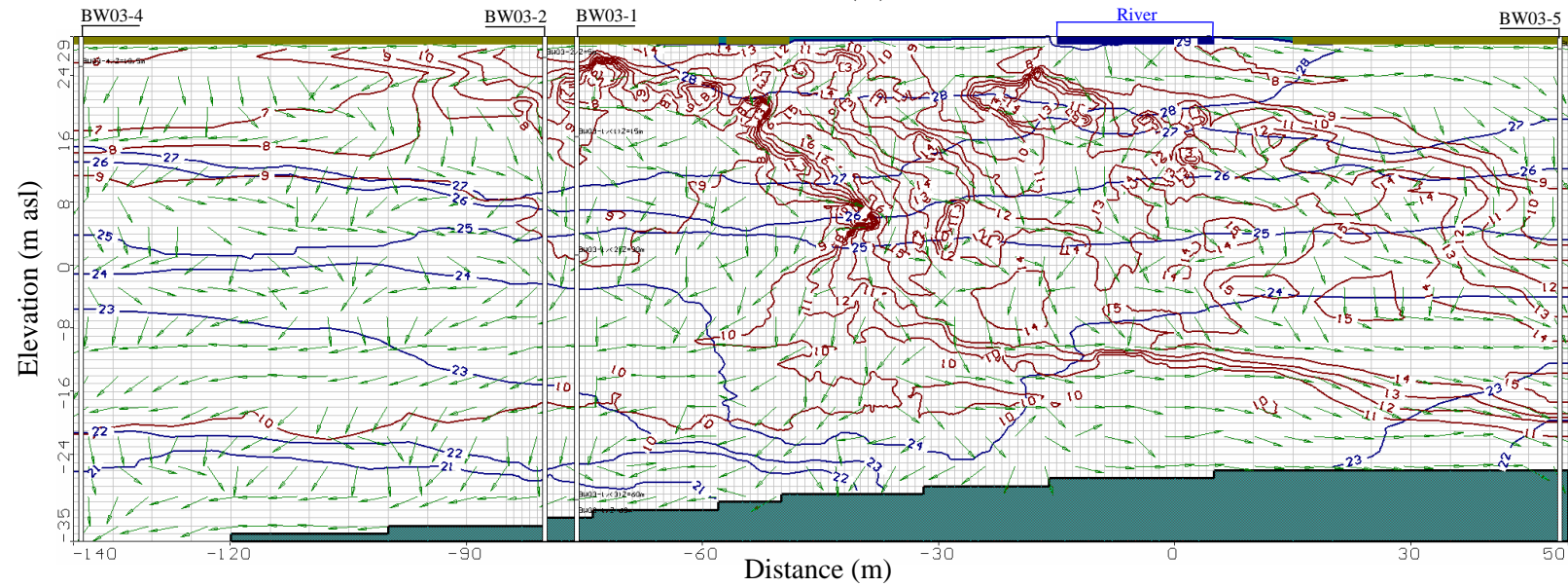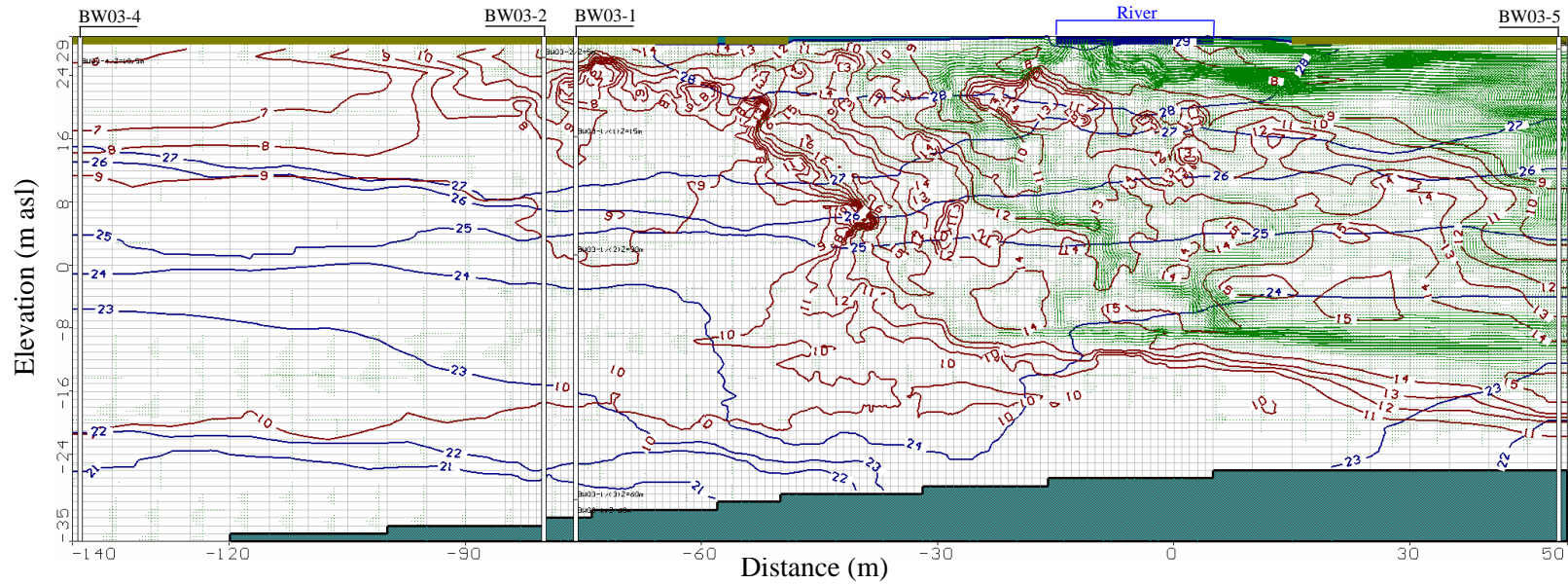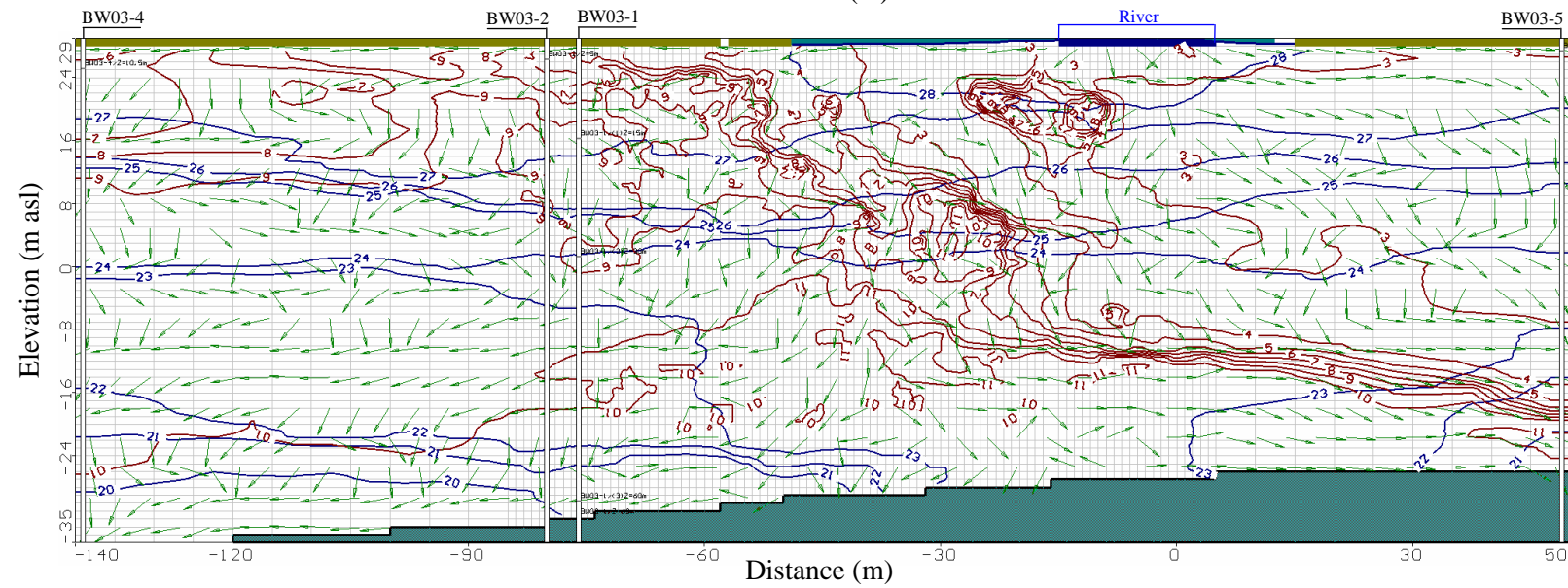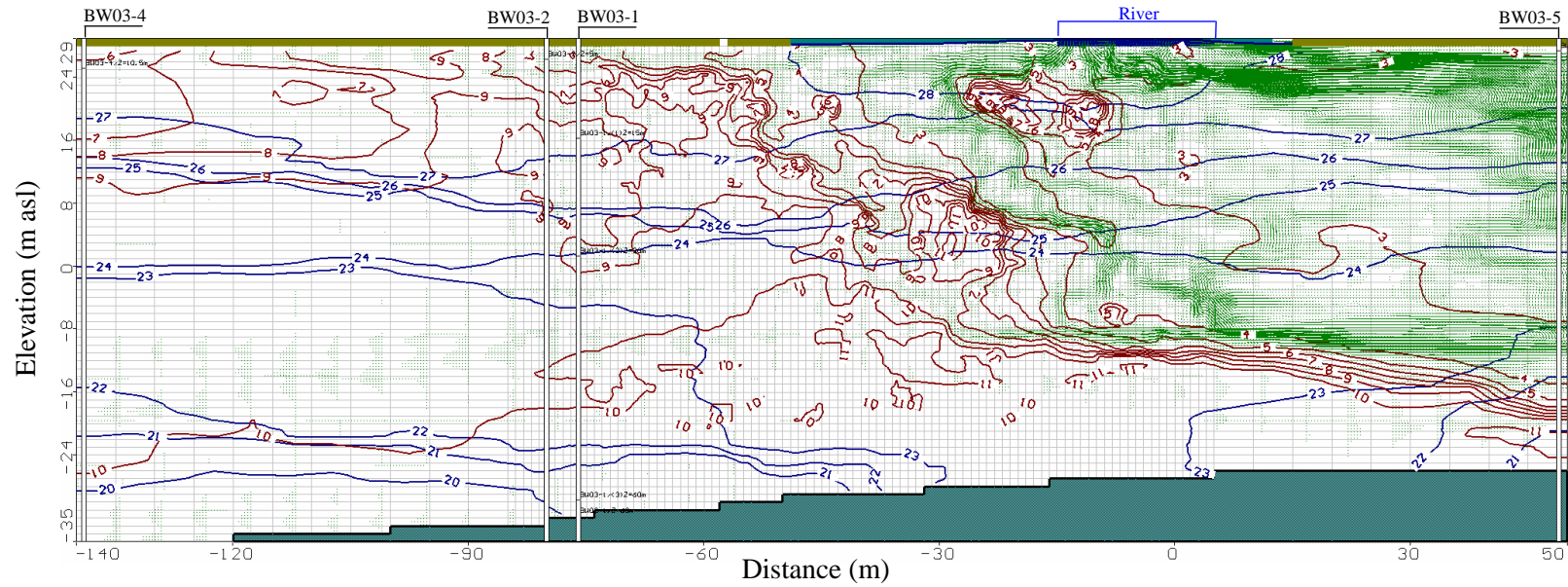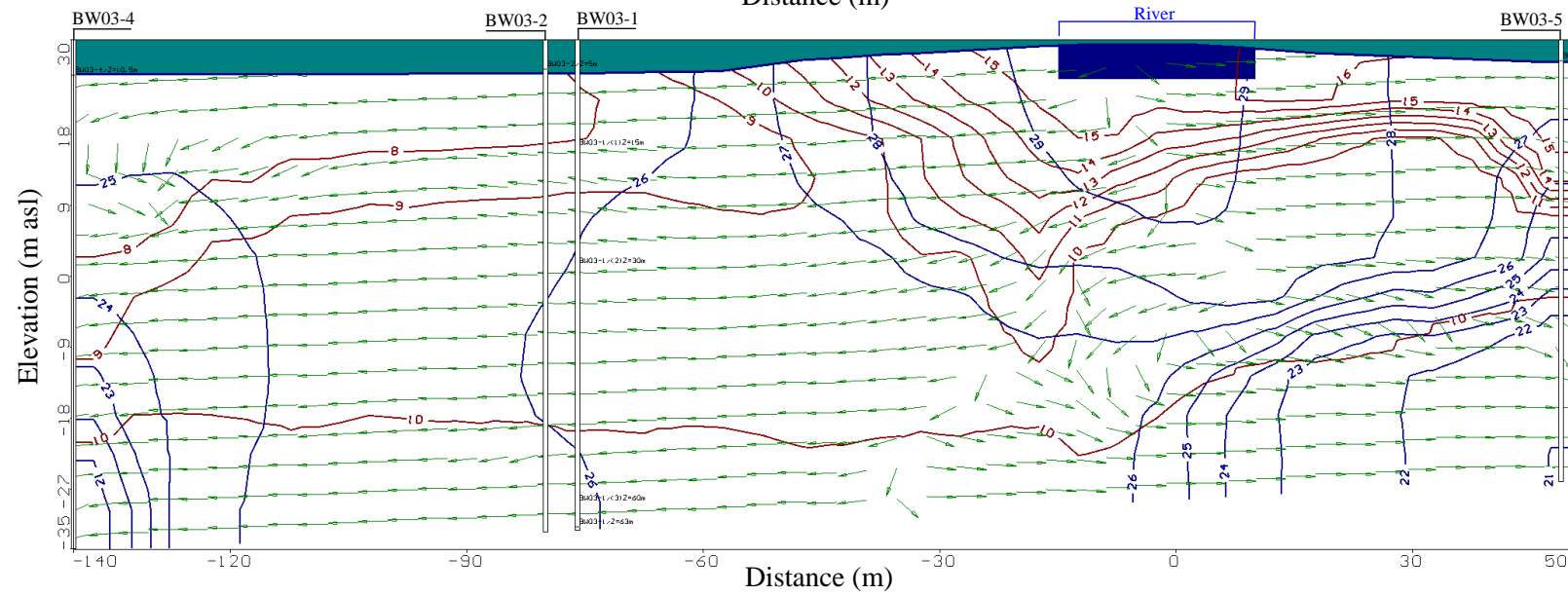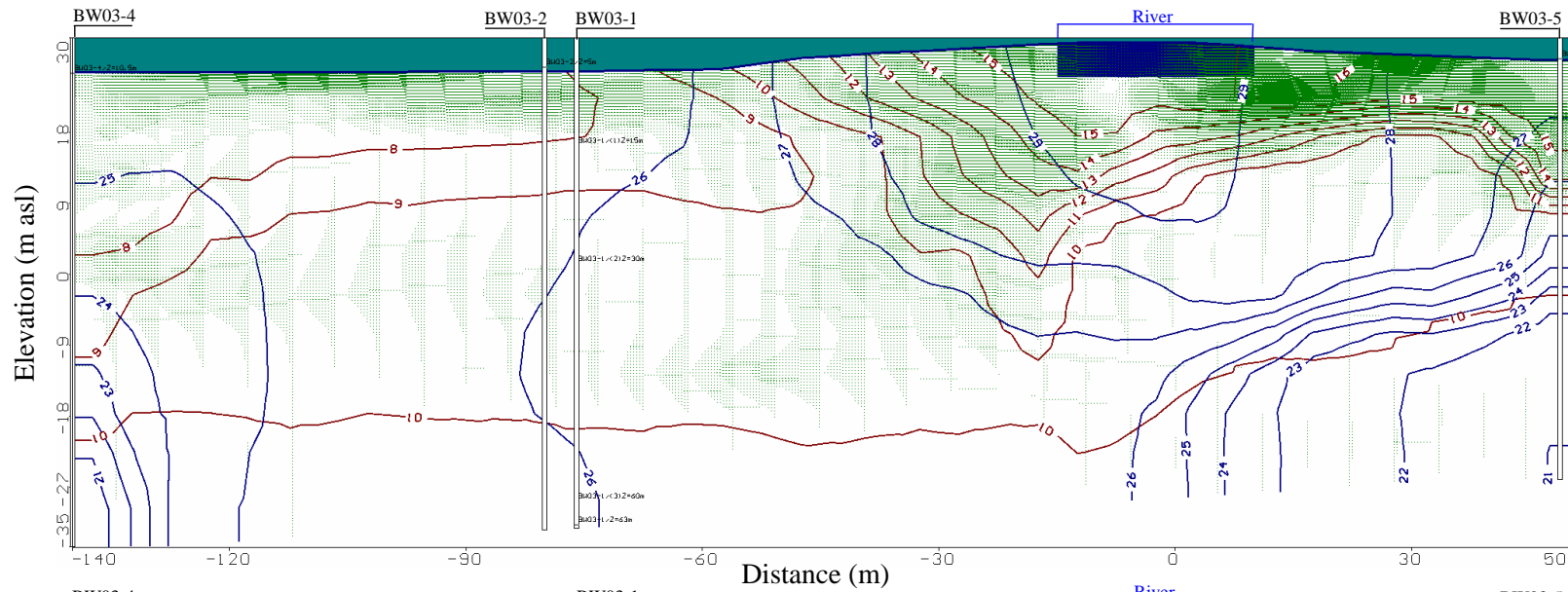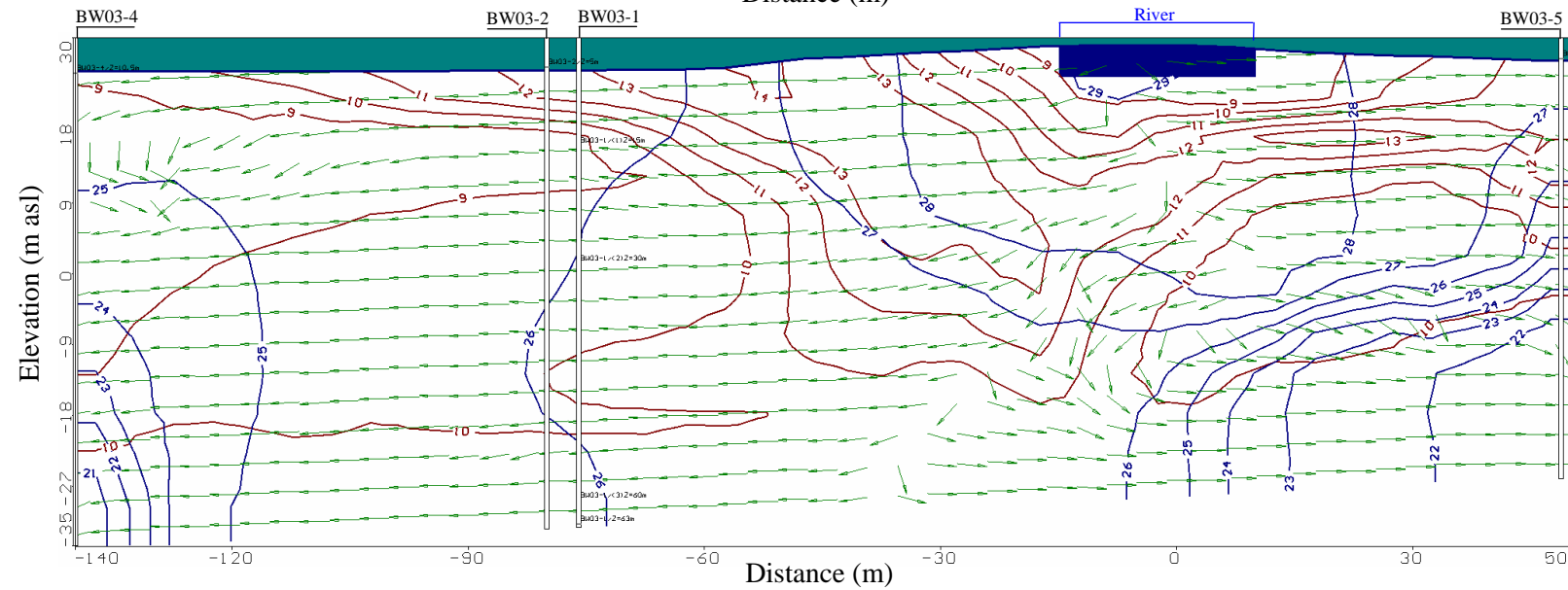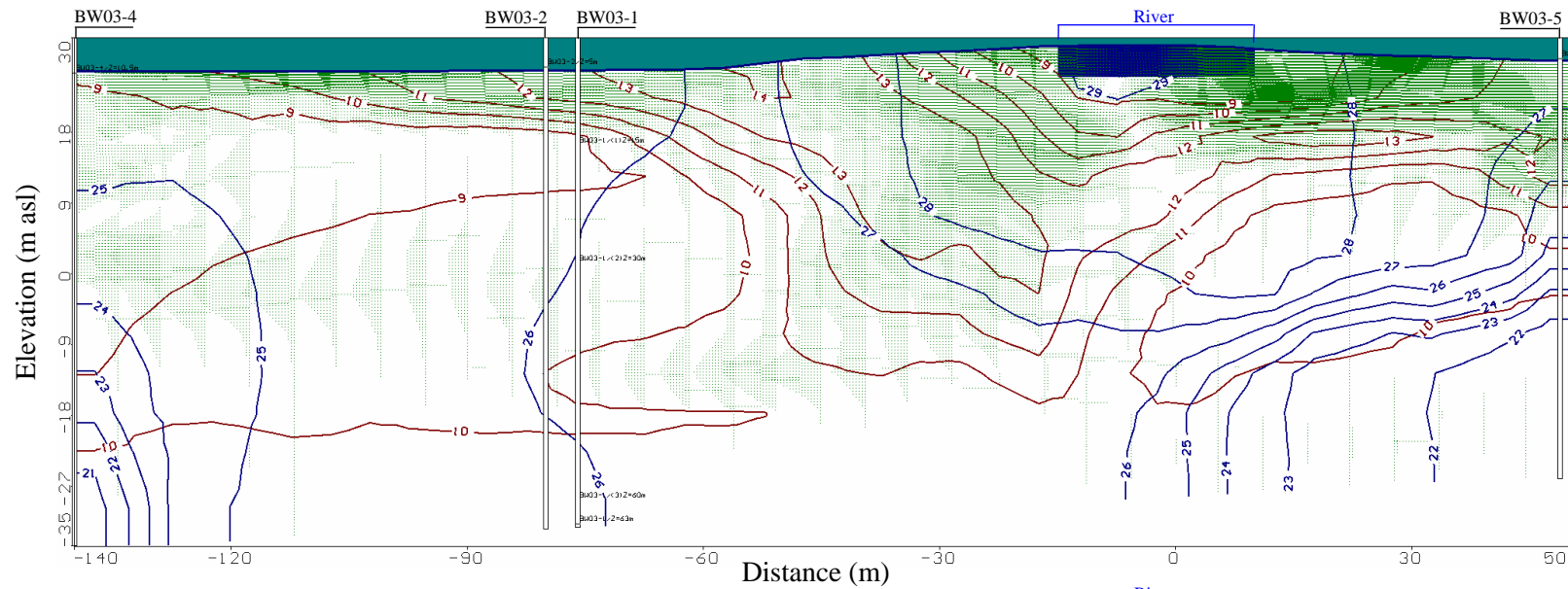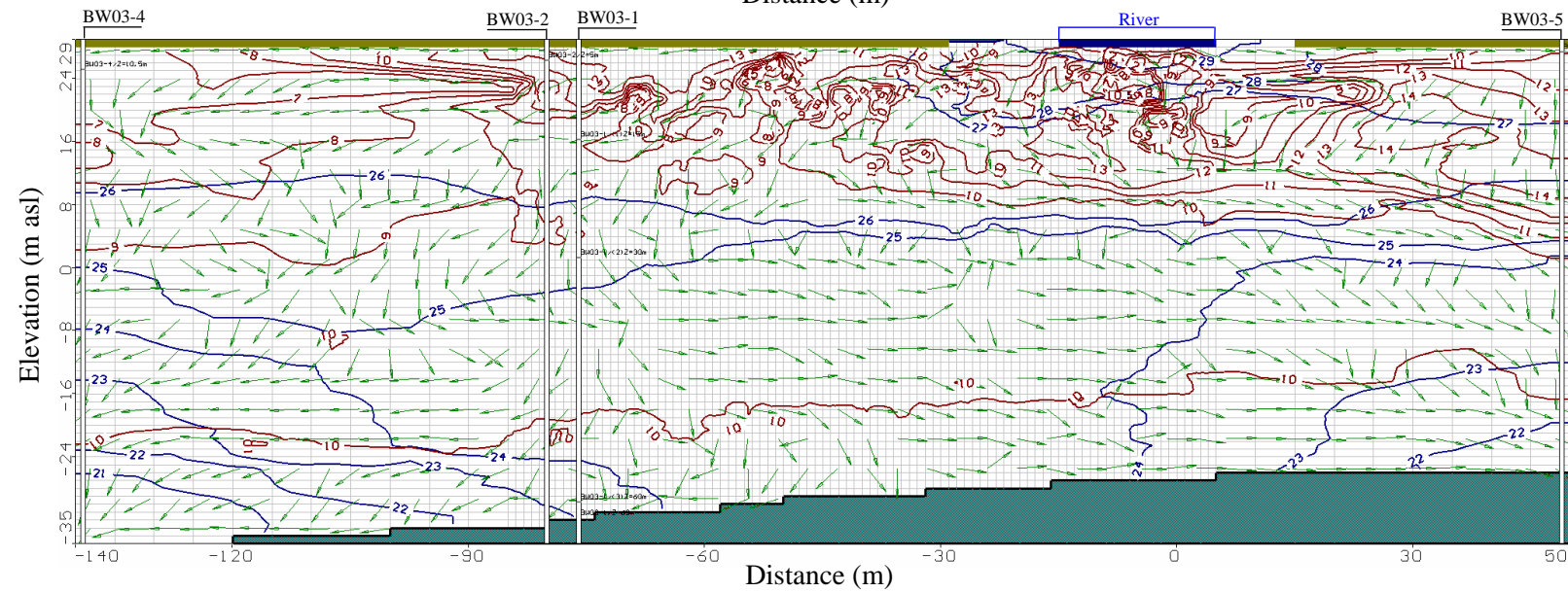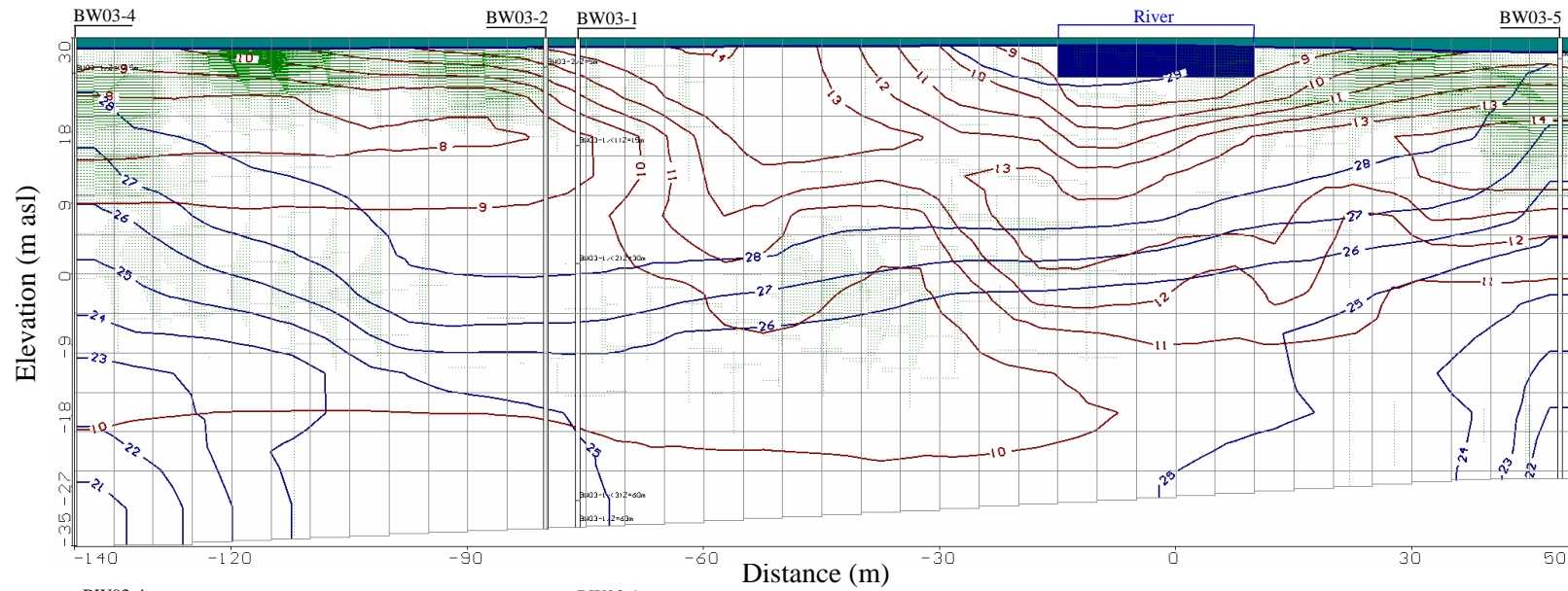
Case 8b

Realization no.17; T=264days; Maximum velocity = 650 m/d
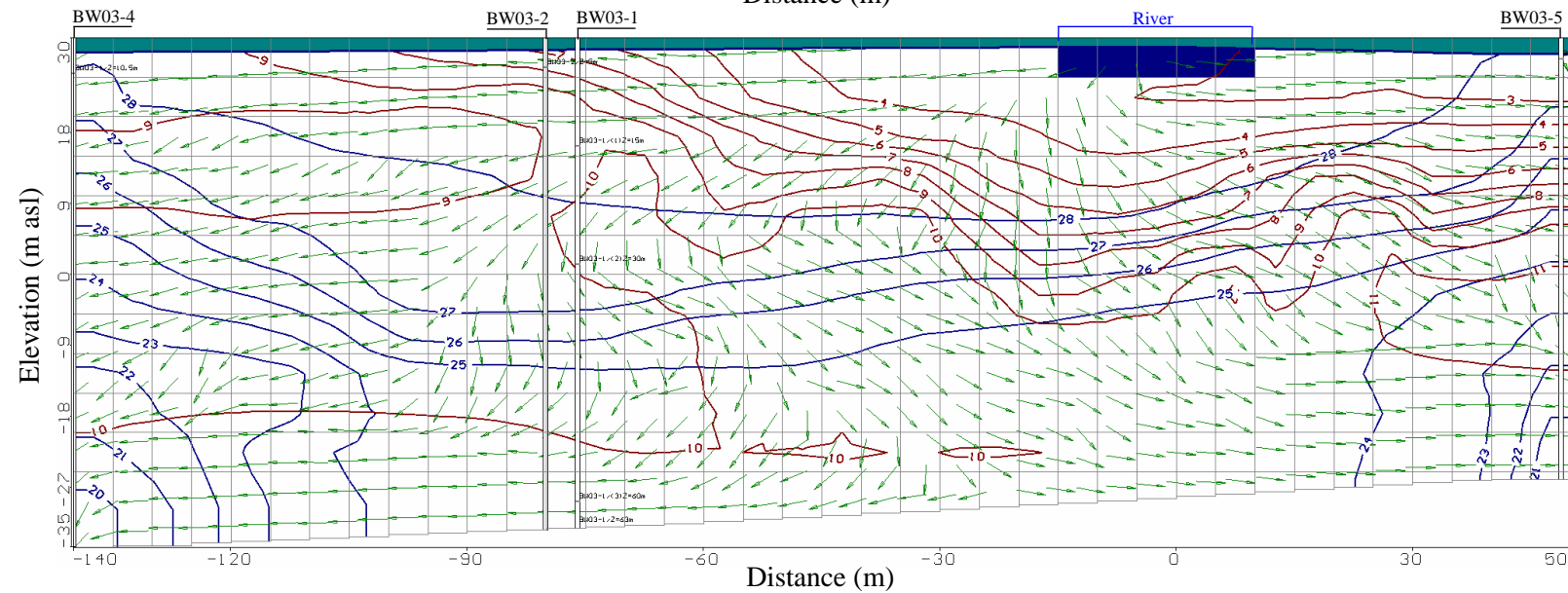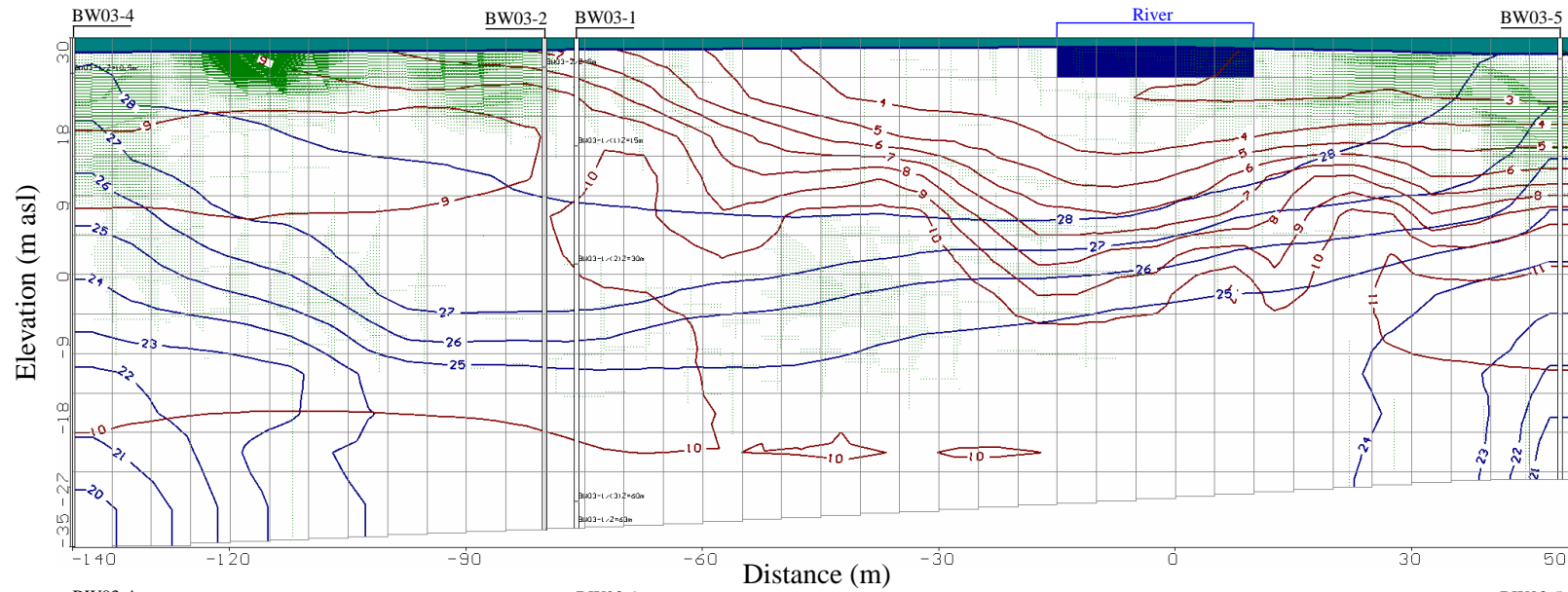
References

Aboufirassi M and Mariño MA (1983) Kriging of water levels in the Souss aquifer, Morocco. *Mathematical Geology*, doi: 10.1007/BF01031176

Abriola LM and Pinder GF (1982) Calculation of velocity in three space dimensions from hydraulic head measurements. *Ground Water*, 20(2), 205-213, doi: 10.1111/j.1745-6584.1982.tb02752.x

Ahmed S, Sarah S, Nabi A and Owais S (2010) Performing unbiased groundwater modeling: application of the theory of regionalized variables, *In Groundwater Modeling in Arid and Semi-Arid Areas* (Ed. Wheater HS, Mathias, SA and Li X). Cambridge University Press

Anderson MP (1989) Hydrogeologic facies models to delineate large-scale spatial trends in glacial and glaciofluvial sediments. *GSA Bulletin* 101:501-511, doi:10.1130/0016-7606

Anderson MP and Woessner WW (1992) *Applied Groundwater Modeling Simulation of Flow and Advective Transport*. Academic press

Anderson MP (2005) Heat as a ground water tracer, *Ground Water*, 43, 951-968

Anderson MP (2010) Heat transport in groundwater systems in Japan. *Journal of Ground Water Hydrology*, 52(4), 355–369

ASCE (American Society of Civil Engineers) (2008) *Standard guideline for fitting saturated hydraulic conductivity using probability density functions*. ASCE

Bear J (1972) *Dynamics of Fluids in Porous Media*. Dover

Bear J (1979) *Hydraulics of Groundwater*. McGraw-Hill

Bennett GL, Weissmann GS, Baker GS and Hyndmann DW (2006) Regional-scale assessment of a sequence-bounding paleosol on fluvial fans using ground-penetrating radar, eastern San Joaquin Valley, California. *Bulletin of the Geological Society of America*, 118, 724–732

Bower H (1978) *Groundwater Hydrology*, McGraw-Hill

Bull WB (1968) Alluvial fans. *Journal of Geologic Education*, 16, 101-106.

Burrough PA and McDonnell RA (1998) *Principles of Geographical Information Systems*. Oxford University Press

Cardenas MB and Jiang XW (2010) Groundwater flow, transport, and residence times through topography-driven basins with exponentially decreasing permeability and porosity. *Water Resoures Research* 46, W11538, doi :10.1029/2010WR009370

Carrera J and Mathias SA (2010) Groundwater flow and transport, *In Groundwater Modeling in Arid and Semi-Arid Areas* (Ed. Wheater HS, Mathias, SA and Li X). Cambridge University Press

Cehrs D (1979) Depositional control of aquifer characteristics in alluvial fans, Fresno Country, Calfornia. *Geologic Society of America Bulletin*, 90(2), 1282-1309

Chen X (2011) Depth-dependent hydraulic conductivity distribution patterns of a streambed. *Hydrological Processes*, 25, 278-287, doi:10.1002/hyp.7844

Cheong JY, Hamm SY, Kim HS, Ko EJ, Yang K and Lee JH (2008) Estimating hydraulic conductivity using grain-size analyses, aquifer tests, and numerical modeling in a riverside alluvial system in South Korea. *Hydrogeology Journal*, 16, 1129-1143, doi: 10.1007/s10040-008-0303-4

Chung JW and JD Rogers (2012) Interpolations of groundwater table elevation in dissected uplands, *Ground Water, 50*(4), 598-607, doi: 10.1111/j.1745-6584.2011.00889.x

Chilès JP and Delfiner P (1999) *Geostatistics: Modeling Spatial Uncertainty*. John Wiley and Sons

Constantz J (2008) Heat as a tracer to determine streambed water exchanges, *Water Resources Research*, 44, W00D10, doi: 10.1029/2008WR006996

Constantz J, Niswonger NRG and Stewart AE (2008) Analysis of Temperature Gradients to Determine Stream Exchanges with Ground Water, In *Field Techniques for Estimating Water Fluxes Between Surface Water and Ground Water* (Ed. Rosenberry DO and LaBaugh JW). USGS

Cressie NAC (1993) *Statistics for Spatial Dat*a *Revised Edition*. John Wiley and Sons

Dagan G (1997) Stochastic modeling of flow and transport: the broad perspective, In *Subsurface Flow and Transport: A Stochastic Approach* (Ed. Dagan G and Neuman SP). Cambridge University Press

Daimaru H (1989) Holocene evolution of the Toyohira River alluvial fan and distal floodplain, Hokkaido, Japan. *Geophysical Review of Japan*, 62(A-8), 589-603, In Japanese

Daimaru H (2003) Toyohira River alluvial fan, In *Regional Geomorphology of the Japanese Islands vol.2 Geomorphology of Hokkaido* (Ed. Koaze T, Nogami M, Ono Y, Hirakawa K). University of Tokyo Press, In Japanese

dell'Arciprete D, Bersezio R, Felletti F, Giudici M, Comunian A and Renard P (2012) Comparison of three geostatistical methods for hydrofacies simulation: a test on alluvial sediments. *Hydrogeology Journal*, 20, 299-311, doi: 10.1007/s10040-011-0808-0

de Marsily G (1986) *Quantitative Hydrogeology Groundwater Hydrology for Engineers*. Academic Press

Desbarats AJ, Logan CE, Hinton MJ and Sharpe DR (2002) On the kriging of water table elevations using collateral information from a digital elevation model. *Journal of Hydrology*, 255, 25-38

Deutsch CV and Journel AG (1998) *GSLIB Geostatistical Software Library and User's Guide Second Edition*. Oxford University Press

Deutsch CV (2002) *Geostatistical Reservoir Modeling*. Oxford Press

Deutsch CV (2007) A review of geostatistical approaches to data fusion, In *Subsurface Hydrology* (Ed. Hyndman DW, Day-Lewis FD and Singha K). AGU

de Vries JJ and Simmers I (2002) Groundwater recharge: an overview of processes and challenges. *Hydrogeology Journal*, 10, 5–17, doi: 0.1007/s10040-001-0171-7

Domenico PA and Schwartz FW (1998) *Physical and chemical hydrogeology 2nd edn*. Wiley

Doppler T, Franssen HJH, Kaiser HP, Kuhlman U and Stauffer F (2007) Field evidence of a dynamic leakage coefficient for modelling river–aquifer interactions. *Journal of Hydrology*, 347, 177-187, doi:10.1016/j.jhydrol.2007.09.017

Eaton TT (2006) On the importance of geological heterogeneity for flow simulation. *Sedimentary Geology*, 184, doi: 10.1016/j.sedgeo.2005.11.002

Einsele G (2000) *Sedimentary Basins 2nd edn*. Springer

Engeler I, Hendricks Franssen HJ, Müller R and Stauffer F (2011) The importance of coupled modelling of variably saturated groundwater flow-heat transport for assessing river–aquifer interactions. *Journal of Hydrology*, 397, 295-305, doi:10.1016/j.jhydrol.2010.12.007

Ezersky M (2008) Geoelectric structure of the Ein Gedi sinkhole occurrence site at the Dead Sea shore in Israel. *Journal of Applied Geophysics*, 64, 56-69, doi: 10.1016/j.jappgeo.2007.12.003

Falivene O, Cabrera L and SáezLarge A (2007) Large to intermediate-scale aquifer heterogeneity in fine-grain dominated alluvial fans (Cenozoic as Pontes Basin, northwestern Spain: insight based on three-dimensional geostatistical reconstruction. *Hydrogeology Journal*, 15, 861-876,

doi: 10.1007/s10040-007-0187-8

Ferreira JT, Ritzi Jr. RW and Dominic DF (2010) Measuring the permeability of open-framework gravel. *Ground Water*, 48, 593-597, doi: 10.1111/j.1745-6584.2010.00675.x

Fetter CW (2001) *Applied hydrogeology 4th edn*. Prentice-Hall

Fleckenstein JH, Niswonger RG and Fogg GE (2006) River-aquifer interactions, geologic heterogeneity, and low-flow management. *Ground Water*, 44(6), 837-852, doi: 10.1111/j.1745-6584.2006.00190.x

Freeze RA and Cherry JA (1979) *Groundwater*. Prentice-Hall

Frei S, Fleckenstein JH, Kollet SJ and Maxwell RM (2009) Patterns and dynamics of river–aquifer exchange with variably-saturated flow using a fully-coupled model. *Journal of Hydrology*, 375, 383–393, doi: 10.1016/j.jhydrol.2009.06.038

Fritz BG and Mackley RD (2010) A wet/wet differential pressure sensor for measuring vertical hydraulic gradient. *Ground Water*, 48(1), 117-121, doi: 10.1111/j.1745-6584.2011.00789.x

(2010)   1   (   ), 443-447

(1928)   (   )   35(418)   382-387

(1997)   ,

Gee GW, Hillel D (1988) Groundwater recharge in arid regions: Review and critique of estimation methods. *Hydrological Processes*, 2(3), 255–266, doi: 10.1002/hyp.3360020306

Genereux DP, Leahy S, Mitasova H, Kennedy CD and Corbett DR (2008) Spatial and temporal variability of streambed hydraulic conductivity in West Bear Creek, North Carolina, USA. *Journal of Hydrology*, 358, doi: 10.1016/j.jhydrol.2008.06.017

Goldschneider AA, Haralampides KA and MacQuarrie KTB (2007) River sediment and flow characteristics near a bank filtration water supply: implications for riverbed clogging. *Journal of Hydrology*, 344, 55-69, doi: 10.1061/j.jhydrol.2007.06.031

Gomez-Hernandez JJ and Journel A (1993) Joint sequential simulation of multigaussian fields, In *Geostatistics Tróia '92*. Springer

Goovaerts P (1997) *Geostatistics for Natural Resources Evaluation*. Oxford University Press

Gray WG and Pinder GF (1976) An Analysis of the Numerical Solution of the Transport Equation. *Water Resources Research*, 12, 547-555

Guo W and Bennett GD (1998) *SEAWAT version 1.1: A computer program for simulations of groundwater flow of variable density*. Missimer International, Inc.

Guo W and Langevin CD (2002) *User's Guide to SEAWAT: A computer program for simulation of three-dimensional variable-density ground-water flow*. USGS

Hails JR (1976) Compaction and diagenesis of very coarse-grained sediments, In *Compaction of Coarse-Grained Sediments, I* (Ed. Chilingarian GV and Wolf KH). Elsevier

Harbaugh AW, Banta ER, Hill MC and McDonald MG (2000) *MODFLOW-2000, The US Geological Survey modular ground-water model-User Guide to modularization concepts and the ground-water flow process*. USGS

Harte PT and Kiah RG (2009) Measured river leakages using conventional streamflow techniques: the case of Souhegan River, New Hampshire, USA. *Hydrogeology Journal*, 17, 409-424, doi: 10.1007/s10040-008-0359-1

Hatanaka M, Uchida A, Taya Y, Takehara N, Hagisawa T, Sakou N and Ogawa S (2001) Permeability Characteristics of High-QualityUndisturbed Gravelly Soils Measured in Laboratory Tests, *Soils and Foundations*, 41(3), 45-55

Hazen A (1911) Discussion: Dams on sand foundations. *Transactions*, ASCE 73:199-203

Healy RW (2010) *Estimating Groundwater Recharge*. Cambridge University Press

Heinz J, Kleineidam S, Teutsch G and Aigner T (2003) Heterogeneity patterns of Quaternary glaciofluvial gravel bodies (SW-Germany): application to hydrogeology. *Sedimentary Geology*, 158, 1-23

Hess KM, Wolf SH and Celia MA (1992) Large-scale natural gradient tracer test in sand and gravel, Cape Cod, Massachusetts: 3. Hydraulic conductivity variability and calculated macrodispersivities. *Water Resources Research*, 28, 2011-2027, doi: 10.1029/92WR00668

Hengel T (2007) *A Practical Guide to Geostatistical Mapping of Environmental Variables*. JRC Science and Technical Reports, EUR 22904 EN-2007, Office for Official Publications of the European Communities

Hoeksema RJ, Clapp RB, Thomas AL, Hunley AE, Farrow ND and Dearstone KC (1989)

Cokriging model for estimation of water table elevation. *Water Resources Research*, *25*(3), 429-438

(2006a)

(2006b)

(2008)

(1992)   (15) 3-2.

34(1)   31-40

Hu SG, Yamazaki M, Sataka H, Akiyama T and Hirano R (2001) Tephrochronological reconsideration on Shikotsu Pumice Flow and Fall Deposits, Hokkaido, Japan. *Earth Science*, 55(3), 145-156, In Japanese

Hu SG, Kobayashi T, Okuda E, Oishi A, Saito M, Kayaki, T and Miyazaki S (2010a) Alluvial fans-importance and relevance: a review of studies of Research group on Hydro-environments around alluvial fans in Japan, In *Groundwater Response to Changing Climate* (ed. Taniguchi M and Holman IP). 131-139, CRC Press, doi: 10.1201/b10530-13

Hu SG, S Miyajima, D Nagaoka, K Koizumi and K Mukai (2010b) Study on the relation between groundwater and surface water in Toyohira-gawa alluvial fan, Hokkaido, Japan, In *Groundwater Response to Changing Climate* (ed. Taniguchi M and Holman IP). 141-158, CRC Press, doi: 10.1201/b10530-13

Hubbert MK (1940) The theory of groundwater motion. *Journal of Geology*, 48, 785-944

Huyakorn PS and Pinder GF (1983) *Computational Methods in Subsurface Flow*. Academic Press

Hvorslev MJ (1951) Time lag and soil permeability in ground water observations. *U.S. Army Waterways Experiment Station, Bulletin*, 36

Institute of Civil Engneers (ICE; 1976) *Manual of applied geology for engineers*. ICE

Ingebritsen SE, Sanford WE and Neuzil CE (2006) *Groundwater in geologic processes 2nd edn.* Cambridge university press

Ishida M, Soya T and Suda Y (1980) *Geological map of Japan 1:200,000 Sapporo*. Geological survey of Japan, NK-54-14

International Organization for Standardization (ISO; 2007) *Hydrometry - Measurement of Liquid Flow in Open Channels Using Current Meters or Floats Fourth edition*. ISO

Jang CS and Liu CW (2005) Contamination potential of nitrogen compounds in the heterogeneous aquifers of the Choushui River alluvial fan, Taiwan, *Journal of Contaminant Hydrology*, 79, 135-155

Jessop AM (1990) *Thermal geophysics*. Elsevier

JGS (Japan Geotechnical Society) (2004) Method for determination of hydraulic properties of aquifer in single borehole, In: *Japanese standards for geotechnical and geoenvironmental investigation methods*. Japan Geotechnical Society

Jiang XW, Wan L, Wang XS, Ge S and Liu J (2009) Effect of exponential decay in hydraulic conductivity with depth on regional groundwater flow. *Geophysical Research Letters*, 36, L24402, doi: 10.1029/2009GL041251

Jumikis AR (1977) *Thermal geotechnics*. Rutgers university press

Jiang XW, Wang XS and Wan L (2010) Semi-empirical equations for the systematic decrease in permeability with depth in porous and fractured media. *Hydrogeology Journal*, 18, 839–850, doi: 10.1007/s10040-010-0575-3

Johnson LE (2009) *Geographic Information Systems in Water Resources Engneering*. CRC Press

Journel AG, Gundeso R, Gringarten E and Yao T (1998) Stochastic modelling of a fluvial reservoir: a comparative review of algorithms. *Journal of Petroleum Science and Engineering*, 21, 95-121.

Journel AG and Huijbregts CJ (1978) *Mining geostatistics*. Academic press

Jussel P, Stauffer F and Dracos T (1994) Transport modeling in heterogeneous aquifers: 1. statistical description and numerical generation of gravel deposits. *Water Resources Research*, 30, 1803-1817

Kamann PJ, Ritzi RW, Dominic DF and Conrad CM (2007) Porosity and permeability in sediment mixtures. *Ground Water*, 45, 429-438, doi: 10.1111/j.1745-6584.2007.00313.x

Kasper JW, Denver JM, McKenna TE and Ullman WJ (2010) Simulated impacts of artificial groundwater recharge and discharge on the source area and source volume of an Atlantic Coastal Plain stream, Delaware, USA. *Hydrogeology Journal*, 18, 1855-1866, doi: 10.1007/s10040-010-0641-x

Katakai T, Ogita A, Sumi T and Tsujimoto T (2006) Experimental study on the clogging soil

porosity on boundary area between water edge and river bed, *Proceedings of Hydraulic Engineering, Japan Society of Civil Engneering*, (50), 241-246, In Japanese

Kato M, Fukatsukawa K, Kikuchi J, Matsumoto K (1995) Subsurface geology and sedimentary structure of alluvium in Sapporo city. *Proceedings of the thirty-five Conference of Hokkaido Branch, Japan Geotechnical Society Engineering*, 82-89, Japanese Geotechniacal Society, In Japanese

Kawata E and Obara T (1958) Underground Water in the Top of the Sapporo-Fan. *Report of the Geological Survey of Hokkaido*, 19, 30-31, Geological Survey of Hokkaido, In Japanese

Kayane I and Yamamoto S (1971) *Hydrologic Cycle in Alluvial Fan*. Kokon-shoin, In Japanese

(1991)

Kendall MG (1975) *Rank Correlation Methods*. Charles Griffin

Kitanidis PK (1993) Generalized covariance functions in estimation. *Mathematical Geology*, 25(5), 525-540

Knotters M, Brus DJ and Oude Voshaar JH (1995) A comparison of kriging, co-kriging and kriging combined with regression for spatial interpolation of horizon depth with censored observations. *Geoderma*, 67, 227-246

Kodama Y and Inokuchi M (1986) Changes in the sedimentary fabric of surface deposits along the lower course of the river Waterase. *Bulletin of the Environmental Research Center*, 10, 67-79 In Japanese

(2006)   .

Koizumi K, Mukai K, Konishi H and Hu SG (2008) Change of Water Balance by Global Warming in the Toyohira-gawa Alluvial Fan. In: *Hydro-environments of Alluvial Fans in Japan* (ed. Secretariat of RHF), 13-28, Research group on Hydro-environment around alluvial Fans

Koltermann CE and Gorelick SM (1995) Fractional packing model for hydraulic conductivity derived sediment mixtures. *Water Resources Research*, 31, 3283-3297

Koltermann CE and Gorelick SM (1996) Heterogeneity in sedimentary deposits: a review of structure-imitating, process-imitating, and descriptive approaches. *Water Resources Research* 32(9), doi:10.1029/96WR00025

(2006)

, e- 2006

Kresic N (2007) *Hydrogeology and groundwater modeling 2nd edn*. CRC Press

Kundzewicz ZW, Mata LJ, Arnell NW, et al. (2007) Freshwater resources and their management. In *Climate Change 2007: Impacts, Adaptation and Vulnerability. Contribution of Working Group II to the Fourth Assessment Report of the Intergovernmental Panel on Climate Change*, ed. Parry ML, Canziani OF, Palutikof JP, van der Linden PJ, aand Hanson CE, 173-210, Cambridge University Press

Langevin CD, Shoemaker WB and Guo W (2003) *MODFLOW-2000, the US Geological Survey modular ground-water model-documentation of the SEAWAT-2000 version with the variable density flow process (VDF) and the Integrated MT3DMS Transport Process (IMT)*. Open File Report 03-426, USGS

Langevin CD, Thorne Jr DT, Dausman AM, Sukop MC and Guo W (2008) *SEAWAT version 4: a computer program for simulation of multi-species solute and heat transport*, USDI/USGS

Lamotte JL and Delay F (1997) On the stability of the 2D interpolation algorithms with uncertain data. *Mathematics and Computers in Simulation*, 43, 183-201

Lapham WW (1989) *Use of Temperature Profiles Beneath Streams to Determine Rates of Vertical Ground-Water Flow and Vertical Hydarulic Conductivit*. Water-Supply Paper 2337, USGS

Lecce SA (1990) The alluvial fan problems, In *Alluvial fans: a field approach* (ed. Rachocki AH and Church M). John Wiley and Sons

Lee JY, Yi MJ and Hwang D (2005) Dependency of hydrologic responses and recharge estimates on water-level monitoring locations within a small catchment. *Geosciences Journal*, 9(3), 277-286, doi: 10.1007/BF02910588

Lee SY, Carle SF and Fogg GE (2007) Geologic heterogeneity and a comparison of two geostatistical models: Sequential Gaussian and transition probability-based geostatistical simulation. *Advances in Water Resources*, 30, doi: 10.1016/j.advwatres.2007.03.005

Lunt IA, Bridge JS and Tye RA (2004) A quantitative, three-dimensional depositional model of gravelly braided rivers. *Sedimentology*, 41, 377-414, doi: 10.1111/j.1365-3091.2004.00627.x

Lunt IA and Bridge JS (2007) Formation and preservation of open-framework gravel strata in unidirectional flows. *Sedimentology*, 54, 71-87, doi: 10.1111/j.1365-3091.2006.00829.x

Luo W, Grudzinski B and Pederson D (2011) Estimating hydraulic conductivity for the Martian subsurface based on drainage patterns-a case study in the Mare Tyrrhenum Quadrangle. *Geomorphology*, 125, 414-420, doi: 10.1016/j.geomorph.2010.10.018

Ma R and Zheng C (2010) Effects of Density and Viscosity in Modeling Heat as a Groundwater Tracer. *Ground Water*, 48(3), 380-389, doi: 10.1111/j.1745-6584.2009.00660.x

Major JJ (1997) Depositional processes in large-scale debris-flow experiments. *The Journal of Geology*, 105, 345-366, doi: 10.1086/515930

Major JJ (2000) Gravity-driven consolidation of granular slurries: implications for debris-flow deposition and deposit characteristics. *Journal of Sedimentary Research*, 70, 64-83, doi: 1073-130X/00/070-64/$03.00

Mann HB (1945) Non-parametric tests against trend. *Econometrica*, 13(2), 245-259

Manning CE and Ingebritsen SE (1999) Permeability of the continental crust: implications of geothermal data and metamorphic systems. *Reviews of Geophysics*, 37, 127-150, doi: 10.1029/1998RG900002

Marion A, Packman AI, Zaramella M and Bottacin-Busolin A (2008) Hyporheic flows in stratified beds. *Water Resoures Research*, 44, W09433, doi: 10.1029/2007WR006079

Matsumoto N and Yamaguchi Y (1991) Interaction between stress and permeability in sand and gravel deposit. *Journal of Geotechnical Engineering*, 430, 59-67, In Japanese

McElwee CD, Butler Jr.JJ and Healey JM (1991) A New sampling system for obtaining relatively undisturbed samples of unconsolidated coarse sand and gravel. *Ground Water Monitoring & Remediation*, 11, 182-191, doi: 10.1111/j.1745-6592.1991.tb00390.x

McIlvride WA and Rector BM (1988) Comparison of short-and long-screen monitoring wells in alluvial sediments. In *Proceedings of the Second National Outdoor Action Conference on Aquifer Restoration, Ground Water Monitoring and Geophysical Methods*, 375-390, National Water Well Association

Mercer JW and Faust CR (1981) *Groundwater modeling*. National Water Well Association

Miall AD (1992) Alluvial deposits. In *Facies models response to sea level change* (Ed. Walker RG and James NP), Geological Association of Canada

Minasny B and McBratney AB (2007) Spatial prediction of soil properties using EBLUP with the

Matérn covariance function.Geo*derma*,140(4),324-336, doi: 10.1016/j.geoderma.2007.04.028

Mitchum RM, Vail PR and Thompson S (1977) Part Two: The depositional sequence as a basin unit for stratigraphic analysis, In "*Seimic Stratigraphy- Application to Hydrocarbon Exploration* (ed. Payton CE), 53-62, American Association of Petroleum Geologists

Morin RH (2006) Negative correlation between porosity and hydraulic conductivity in sand-and-gravel aquifers at Cape Cod, Massachusetts, USA. *Journal of hydrology*, 316, 43-52, doi: 10.1016/j.jhydrol.2005.04.013

Nagaoka D, Koizumi K, Mukai K and Hu SG (2008) Geomorphological development and hydrogeology in the Toyohira-gawa Alluvial Fan, Central Hokkaido, Japan. In: *Hydro-environments of Alluvial Fans in Japan* (ed. Secretariat of RHF), 13-28, Research group on Hydro-environment around alluvial Fans

(2009) Excel

(1983)   47-63

National and Regional Policy Bureau (2007) *Water Well Data in Japan*. Geographical information system portal site (http://www.gis.go.jp/contents/list/detail/000005.html), Accessed 25 June 2010.

Neton MJ, Dorsch J, Olson CFD and Young SC (1994) Architecture and directional scales of heterogeneity in alluvail-fan aquifers. *Journal of Sedimentary Research*, 2, 245-257

Nikroo L, Kompani-Zare M, Sepaskhah AR and Shamsi SRF (2010) Groundwater depth and elevation interpolation by kriging methods in Mohr Basin of Fars province in Iran. *Environmental Monitoring and Assessment*, doi: 10.1007/s10661-009-1010-x

Oka T (2005) Analyzing the subsurface geologic structure of the central part of Sapporo City and its northwest suburb by drilling data of fluid resources, with notes on geological explanation for six profiles of seimic prospecting performed by the municipal authorities of Sapporo City and so on. *Report of the Geological Survey of Hokkaido*, 76, 1-54, Geological Survey of Hokkaido, In Japanese

(2000)   1988 1999

                                                    12   20-32

Obara T (1971) On the fluctuation of the ground water level in Toyohira-gawa Fan, Sapporo. *Report of the Geological Survey of Hokkaido*, 44, 79-86, Geological Survey of Hokkaido, In Japanese

(1969)   , 39,

Report of the Geological Survey of Hokkaido, 76, 1-54, Geological Survey of Hokkaido, In Japanese

Ono Y (1990) Alluvial fans in Japan and South Korea, In *Alluvial fans: a field approach* (ed. Rachocki AH and Church M). John Wiley and Sons

Ohta A, Tani K, Yamada S and Kaneko S (2007) Mechanical characteristics of undisturbed sandy gravel including water channel. *Proceedings of the forty-second Japan National Conference of Geotechnical Engineering*, Nagoya, Japan, 447-448, the Japanese Geotechniacal Society.

(1974)   No.1

Ozaki T, Kishi K, Koma T and Yokota S (1965) Areal Investigation for Ground Water Resources on the Lower Steams of Toyohira River Basin and Hassamu River Basin, Hokkaido, *Bulletin of the Geological Survey of Japan*, 16(1), 1-24, Geological Survey of Japan, In Japanese

Pardo-Igúzquiza E and Chica-Olmo M (2004) Estimation of gradients from sparse data by universal kriging. *Water Resources Research*, 40(12), doi: 10.1029/2004WR003081

Philip RD and Kitanidis PK (1989) Geostatistical estimation of hydraulic head gradients. *Ground Water*, 27(6), 855-865, doi: 10.1111/j.1745-6584.1989.tb01049.x

Proce CJ, Ritzi RW, Dominic DF and Zhenxue D (2004) Modeling multiscale heterogeneity and aquifer interconnectivity. *GroundWater,* 42(5), 658-670, doi10.1111/j.1745-6584.2004.tb02720.x

Public Works Research Institute   2002   14

Rehmel M (2007) Application of acoustic doppler velocimeters for streamflow. *Journal of Hyrdraulic Engineering*, 133, doi: 10.1061/(ASCE)0733-9429(2007)133:12(1433)

Rivest M, Marcotte D and Pasquier P (2008) Hydraulic head field estimation using kriging with an external drift: A way to consider conceptual model information, *Journal of Hydrology, 361*,

349–361, doi: 10.1016/j.jhydrol.2008.08.006

Rossi P, De Carvalho-Dill A, Müller I and Aragno M (1994) Comparative tracing experiments in a porous aquifer using bacteriophages and fluorescent dye on a test field located at Wilerwald (Switzerland) and simultaneously surveyed in detail on a local scale by radio-magneto-tellury (12–240 kHz). *Environmental Geology*, 23(3), 192-200, doi: 10.1007/BF00771788

Rubin Y (2003) *Applied stochastic hydrogeology*. Oxford university press

Rushton KR (2003) *Groundwater Hydrology Conceptual and Computational Models*. John Wiley and Sons

Rust BR (1979) Facies Models 2. Coarse Alluvial Deposits. In *Facies Models 2nd edition* (Ed. Walker RG). Toronto, Canada: Geological Association of Canada

Saar MO and Manga M (2004) Depth dependence of permeability in the Oregon Cascades inferred from hydrogeologic, thermal, seismic, and magmatic modeling constraints. *Journal of Geophysical Research*, 109, B04204, doi: 10.1029/2003JB002855

Sagayama T, Igarashi Y, Kondou T, Kamada K, Yoshida M, Chitoku T, Sotozaki T, Kudou C, Okamura S and Katou M (2007) Quarternary stratigraphy of teh 150 m core in the central part of Sapporo, Japan. *Journal of Geological Society Japan*, 113(8), 391-405, In Japanese

Saito H and Goovaerts P (2002) Accounting for measurement error in uncertainty modeling and decision-making using indicator kriging and p-field simulation: application to a dioxin contaminated site. *Environmetrics*, doi: 10.1002/env.545

(1998)

2009

2009

Sakata Y, Ito K, Isozaki S and Ikeda R (2011) A distribution model of permeability derived from undisturbed gravelly samples in alluvial fan. *Japanese Geotechnical Journal*, 6(1), 109–119

Sakata Y and Ikeda R (2012a) Quantification of longitudinal river discharge and leakage in an alluvial Fan by synoptic survey using handheld ADV. *Journal of Japan Society of Hydrology and Water Resources*, *25*(2), 89-102

Sakata Y and Ikeda R (2012b) Effectiveness of a high resolution model on groundwater simulation

in an alluvial fan. *Geophysical Bulletin of Hokkaido University*, 75, 73-89

Sakata Y and Ikeda R (2013) Depth dependence and exponential models of permeability in alluvial fan gravel deposits. *Hydrogeology Journal*, 21, 773-786, doi: 10.1007/s10040-013-0961-8

Salmi T, Määttä A, Anttila P, Ruoho-Airola T and Amnell T (2002) *Detecting trends of annual values of atmospheric pollutants by the Mann-Kendall test and Sen's slope estimates-the Excel template application MAKESENS*. Finnish Meteorological Institute

Scanlon BR, Healy RW and Cook PG (2002) Choosing appropriate techniques for quantifying groundwater recharge. *Hydrogeology Journal*, 10, 18-39, doi: 10.1007/s10040-002-0200-1

Sasaki S (1974) On the influent seepage from rivers on alluvial fans. *Hydrology*, 6, 35-38, In Japanese

札幌市環境局 (2008) 札幌市の環境－大気・水質・騒音等のデータ集－（平成 20 年度測定結果），札幌市，159-160

札幌市環境局(2011)地下水質の現況，札幌市

札樽経済協議会 (1963) 豊平川扇状地地下水調査報告書. 札樽経済協議会

Scanlon BR, Healy RW and Cook PG (2002) Choosing appropriate techniques for quantifying groundwater recharge, *Hydrogeology Journal*, 10, 18-39, doi: 10.1007/s10040-0010176-2

Selley RC (2000) *Applied Sedimentology second edition*. Academic Press

Sen PK (1968) Estimates of the regression coefficient based on Kendall'Tau. *Journal of the American Statistical Association*, 63, 1379-1389

Shepherd RG (1989) Correlations of permeability and grain size. *Ground Water*, 27, 633-638, doi: 10.1111/j.1745-6584.1989.tb00476.x

Simonds FW and KA Sinclair (2002) Surface Water-Ground Water Interactions Along the Lower Dungeness River and Vertical Hydraulic Conductivity of Streambed Sediments, Clallam County, Washington, September 1999-July 2001. *Water-Resources Investigations Report*, 02-4161, USGS

Singhal BBS and Gupta RP (1999) *Applied hydrogeology of fractured rocks*. Kluwer academic publishers

Snow DT (1969) Anisotropic permeability of fractured media. *Water Resources Research,* 5, doi: 10.1029/WR005i006p01273

Soderberg K and Hennet RJC (2007) Uncertainty and Trend Analysis-Radium in Ground Water and Drinking Water. *Ground Water Monitoring and Remediation*, doi: 10.1111/j.1745-6592.2007.00167.x

Song J, Chen X, Cheng C, Wang D, Lackey S and Xu Z (2009) Feasibility of grain-size analysis methods for determination of vertical hydraulic conductivity of streambeds. *Journal of Hydrology*, 375, 428-437, doi: 10.1016/j.jhydrol.2009.06.043

SonTek/YSI (2009) *FlowTracker Handheld ADV Technical Manual*. SonTek/YSI

Sposito G (1998) *Scale Dependence and Scale Invariance in Hydrology*. Cambridge university press

Stonestrom DA and Constantz J (2003) *Heat as a tool for studying the movement of ground water near streams*. Circular 1260, USGS

Stone MC and Hotchkiss RH (2007) Evaluating velocity measurement techniques in shallow streams. *Journal of Hydraulic Research*, 45, 752-762, doi: 10.1080/00221686.2007.9521813

Takizawa S (2008) Groundwater use and management in urban areas, In *Groundwater Management in Asian Cities Technology and Policy for Sustainability* (Ed. Takizawa S), 13-33, Springer (2009)

—   20

Tanaka Y, Kudo K, Yosida Y, Nisi K, Aida M and Suzuki H (1990) On the applicability of various sampling methods to the gravelly ground. *Abiko Research Laboratory Reports*, U90046, Central Research Institute of Electric Power Industry

Uchida Y, Sakura Y and Taniguchi M (2001) Shallow subsurface thermal regime in Japan – new concept of subsurface thermal regime-. *Journal of geothermal research society of Japan*, 23(3), 167-180, In Japanese

Taniguchi M (1993) Evaluation of vertical groundwater fluxes and thermal properties of aquifers based on transient temperature-depth profiles. *Water Resources Research*, 29(7), 2021-2026, doi: 10.1029/93WR00541

Taniguchi M, Shimada J, Tanaka T, Kayane I, Sakura Y, Shimano Y, Dapaah-Siakwan S and Kawashima S (1999) Disturbances of temperature-depth profiles due to surface climate

change and subsurface water flow: 1. An effect of linear increase in surface temperature caused by global warming and urbanization in the Tokyo metropolitan area, Japan. *Water Resources Research*, 35(5), 1507-1517, doi: 10.1029/1999WR900009

Taniguchi M and Uemura T (2005) Effects of urbanization and groundwater flow on the subsurface temperature in Osaka, Japan. Physics of the earth and planetary interiors, 152, 305–313, doi:10.1016/j.pepi.2005.04.006

Taylor CJ and Alley WM (2001) *Ground-water-level monitoring and the importance of long-term water-level data, U.S. Geological Survey Circular 1217*. U.S. Geological Survey

Tebakari T (2010) Example of Flow Regime and Discharge Observation Using the ADCP in the Uchikawa and the *Kurobegawa*, 1

Thorne D, Langevin CD and Sukopc MC (2006) Addition of simultaneous heat and solute transport and variable fluid viscosity to SEAWAT. *Computers & Geosciences*, 32, 1758-1768, doi: 10.1016/j.cageo.2006.04.005

Todd DK and Mays LW (2005) *Groundwater Hydrology 3rd edn*. Willey and Sons

Tolman CF (1937) *Groundwater*. McGraw-Hill

Tonkin MJ and Larson SP (2002) Kriging water levels with a regional-linear and point-logarithmic drift. *Ground Water*, doi:10.1111/j.1745-6584.2002.tb02503.x

Tóth J (2009) *Gravitational Systems of Groundwater Flow Theory, Evaluation, Utilization*. Cambridge University Press

Toyota M, Taira A, Hikita M and Miyahara Y (2010) Field measurements of lake currents in Lake Suwa by means of ADCP. *Japanese Journal of Limnology*, 71, 45-52, In Japanese

Turnipseed DP and Sauer VB (2010) *Discharge Measurements at Gaging Stations*. Techniques and Methods 3–A8, USGS

United Nations Environment Programme (UNEP) (1992) *World Atlas of Desertification*. London: Edward Arnold.

Varouchakis EA and Hristopulos DT (2012) Comparison of stochastic and deterministic methods for mapping groundwater level spatial variability in sparsely monitored basins. *Environmental Monitoring and Assessment*, doi: 10.1007/s10661-012-2527-y

Vandenbohede A and Lebbe L (2010) Parameter estimation based on vertical heat transport in the surficial zone. *Hydrogeology Journal*, 18, 931–943, doi: 10.1007/s10040-009-0557-5

Vienken T and Dietrich P (2011) Field evaluation of methods for determining hydraulic conductivity from grain size data. *Journal of Hydrology*, 400, 58-71, doi: 10.1016/j.jhydrol.2011.01.022

Vukovic M and Soro A (1992) Determination of hydraulic conductivity of porous media from grain-size composition. *Water Resources Publications*

Wackernagel H (2003) *Multivariate Geostatistics: An Introduction with Application 2nd edition*. Springer

Wang XS, Jiang XW, Wan L, Song G and Xia Q (2009) Evaluation of depth-dependent porosity and bulk modulus of a shear using permeability-depth trends. *International Journal of Rock Mechanics & Mining Sciences*, 46, 1175-1181, doi: 10.1016/j.ijrmms.2009.02.002

Wen F and Chen X (2006) Evaluation of the impact of groundwater irrigation on streamflow in Nebraska. *Journal of Hydrology*, 327, doi: 10.1016/j.jhydrol.2005.12.016

Weight WD (2008) *Hydrogeology Field Manual 2nd Edition*. McGraw-Hill

Weismann GS and Fogg GE (1999) Multi-scale alluvial fan heterogeneity modeled with transition probability geostatistics in a sequence stratigraphic framework. *Jounral of Hydrology*, 226, 48-65

Weissmann GS, Carle SA and Fogg GE (1999) Three-dimensional hydrofacies modeling based on soil survey analysis and transition probability geostatistics. *Water Resources Research*, 35(6), 1761-1770

Weissmann GS, Mount JF and Fogg GE (2002) Glacially-driven cycles in accumulation space and sequence stratigraphy of a stream-dominated alluvial fan, San Joaquin Valley, California, U.S.A. *Journal of Sedimentary Research*, 72(2), 240-251

Whiting PJ (2003) Flow Measurement and Characterization. In *Tools in Fluvial Geomorphology* (Ed. Kondolf GM and Piégay H), John Wiley and Sons

Wiberg PL and Smith JD (1991) Velocity distribution and bed roughness in high-gradient streams. *Water Resources* Research, 27(5), 825–838, doi: 10.1029/90WR02770

Winter TC, Harvey JW, Franke OL and Alley WM (1998) *Groundwater and Surface Water A Single Resource*. Circular 1139, USGS

Woessner WW (2000) Stream and fluvial plain ground water interactions: rescaling hydrogeologic thought. *Ground Water*, 38(3), 423-429, doi: 10.1111/j.1745-6584.2000.tb00228.x

Yamaguchi H, Osanai H, Sato O, Futamase K, Obara T, Hayakawa F and Yokoyama E (1965) *Explanatory text of hydrogeological maps of Hokkaido No. 8, Sapporo, special part "the grounds and groundwater of Sapporo environments."* Geological survey of Hokkaido, In Japanese

(1983)   79-93

(1995)   37(6),
4-10

Ye M and Khaleel R (2008) A Markov chain model for characterizing medium heterogeneity and sediment layering structure. *Water Resources Research*, 44, W09427, doi: 10.1029/2008WR006924

Zappa G, Bersezio R, Felletti F and Giudici M (2006) Modeling heterogeneity of gravel-sand, braided stream, alluvial aquifers at the facies scale. *Journal of Hydrology*, 325, 134-153, doi: 10.1016/j.jhydrol.2005.10.016

Zhang Y, Gable CW and Person M (2006) Equivalent hydraulic conductivity of an experimental stratigraphy: implications for basin-scale flow simulations. *Water Resources Research*, 42, W05404, doi:10.1029/2005WR004720

Zhang Y, Gable CW and Sheets B (2010) Equivalent hydraulic conductivity of three-dimensional heterogeneous porous media: an upscaling study based on an experimental stratigraphy. *Journal of Hydrology*, 388, 304-320, doi: 10.1016/j.jhydrol.2010.05.009

Zheng C and Bennett GD (1995) *Applied Contaminant Transport Modeling: Theory and Practic*e. John Wiley & Sons

Zheng C and Wang PP (1999) *MT3DMS: A modular threedimensional multispecies transport model for simulation of advection, dispersion, and chemical reactions of contaminants in groundwater systems; documentation and user's guide, Contract Report SERDP-99-1.* US Army Engineer Research and Development Center

Zlotnik VA, Cardenas MB and Toundykov D (2011) Effects of multiscale snisotropy on basin and hyporheic groundwater Flow. *Ground Water*, 49, 576-583, doi: